UNIVERSITY OF NAVARRA
**SCHOOL OF ENGINEERING**
DONOSTIA-SAN SEBASTIÁN

# Planning and registration techniques for image-guided robotic spinal surgery

DISSERTATION
submitted for the
Degree of Doctor of Philosophy
of the University of Navarra by

**Álvaro Bertelsen Simonetti**

under the supervision of

**Diego Borro Yágüez**

December, 2012

Servicio de Publicaciones de la Universidad de Navarra

ISBN 978-84-8081-342-6

*A mi esposa Nerea*

# Agradecimientos

El tiempo de mi tesis doctoral está llegando a su fin y ha llegado la hora de escribir los agradecimientos. No puedo comenzar sin darle las gracias a Dios, por haberme dado todo lo que tengo en esta vida, también la oportunidad de hacer esta tesis ¡Aunque no ha sido nada fácil! Aún así quiero darle a Él las gracias, incluso por los momentos difíciles que me han hecho crecer y hacerme un poco más fuerte. Espero, con este trabajo, haber aprovechado bien los talentos que Él me ha dado y espero seguir haciéndolo así durante toda mi vida.

Quiero agradecer a mi esposa Nerea –a quien va dedicada esta tesis– por haber estado siempre a mi lado y haberme dado los mejores años de mi vida. Nunca me ha faltado su apoyo, su comprensión y su cariño en los momentos difíciles. Tampoco ha fallado en todas las ocasiones –¡tantas!– en las que he tenido que trabajar hasta tarde y ella se ha quedado completamente a cargo de nuestra casa y de nuestros dos hijos: Pablo y Ángela. Un párrafo aquí es bien poca cosa para agradecer tanto. . .

Quisiera agradecer a mis padres Raúl y Liliana, de quienes he recibido tanto y que nunca han dejado de apoyarme. A mi padre quisiera agradecer de modo especial el gusto que he heredado por la vida universitaria y a ambos los ánimos y consejos tan oportunos en los momentos más difíciles de esta tesis. Gracias también a mis todos mis hermanos –Verónica, Carolina, Alejandro y Soledad– que desde la distancia han estado siempre conmigo.

Quiero darle las gracias a Diego, que ha sido mi supervisor en el desarrollo de la tesis y con quien –aunque quizá suene un poco pretensioso– hemos dado los primeros pasos de la Escuela de Ingenieros y del CEIT en el campo de la Robótica Médica. Muchas gracias también a Emilio, que ha cumplido un rol importante en el desarrollo de este trabajo, y también a la Asociación de Amigos de la Universidad de Navarra por haberme otorgado la Beca para

la Realización de los Estudios de Doctorado.

Muchas gracias también al equipo de Neurocirugía de la Clínica Universidad de Navarra –Ricardo Diez y Sonia Tejada– de quienes siempre me ha sorprendido su entusiasmo por la investigación, muchas veces sin más recompensa que la satisfacción de haber hecho un buen trabajo. Un agradecimiento muy especial también a Yolanda, Gloria y Guadalupe, que tantas veces me ayudaron en mis viajes a Pamplona para adquirir las imágenes que necesitaba para el desarrollo de mi proyecto.

Esta sección no quedaría completa sin darle un agradecimiento especial a Javi quien, con su trabajo de control del robot PA-10, ha hecho el complemento fundamental de esta tesis. Sin este, este proyecto hubiera quedado a medio hacer. También quisiera agradecer a Aiert y Fran, quienes me prestaron las cámaras de captura de movimiento, las que han cumplido una tarea muy importante en este trabajo. Gracias por vuestra generosidad y buena disposición ya que, pese a las dificultades de coordinación para utilizar los equipos, nunca recibí de vosotros una sola queja. Quiero dar un agradecimiento muy especial también al equipo de diseño mecánico del Departamento: Edu, Mikel y Xabi J., que me brindaron tanta ayuda en la fabricación de las piezas que necesité durante el desarrollo de mi proyecto, sobre todo el tambor de calibración. Sin temor a exagerar, ¡esta tesis no hubiera sido posible sin vuestra ayuda! Espero que ahora que he acabado pueda disminuir en algo vuestra siempre alta demanda de trabajo. . .

Quisiera agradecer también al Image Sciences Institute de la Universidad de Utrecht por haberme proporcionado las imágenes de 3DRX, TAC, RM y radiografías utilizadas para la evaluación de los algoritmos de registro 2D-3D hechos en esta tesis. También quisiera agradecer a Jian Wu, Aviv Hurvitz y Martjn van der Bom por las ayudas que me brindaron desarrollando los mismos. Quiero dar un agradecimiento especial también al Profesor Leo Joskowicz de la Universidad Hebrea de Jerusalén, por su valiosa ayuda y consejos para el diseño del tambor de calibración.

Por último –pero no por ello menos importante– quisiera agradecer a todos mis superiores y compañeros del CEIT y Tecnun: Luis M., Jordi V., Alejo A., Joseba C., José María B., Raúl, Carlos, Hugo, Jairo, Gaizka, Imanol H., Goretti, Ilaria, Iker, Yaiza, Ángel, Denis, Aitor, Gorka, Borja, Ibon, Iñaki, Jorge Juan, Baudouin, Javier D., Martín, Jacobo, Pablo, Ainitze, Imanol P. y Manolo (nombrados en ningún orden particular . . . ¡espero no haberme olvidado de ninguno de vosotros!).

# Abstract

This work presents the planning and guidance systems of a novel cooperative robot designed for spinal surgery. The latter has been developed for transpedicular fixation, a particular intervention consisting in the immobilisation of two or more vertebrae by means of screws and metal bars. Its conventional clinical protocols have high levels of invasiveness, increased radiation exposure, difficult visualisation of the surgical field and considerable probabilities of screw misplacement. All these problems could be solved by means of a surgical robotic assistant, which would work cooperatively with the surgeon providing stable and accurate instrument placement.

A comprehensive review of the state-of-the-art in surgical robotics for spinal interventions is given in this thesis, focusing on the research done in the last ten years. This study shows that spinal surgical robotics is still in an early stage of development and faces considerable challenges, in particular reaching the theoretical accuracy level demanded by clinical studies.

A novel surgical planning application is also presented in this thesis along with a new software library for 2D-3D registration. The latter is a key problem of the proposed robotic system, as it permits accurate localisation of the patient by matching his pre-operative (3D) data and intra-operative (2D) x-ray images. Despite that 2D-3D registration has been studied for many years, researchers were faced with a lack of appropriate software, which was effectively solved with the library presented in this work.

2D-3D registration involves the additional sub-problems of calibration and distortion correction of x-ray imaging devices. These were addressed in this thesis proposing a novel algorithm able to solve both, also providing precise reconstruction of 3D points from their 2D projections. The proposed method is simultaneously accurate, robust and fast, fitting well into the

requirements of surgical applications.

Finally, integration of the robotic system's components was studied in this thesis, reporting the first experimental results on phantoms. Despite that full integration with the presented 2D-3D registration methods has not been carried out, the robotic system was found to be accurate enough for surgical practice. Full integration and tests with cadavers or animals should be the subject of future works.

# Resumen

Este trabajo presenta los sistemas de planificación y guiado de un nuevo robot cooperativo diseñado para la cirugía de columna. Este ha sido desarrollado específicamente para la artodresis lumbar, la cual consiste en la inmovilización de dos o más vértebras mediate tornillos y barras metálicas. Sus protocolos clinicos convencionales tienen altos niveles de invasividad, elevada exposición a radiación ionizante, difícil visualización del área de trabajo y probabilidades considerables de inserciones incorrectas de los tornillos. Todos estos problemas pueden ser resueltos usando un robot asistente, capaz de trabajar de manera cooperativa con el cirujano proporcionándole un posicionamiento estable y preciso del instrumental quirúrgico.

En esta tesis se presenta una revisión exhaustiva del estado del arte en la robótica quirúrgica para las operaciones de columna, con éfasis en la investigación hecha en los últimos diez años. Este estudio muestra que estos robots aún están en una fase temprana de su desarrollo y se ven enfrentados a desafíos considerables, sobre todo llegar a los niveles de precisión exigida por estudios clínicos.

En esta tesis se presenta también una nueva aplicación informática para la planificación de cirugías junto con una nueva librería de software para el registro 2D-3D. Este último es una pieza fundamental del sistema robótico propuesto, ya que permite la localización precisa del paciente a partir de sus datos pre (3D) e intra-operatorios (2D), estos útimos en forma de radiografías. Pese a que el registro 2D-3D ha sido estudiado durante muchos años, los investigadores se han visto afectados por la falta de software apropiado, la cual ha sido cubierta con la librería propuesta en este trabajo.

El registro 2D-3D incluye los sub-problemas de calibración y corrección de la distorsión en los arcos quirúrgicos. Estos han sido abordados en esta

tesis proponiendo un nuevo algoritmo capaz de resolver ambos, permitiendo también la reconstrucción de puntos tridimensionales a partir de sus proyecciones. El método propuesto es preciso, robusto y rápido a la vez, encajando de manera adecuada dentro de los estándares exigidos para una aplicación quirúrgica.

Finalmente, durante esta tesis se ha estudiado la integración de los diferentes componentes del sistema robótico propuesto, exponiendo los primeros resultados experimentales obtenidos en modelos sintéticos. Pese a que no ha sido posible llevar a cabo la integración del sistema de registro 2D-3D, se ha observado que el sistema completo tiene el nivel de precisión necesario para su uso en cirugía. Como trabajo futuro se contempla completar el proceso de integración y realizar los primeros experimentos con cadáveres o animales.

# Contents

**1 Introduction** **1**

1.1 Brief anatomy of the spine and vertebrae . . . . . . . . . . 2

1.2 Conventional surgery and its problems . . . . . . . . . . . . 4

1.2.1 Invasiveness . . . . . . . . . . . . . . . . . . . . . . . 6

1.2.2 High radiation . . . . . . . . . . . . . . . . . . . . . . 7

1.2.3 Difficult visualisation . . . . . . . . . . . . . . . . . . . 7

1.2.4 Low accuracy . . . . . . . . . . . . . . . . . . . . . . 8

1.3 Proposed solution . . . . . . . . . . . . . . . . . . . . . . . 9

1.3.1 Planning software . . . . . . . . . . . . . . . . . . . . 11

1.3.2 Computer assisted surgery system . . . . . . . . . . 12

1.3.3 Surgical robot . . . . . . . . . . . . . . . . . . . . . . 12

1.4 Thesis outline . . . . . . . . . . . . . . . . . . . . . . . . . 14

**2 State of the art** **15**

2.1 Methods . . . . . . . . . . . . . . . . . . . . . . . . . . . . 16

2.2 Results . . . . . . . . . . . . . . . . . . . . . . . . . . . . . 17

2.2.1 Early systems (before 2002) . . . . . . . . . . . . . . 17

2.2.2 Robots for screw insertion . . . . . . . . . . . . . . . 19

2.2.2.1 SpineAssist/Renaissance . . . . . . . . . . 23

2.2.2.2 SPINEBOT, SPINEBOT v2 and CoRA . . 26

2.2.2.3 VectorBot/Kinemedic . . . . . . . . . . . . 30

2.2.2.4 Neuroglide . . . . . . . . . . . . . . . . . . 32

2.2.2.5 RIME . . . . . . . . . . . . . . . . . . . . . 33

2.2.2.6 RSSS . . . . . . . . . . . . . . . . . . . . . 34
2.2.3 Robot for laminectomy . . . . . . . . . . . . . . . . 34
2.2.4 Robots for needle-based interventions . . . . . . . . 35
2.2.4.1 AcuBot . . . . . . . . . . . . . . . . . . . . 37
2.2.4.2 Innomotion . . . . . . . . . . . . . . . . . . 38
2.2.4.3 DLR's LWR III . . . . . . . . . . . . . . . 40
2.2.4.4 University of Tokyo's robot for vertebroplasty 41
2.2.4.5 SpineNav . . . . . . . . . . . . . . . . . . . 41
2.2.5 Robots for endoscopic interventions . . . . . . . . . 41
2.2.5.1 MINOSC - Sub-arachnoid space exploration 41
2.2.5.2 Da Vinci . . . . . . . . . . . . . . . . . . . 42
2.2.6 Radiosurgery robotic systems . . . . . . . . . . . . . 43
2.3 Discussion . . . . . . . . . . . . . . . . . . . . . . . . . . 44
2.3.1 Robots' design and safety . . . . . . . . . . . . . . . 44
2.3.2 Accuracy . . . . . . . . . . . . . . . . . . . . . . . . 45
2.3.3 Registration and tracking technologies . . . . . . . . 46
2.3.4 Project development . . . . . . . . . . . . . . . . . . 47
2.3.5 Economic analysis . . . . . . . . . . . . . . . . . . . 48
2.4 Conclusions . . . . . . . . . . . . . . . . . . . . . . . . . 48

**3 Problem definition 51**
3.1 Main concepts . . . . . . . . . . . . . . . . . . . . . . . . 51
3.2 Coordinates systems definition . . . . . . . . . . . . . . . 54

**4 Surgical planning software 59**
4.1 Motivation . . . . . . . . . . . . . . . . . . . . . . . . . . 59
4.2 Workflow . . . . . . . . . . . . . . . . . . . . . . . . . . . 61
4.2.1 Loading of pre-operative images . . . . . . . . . . . 61
4.2.2 Screw placement and manipulation . . . . . . . . . . 63
4.2.3 DRR simulation and export . . . . . . . . . . . . . . 64
4.2.4 Importing intra-operative images . . . . . . . . . . . 65
4.2.5 Registration . . . . . . . . . . . . . . . . . . . . . . 65

- 4.2.6 Tracking . . . . . . . . . . . . . . . . . . . . . . . . 67
- 4.2.7 Robot driving . . . . . . . . . . . . . . . . . . . . . 68
- 4.3 Closing remarks . . . . . . . . . . . . . . . . . . . . . . . . 68

**5 Registration of 2D and 3D images 69**

- 5.1 Problem description . . . . . . . . . . . . . . . . . . . . . . 70
  - 5.1.1 2D-3D registration definition . . . . . . . . . . . . . 70
  - 5.1.2 Measures of registration errors . . . . . . . . . . . . 72
  - 5.1.3 Standard datasets and protocols . . . . . . . . . . . 75
  - 5.1.4 Available software . . . . . . . . . . . . . . . . . . 77
- 5.2 Proposed solution . . . . . . . . . . . . . . . . . . . . . . . 78
  - 5.2.1 Proposed library and application . . . . . . . . . . 78
  - 5.2.2 Point-based registration . . . . . . . . . . . . . . . 79
  - 5.2.3 Intensity-based registration . . . . . . . . . . . . . 81
    - 5.2.3.1 Normalised Gradient Correlation . . . . . . 83
    - 5.2.3.2 Gradient Difference . . . . . . . . . . . . . 83
    - 5.2.3.3 Pattern Intensity . . . . . . . . . . . . . . . 84
    - 5.2.3.4 Multi-resolution . . . . . . . . . . . . . . . 85
    - 5.2.3.5 Optimisers . . . . . . . . . . . . . . . . . . 86
- 5.3 Evaluation . . . . . . . . . . . . . . . . . . . . . . . . . . . 91
- 5.4 Discussion . . . . . . . . . . . . . . . . . . . . . . . . . . . 94
- 5.5 Closing remarks . . . . . . . . . . . . . . . . . . . . . . . . 95

**6 Calibration and distortion correction of x-ray images 97**

- 6.1 Problem description . . . . . . . . . . . . . . . . . . . . . . 97
- 6.2 Previous work . . . . . . . . . . . . . . . . . . . . . . . . . 99
- 6.3 Proposed solution . . . . . . . . . . . . . . . . . . . . . . . 101
  - 6.3.1 Prototype calibration drum . . . . . . . . . . . . . . 101
  - 6.3.2 Segmentation . . . . . . . . . . . . . . . . . . . . . 102
  - 6.3.3 Bead identification . . . . . . . . . . . . . . . . . . 104
  - 6.3.4 Distortion correction . . . . . . . . . . . . . . . . . 104
  - 6.3.5 C-arm calibration . . . . . . . . . . . . . . . . . . 106

6.4 Evaluation . . . . . . . . . . . . . . . . . . . . . . . . . . . . . 108
    6.4.1 Segmentation . . . . . . . . . . . . . . . . . . . . . . . . 109
    6.4.2 Calibration . . . . . . . . . . . . . . . . . . . . . . . . 109
    6.4.3 Registration using back-projection . . . . . . . . . . . 112
    6.4.4 Registration using motion capture . . . . . . . . . . . 118
6.5 Closing remarks . . . . . . . . . . . . . . . . . . . . . . . . . 124

**7 Prototype integration 125**
7.1 Robot description . . . . . . . . . . . . . . . . . . . . . . . . 126
7.2 Motion capture system description . . . . . . . . . . . . . . 127
7.3 Tool tip calibration . . . . . . . . . . . . . . . . . . . . . . . 128
7.4 Robot base registration . . . . . . . . . . . . . . . . . . . . . 132
7.5 Correction of screws' normal vectors . . . . . . . . . . . . . 133
7.6 Overall positioning accuracy . . . . . . . . . . . . . . . . . . 135
7.7 Closing remarks . . . . . . . . . . . . . . . . . . . . . . . . . 139

**8 Conclusions 141**
8.1 Conclusions . . . . . . . . . . . . . . . . . . . . . . . . . . . . 141
8.2 Future work . . . . . . . . . . . . . . . . . . . . . . . . . . . . 142

**A Generated Publications 145**

**B Skull segmentation from MR $T_1$ images 147**
B.1 Introduction . . . . . . . . . . . . . . . . . . . . . . . . . . . 147
B.2 Methodology . . . . . . . . . . . . . . . . . . . . . . . . . . . 149
B.3 Experiments and results . . . . . . . . . . . . . . . . . . . . 150
B.4 Discussion . . . . . . . . . . . . . . . . . . . . . . . . . . . . 153
B.5 Conclusions . . . . . . . . . . . . . . . . . . . . . . . . . . . . 155

**C Used software libraries 157**
C.1 ITK . . . . . . . . . . . . . . . . . . . . . . . . . . . . . . . . 157
C.2 VTK . . . . . . . . . . . . . . . . . . . . . . . . . . . . . . . . 158
C.3 OpenIGTLink . . . . . . . . . . . . . . . . . . . . . . . . . . . 158

C.4 Eigen . . . . . . . . . . . . . . . . . . . . . . . . . . . . 161
C.5 Qt . . . . . . . . . . . . . . . . . . . . . . . . . . . . . 161
C.6 CMake . . . . . . . . . . . . . . . . . . . . . . . . . . . 162

**D An ITK Framework for 2D-3D Registration 163**
D.1 Introduction . . . . . . . . . . . . . . . . . . . . . . . . . 163
D.2 Definition of the 2D-3D registration problem . . . . . . . . 165
D.3 Framework for intensity-based registration . . . . . . . . . . 166
D.3.1 Registration methods . . . . . . . . . . . . . . . . . 168
D.3.2 Transform . . . . . . . . . . . . . . . . . . . . . . . 172
D.3.3 Metric . . . . . . . . . . . . . . . . . . . . . . . . . 172
D.3.3.1 Mean Squares . . . . . . . . . . . . . . . . 173
D.3.3.2 Gradient Difference . . . . . . . . . . . . . 173
D.3.3.3 Normalized Gradient Correlation . . . . . . 175
D.3.3.4 Pattern Intensity . . . . . . . . . . . . . . . 175
D.3.4 Optimizer . . . . . . . . . . . . . . . . . . . . . . . . 176
D.3.5 Interpolator . . . . . . . . . . . . . . . . . . . . . . . 177
D.4 Example applications . . . . . . . . . . . . . . . . . . . . . 178
D.4.1 Exhaustive search for intensity-based registration . . 178
D.4.2 Multi-resolution intensity-based registration . . . . . 182
D.5 Conclusions and future work . . . . . . . . . . . . . . . . . 185

**References 187**

# List of Figures

1.1 The human spine . . . . . . . . . . . . . . . . . . . . . . . . . 3
1.2 A vertebra and its parts. . . . . . . . . . . . . . . . . . . . . . . 4
1.3 Conventional spine surgery . . . . . . . . . . . . . . . . . . . . 5
1.4 Pedicle screw trajectories . . . . . . . . . . . . . . . . . . . . 8
1.5 Photograph of the proposed system . . . . . . . . . . . . . . . 9
1.6 Architecture of the proposed solution . . . . . . . . . . . . . 10
1.7 viewit-Spine main window . . . . . . . . . . . . . . . . . . . 11

2.1 The SpineAssist robot . . . . . . . . . . . . . . . . . . . . . 24
2.2 The SPINEBOT robot . . . . . . . . . . . . . . . . . . . . . . 27
2.3 The CoRA robot . . . . . . . . . . . . . . . . . . . . . . . . . 28
2.4 The second version of the SPINEBOT robot . . . . . . . . . 29
2.5 The DLR's surgical systems . . . . . . . . . . . . . . . . . . 30
2.6 The Neuroglide robot . . . . . . . . . . . . . . . . . . . . . . 33
2.7 The AcuBot . . . . . . . . . . . . . . . . . . . . . . . . . . . . 37
2.8 The Innomotion robot . . . . . . . . . . . . . . . . . . . . . . 39

3.1 All coordinate systems and transforms . . . . . . . . . . . . 54

4.1 viewit-Spine's main window . . . . . . . . . . . . . . . . . . 62
4.2 Measure Distance tool . . . . . . . . . . . . . . . . . . . . . . 63
4.3 viewit-Spine's transfer styles . . . . . . . . . . . . . . . . . . 63
4.4 Adding a new screw to the surgical plan . . . . . . . . . . . 64
4.5 Simulated radiographs of a screw and its insertion tool . . . 64

4.6 Fiducial placement on a CAT scan. . . . . . . . . . . . . . . 66
4.7 Fiducial placement on an x-ray image . . . . . . . . . . . . 67

5.1 The 2D-3D registration problem . . . . . . . . . . . . . . . 71
5.2 Different measures of registration error . . . . . . . . . . . . 73
5.3 Images from the Utrecht Dataset . . . . . . . . . . . . . . . 75
5.4 A 3D point reconstruction from multiple 2D projections . . 79
5.5 Ray casting illustration . . . . . . . . . . . . . . . . . . . 81
5.6 X-ray image at multiple resolution levels . . . . . . . . . . . 86
5.7 Exhaustive search without downsampling . . . . . . . . . . 87
5.8 Exhaustive search, 2x downsampling . . . . . . . . . . . . . 88
5.9 Exhaustive search, 4x downsampling . . . . . . . . . . . . . 89
5.10 Exhaustive search, 8x downsampling . . . . . . . . . . . . . 90
5.11 Intensity-based registration scatter diagrams. . . . . . . . . 93

6.1 Prototype calibration drum photographs . . . . . . . . . . . 100
6.2 Calibration drum schematic . . . . . . . . . . . . . . . . . . 102
6.3 Segmentation process . . . . . . . . . . . . . . . . . . . . . 103
6.4 Correction of distortion effects . . . . . . . . . . . . . . . . 105
6.5 Focal distance distribution for 1.0 pix segmentation noise. . 111
6.6 Images of the calibration phantom. . . . . . . . . . . . . . . 112
6.7 Determination of transform $\mathbf{T}_D^X$ . . . . . . . . . . . . . . . 118

7.1 OptiTrack motion capture system . . . . . . . . . . . . . . . 127
7.2 Pivot calibration . . . . . . . . . . . . . . . . . . . . . . . 129
7.3 Errors for pivot calibration . . . . . . . . . . . . . . . . . . 131
7.4 Frames $T$ and $B$ with respect to the patient . . . . . . . . . 134
7.5 Overall positioning errors . . . . . . . . . . . . . . . . . . . 138

B.1 Sample segmentation on synthetic data . . . . . . . . . . . 150
B.2 Dice Coefficient with respect to the number of atlases . . . 151
B.3 Evaluation of segmentation algorithms . . . . . . . . . . . . 152
B.4 Sample segmentation on real data . . . . . . . . . . . . . . 154

D.1 Proposed framework's classes. . . . . . . . . . . . . . . . . . . 167
D.2 Sample DRRs used as fixed images . . . . . . . . . . . . . . . 179
D.3 Metric's plot around the optimum using 2 fixed images . . . 180
D.4 Metric's plot around the optimum using 4 fixed images . . . 181
D.5 Sample registration result . . . . . . . . . . . . . . . . . . . . 183
D.6 Normalised Gradient Correlation plots . . . . . . . . . . . . 183
D.7 Standardised evaluation of the registration algorithm . . . . 184

# List of Tables

2.1 Summary of surgical robots for spinal interventions . . . . . 18
2.2 Summary of experiments with robots for screw insertion. . . 22
2.3 Summary of experiments with robots for needle-based interventions . . . . . . . . . . . . . . . . . . . . . . . . . . . 36

5.1 Sample registration evaluation . . . . . . . . . . . . . . . . . 92
5.2 Comparison with other registration methods . . . . . . . . . 94

6.1 Beads' coordinates . . . . . . . . . . . . . . . . . . . . . . . 101
6.2 Rules for the identification of large beads . . . . . . . . . . 104
6.3 Segmentation errors for large beads . . . . . . . . . . . . . . 110
6.4 Segmentation errors for small beads . . . . . . . . . . . . . 110
6.5 Focal point errors for 0.5 pix segmentation noise. . . . . . . 111
6.6 Focal point errors for 1.0 pix segmentation noise. . . . . . . 111
6.7 Computed image parameters, first experiment . . . . . . . . 113
6.8 Projection FRE, first experiment . . . . . . . . . . . . . . . 115
6.9 Projection TRE, first experiment . . . . . . . . . . . . . . . 115
6.10 Reconstruction FRE, first experiment . . . . . . . . . . . . 117
6.11 Reconstruction TRE, first experiment . . . . . . . . . . . . 117
6.12 Computed image parameters, second experiment . . . . . . 119
6.13 Projection TRE, second experiment . . . . . . . . . . . . . 120
6.14 Reconstruction TRE, second experiment . . . . . . . . . . . 122

7.1 Pivot calibration errors . . . . . . . . . . . . . . . . . . . . . 130

7.2 Robot tool calibration errors . . . . . . . . . . . . . . . . . . 130
7.3 Robot base registration errors . . . . . . . . . . . . . . . . . . 132
7.4 Overall positioning errors . . . . . . . . . . . . . . . . . . . . 137

B.1 Confidence intervals for comparisons of AVD and DC . . . . 154
B.2 Confidence intervals for comparisons of FPD and FND. . . 155

C.1 OpenIGTLink message types . . . . . . . . . . . . . . . . . . 160

## Chapter 1

# Introduction

A synthesis of this chapter has been published in

> *Bertelsen, A., Melo, J., Sánchez, E., and Borro, D. "Implementation of a cooperative human-robot system for transpedicular fixation surgery". In Actas del XXIX Congreso Anual de la Sociedad Española de Ingeniería Biomédica (CASEIB 2011), pp. 303–306. 2011.*

The objective of this thesis is the study and implementation of the image processing applications required by a robotic assistant designed for transpedicular fixation, a particular type of spine surgery consisting in the immobilisation of multiple vertebrae by means of screws connected by metal bars. Usually, transpedicular fixation –also known as inter-body fusion– is done to prevent further damage on a vertebra affected by fracture, disc problems or tumours. This surgery demands high levels of precision, as a badly inserted screw can damage the spinal cord, the surrounding blood vessels or the pedicle itself. Misplacement of screws is not uncommon: figures vary between studies but can reach values up to 30%, which can be effectively lowered by the use of Computer Assisted Surgery (CAS) systems (Holly, 2006). However, further improvement could be obtained by means of a robotic assistant like the one described here, which would cooperate with the surgeon steadily holding the instrumental on precise locations. In this way, the surgeon would always remain in charge of the intervention, while the robot performs tasks which are either repetitive or demand too much precision.

## 1.1 Brief anatomy of the spine and vertebrae

The spine –shown on Figure 1.1– is a flexible column formed by a series of bones called vertebrae. There are thirty-three vertebrae divided in *cervical*, *thoracic*, *lumbar*, *sacral* and *coccygeal* regions. Usually, there are seven vertebrae in the cervical region, twelve in the thoracic, five in the lumbar, five in the sacral and four in the coccygeal. Sometimes these numbers are varied by an extra vertebra in one region, usually compensated by a missing one in other. However, the number of cervical vertebrae very rarely changes. Vertebrae in the cervical, thoracic and lumbar regions are known as *true* or *movable* vertebrae, whereas the ones in the sacral and coccygeal regions are known as *fixed* or *false*, as they are united in the adult forming two bones: the *sacrum* and the *coccyx* (Gray, 1918). Vertebrae are named using a letter and number, indicating the region to which they belong and their position, ordered from head to feet. Vertebrae are noted with a letter C, T, L or S if they belong to the cervical, thoracic, lumbar and sacral regions respectively.

With the exception of the first two cervical vertebrae –C1 and C2, also known as *atlas* and *axis*– movable vertebrae share some common features as the one depicted on Figure 1.2. They consist of two parts: an anterior segment or *body* and a posterior one known as *vertebral* or *neural arch*. These enclose the *spinal canal* or *vertebral foramen*, which serves as a protection for the *medulla spinalis* or *spinal cord*. The *vertebral body* (corpus vertebrae) is the largest part of the vertebrae and is more or less cylindrical in shape. Its upper and lower surfaces are flattened and rough and give attachment to the intervertebral fibrocartilages. Vertebrae are connected to each other by their bodies, forming a strong pillar for the support of the head and trunk (Gray, 1918).

The vertebral arch is formed by a pair of *pedicles* and seven bony extrusions or *processes* which serve as attachment of muscles and ligaments (Gray, 1918). All bony parts of the vertebrae are composed of *cancellous tissue* enclosed by a layer of the more compact *cortical bone*. Cortical coating are thinner in the vertebral body, whereas it is considerably thicker in the vertebral arch and processes (Gray, 1918).

The *pedicles* (radices arci vertebrae) are two short and thick processes projected backwards, one from each side of the vertebral body. They are connected to the laminae, a pair of broad plates directed backwards and

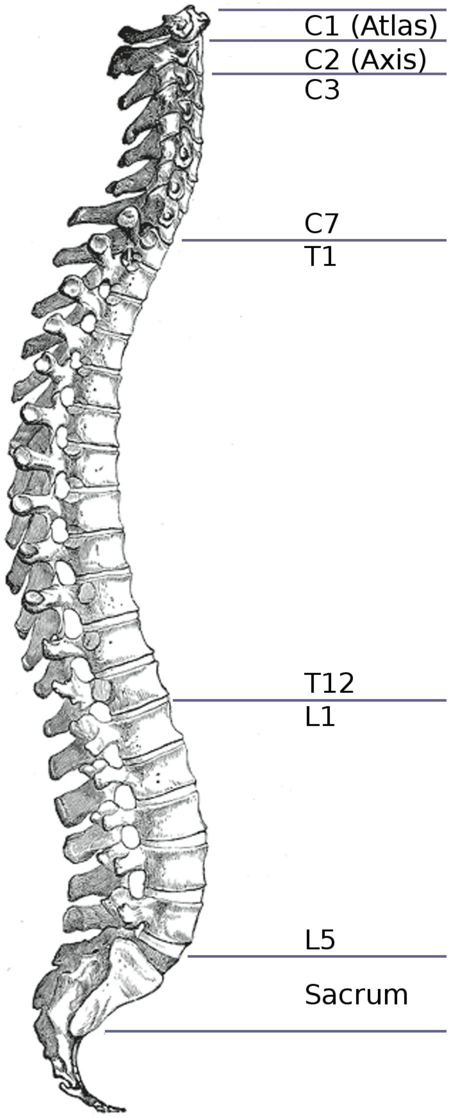

Figure 1.1: A sagittal view of the human spine, showing its location of the cervical (C), thoracic (T), lumbar (L) and sacral regions (Gray, 1918).

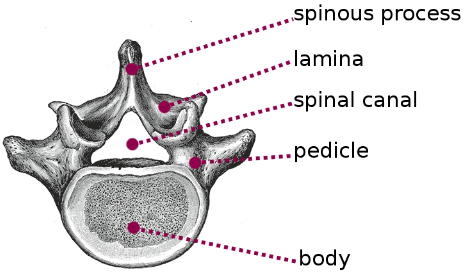

Figure 1.2: A human vertebra and its main parts.

medialward, which fuse in the medial line completing the posterior side of the vertebral foramen, also shown of Figure 1.2 (Gray, 1918).

## 1.2 Conventional surgery and its problems

The clinical application studied in this thesis is the screw insertion, part of the *transpedicular fixation* surgery, also known as *spinal* or *inter-body fusion*. This intervention is indicated for the treatment of vertebral fractures, degenerative disc diseases (such as herniation), spinal tumours and scoliosis. Transpedicular fixation consists in the insertion of two screws through the vertebral pedicles, following a trajectory avoiding the spinal cord and the outer pedicular walls. Once in place, screws are fitted with a slotted head into which a metallic rod is inserted. Screws are inserted into two or more vertebrae and their heads are connected forming a single rigid body, preventing relative motion between vertebrae. In this way, further damage to the affected vertebra is prevented and spinal stability is increased (Shoham et al., 2003).

Conventional transpedicular fixation is normally carried out following the protocol illustrated on Figure 1.3. Before the intervention, a three-dimensional (3D) Computerised Axial Tomography (CAT) or Magnetic Resonance (MR) scan of the patient is acquired and displayed in the operating room. There, the surgeon studies the anatomy around the diseased vertebrae and decides the optimal location and orientation of the screws that need to be inserted. Afterwards, a large incision is made on the patient's back exposing his or her spine. Then, the surgeon places a surgical

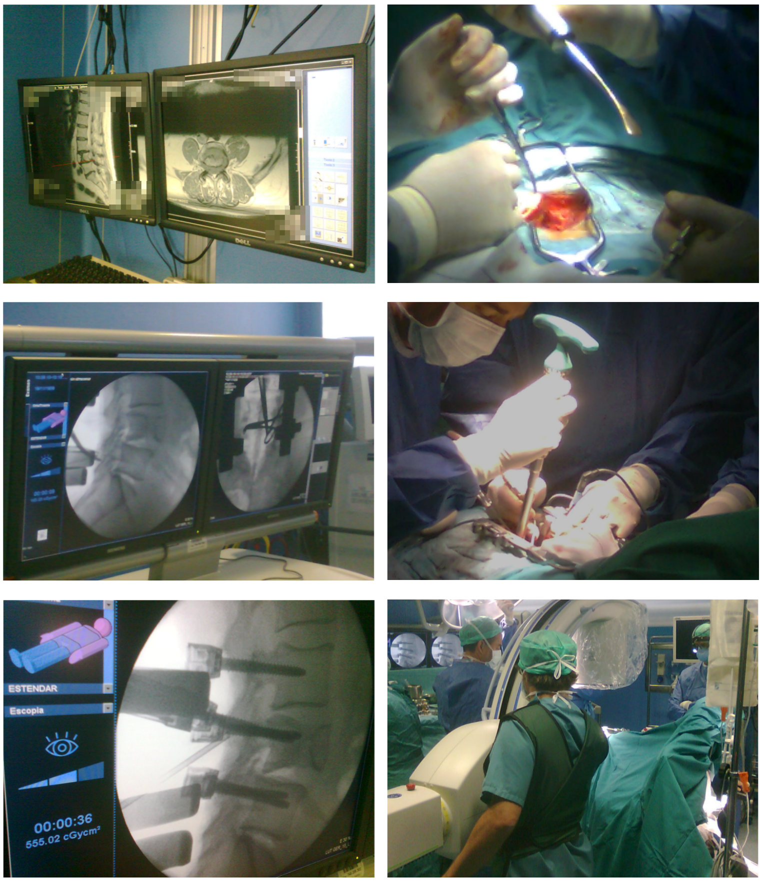

Figure 1.3: Scenes from a conventional transpedicular fixation surgery. Planning of screw placement is based on pre-operative scans, although, differing from the 'planning' idea used in this thesis, no specialised software (top left). Then, the vertebrae are exposed (top right) and the surgeon probes the pedicles with the surgical tool, checking if its position and orientation coincide with the planned trajectories using lateral x-ray images (centre left). When an acceptable orientation has been reached, the surgeon makes the perforation and immediately inserts a screw (centre right), repeating the process until are screws are in place (bottom left). Finally, an AP x-ray is taken to verify if all screws were correctly inserted (bottom right). A detected misplaced screws requires immediate re-insertion.

tool on a pedicle and asks for a lateral x-ray image. Without removing the tool, the surgeon checks the x-ray image, which should depict the vertebra and the tool's projection. As the latter's orientation and position may not be the desired one, the surgeon makes some adjustments and asks for an additional radiographs, repeating the process until he or she is satisfied with the images' aspect. Then, the surgeon perforates the pedicle and inserts a screw. Afterwards, the surgeons moves to the following pedicle, repeating the whole process of tool placement and x-ray imaging for each pedicle that needs to be instrumented. After that, an antero-posterior (AP) image of the spine is acquired to check whether all screws had been placed correctly. As it is only possible to acquire lateral images during insertion, a misplaced screw may remain undetected up to this point, as it may show up correctly on the lateral images. Immediate repositioning of the detected misplaced screws is performed and, finally, connection of the screws' heads is made using a set of metal rods.

The described conventional protocol has four main problems, namely *invasiveness*, *high radiation*, *difficult visualisation* and *low accuracy*. These will be described in the following sections.

### 1.2.1 Invasiveness

Transpedicular fixation is considered invasive as a large incision on the patient's back is required to expose the diseased vertebra and the surrounding ones. This translates into longer recovery times, higher post-operative pain and increased risk of infection. Nowadays, current technology makes *minimally invasive* procedures possible, on which the surgery is performed through a group of small incisions rather than the large ones used in conventional surgery. However, minimally invasive surgery has considerable drawbacks, most notably reduced field of view and difficult control of the surgical instruments, which has slowed its adoption by surgeons. Taking spinal fusion as an example, data from 2009 shows that only 4960 out of the 101,044 procedures (5%) carried out in Europe were performed using minimally invasive techniques (Devito et al., 2010).

### 1.2.2 High radiation

A considerable amount of x-ray images are required during conventional surgery, which translates into high radiation doses on patients, clinical staff and surgeons. However, the benefits of using alternative CAS systems are unclear from the patient's point of view. They may reduce the number of x-ray images taken during surgery, but may demand the use of a pre-operative CAT scan, which could even increase the overall amount of radiation taken by the patient (Tjardes et al., 2010). In fact, some modern hospital do not use pre-operative CAT scans at all, replacing them by MR images, effectively reducing the patient's exposure.

Although using CAS systems may not reduce radiation doses on patients, they would definitively have a positive impact on surgeons. The latter are the ones most affected by intra-operative radiation, as they must stand close to the x-rays' trajectories on each intervention they perform. In fact, studies published in 2005 have corroborated that orthopaedic (and, thus, spinal) surgeons have increased risk of suffering from cancer due to this factor. Singer et al. estimated that the use of a c-arm could easily surpass the yearly recommended amount of radiation on the surgeons' hands, which are more affected than other body parts as they are closer to the device's main beam (Singer, 2005). Mastrangelo et al. studied the incidence of cancer among a group of hospital workers and observed that cancer incidence was 29% for orthopaedic workers, higher than the 6 and 4% found for non-orthopaedic exposed and unexposed workers respectively. In addition, the authors observed a statistically significant increased risk for orthopaedic surgeons (Mastrangelo et al., 2005). This evidence shows that intra-operative radiation is a serious operational hazard and measures should be taken to reduce it, benefiting surgeons and nurses as well.

### 1.2.3 Difficult visualisation

The conventional protocol demands the surgeon to visualise the screws' trajectories into the pedicles, based on flat x-ray images without depth information. Besides, as the surgeon must hold the tool steady while the radiographs are acquired, these can only be taken in the lateral orientation. It has already been said that a single view is not enough to verify the correct placement of screws. In fact, a screw which looks correctly placed on a lateral image may be actually misplaced and this could only be detected

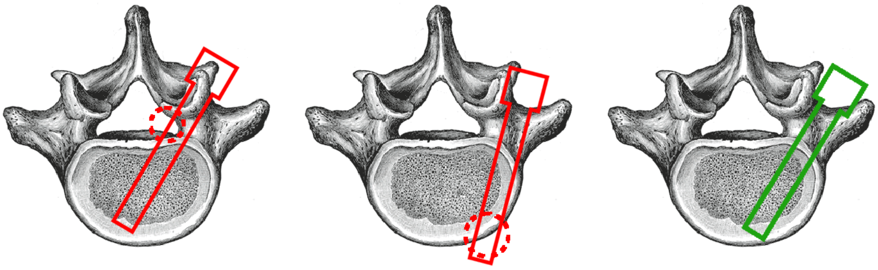

Figure 1.4: Sample screw trajectories: a misplaced screw may breach the pedicular wall and invade the spinal canal (left) or breach the vertebral body and damage the outer blood vessels (centre). A well placed screw should be completely contained within the pedicle and firmly anchored on the cortical bone (right).

by an AP radiograph, taken at the end of the surgery.

### 1.2.4 Low accuracy

Transpedicular fixation requires placement of screws that have diameters between 4.5 and 8.0 mm into the vertebral pedicles, which have diameters between 6 and 10 mm (Lee et al., 2011). This leaves a very small margin of error as pointed out by Rampersaud et al., who showed that the desired accuracy for the pedicular screw insertion varied between 0.0 and 3.8 mm depending on the vertebra, with many requiring sub-millimetre precision (Rampersaud et al., 2001). As shown on Figure 1.4, misplaced screws can breach the pedicular walls or damage the blood vessels that surround the spinal column, producing internal haemorrhage. Making things worse, a misplaced screw can also produce nerve damage on the spinal cord, producing side effects which range from pain up to paralysis. Screw misplacement is not uncommon, with figures varying between 10 to 30% depending on the study. Interested readers are referred to the recent reviews by Holly (Holly, 2006) and Tjardes et al. (Tjardes et al., 2010).

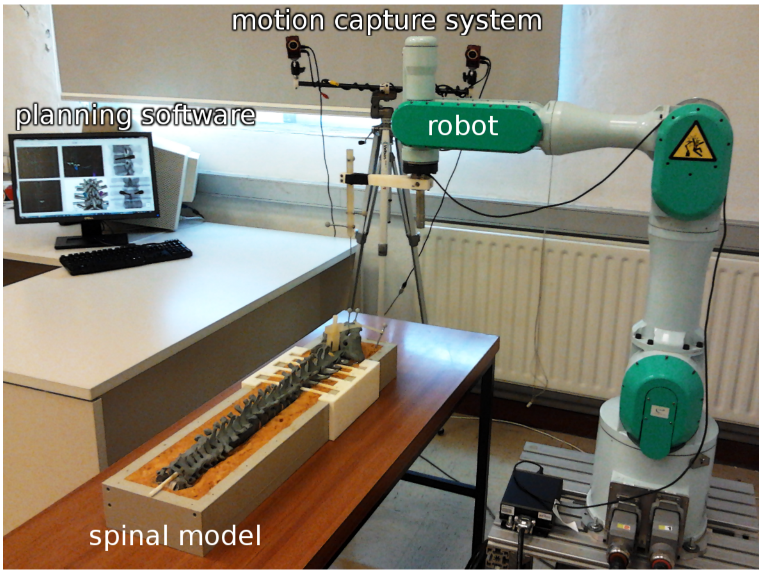

Figure 1.5: Photograph of the proposed system showing the planning software, robot and motion capture cameras (part of the CAS system, which also includes the x-ray imaging device). Also shown is a spinal model using during development.

## 1.3 Proposed solution

To solve the aforementioned problems of conventional spinal fusion, we propose a solution based on a robotic arm which would be able to place a tool guide on precise locations over the pedicles, allowing the surgeon to insert the instrumental through it. The solution consists on three different parts: *planning software*, a *CAS system* and a *surgical robot*, as shown on Figure 1.5. The surgeon should plan the surgery in advance with the software, determining the location of screws based on pre-operative images of the patient. Inside the operating room, the CAS system should bring the pre-operative plan in geometrical alignment with the patient's actual position, obtained from a reduced set of radiographs. Once the alignment is known, it should be transmitted to the robot, giving the latter a representation of the surgical scenario which would allow it to move to the spine's surroundings with high precision and avoiding any neighbouring critical structures. In addition, the surgeon and robot should be able to co-manipulate the surgical tools, that is, the first could move

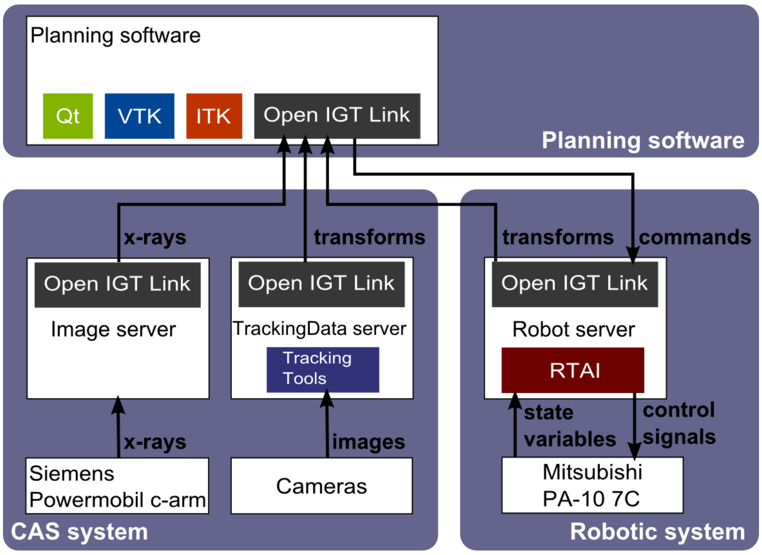

Figure 1.6: Architecture of the solution proposed in this thesis, showing the data transmission between the planning software, CAS system and robot. Used software libraries are also shown.

the instrument and the robot should follow his or her motion without opposing any resistance, but preventing entrance to critical zones and filtering undesirable effects such as vibrations and reactive forces (Casals et al., 2009).

The proposed solution allows the use of minimally-invasive surgery techniques and reduces the number of radiographs required in the operating room. Furthermore, it renders the vertebrae and surgical tools in a 3D scene in real time, relieving the surgeon from the demanding task of inferring the tools positions from the radiographs. In addition, the use of the robotic arm provides guidance of the surgical tool in a stable manner, unaffected by fatigue or tremor and with levels of precision not achievable by humans, minimising the possibilities of patient damage during the intervention.

A scheme of the proposed system is shown on Figure 1.6. In the following sections, descriptions will be given of the system's main components, that is, the planning software, CAS system and surgical robot.

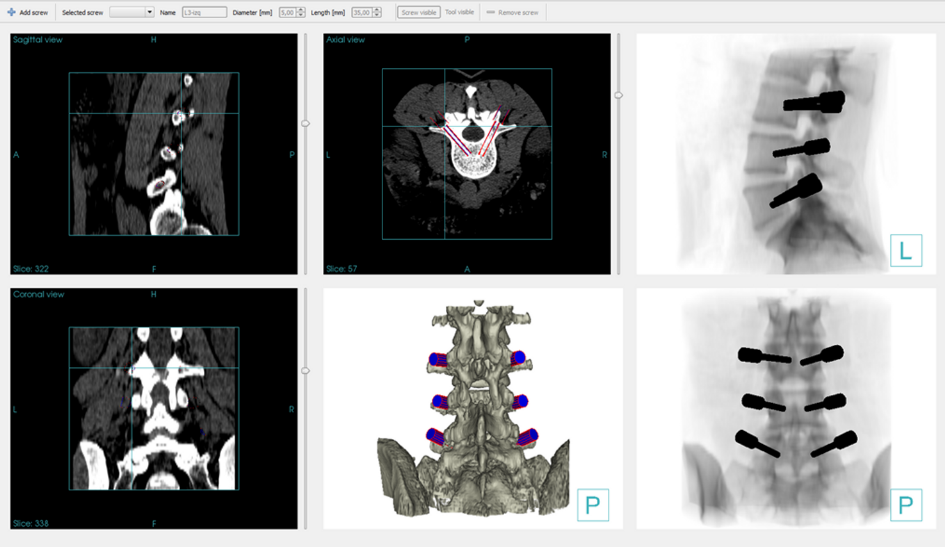

Name L3-izq

Diameter [mm] 5,00

Length [mm] 35,00

Figure 1.7: The main window of the viewit-Spine application.

### 1.3.1 Planning software

We developed a surgical planning application –named *viewit-Spine*– which serves as core for the proposed surgical system of this thesis. As shown on Figure 1.7, the application permits the surgeon to plan the number and orientation of screws based on pre-operative scans of the patient, rendered on three orthogonal views and three 3D volumetric views. Two of the latter are used to generate Digitally Reconstructed Radiographs (DRR) which simulate how the spine and screws would look like in an actual x-ray image. The software also permits simulation of DRRs showing tools instead of screws, placed on the exact locations on which perforations have to be made. These DRRs can be saved and later retrieved inside the operating room to be used as reference images.

In addition to its planning features, viewit-Spine includes modules for registration, navigation and robot control. During the surgery, viewit-Spine can retrieve intra-operative x-ray images as well as the spatial position on which they were acquired, transmitted from a motion capture device. This data can be registered to the pre-operative 3D image, allowing the localisation of the patient's spine. Once registration is successfully calculated, it is also possible to track the surgical tools in real time and display them on the 3D panels of viewit-Spine. Furthermore, viewit-Spine also includes software modules to calibrate and control the surgical robot, commanding the latter to move automatically to the optimal locations were screws should be inserted.

### 1.3.2 Computer assisted surgery system

Use of a CAS system is mandatory to guide the robot during surgery, as the patient's position in the operating room, calculated from intra-operative data, needs to be registered to the surgical plan. Besides, the CAS system should be able to render the vertebrae and the tracked surgical tools in real time, showing the procedure's state to the surgeon in each moment.

To achieve the minimally invasive requirements of the system, the intra-operative data required for registration must come in the form of images. Radiographies acquired with a c-arm are preferred, as they are available in most modern operating rooms. Registration of these images, which falls into the category of 2D-3D registration, was implemented using a custom software framework able to handle multiple x-ray acquired in arbitrary orientations (Bertelsen and Borro, 2011) and is presented in Chapter 5.

2D-3D registration requires knowledge of the c-arm's extrinsic and intrinsic parameters, which are the device's position, focal distance and pixel size. As the values of intrinsic parameters are not given by most commercial units, a calibration device is needed. For this purpose, we built a prototype calibration device, consisting of two parallel plastic plates with embedded steel fiducials, and implemented a calibration algorithm, also able to correct the distortion present in the x-ray image formation (see Chapter 6 for more details). This device is also equipped with optical markers, tracked by a set of cameras which capture the c-arm's position and orientation at the moments in which each x-ray image is acquired. The same markers are used to track the instrumental attached to the robot's end-effector.

### 1.3.3 Surgical robot

The basic concept of this project is Human-Machine Collaborative System (HMCS), defined as a system that amplifies or assists the human skills, while performing tasks that require both the capacity of the human and as the accuracy of the robot. HMCSs are also called 'Cobots', which is a shortening of the term 'collaborative robots'. Here, we propose a cobot that can be moved freely by the surgeon, who can drag it from its end-effector without feeling any resistance. However, in proximity of a critical structure, it would oppose the motion and prevent the surgeon from going any further. In addition, the robot can be ordered to move autonomously to a defined point after receiving an order from the console.

The used robot is a PA10-7C (Mitsubishi Heavy Industries Ltd., Kobe, Japan), an industrial robotic arm with 7 DoF which offers a high level of dexterity thanks to its redundant joint. In addition, its large workspace allows access to more sections of the patient's spine, which alleviates the problems experienced with other systems. In the proposed configuration, the robot is equipped with a mini45 force sensor (ATI Industial Automation, NC, USA) attached to its end-effector, which measures forces applied by the operator as well as collisions with the environment.

The chosen platform for execution of the robot control loop is the Real Time Application Interface (RTAI) extension for Linux, which permits the use of generic data-acquisition boards and high-level programming languages on 32 bit computers (Dozio and Mantegazza, 2003). The core of RTAI is a nano-kernel which serves as a bridge between the hardware and Linux, keeping most of its features while allowing the execution of real-time processes.

The control architecture corresponds to an admittance loop, in which the system measures the force exerted by the user and generates a response, in form of acceleration, speed and position. The control loop is complemented by the definition of virtual fixtures, or active constraints, for both force and position. These are predefined margins, within which the robot will have its area of safe operation. Virtual fixtures are obtained directly from the surgical plan, defined as a cylinders placed around a screw's insertion point (Melo et al., 2012a; Melo et al., 2012b).

It must be remarked that the main subject of this thesis is development of the first two components of the surgical system, that is, the planning software and the CAS system. Thus, implementation of the control strategies for the surgical robot falls outside the scope of this work.

## 1.4 Thesis outline

This thesis is organised on seven chapters, the first one being the current introduction to the problem of pedicular screw insertion and its proposed solution. Chapter 2 describes the state of the art in surgical robots for spinal interventions, as well as the challenges faced by researchers today. Chapter 3 gives a set of mathematical definitions that are used in the following chapters of this work. Chapter 4 describes the viewit-Spine planning software. Chapter 5 describes the application developed for the problem of 2D-3D registration. Chapter 6 describes the algorithm developed for the calibration of the intra-operative x-ray machine, required for successful registration using the algorithm presented in the previous chapter. Chapter 7 describes the integration of the systems presented on the preceding chapters, along with the interface to control the surgical robot. Finally, conclusions are presented on Chapter 8, along with lines of future work.

Besides its main chapters, this thesis includes four appendices. Appendix A lists the publications generated during the making of this work, including conference presentations and articles published on scientific and technical journals. Appendix B presents an algorithm developed for segmentation of the human skull from MR images. Although this topic differs from this Thesis' main subject, the presented method could be adapted –with minor adjustments– for vertebrae segmentation and, thus, be included in a CAS system like the one described in this work. Appendix C lists the software libraries used for the development of the viewit-Spine planning application, a subject considered too technical to be included as a chapter of this thesis. Finally, Appendix D gives a technical description of the software library developed for 2D-3D registration, aimed at programmers interested in their use for their own projects.

# Chapter 2

# State of the art

This chapter has been accepted in:

> *Bertelsen, A., Melo, J., Sánchez, E., and Borro, D. "A review of surgical robot for spinal interventions". The international journal of medical robotics and computer assisted surgery, (Accepted for publication).*

This chapter aims to describe the state-of-the-art in robotics for spinal surgery, a demanding medical field for which robots already provide valuable assistance, although there is still plenty of room for improvement. Spinal surgery requires a very high level of precision, as it has considerable risks due to the critical structures that surround the spinal column: blood vessels are found closely to the vertebrae and nerves connected to all the human body are rooted to the spinal canal. Damage to any of these structures can produce considerable side effects, ranging from pain up to paralysis. These higher than normal requirements make robots ideal candidates for surgical assistants, as they can achieve superior levels of precision, are not affected by fatigue and can perform repetitive tasks without decreasing their performance.

Development of robots for spinal surgery date back to 1992, although the largest part of the research effort is found during the last ten years –that is, from 2002 to 2012– which is the period covered by this work.

Nowadays, robots are used for a variety of surgical procedures such as transpedicular fixation. This type of surgery, which has attracted a lot of attention from robotic scientists, consists in the fixation of two or more vertebrae by means of screws inserted through the pedicles, which are later connected by metal bars. The screws and rods form a rigid structure which prevents relative motion between the vertebrae, hence preventing further damage to the one affected by fracture or herniation. Transpedicular fixation, apart from the dangers inherent to all spinal surgeries, has additional problems such as possible pedicle fracture, difficult visualisation of the surgical area and high exposure of the patient, surgeon and clinical staff to ionising radiation if x-ray imaging is used to guide the intervention. All the aforementioned problems can be solved –or at least alleviated– by the use of surgical robotic assistants, which can help the surgeon to insert screws in precisely selected positions with minimal deviation.

Apart from transpedicular fixation, robots are now used for needle-based procedures such as biopsies (Stoianovici et al., 2003; Melzer et al., 2008), vertebroplasties (Tovar-Arriaga et al., 2011; Onogi et al., 2005) and facet blocks (Cleary et al., 2005). Robotic systems are also used for tumour ablation (Romanelli and Adler, 2008) and, to a lesser extent, for tumour resection (Yang et al., 2010). They also help to reduce radiation doses on surgeons, patients and clinical staff during interventions (Kantelhardt et al., 2011). Even more, ongoing research aims to develop robotised endoscopes capable of exploration and surgery in the sub-arachnoid space, which is only a few millimetres wide (Ascari et al., 2010).

This chapter is divided in four sections: Methods, Results, Discussion and Conclusions. Criteria for article inclusions will be given on Methods, whereas chosen projects will be described on the Results. An analysis of the state of the art will be given on the Discussion with final remarks on the Conclusions.

## 2.1 Methods

Publications about surgical robots for the spine were searched on the IEEE Xplore, PubMed, Google Scholar and CiteSeerX databases. On them, searches were performed for articles including the terms 'spine', 'vertebra' or 'pedicle' but always with accompanied by the word 'robot'. In addition, the Medical Robotics Database (MERODA)[1] hosted by the University

---

[1] http://www.umm.uni-heidelberg.de/apps/ortho/meroda/robdat.php

of Heidelberg was searched for the same terms. Only the results which described mechatronic systems which performed clearly defined surgical tasks in an autonomous or semi-autonomous manner were included.

In particular, robotic systems designed for the following applications were discarded, as they fell out of the scope of this study:

- Simulators for surgical training.
- Testing of spinal specimens (e.g. load bearing or kinematic analysis) helped by robots.
- General purpose robots which, in theory, could be deployed in spinal surgery but without reports of actual experiments.
- Robotic systems which only performed image acquisition tasks (e.g. cone based computerised tomography).

## 2.2 Results

Applying the methods described in the previous section, a total of 18 robotic projects were found, which are summarised on Table 2.1. Descriptions of them are given in the following sections, citing the application for which they were designed, their main technological features and a summary of their performance results.

### 2.2.1 Early systems (before 2002)

The earliest work on robotic-assisted spine surgery was traced back to 1992 and was reported by a research team from Grenoble, France (Sautot et al., 1992). As many other early works on surgical robotics, the authors adapted an industrial robot, in this case a PUMA 260, for use in the operating room. The robot was designed as an assistant for transpedicular fixation, holding a laser guide which pointed drilling trajectories over the patient's vertebrae. Surgical planning was carried out on a segmented pre-operative Computerised Tomography (CT) scan, which was registered to intra-operative x-ray images. The authors presented a drilling experiment on plastic vertebrae on which they claimed to obtain sub-millimetre accuracy.

| | Name (or reference) | Applications | Availability[a] | Modes[b] | DoF | Tracking[c] |
|---|---|---|---|---|---|---|
| 1 | SpineAssist | Transpedicular fixation, vertebroplasty, biopsy, GO-LIF | FDA, CE | Co | 6 | XR |
| 2 | SPINEBOT | Transpedicular fixation | No | Co, Au | 7 | IR |
| 3 | CoRA | Transpedicular fixation | No | Co, Te | 6 | IR |
| 4 | SPINEBOT v2 | Transpedicular fixation | No | Co | 5 | 2PXR |
| 5 | VectorBot/Kinemedic | Transpedicular fixation | No | Co | 7 | IR |
| 6 | Neuroglide | Cervical interbody fusion | No | Co | 4 | IR |
| 7 | (Wang et al., 2010) | Laminectomy | No | Au | 2 | FS |
| 8 | MINOSC | Sub-arachnoid space exploration, localised electro-stimulation | No | Te | 5 | ES |
| 9 | AcuBot | Vertebroplasty, biopsy, nerve blocks | FDA | Co, Te | 6 | XR, iCT |
| 10 | Innomotion | Biopsy | CE[d] | Te | 5 | iMR, iCT |
| 11 | DLR LWRIII | Biopsy, vertebroplasty | No | Co, Te | 7 | IR, 3DRX |
| 12 | Cyberknife | Tumor ablation | FDA, CE | Au | 6 | XR |
| 13 | Novalis | Tumor ablation | FDA, CE | Au | 6 | XR |
| 14 | da Vinci | Tumor resection | FDA, CE | Te | 7[e] | ES |
| 15 | RIME | Transpedicular fixation | No | Te | 6 | IR |
| 16 | (Onogi et al., 2005) | Vertebroplasty | No | Au | 5 | XR, IR |
| 17 | SpineNav | Vertebroplasty | No | Au, Te | 5 | iCT |
| 18 | RSSS | Transpedicular fixation | No | Co | 5 | IR |

Table 2.1: Summary of the main applications and features of the studied robotic systems.

---

[a] No: robot is commercially unavailable; FDA: robot has FDA clearance; CE: robot has CE mark

[b] Co: Colaborative; Au: Autonomous; Te: Tele-operated

[c] XR: fluoroscopy; 2PXR: bi-planar fluoroscopy; IR: infra-red cameras; FS: force sensing; ES: endoscope; iCT: intra-operative CT; iMR: intra-operative MR; 3DRX: three-dimensional radiography.

[d] The Innomotion commersialisation was stopped in 2010, although it is expected to be restarted in 2012

[e] The da Vinci has 7 DoF per arm.

On 1995, Santos-Munné et al. proposed another robotic system for transpedicular fixation, which shared many similarities with the project first presented in Grenoble: it also advocated the use of an industrial robot (a PUMA 560), intra-operative x-ray imaging system and planning of drilling trajectories on pre-operative CT scans. Differing from previous work, the proposed system placed a drill guide on the robot's end-effector, which was made of radiolucent material with embedded metal spheres. In this way, it could be located on the intra-operative x-ray images and registered to the coordinates of the planned trajectories. The authors neither reported about the project's implementation nor gave experimental results (Santos-Munné et al., 1995).

Some years later researchers from the Fraunhofer Institute developed the Evolution 1 surgical robot, which was commercialised by Universal Robot Systems (URS) and deployed on multiple clinical institutions. Although Evolution 1 was designed for neurosurgery, a research effort was made to extend its use to spinal interventions under the project named Robots and Manipulators for Medical Applications or RoMed (Niesing, 2001). However, URS went out of business some time later, forcing its former clients to stop using their robot due to the cessation of maintenance and technical support (Gomes, 2011).

### 2.2.2 Robots for screw insertion

The majority of robotics projects developed between 2002 and 2012 –more precisely 8 out of 18– have focused on screw insertion, task required for surgeries such as transpedicular fixation and cervical body fusion. Detailed descriptions of these robots will be given in the following sections and a summary of the most relevant experiments using them can be found on Table 2.2.

| Robot | Brief description | Evaluation criteria | Results | Segment | Reference |
|---|---|---|---|---|---|
| SpineAssist | Insertions of 32 guide wires and 4 screws on 6 cadavers. Accuracy checked using post-operative CT scans. | Implants' measured deviations on all planes (sagittal, coronal and axial) with respect to the surgical plan are less than 1.5 mm | 32 of 36 implants correctly inserted (88.89%) | L1-L5 and S1 | (Togawa et al., 2007) |
| SpineAssist | Retrospective study of 3912 screws and guide wires inserted on patients operated on 14 institutions between June 2005 and June 2009. | Surgeons' judgment if post-operative CT scans were unavailable. Otherwise, screws were considered correctly inserted if, at most, breaches of less than 2 mm were observed. | Without CT: 3204 of 3271 screws correctly inserted (98%) With CT: 635 of 646 screws correctly inserted (98.3%) | Unavailable | (Devito et al., 2010) |
| SpineAssist | Retrospective study of 112 patients, 55 operated using SpineAssist and 57 with a conventional protocol. | Screw completely contained within pedicle or, at most, encroaching the cortical bone region. | 94.5% using SpineAssist. 91.5% using conventional protocol | Unspecified segments on thoracic, lumbar and sacral regions | (Kantelhardt et al., 2011) |

| Robot | Brief description | Evaluation criteria | Results | Segment | Reference |
|---|---|---|---|---|---|
| SPINEBOT | Target following experiment, tracking a moving target which emulated the patient's breathing. | Measurement of error by means of an optical tracking system. | Deviation bounded by ± 1.5 mm with a maximum of 0.45 mm | None | (Chung et al., 2006) |
| SPINEBOT | Drilling of a moving plastic phantom, using the robot as tool holder and then by completely autonomous drilling. | Error measured as distance between planned and actual perforation points using a post-operative CT scan. | Observed error in the 1-2 mm range for both cases | None | (Chung et al., 2006) |
| SPINEBOT v2 | Insertion of screws on 14 spinal levels of 2 cadavers. | Screws completely contained within bones with no breaches. Axial and lateral angles measured using a post-operative CT scan. | 26 of 28 screws correctly inserted (92.86%) Axial deviation of 2.45 ± 2.56°. Lateral deviation of $0.71 \pm 0.21^\circ$. | T11-T12, L1-L5 | (Kim et al., 2010b) |

| Robot | Brief description | Evaluation criteria | Results | Segment | Reference |
|---|---|---|---|---|---|
| VectorBot | Machining experiments on artificial bone and a bovine spine, observing the influence of various parameters such as tool choice, drilling speed, controller gains, entry angles and optical tracker sampling rate. No screws were inserted. | Measurement of deviation errors between planned and actual entry points. Measurement of force profiles. | Milling better than drilling in terms of forces and accuracy. Reactive forces always below 15 N. Mean deviation for milling of 0.42 mm with a maximum of 1.7 mm. High speeds (30 000 rpm) and sampling rates (20 Hz) increase accuracy. High proportional and integral gains reduce pose errors and settling time while increasing the robot's stiffness. | None | (Ortmaier et al., 2006a) |
| Neuroglide | Screw insertion on the cervical sections of 6 cadavers. | Post-operative CT scans measuring the translational and angular errors of inserted screws. | 8 of 10 screws correctly inserted (80%) with mean translational and angular errors of 1.94 mm and 4.35° | C1-C2 | (Kostrzewski et al., 2012) |

Table 2.2: Summary of experiments for robots designed for screw insertion. Brief descriptions of the experiments are given, as well as the used criteria for analysis. Summary of results are given, with special emphasis on proportion of successfully inserted implants (i.e. screws or guide wires) and their observed deviations.

#### 2.2.2.1 SpineAssist/Renaissance

A major breakthrough for spinal robotic surgery came in 2003 when a team of Israeli researchers presented the MiniAture Robot for Surgical procedures or MARS (Shoham et al., 2003). MARS evolved into the SpineAssist, now commercialised by Mazor Robotics (Cesarea, Israel), which is still the only robot available in the market –with FDA and CE clearances– specifically designed for spinal interventions such as biopsies, transpedicular fixation, scoliotic back correction and vertebroplasty. To this date, SpineAssist has been validated by 2500 procedures worldwide, on which over 15000 implants have been placed without reported cases of nerve damage (Hadomi, 2012). Recently, Mazor Robotics introduced the Renaissance, a new version of SpineAssist, which despite keeping its core technologies had a complete overhaul in its software and user interface. It also added new features such as the C-OnSite, which permits the acquisition of 3D images using a normal c-arm, by manually rotating it around the patient. The Renaissance is also expanding its clinical field beyond the thoracic and lumbar spine: it has successfully been used for brain biopsies and in the world's first robot-assisted surgery on the cervical spine[2].

MARS/SpineAssist was designed as an intelligent tool holder for interventions that required percutaneous insertions of needles and screws. Its main innovation was its reduced size and weight, which permitted its direct attachment on the patient's bony structure. This greatly simplifies the registration on pre- and intra-operative images, as neither tracking nor immobilisation are needed, as no relative motion between the patient and the robot are possible.

The MARS prototype was a high-precision parallel manipulator with 6 degrees of freedom (DoF) which had a cylindrical shape (base of 25 $\text{cm}^2$ and height of 7 cm), a weight of 200g, positioning errors of less than 0.1 mm and could stand forces up to 10 N (Shoham et al., 2003). The team behind MARS advocated the use of small robots as they occupy less space of the operation room. This, however, reduces their working volume and makes them less able to withstand reactive forces which, in the case of drilling, can reach 15 N. Although small robots are considered safer as they are less able to damage the clinical staff in case of a malfunction, it must be noted that

---

[2] http://ryortho.com/spine.php?news=1898_First-RobotGuided-Cervical-Spine-Surgery

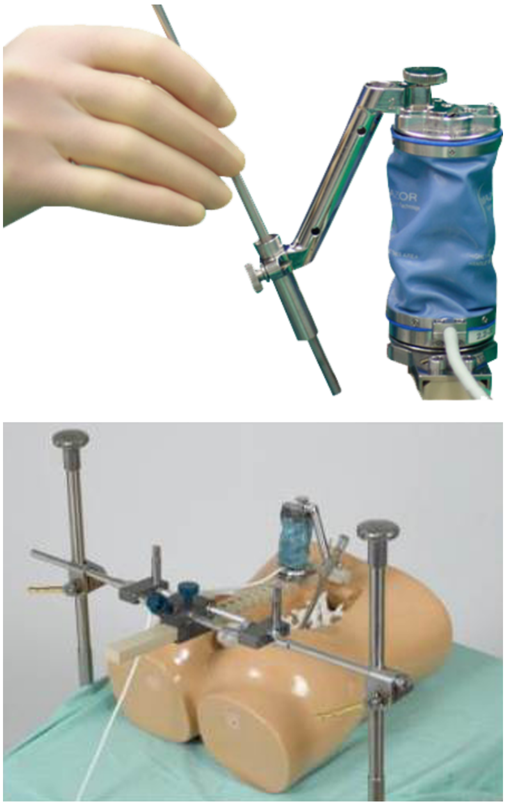

Figure 2.1: Top: the SpineAssist robot with an instrument guide. Bottom: SpineAssist mounted over the Hover-T system. Copyright Mazor Robotics Inc. Used with permission.

even small forces exerted on nerves or blood vessels can severely damage the patient.

SpineAssist, shown on Figure 2.1, is an improved version of MARS, slightly bigger (base diameter of 5 cms, height of 8 cms and 250 grams of weight) and complemented with different mounting platforms. For minimally invasive interventions SpineAssist can be used with the Hover-T, also shown on Figure 2.1, which is a plastic railing anchored on two points of the patient's pelvis and one of the spinous process of an upper vertebra. For open procedures, the robot can be mounted directly over the spine using a clamp and bridge. In addition, two different bed mounted platforms are available for biopsies, cervical interventions and Guided Oblique Lumbar

Interbody Fusion procedures, which will be described later. It must be noted that SpineAssist suffers from its limited working space, so it may not be able to reach a required position during intervention, so additional extensions must be attached to the mounting platforms to solve this problem (Sukovich et al., 2006; Lieberman et al., 2006; Togawa et al., 2007).

The surgical workflow with SpineAssist consists of five steps: 1) planning of the optimal positions and dimensions of implants based on pre-operative CT scans, 2) attachment of the needed mounting platform to the patient's bony anatomy, 3) acquisition of two x-ray images, which are automatically registered to the CT scan, 4) mounting of the robot on the platform, which latter aligns its arm with the planned screw (or tool) trajectory, and 5) drilling through the guiding tube held by the robot's arm, followed by the insertion of the guide wire and screw. Robot motion, drilling and insertion are repeated for all required implants.

After attainment of the FDA clearance, SpineAssist has been used by clinical teams worldwide, mostly in Israel, Germany and the USA, which have reported their experiences on multiple peer-reviewed publications. In 2007, Togawa et al. published the results of a cadaveric study using SpineAssist for insertion of pedicle and translaminar facet screws. For the first type of surgery, 32 guide wires and 4 pedicle screws were inserted into 6 cadavers, evaluating the implants' accuracy by post-operative CT scans. Results revealed that 32 out of the 36 placements (88.89%) were within ± 1.5 mm of the planned position with an overall deviation of 0.87 ± 0.63 mm (Togawa et al., 2007). In 2010, Devito et al. published a retrospective study about the use of SpineAssist between June 2005 and June 2009 on 14 different hospitals worldwide, analysing a total of 842 patients. Intra-operative fluoroscopy was used to assess 3271 screws and guide wires inserted on 635 patients, of which 3204 (98%) were found to be correctly placed. On 139 cases, more detailed quantitative analyses using post-operative CT scans were made, which revealed that 635 out of 646 implants (98.3%) were correctly inserted, with 577 (89.3%) being completely contained within the pedicle and 58 (9%) showing breaches of less than 2 mm. No cases of permanent nerve damage were observed and 49% of the interventions were made percutaneously, a considerable higher rate than the common 5% rate using non-robotic approaches cited by the authors (Devito et al., 2010). In 2011, Kantelhardt et al. published a retrospective study on which 55 patients underwent pedicle screw placement surgeries using SpineAssist and 57 were operated following a conventional protocol. The authors found that patients in the first group had a significant increase in the proportion of screws placed with no breaches (94.5% against 91.4%), reduced times of x-ray exposure per screw (34 s against 77 s) and better recoveries after the interventions (8). In addition to the articles cited here, Mazor Robotics' website hosts an extensive list of publications about SpineAssist, which should be consulted by interested readers[3].

SpineAssist has also enabled a new type of surgery named Guided Oblique Lumbar Interbody Fusion (GO-LIF), which consists in the fixation of two vertebrae by insertion of two screws from the inferior vertebra to the superior one, crossing the intermediate inter-body disc space. In this way, only two screws are needed for fixation instead of the typical four and the connecting rods. This type of surgery is inapplicable by conventional free-hand techniques due to the high level of precision it requires. A recent preclinical study on cadavers has demonstrated its feasibility, with an error level of 1.3 ± 0.2 mm with respect to the pre-operative plan (Shoham, 2011).

#### 2.2.2.2 SPINEBOT, SPINEBOT v2 and CoRA

Three different surgical robots have been presented by Korean researchers, all of them designed for transpedicular fixation. In 2005 a team from Hanyang University presented the SPINEBOT, a robot capable of automatic drilling, a feature missing from previously existing projects for this intervention (Chung et al., 2006). SPINEBOT used in-house planning software and an optical tracking system based on spherical reflective markers for localisation of the surgical tools and patient. In 2009, a team from the Pohang University of Science and Technology (POSTECH) used SPINEBOT's planning and tracking system with a different robot named the Cooperative Robotic Assistant (CoRA), a more robust prototype capable of automated screw insertion and haptic feedback (Lee et al., 2009). In 2010, a cadaveric study was reported using a completely re-designed SPINEBOT (which will be named 'SPINEBOT v2'), with fewer DoF and without the automatic drilling capabilities (Kim et al., 2010a).

As said in the previous paragraph, the original SPINEBOT project comprised not only the surgical robot, but also planning software and an optical tracking system. The proposed software, named HexaView,

---

[3] http://www.mazorrobotics.com/int/physicians-int/peer-review-library-int.html

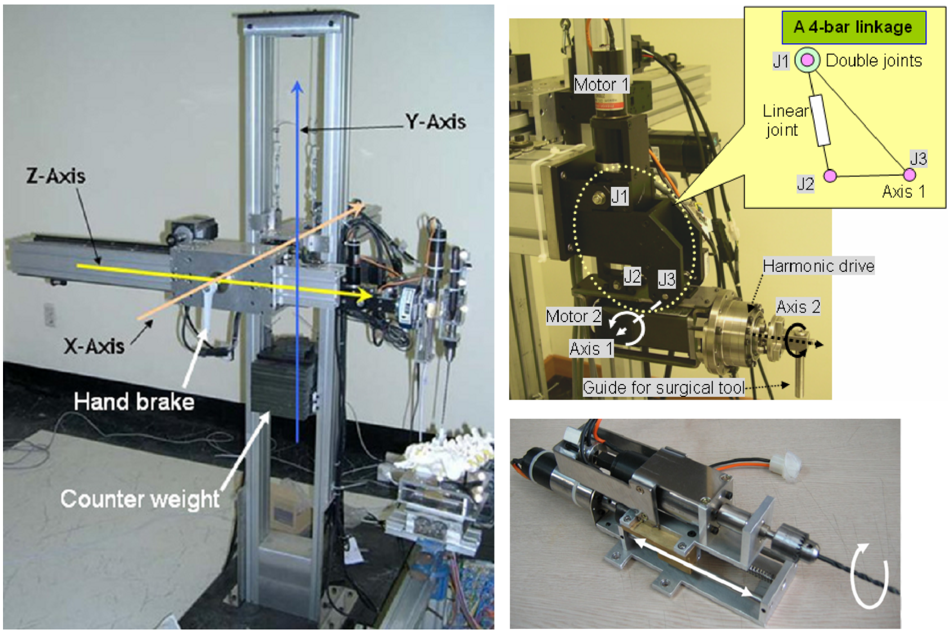

Figure 2.2: The first version of SPINEBOT (Chung et al., 2006). Left: A picture of the whole system, showing the 3 DoFs of the Cartesian mechanism. Top right: A close-up of the gimbal which provides 2 DoFs and holds the tool guide. Bottom right: a close-up of the linear tool guide, with its additional 2 DoFs. Copyright Centre for Intelligent Surgery Systems, Hanyang University. Used with permission.

allowed the surgeons to plan the screw insertions using six different views of a CT or Magnetic Resonance (MR) scan of the patient. The optical tracking system was commercialised by NDI (Waterloo, Ontario, Canada) and offered feedback at 30 Hz for redundant position control of the robot, in addition to its embedded encoders. The robot, as shown on Figure 2.2, consisted of a Cartesian positioner, a gimbal and a tool holder which provided 3, 2 and 2 DoF respectively, giving 7 DoF in total. The robot was able to do the gross and fine positioning of the surgical tools and keep them in place while the surgeon carried out the drilling, although it was capable of doing this task autonomously if desired. SPINEBOT also included a motion correction system, a remarkable feature missing from earlier projects, which was based on the optical feedback and could correct the patient's motion produced by breathing, which had an amplitude of

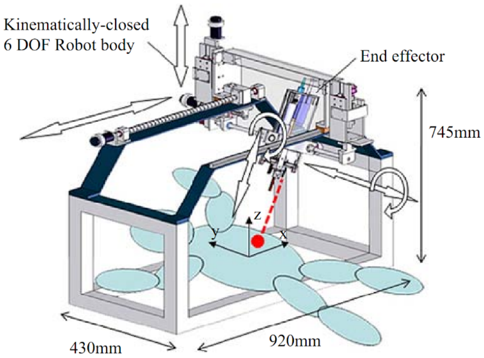

Figure 2.3: A schematic of the CoRA, with its dimensions and DoFs(Lee et al., 2009). Copyright Haptics and Virtual Reality Laboratory, Pohang University of Science and Technology (POSTECH). Used with permission.

3 mm in the antero-posterior direction according to the authors (Chung et al., 2006).

Chung et al. reported multiple experiments using SPINEBOT. On one, they made the robot follow a moving target, which performed a sinusoidal motion with amplitude of 2 mm and a period of 5 s, emulating a breathing patient. SPINEBOT was able to follow the target with an error bounded by ± 0.15 mm and a maximum of 0.45 mm, values close to the 0.35 mm error introduced by the optical tracking system. On a second experiment, holes were drilled on a moving plastic phantom first by a person who used the SPINEBOT as a tool holder and then by the robot working on fully autonomous mode. In both cases, observed deviations were in the 1-2 mm range, although the robot's accuracy seemed slightly superior (Chung et al., 2006).

Lee et al. used the SPINEBOT's planning and tracking systems with the improved robot CoRA, a sophisticated device capable of automated drilling and screw insertion, a feature which, according to the authors, was implemented for the first time (Lee et al., 2009). The robot, as shown on Figure **??**, was built with a more robust frame which permitted it to withstand larger reaction forces, but hindered the surgeon's access to the patient. In addition, CoRA offered cooperative control, a teleoperated drilling system with realistic haptic feedback and a small and lightweight end-effector. Lee et al. published some proof-of-concept experiments on

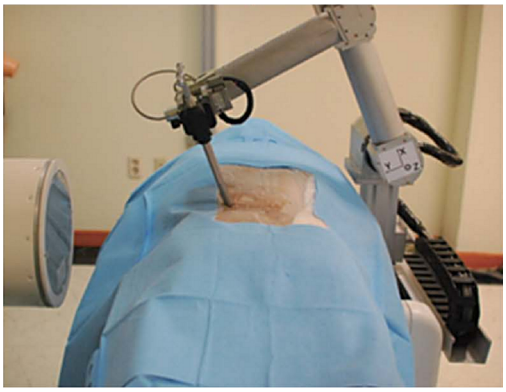

Figure 2.4: The SPINEBOT v2 (Kim et al., 2010b)). The treadmill on the bottom right corresponds to the robot's prismatic joint. Copyright Centre for Intelligent Surgery Systems, Hanyang University. Used with permission.

their article, but did not provide a quantitative analysis of CoRA's performance. As the planning and tracking systems were identical to SPINEBOT's, the authors expected CoRA to have similar levels of errors in screw placement -1 to 2 mm- as the main source of inaccuracies –that is, the optical system–remained unchanged. At the time of writing of this document, no further experiments on phantoms or cadavers using CoRA have been published.

The SPINEBOT v2, presented in 2010, was completely different from the first SPINEBOT despite keeping the same name. As can be seen on Figure 2.4, the new robot had only 5 DoF –1 prismatic and 4 rotational joints– and, more importantly, it lacked the automated drilling capabilities, replacing the original end-effector by a simpler tool holder. Its planning software also went through a complete re-design and the tracking system was replaced by bi-planar continuous fluoroscopy. Instead of relying on optical tracking, SPINEBOT v2 detected the patient's and tool positions by processing the fluoroscopic images –updated at 20 Hz– and by means of custom 2D-3D registration algorithms (Kim et al., 2010b).

The authors performed laboratory experiments to estimate the overall positioning errors of SPINEBOT v2, which was found to be 1.38 ± 0.21 mm. On the cadaveric tests, 28 screws were inserted on 14 different vertebrae of 2 cadavers and post-operative CT scans were made to assess the screws'

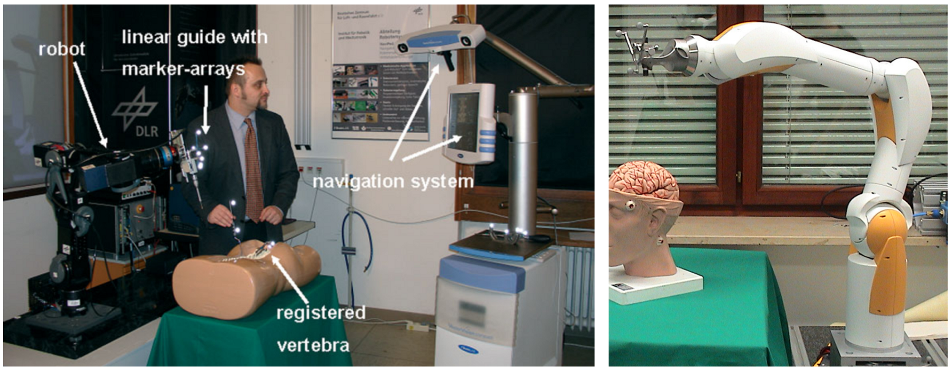

Figure 2.5: The DLR's surgical systems. Left: the prototype using the LWR II coupled with the navigation system and reflective markers. Right: the Kinemedic robot, successor of the LWRII. Left figure reproduced from (Ortmaier et al., 2006a). Copyright 2006 John Wiley and Sons Ltd. Right figure: Copyright Institute of Robotics and Mechatronics, DLR. Used with permission.

insertions and measure their angular deviations. Out of the 28 total screws, 26 were correctly positioned (success rate of 92.86%) with no observed perforations into the spinal canal. Average angular errors were of $2.45 \pm 2.56°$ and $0.71 \pm 1.21°$ on the axial and lateral planes respectively (Kim et al., 2010b).

#### 2.2.2.3 VectorBot/Kinemedic

The Deutsches Zentrum für Luft- und Raumfahrt (German Aerospace Centre, DLR) has developed a series of light weight robots designed for multiple surgical scenarios, giving a desirable degree of versatility that could compensate the increasing cost and complexity of medical robotic systems. DLR's research has also covered spinal surgery, specifically transpedicular fixation, as described by the publications by Ortmaier et al. (Ortmaier et al., 2006b; Ortmaier et al., 2006a). This project was given the name VectorBot by BrainLab (Feldkirchen, Germany), who sponsored it with a $ 5 million investment but, unfortunately, cancelled it before its introduction to the market (Gomes, 2011).

The VectorBot consisted of the DLR's Kinemedic robot coupled with the VectorVision optical tracking system developed by BrainLab, although early prototypes were developed using the preceding Light Weight Robot II (LWRII). Both robots are shown on Figure 2.5. The VectorBot required no x-ray images, as all the tracking was made using markers attached to the patient's vertebrae and points collected by the optical system. Thus, radiation was reduced to a minimum, but at a cost of increased invasiveness due to the large incisions required to expose the spine. In line with other research projects, the authors preferred a robot who worked as an assistant, providing help to the surgeon rather than executing the intervention autonomously. This assistance came in the form of virtual fixtures, that is, physical limits imposed by the robot which prevented the surgeon from deviating too much from the planned trajectories. The robot was not capable of automatic drilling or screwing, although it kept the surgical instrument in a safe and stable location while the surgeon remained in control of these tasks.

In 2006, Ortmaier et al. published the results of a series of evaluation experiments with their proposed system (Ortmaier et al., 2006a). In them, the authors carried out two different machining tasks –drilling and milling– on a block of artificial bone and a bovine spine, measuring hole diameters, pose errors and reactive forces for different machining tools, entrance angles and values of control parameters. Summarising their results, they concluded that milling was superior to drilling in terms of deviation errors and reactive forces, due to the larger slippage of the drill tip observed during drilling, which bent the instrument and increased friction inside its guide. Mean deviation error for milling in the plane perpendicular to the instrument axis was of 0.42 mm, with the maximum reaching up to 1.7 mm. Maximum forces reached up to 15 N, well below the limit of 30 N which could be handled by the robot. In terms of control parameters, the authors concluded that the optimum was reached with high proportional and integral gains, which led to higher robot stiffness, lower pose errors, reduced settling time and decreased overshoot. The authors identified the accuracy and latency of the optical tracking system as critical factors. However, they acknowledged that additional sources of errors in the system were not taken in account in their study, such as pre-operative images' resolution, segmentation accuracy and intra-operative registration errors.

#### 2.2.2.4 Neuroglide

The majority of robots for screw insertion were designed to operate in the lumbar section. This has technical advantages –lumbar pedicles are larger than thoracic and cervical ones so precision requirements are less demanding– but also clinical relevance, as the fusions in the lumbar area are more common than the ones carried out in other spinal regions. This has reduced interest in interventions at the cervical level, a problem addressed by Kostrzewski et al. who proposed the Neuroglide robot for cervical inter-body fusion on 2012 (Kostrzewski et al., 2012). The proposed system was designed specifically for atlanto-axial fusion, that is, the fusion of the upper two vertebrae –C1 and C2– by means of screws inserted through both of them.

The Neuroglide consisted in a high-precision parallel 4 DoF mechanism which held a drill guide, as shown on Figure 2.6. The robot's reduced size limited its workspace, but gross positioning was carried out by means of a passive serial arm on which the robot was mounted, also shown on Figure 2.6. Navigation was implemented using an infra-red optical tracker and active markers attached to the robot and vertebrae, previously exposed by an incision and registered to the pre-operative space by probing points on the bony surface. The authors also developed a custom joystick for robot control and software for navigation and surgical planning, which was used to determine the screw trajectories based on pre-operative CT scans.

The Neuroglide was evaluated on a feasibility experiment with six cadavers, on which an experienced neurosurgeon inserted a total of 10 screws fusing the C1 and C2 vertebrae and then evaluated the insertions with post-operative CT scans. The mean translational error reported by the authors was of 1.94 mm and the mean rotational error was of 4.35°, although two screws were dropped from the statistical sample due to their abnormally large errors produced by drill slippage. It must be noted that the authors improved multiple aspects of their system while the experiments were underway, so results are not comparable directly as they were not obtained under the same conditions. Furthermore, the sample size was not large enough to draw meaningful conclusions. However, the authors reported a remarkable result after all their improvements were in place (0.41 mm and 2.56° for the last screw) and planned further cadaver testing. In addition, Kostrzewski et al. measured the average time needed to use their system and claimed that a conventional image-guided procedure was only

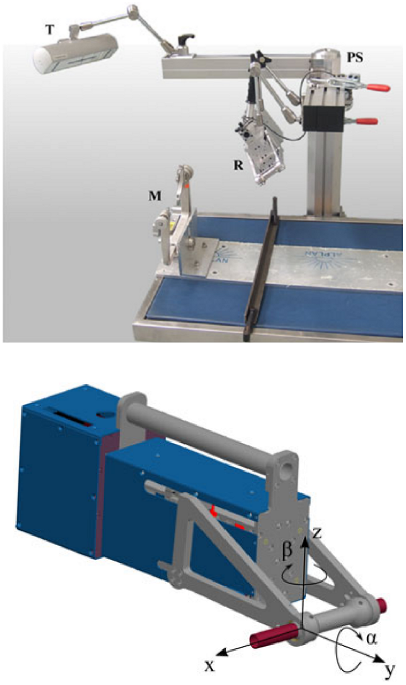

Figure 2.6: The Neuroglide robot for cervical surgery. Top: aspect of the complete system with the robot (R), passive mounting structure (PS), optical tracker (T) and Mayfield clamp (M) for skull attachment. Bottom: Illustration of the robot with the drill holder coloured in red. Robot's DoF are along the y and z axis and around angles $\alpha$ and $\beta$. Figures reproduced from (Kostrzewski et al., 2012). Copyright 2012 John Wiley and Sons Ltd.

3 minutes shorter, a negligible difference for an intervention lasting several hours.

#### 2.2.2.5 RIME

Boschetti et al. proposed on 2005 the Robot In Medical Environment (RIME) project, a robotic system, designed for drilling on transpedicular fixation surgeries (Boschetti et al., 2005). The project main contributions were development of a fully teleoperated system, which permitted the surgeon to operate a patient who could be kilometres away; and haptic feedback, provided to the surgeon using the custom PiRoGa5 device.

Experiments reported on 2007 by Rosati et al. demonstrated the feasibility of haptic feedback transmission and control of a 6 DoF industrial robot between two cities separated by 35 km, although the authors still needed to integrate the optical tracking device proposed by Boschetti et al. into the whole system (Rosati et al., 2007). No publications about experiments with cadavers or animals were found at the time of writing of this study.

#### 2.2.2.6 RSSS

Jin et al. have recently proposed a new surgical robot for pedicle screw insertion, named the Robot Spinal Surgical System (RSSS), based on a 5 DoF SCARA robot equipped with an infrared tracking device (Jin et al., 2011b). RSSS' mechanical design ensures that the robot should not collapse under its own weight in case of a power failure, ensuring the patient's safety. RSSS offers haptic feedback, virtual fixtures, a screw implanting mechanism and a control strategy for automated drilling, which is able to identify the force profiles for each drilling stage and automatically stop before breaching the vertebra (Jin et al., 2011a). Currently, this project is on an experimental stage and only experiments for tuning of control parameters have been reported.

### 2.2.3 Robot for laminectomy

On 2010, Wang et al proposed a robot for laminectomies, that is, removal of posterior bony sections of vertebrae to alleviate nerve compression produced by diseases such as stenosis. This type of procedures requires milling of bone in the vicinity of the spinal cord, thus a high level of precision is required as damage to the latter must be prevented at all costs. The authors proposed a robot with 2 translational DoF capable of automatic machining of the lamina and able to stop just before penetration into the spinal canal, leaving a thin layer of bone which should be later removed by the surgeon. The robot was equipped with force sensors and custom algorithms able to identify the bone layer being machined, according to the measured force profiles. The authors reported experimental results on 10 bovine spine samples, on which they measured the thickness of the bone layer left by the robot, which had an average value of 1.1 mm. No breaching into the spinal canal was observed and the robot's recorded working times were between 10 and 14 min, similar to the times taken by surgeons doing the same task.

Further work was planned by the authors to build a more stable mounting platform for the robot as well as additional experiments (Wang et al., 2010).

### 2.2.4 Robots for needle-based interventions

A considerable number of recent robotics projects –5 out of 18– have addressed needle-based interventions such as biopsies and vertebroplasties. As it will be seen, many of these were not specifically designed for use in the spine, as needle-based interventions can be executed in many other anatomical regions. A summary of the most relevant experiments using these robots is given on Table 2.3 and detailed descriptions will be given in the sections below.

| Robot | Brief description | Evaluation criteria | Results | Reference |
|---|---|---|---|---|
| AcuBot | Randomised clinical trial with 20 patients, of which 10 were operated with the robot and 10 using a conventional manual technique. | Measurement of needle deviation from the planned target point using bi-planar fluoroscopy. | Mean deviation with robot: 1.105 mm. Mean deviation with manual technique: 1.238 mm | (Cleary et al., 2005) |
| Innomotion | Testing of robot-guided percutaneous needle insertions on four pigs put under general anaesthesia. | Target deviation measured using MR imaging. | Axial deviation in the ± 1 mm range (min: 0.5 mm, max: 3 mm). Transverse angular deviation in the ± 1° range (min: 0.5°, max: 3°) | (Melzer et al., 2008) |
| Innomotion | 25 MR-guided punctures on phantoms placed within water filled containers. | Deviations from planned target points measured by hand, using rulers. | Observed deviation of $2.2 \pm 0.7$ mm. | (Moche et al., 2010) |
| DLR LWR III | In-vitro mechanical trials using a precisely constructed phantom. | Deviation measured from post-operative 3D radiographies. | $1.2 \pm 0.4$ mm (max: 1.98 mm) | (Tovar-Arriaga et al., 2011) |
| (Onogi et al., 2009) | In vitro test of 50 punctures on the pedicles of 5 spinal phantoms. | Deviation measured with post-operative CT scans. | Translational deviation: $1.46 \pm 0.80$ mm. Angular deviation: $1.49 \pm 0.64°$. | (Onogi et al., 2009) |
| SpineNav | In-vitro mechanical trials, measuring errors in 30 positions within the robot's workspace. | Deviation measured using a three-dimensional digitising arm. | 0.89 mm (max: 1.14 mm) | (Song et al., 2009) |

Table 2.3: Brief description of reported experiments for robots designed for needle insertion tasks.

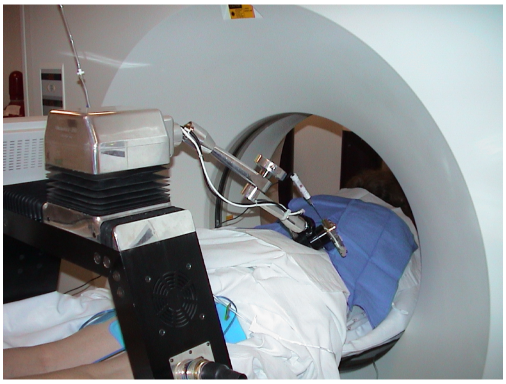

Figure 2.7: The AcuBot being used in a CT-guided needle insertion. The 3 DoF Cartesian manipulator is placed over the black bridge attached to the scanner's table. The RCM and the linear end-effector are placed at the end of the passive articulated arm, which comes out from the right side of the Cartesian mechanism. Copyright 2012 URobotics Lab, Johns Hopkins University. Used with permission.

#### 2.2.4.1 AcuBot

One year before publication of the MARS robot, Cleary et al presented a plan for development of a minimally-invasive system for spinal surgery (Cleary et al., 2002). In this article, the authors identified multiple technical problems found in the implementation of a system of this kind: unavailability of intra-operative axial images, difficult fusion of CT and MR data, lack of visualisation of oblique trajectories, unavailability of spinal tracking systems, slow and difficult instrument insertion and lack of appropriate software. The authors, to solve the aforementioned problems, advocated the use of intra-operative CT, 3D visualisation, optical tracking systems, robotic tool holders and development of specialised software. This technical plan lead to the development on 2003 of the AcuBot, a robot designed for percutaneous needle insertion guided by fluoroscopy –using one or two planes– or intra-operative CT scans (Stoianovici et al., 2003). AcuBot received clearance from the FDA and clinical trials with 20 patients that underwent spinal nerve blockade were published on 2005 (Cleary et al., 2005).

AcuBot, shown on Figure 2.7, had a total of 6 DoF, decoupled in positioning, rotation and instrument insertion. A 3 DoF Cartesian manipulator, mounted on a bridge attached to the scanner's table, supported a Remote Centre of Motion (RCM) mechanism with 2 DoF with the instrument mounted on its end-effector, which had an additional translational DoF along the instrument axis. Normally, the Cartesian manipulator brought the needle close to the insertion point, the RCM corrected its orientation and, after approval of the surgeon, the instrument was inserted to reach the target point inside the patient's body. In addition, a 7 DoF passive mechanism was mounted between the Cartesian manipulator and the RCM mechanism, which was manually adjusted by the surgeon before the procedure, bringing the instrument close to the entry points. The AcuBot also included a display and a joystick, used by the surgeon to control the robot remotely.

A clinical trial was reported by Cleary et al., on which the AcuBot was used to perform bi-planar fluoroscopy guided nerve and facet blocks (Cleary et al., 2005). This type of procedure consists in the localisation of the source of back pain by insertion of 22-gauge needles on precise locations of the spine followed by injection of local anaesthetics. On the reported trial, a randomised study was performed on the Georgetown University Medical Centre with 20 patients, 10 of which underwent the conventional procedure and the remaining 10 were operated using the AcuBot. Needle insertion accuracy and pain relief were measured for both groups of patients and results were similar for both measures. Mean deviation for the robot and manual methods were 1.105 mm and 1.238 mm respectively. Pain scores –measured from 0 to 10– were reduced from 6.3 to 1.8 using the robot and from 6.0 to 0.9 using the manual method. Although the results give the impression that the AcuBot is as accurate and effective as the manual method, the authors acknowledged that the statistical sample was too small to draw significant conclusions. Currently, research with the AcuBot is focused on development of a rotating needle holder for improved lesion targeting in soft organs such as the liver and lung, giving less attention to spinal procedures (Badaan et al., 2011).

#### 2.2.4.2 Innomotion

MR offers interesting advantages for robotic and image-guided surgery, as it offers superior soft tissue contrast and does not irradiate the patient. However, the strong magnetic fields present in all MR systems

Figure 2.8: The Innomotion robot, used for CT and MR guided needle-based procedures. Copyright Innomedic GmbH. Used with permission.

greatly complicate the robotic design, as compatible materials, sensors and actuators must be used. In addition, an MR-compatible robot should have a reduced size to fit into the small space of the magnet's bore, largely occupied by the patient. All of these factors make development of MR-compatible robots a formidable challenge. A remarkable example, used in spinal procedures, is the work by Hempel et al. (Hempel et al., 2003), who presented in 2003 the Manipulator for Interventional Radiology (MIRA), which evolved into the Innomotion system (Melzer et al., 2008). The latter obtained CE clearance and was introduced to the market by Innomedic GmbH (Herxheim, Germany), which was acquired by Synthes (Solothurn, Switzerland) in 2008. The Innomotion's commercialisation was stopped in the early 2010 and is expected to be restarted in 2012 by IBSmm (Brno, Czech Republic), company which is now working on the robot's improvement.

Innomotion, shown on Figure 2.8, was designed as a telemanipulator for MR-guided insertion of cannulae and probes for biopsy, drainage, drug delivery and energetic tumour destruction. Although direct interventions in the central nervous system were left out due to the demanding regulations and long approval process, Innomotion can still be used for interventions in the spine's periphery. The robot's kinematics consists of an arm driven in 5 DoF, attached to an orbiting ring mounted on the scanner's table, and is equipped with linear pneumatic actuators and optical limit switches, rotational and linear encoders. Innomotion's instrument holder was designed as a RCM with 2 DoF and was equipped with gadolinium filled spheres, which could be easily segmented from intra-operative MR images to detect its position and orientation.

Melzer et al. published results of animal tests in which the robot's deviation in the axial plane was estimated to be within the ± 1 mm range (minimum: 0.5 mm, maximum: 3 mm) and its angular deviation to be in the ± 1° (minimum: 0.5°, maximum: 3°) These results were compliant with the CE standard, although they were not sufficient for interventions in the central nervous system (Melzer et al., 2008) In 2010, Moche et al. published a study with accuracy measurements of Innomotion using phantoms as well as clinical trials. On the phantom study, 25 needle insertions were performed with observed deviation between the target and observed points of 2.2 ± 0.7 mm, measured by hand using rulers. The reported clinical trials consisted of diagnostic biopsies which required planning and execution times of 25 and 44 minutes respectively. Of the six reported interventions, two were carried out successfully around the spine: one was a bone biopsy in the iliac crest and one was an abscess aspiration in the L5-S1 region. No complications were observed on all six cases (Moche et al., 2010).

#### 2.2.4.3 DLR's LWR III

A following version of DLR's LWR –the LWRIII– is now commercialised by KUKA and is increasingly being adopted for surgical robotics projects, such as the one designed for spine biopsies and vertebroplasties presented by Tovar-Arriaga et al. (Tovar-Arriaga et al., 2011). This project consisted in the aforementioned robot guided by intra-operative 3D radiographies, acquired by a rotational c-arm, and an optical infra-red tracking system. The authors reported two experiments. On the first, they measured the errors of the calibration between the tooltip positions measured by the optical system and the robot's controller, which had a mean of 0.23 mm, a deviation of 0.1 mm and a maximum value of 0.47 mm. On the second experiment, the authors positioned the tooltip on various locations over a precisely manufactured phantom and measured the deviations with 3D radiographies. On it, the authors estimated the error to be in the 1.2 ± 0.4 mm range, with minimum and maximum values of 0.3 and 1.98 mm respectively. Overall, the reported accuracies were acceptable for the demands of surgery, although the authors cited the optical system's accuracy and low sampling rate –20 Hz– as limiting factors that should be improved in future versions.

#### 2.2.4.4 University of Tokyo's robot for vertebroplasty

A group of Japanese researchers from the cities of Tokyo and Osaka presented a robotic system for vertebroplasty, based on a robot with a compact end-effector which could be inserted in the space between the c-arm and the patient. Surgical planning was carried out on pre-operative CT scans, whilst intra-operative guidance relied on fluoroscopy. For this purpose, the needle holder was built with plastic material to make it partially radiolucent. In addition, this mechanical device could be automatically detached from the robot by a safety mechanism, triggered when excessive forces were applied to the needle (Onogi et al., 2005). On 2009, Onogi et al. reported an in-vitro experiment on which the robot was used for 50 punctures on the pedicles of five polyurethane phantoms of lumbar spines. Deviation, measured from post-operative CT scans, was estimated to be 1.46 ± 0.80 mm and 1.49 ± 0.64° (Onogi et al., 2009).

#### 2.2.4.5 SpineNav

In 2008 Ju et al. presented the SpineNav, a robot for percutaneous vertebroplasty which could insert needles autonomously or using a tele-operated mechanism with 5 DoF (Ju et al., 2008). This robot is designed to be used inside a CT scanner and its mounting platform has a metal mask which can be easily segmented from the intra-operative images to estimate the robot's base position and orientation with respect to the patient. Accuracy tests carried out by the authors estimate SpineNav's mean positioning error on 0.89 mm, with a maximum of 1.14 mm (Song et al., 2009). To this date, no reports about experiments with cadavers or clinical trials using SpineNav are available.

### 2.2.5 Robots for endoscopic interventions

#### 2.2.5.1 MINOSC - Sub-arachnoid space exploration

The Microneuroendoscopy of spinal cord (MINOSC) European project lead to the development of a robotic system for interventions of the spinal cord from within the sub-arachnoid space. This is a challenging task, as this section of the spine is only a few millimetres wide and is surrounded by delicate structures which can easily become damaged. Ascari et al. published results of the design of a robot-assisted endoscope, which provides the surgeon with direct vision of the surrounding structures –spinal cord, blood vessels and nerve roots– and permits operations such as localised electro-stimulation. The system uses image processing techniques to analyse its surroundings and give feedback to its control unit, which can steer the endoscope tip to avoid obstacles which may not be even present in the endoscope's field of view. Steering is implemented by a 2 DoF cable-driven mechanism and 3 lateral hydraulic jets that stabilise the endoscope's tip (Ascari et al., 2010).

In 2010, Ascari et al. reported a series of in vitro, ex vivo and in vivo experiments, which validated all the prototype's subsystems excluding navigation, which was tested up to in vitro experiments. In addition, localised electro-stimulation of nerve roots was successfully accomplished in an additional in vivo test. According to the authors, the prototype is still far from reaching clinical use, but the major implementation problems were already solved in its current stage (Ascari et al., 2010).

#### 2.2.5.2 Da Vinci

The da Vinci surgical robot (Intuitive Surgical, Sunnyvale, California), mostly used in urological and gynaecological surgeries, has also been tested for endoscopic spinal interventions although its applications are limited. In fact, the da Vinci's end-effectors are not well suited for bone drilling due to the limited range of force they offer, as they were designed primarily for manipulation of soft tissue (Karas and Chiocca, 2007). However, there are reports of successful experiments using it for spinal interventions, although all are at an early experimental stage.

Yang et al. published a review of experimental uses of the da Vinci on spinal procedures along with a report of five successful cases of paravertebral tumour resections (Yang et al., 2010). Lee et al. published a study on two cadavers which demonstrated the feasibitlity of using the da Vinci for transoral decompression of the cranio-cervical junction (Lee et al., 2010) and Ponnusamy et al. reported successful laminotomy, laminectomy, disc incision and dural suturing procedures on a pig using a posterior approach (Ponnusamy et al., 2009). The lack of appropriate tools for the da Vinci is repeatedly cited as a problem, although Ponnusamy et al. reported the use of a prototype burr, rongeur and laser instrument, the last one used for rapid coagulation.

Kim et al. reported an experiment of anterior lumbar interbody fusion (ALIF) using the da Vinci on a pig, inserting a metal cage in the inter-disc space. Although ALIF was proposed several years ago, post-operative complications have prevented its widespread use. The work of Kim et al. expects to increase this surgery's safety by incorporating robotic assistance, although it is still on an early stage (Kim et al., 2010a).

### 2.2.6 Radiosurgery robotic systems

Current radiosurgical systems employ heavy-duty robots to move a linear accelerator (LINAC) around the patient, firing high-energy beams according to a pre-defined plan, ablating internal tumours and minimising damage to surrounding healthy tissue. Although radiosurgical system do not come in contact –or even near– the patient, we considered that they should be included in this review as they are currently used for treatment of spinal lesions and they fit the criteria exposed in the Methods Section, as they autonomously perform a clearly defined surgical task with direct impact on the patient's body.

Radiosurgery was conceived as treatment for deep-seated intracranial tumours, for which conventional surgery is considered too dangerous or unfeasible. The first commercially available radiosurgical system was the GammaKnife (Elekta AB, Stockholm, Sweden) which was introduced to the market on 1968 and, since then, radiosurgery has gained worldwide acceptance and is now considered within standard oncological practice. Nowadays, the market is dominated by the CyberKnife (Accuray Inc, Sunnyvale, CA) and the Novalis (BrainLAB, Heimstetten, Germany), which permit interventions guided by intra-operative imaging, without the need of stereotactical frames. Using this, a pair of x-ray devices acquires images of the patient at regular intervals, which are processed to monitor the patient's position and adjust the LINAC accordingly, minimising deviations from the surgical plan.

Nowadays, radiosurgery is used for treatment of lesions found in many extra-cranial regions, including the spine. A recent review by Romanelli and Adler cites multiple clinical studies of spinal radiosurgery, stating that this technique is well suited for treatment of neoplastic lesions and intramedullary arteriovenous malformations (Romanelli and Adler, 2008). In addition, spinal radiosurgery offers an effective and well-tolerated option, as an study made in Pittsburgh suggests, which followed 393 patients and observed high rates of long-term pain control (86%) and long-term tumour control (88%) with no cases of neurological damage induced by radiation (Gerszten et al., 2007). Radiosurgery was not considered practical before the introduction of image-guidance, as the first reported cases used a stereotactic frame which had to be attached to the spinous processes of the vertebrae, previously exposed by multiple incisions. This was naturally too cumbersome and not usable in treatments that required multiple radiation doses distributed along multiple sessions (Hamilton et al., 1995). The introduction of frameless image-guidance permitted more practical uses in spinal surgery, although the first reported studies still relied on fiducial markers inserted into the vertebrae adjacent to the lesion. Further development of image-guidance technology permitted interventions without the need of any type of markers and without noticeable reductions in accuracy: studies estimate that fiducial-based spinal radiosurgery is accurate to within a mean distance of 0.7 mm (Yu et al., 2004) and image-based is accurate to a mean distance between 0.5 and 0.6 mm (Muacevic et al., 2006; Ho et al., 2007).

Accuray and BrainLAB host extensive lists of publications related to the CyberKnife[4] and Novalis[5] systems on their respective websites. Interested readers should consult them for additional information.

## 2.3 Discussion

### 2.3.1 Robots' design and safety

In the early days of surgical robotics researchers adapted industrial robots for use in the operating room but, in the last decade, there is a clear tendency in favour of specifically designed ones. Spinal surgery has been

---

[4] http://www.accuray.com/healthcare-professionals/clinical-publications/cyberknife-publications#spine

[5] http://www.novalis-radiosurgery.com/wp-content/uploads/2009/07/NTx+NV_Biblio_DEC0709_SPINE.pdf

no exception. In the early years, that is 1992 to 2002, researchers such as Sautot et al. (Sautot et al., 1992) and Santos-Munné et al. (Santos-Munné et al., 1995) adapted industrial robots for surgical use. In the last decade, we have seen the appearance of robots specialised for surgical applications. Remarkable examples are SpineAssist (Shoham et al., 2003), AcuBot (Stoianovici et al., 2003), Innomotion (Melzer et al., 2008), the SPINEBOT series (Chung et al., 2006; Kim et al., 2010b), CoRA (Lee et al., 2009) and the DLR's LWR series (Tovar-Arriaga et al., 2011; Ortmaier et al., 2006b). More recent works continue in the same line, proposing new models rather than adapting industrial robots. Examples are SpineNav (Ju et al., 2008), RSSS (Jin et al., 2011b) and the works by Onogi et al. (Onogi et al., 2005). This shift has been caused by safety requirements: industrial robots are designed to perform tasks –usually involving high torque or speed– in the absence of humans, whereas surgical robots must constantly interact with the surgeon, clinical staff and the patient (who is absolutely unable to react in case of emergency). Besides, it must be possible to make them sterile using draping to reduce risk of infection. It is worthy to notice that, as medical robots are relatively new, no international standards exist for them yet, although the International Standardisation Organisation (ISO) and the International Electrotechnical Commission (IEC) are currently working on their development.

There is also a tendency to increase safety by giving less autonomy to robots in the operating room. In fact, surgeons seem to prefer to be in control of all the intervention's tasks, restricting the use of robots for assistance. This approach is desirable, as it combines the strengths of robots –stability, precision and immunity to fatigue– and humans –better analysis, judgement and response in unexpected situations– who work cooperatively and increase the surgery's safety. A remarkable example is the SPINEBOT series: its first prototype had automated motion and drilling (Chung et al., 2006), but these features were not present in the second model. In fact, SPINEBOT v2 main capability was keeping the instrument in a stable position, leaving gross positioning and drilling in hands of the surgeon (Kim et al., 2010b).

### 2.3.2 Accuracy

A summary of accuracy experiments for robots designed for screw insertion is given on Table 2.2, which shows that many are capable of inserting screws with more than 85% possibility of success and a deviation between 1-2 mm. Of particular interest is the retrospective clinical study by Devito et al. (Devito et al., 2010), which analysed 646 insertions performed using SpineAssist and concluded that 635 (98.3%) were inserted with errors below 2 mm. Table 2.3 also shows a summary of experiments, but only for robots designed for needle-based procedures. The table's data shows that these robots are also capable of precise insertions with errors bounded by the same values. It can be concluded that current robotic technology is capable of accurate instrument placement in the 1-2 mm range, but not yet able to reach sub-millimetre accuracy in realistic conditions (i.e. in actual interventions or in-vivo experiments) In the current situation, we could say that robots are faced with a '1 mm barrier' which they have not been able to overcome yet. Going below this limit has clinical relevance as pointed out by Rampersaud et al., who estimated that 1 mm and 5° were the maximum translational and rotational errors that could be admitted in screw insertion on the midcervical spine, the midthoracic spine and the thoracolumbar junction (Rampersaud et al., 2001). Among the factors that influence this we can cite imaging system's resolution, registration inaccuracies and the vertebrae's motion. Robots for screw insertion are also affected by drill slippage, vibrations and reactive forces whereas needle-based ones' main sources of error are needle deflection and tissue deformation.

### 2.3.3 Registration and tracking technologies

In terms of tracking and registration technology, projects designed for screw insertion have preferred optical tracking, with the remarkable exceptions of SpineAssist and SPINEBOT v2. Robots for biopsies and other needle-based procedures prefer less invasive tracking technologies such as fluoroscopy and intra-operative CT, which prevent unnecessary incisions. Today, all available technologies for tracking and registration have inconveniences. On one hand, optical tracking offers sub-millimetre precision at a reasonable cost and can reduce the required number of x-rays, as periodic imaging to locate the surgical tools become less necessary. However, optical tracking suffers from marker occlusions and low sampling rates –something which has been repeatedly cited as a problem (Tovar-Arriaga et al., 2011; Ortmaier et al., 2006a)– and mounting of markers requires rigid attachment to the patient's bony structures, which translates into more incisions and higher invasiveness. On the other hand, fluoroscopy and intra-operative CT are less invasive, but their use exposes the patient, surgeon and clinical staff to higher doses of radiation, which is undesirable. Intra-operative MR is not well-suited for spinal surgery, as bone is not visible on MR images as it produces no signal. Besides, it is still uncommon on most hospitals and its strong magnetic field mandates the replacement of all surgical tools and implants by their MR-compatible versions.

Patient's registration has the additional problem of the vertebrae relative motion. If a single vertebra is tracked, it is unrealistic to assume that the adjacent ones will move in the same manner or, in other words, to consider the spine as a rigid body. One option to solve this problem is reduction of the spine's range of motion by means of additional hardware such as the SpineAssist's Hover-T. Another interesting approach is the one used by SPINEBOT v2, which uses individual registration of vertebrae from bi-planar fluoroscopic images updated in real time which, obviously, has the inconvenience of higher radiation (Kim et al., 2010b). The spine's relative motion cited here and the tracking systems' tradeoffs make the choice of a registration strategy a problem for which no obvious solution exists yet.

### 2.3.4 Project development

Nowadays, Mazor Robotcs' SpineAssist is the only commercially available robot –with FDA and CE clearances– specifically designed for spinal surgery, in particular, transpedicular fixation. There are 7 other projects for similar applications, but, as far as we know, none of them have obtained any of the aforementioned clearances yet. The difficult and expensive certification procedures and the high cost of robotics projects per se are big hindrances for companies wishing to enter the medical robotics market. All this forms a scenario on which Mazor Robotics should remain without direct competitors for some time.

However, other commercial robots are now used for spinal surgery although they, differing from SpineAssist, were not specifically designed for this application. In fact, CyberKnife and Novalis are used for spine-related procedures and the da Vinci has also been used for them, although the reported cases are still at experimental stages and its adoption in a clinical environment does not seem to happen soon.

### 2.3.5 Economic analysis

To the best of our knowledge, there is no publication available which analyses the costs and benefits, from the clinical point of view, of robotics in spinal surgery. Even more, there are no studies today regarding the cost-efectiveness of image-guided spinal surgeries, according to Tjardes et al. (Tjardes et al., 2010). It is necessary for hospitals to ensure that the benefits brought by robotic surgery outweigh the costs, which are very high. As an example, installation of a Mazor Robotics' Renaissance system has a cost of 789K USD (including the robot, workstation, instrument tray and one year of technical support) while each intervention requires disposable materials which cost 1.2K USD and implants valued between 6K and 8K USD. In addition, technical support from Mazor must be renewed annually, signing contracts of 10% of the installation price per year (Hadomi, 2012).

## 2.4 Conclusions

This chapter has reviewed the state of the art in surgical robotics for spinal interventions. Several prototypes and commercially available systems have been analysed, showing that this particular field is still at an early stage of development. Up to this date, only one robot specifically designed for spine surgeries is available in the market –SpineAssist/Renaissance– while the others are research prototypes or commercial robots originally designed for other uses.

Among spine-specific applications, the most studied one has been screw insertion, for which current technology offers increased levels of safety, considerably reducing the number of misplaced screws. The accuracy of robots for this application –and also for needle insertion– permits instrument placements with deviations between 1 and 2 mm.

Robots not only make existing surgeries safer: they also enable surgeons to do interventions which, without their assistance, would be absolutely unfeasible. Two remarkable examples are SpineAssist's GO-LIF (Shoham, 2011) and the sub-arachnoid space exploration permitted by MINOSC (Ascari et al., 2010). These projects are examples that robotic surgery can not only improve existing interventions, as they can also be 'enabling' technology (Shoham, 2011).

However, the field of robotics for spinal surgery still faces considerable challenges. Sub-millimetre precision in instrument placement –in realistic conditions– has not yet been achieved. Patient tracking and registration still have demanding problems, as no technology is capable of offering high accuracy, low invasiveness, low radiation and high robustness simultaneously. Also, the vertebrae relative motion introduces an additional problem in registration which still needs to be addressed properly. In economic terms, ingenious solutions are needed to bring down the cost of robotics systems. The latter is still high and has prevented a more widespread use of surgical robots, as hospitals are unsure if their clinical benefits outweigh their elevated price. All these present challenges show that spinal surgical robotics still has potential that can be transformed into increased patient well-being.

In this thesis, we aim to develop a versatile robotic system based, as written in the Introduction, on a 7 DoF arm. This gives the system a desirable degree of versatility, in line with the ideas pursued by the DLR LWR's design team. As surgical robots are expensive, it is convenient that they could be used for multiple interventions, to get the maximum possible benefit. Our system could be deployed on multiple surgical scenarios, although its initial phase of development has been centred on spinal screw insertion applications. Our choice of registration strategy is a combination of the two most popular approaches: we chose optical tracking, but without exposition of the whole spinal section. Instead, a single marker is mounted on a vertebra's spinous process, setting the origin of a coordinate frame in the operating room. Then, an optically tracked x-ray imaging device acquires a reduced set of radiographies –normally two– and locates the patient combining the data coming from the x-ray images and the motion capture cameras. A system of this kind balances the benefits of both approaches: invasiveness is kept to a minimum by means of x-ray imaging and the number of radiographies is reduced by the optical system's help, which also permits real-time tracking. In this way, we strive to obtain a balance between invasiness and radiation, while providing surgeons real-time information and, most importantly, a sufficient level of accuracy to ensure safe screw insertions.

## Chapter 3

# Problem definition

## 3.1 Main concepts

One of the core problems in robotic assisted surgery is registration, defined as the *process of determining the spatial transform that maps points on one coordinate system to the homologous points on a second coordinate system.* Registration will be a core concept of Chapters 5, 6 and 7, so a proper background about it and its related concepts will be given here.

Let $\mathbf{x}_A$ be a point measured in the three-dimensional coordinate system $A$. In this thesis, subscripts will normally indicate the coordinate system in which points are measured.

$$\mathbf{x}_A = \begin{bmatrix} x_A \\ y_A \\ z_A \end{bmatrix} \tag{3.1}$$

Let $\mathbf{x}_B$ be an homologous point, but measured in a different coordinate system $B$. The registration problem consists in finding a transform function $\mathcal{T}_B^A$ which maps points from coordinate system $B$ to coordinate system $A$

$$\mathbf{x}_A = \mathcal{T}_B^A(\mathbf{x}_B) \tag{3.2}$$

$\mathcal{T}_B^A$ can be any function that goes from $\Re_3$ to $\Re_3$. However, of particular interest are rigid transforms, which preserve the distance between points. Rigid transforms are composed of a rotation and an offset, which are represented by a 3 by 3 matrix and a 3 element vector.

$$\mathcal{T}_B^A(\mathbf{x}_B) = \mathbf{R}\mathbf{x}_B + \mathbf{s} \tag{3.3}$$

This representation of rigid transforms has a considerable inconvenience, which is that rotations are always carried out around the origin of coordinate system $B$. Alternatively, it is possible to define a centre of rotation $\mathbf{c}$. By doing so, the coordinate system is first displaced to the centre of rotation, rotation is applied and the coordinate system is taken back to its original centre. Finally, points are displaced by a translation $\mathbf{t}$ which is not the same as the previously defined offset $\mathbf{s}$

$$\mathcal{T}_B^A(\mathbf{x}_B) = \mathbf{R}(\mathbf{x}_B - \mathbf{c}) + \mathbf{c} + \mathbf{t} \tag{3.4}$$

It is not difficult to see that the representation of a rigid transform using the rotation matrix, centre of rotation and translation has an equivalent representation using a rotation matrix and offset.

$$\mathcal{T}_B^A(\mathbf{x}_B) = \mathbf{R}\mathbf{x}_B + \underbrace{(-\mathbf{R}\mathbf{c} + \mathbf{c} + \mathbf{t})}_{\mathbf{s}} \tag{3.5}$$

A more compact representation of rigid transforms can be obtained by using homogeneous coordinates

$$\tilde{\mathbf{x}}_A = \begin{bmatrix} x_A \\ y_A \\ z_A \\ 1 \end{bmatrix} \tag{3.6}$$

By doing so, it is possible to group the rotation matrix and offset into a single 4 by 4 matrix $\mathbf{T}_B^A$ and, therefore, the transform process becomes a single matrix multiplication $\tilde{\mathbf{x}}_A = \mathbf{T}_B^A \tilde{\mathbf{x}}_B$

$$\mathbf{T}_B^A = \begin{bmatrix} & \mathbf{R} & & \mathbf{s} \\ & & & \\ 0 & 0 & 0 & 1 \end{bmatrix} \tag{3.7}$$

Rotation matrices can be defined using 3 parameters. The most popular parametrisation are the *Euler angles*, which decompose the rotation matrix into the product of three elemental matrices representing the rotations around three axes, such as the three matrices written below for rotations around $x$, $y$ and $z$

$$\mathbf{R}_x = \begin{bmatrix} 1 & 0 & 0 \\ 0 & \cos(\varphi_x) & -\sin(\varphi_x) \\ 0 & \sin(\varphi_x) & \cos(\varphi_x) \end{bmatrix} \tag{3.8}$$

$$\mathbf{R}_y = \begin{bmatrix} \cos(\varphi_y) & 0 & \sin(\varphi_y) \\ 0 & 1 & 0 \\ -\sin(\varphi_y) & 0 & \cos(\varphi_y) \end{bmatrix} \tag{3.9}$$

$$\mathbf{R}_z = \begin{bmatrix} \cos(\varphi_z) & -\sin(\varphi_z) & 0 \\ \sin(\varphi_z) & \cos(\varphi_z) & 0 \\ 0 & 0 & 1 \end{bmatrix} \tag{3.10}$$

Euler angles have serious inconveniences, the first being that the order in which rotations are applied is not standardised. As an example, it is possible to define a set of Euler angles rotating first around $x$, then $y$ and finally $z$. It is also possible to rotate twice around a single angle defining the rotation matrix as, for example, a rotation around $z$, then $y$ and finally $z$ again. To make matters worse, it is also possible to define rotations following the *right* or *left* hand rules by changing the signs of the sinuses of the elemental rotation matrices given above. All this gives a total of 24 different conventions for Euler angles [1]. In this thesis, rotations are assumed be carried out first around the $y$ axis, then $x$ and finally $z$.

$$\mathbf{R} = \mathbf{R}_z \mathbf{R}_x \mathbf{R}_y \tag{3.11}$$

Rigid transforms are invertible by definition. Therefore, if a transform that goes from system $A$ to $B$ is known the inverse transform that goes from $B$ to $A$ can be obtained directly by inverting the original matrix.

$$\mathbf{T}_B^A = (\mathbf{T}_A^B)^{-1} \tag{3.12}$$

In addition, if three coordinate systems are present $-A$, $B$ and $C-$ and the transforms from $A$ to $B$ and from $B$ to $C$ are known, it is possible

---

[1] http://en.wikipedia.org/wiki/Euler_angles (visited on September 2012)

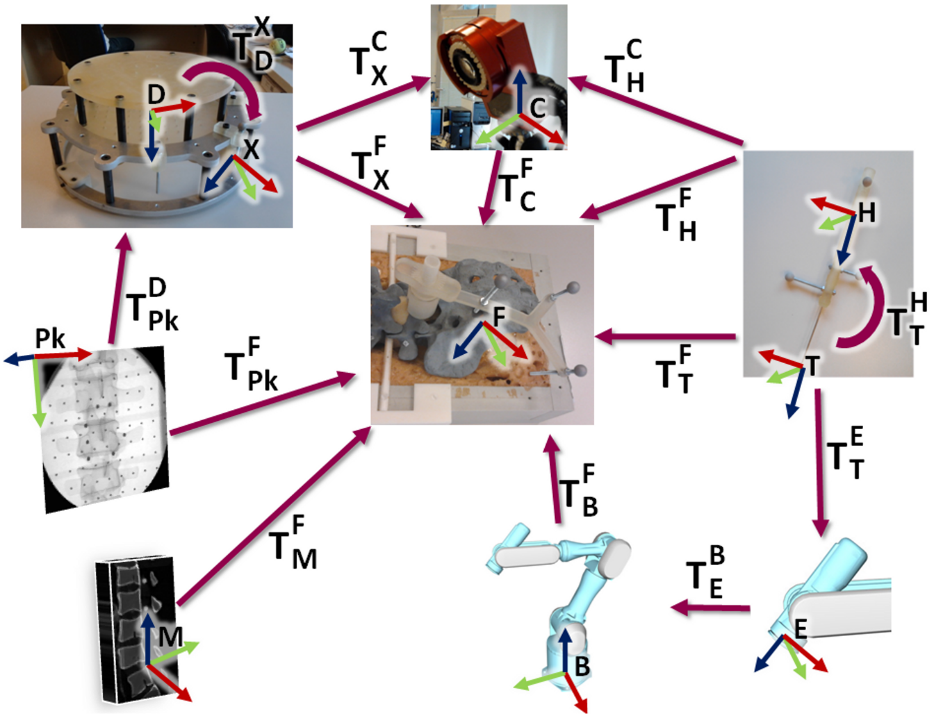

Figure 3.1: All the proposed system's coordinate systems and transforms. Please refer to the text for the description of each one.

to obtain the transform that goes from $A$ to $C$ by left-multiplying the transform matrices.

$$\mathbf{T}_A^C = \mathbf{T}_B^C \mathbf{T}_A^B \tag{3.13}$$

## 3.2 Coordinates systems definition

The proposed robotic system has a large number of coordinate systems and related transforms, all of them illustrated on Figure 3.1. This figure is quite complex and we don't expect the reader to understand it completely at this point. We suggest to keep it as a reference and consult it while reading the rest of the thesis, as more detailed descriptions of the coordinate systems and transforms will be given in following chapters.

A brief description of the coordinate systems will be given below:

**C** corresponds to the **c**ameras' coordinate system, defined by the motion capture system.

**F** corresponds to the coordinate system centred on an optical marker attached to the patient's vertebra. As in the 2D-3D registration the fixed images are defined in this coordinate system, letter **F** was chosen to name it.

**X** corresponds to the coordinate system centred on the optical marker attached to the calibration drum, used to estimate the **x**-ray machine parameters and correct its distortion.

**H** correspond to the coordinate system defined by the optical markers attached to the surgical tool **h**older.

In reality, coordinate system $C$ is rarely used and the location of the calibration drum ($X$) and surgical tool ($H$) are referred to the marker attached to the patient ($F$). In mathematical terms, this involves the calculation of $\mathbf{T}_X^F$ and $\mathbf{T}_H^F$ by multiplication of the transform matrices given by the motion capture system.

$$\mathbf{T}_X^F = \mathbf{T}_C^F \mathbf{T}_X^C \tag{3.14}$$

$$\mathbf{T}_H^F = \mathbf{T}_C^F \mathbf{T}_H^C \tag{3.15}$$

The following coordinate systems are related to the CAS system and the intra-operative x-ray images:

**D** is the coordinate system of the calibration **d**rum. Differing from $X$, this system is centred on the drum's proximal plate and its axes coincide with the ones of the drum's embedded fiducial pattern.

**Pk** is the coordinate system of the $k$-th x-ray image, centred on its corner and with the axes aligned to its **p**ixel grid.

Successful registration of the intra-operative x-ray images to the pre-operative data requires an exact localisation of each of the former, or, in mathematical terms, the determination of matrices $\mathbf{T}^F_{Pk}$, for each radiograph $k$. As this information is not given by the c-arm, it is necessary to obtain using the following matrix multiplication.

$$\mathbf{T}^F_{Pk} = \mathbf{T}^F_X \mathbf{T}^X_D \mathbf{T}^D_{Pk} \tag{3.16}$$

As said previously, $\mathbf{T}^F_X$ is obtained from the motion capture system. $\mathbf{T}^X_D$ is a calibration relating the position of the drum's markers to its axes, which needs to be performed only once and remains constant during the whole surgery. $\mathbf{T}^D_{Pk}$ can be obtained by image processing techniques, analysing the fiducials' projections on the $k$-th x-ray image. Calculation of the latter two matrices will be detailed on Chapter 6.

**M** is the coordinate system of the pre-operative CAT scan. Letter M was chosen to name as this image correspond to the moving one in the 2D-3D registration process.

Differing from the c-arm, the CAT scanner gives information about the pixel sizes and patient location –in scanner coordinates– which corresponds to the coordinate system $M$. All the 2D-3D registration problem, required to locate the patient in the operating room, can be expressed as the calculation of transform $\mathbf{T}^F_M$, which relates the pre-operative CAT scan coordinates to the actual situation found in the operating room. Calculation of the cited transform will be the subject of Chapter 5.

The rest of the coordinate systems are related to the surgical robot:

**T** is the coordinate system centred on the surgical tool's **t**ip.

**B** is the coordinate system centred on the robot's **b**ase, used in the resolution of the robot's kinematics.

**E** is the coordinate system centred on the robot's **e**nd-effector, also used in the calculation of the robot's kinematics.

Similar to the relationship between coordinate systems $X$ and $D$, the motion capture system is able to detect the system $H$, which is not centred on the tool's tip. Therefore, a calibration procedure is required to determine the tip's location, determining the matrix $\mathbf{T}^H_T$. This calibration needs only to be performed once and remains constant during the whole procedure.

Inclusion of the surgical robot requires the determination of additional transforms. Basically, the robot has two coordinate systems: $B$ and $E$ which correspond to its base and end-effector. The robot controller is able to calculate the relative position between the end-effector and the base –that is, matrix $\mathbf{T}_E^B$– by reading its encoders and resolving its direct kinematics' equations. However, the robot is not aware of the surgical tool's location with respect to its end-effector or the relative position of its base with respect to the patient. The first problem, which boils down to the calculation of matrix $\mathbf{T}_T^E$, can be resolved by a pre-operative calibration, which remains constant during the surgery. The second problem requires the estimation of transform $\mathbf{T}_B^F$ by registering a set of points, measured simultaneously with the motion capture system and the robot's controller. Once calculated, this transform remains constant as long as the relative position between the patient and the robot remains constant. If motion occurs, it is necessary to perform the registration again. The procedures for calculation of $\mathbf{T}_T^H$, $\mathbf{T}_T^E$ and $\mathbf{T}_B^F$ will be described on Chapter 7.

## Chapter 4

# Surgical planning software

Computer assisted interventions begin with a planning stage, on which the surgeon, among other tasks, inspects the patient's pre-operative data, decides the optimal placement of surgical instruments and defines trajectories to reach the organ of interest. In our case of interest –that is, transpedicular fixation– the main planning task is the definition of the number and placement of screws that need to be inserted to fix the patient's vertebrae. For this purpose, we developed a specialised software named viewit-Spine, which permits planning of spinal fusion surgeries based on pre-operative CAT scans. This applications permits the surgeon to define in advance the optimal placement of screws, varying their dimensions and adjusting their positions to prevent any damage to the patient. Furthermore, viewit-Spine also includes functionality for the surgery's execution, providing support for intra-operative registration, real-time navigation and control of the surgical robot.

This chapter begins with the motivation behind viewit-Spine, followed with a description of its typical workflow, which gives a detailed tour by its main features. Additional information about the software libraries used during the development of viewit-Spine has been included in Appendix C.

## 4.1 Motivation

From the beginning of the project, it was clear that we needed a custom software to address the needs raised by the surgeons who were in our team. They complained that available software were either too expensive or too complicated. In fact, they usually complained about the multiplicity of features present in existing applications, which made their use unnecessarily difficult. For these reasons, we decided to develop our own software framework, aimed at the development of multiple and easy-to-use surgical planners. In other words, we opted to have our own framework which allowed us to quickly deploy multiple lightweight and highly specialised surgical applications, rather than having a single and highly complex piece of software that could be used for many different purposes.

As said previously, commercial surgical planners are available, although they are included in larger and expensive product packages. Besides, they normally come with proprietary licences, forcing researchers to negotiate access rights to the source code. As examples we can cite the Brainlab's iPlan[1], Siemens PreOPlan[2] and Medtronic's StealthStation[3]. Lately, researchers have benefited from the freely available Slicer[4], an open source software package for visualisation and image analysis. Slicer was initiated in 1998 as a joint project between the Surgical Planning Laboratory at the Brigham and Women's Hospital (Boston, Massachusetts) and the Artificial Intelligence Laboratory of the Massachusetts Institute of Technology (MIT). Since then, it has evolved into a massive project with over a million lines of code, an large user community and with active funding received from multiple initiatives backed by the National Institute of Health (NIH). However, it must be noted that Slicer is a research tool and has not been approved for clinical use (Pieper et al., 2006).

Initially, we considered Slicer for development of our system, but decided that it was not appropriate for our plans. We realised that it had too many features and a complicated interface, which made its use quite difficult (an opinion shared with the surgeons in our team). Besides, Slicer's version when viewit-Spine's development began (version 3.4, released on the June 21th, 2005) had poor performance, was unstable and had a poor framework for extension of its graphical interface (although newer versions have improved on this point by adopting the Qt library). In addition, it was clear from the beginning that we wanted a software framework that

---

[1] http://www.brainlab.com/art/3124/4/spinal-planning-software/ (visited September 2012)

[2] http://healthcare.siemens.com/surgical-c-arms-and-navigation/navigation/preoplan (visited September 2012)

[3] http://www.medtronic.com/for-healthcare-professionals/products-therapies/spinal-orthopedics/surgical-navigation-imaging/index.htm (visited September 2012)

[4] http://www.slicer.org (visited September 2012)

imposed no restrictions for commercialisation (which made us discard most commercial packages) and allowed us full customisation of the source code, as programming of low-level routines was necessary. Therefore, we opted to develop our own software framework, but on top of other open source libraries: ITK, VTK, Qt, OpenIGTLink, Eigen and GDCM.

Development of viewit-Spine –described in this chapter– and later gave birth to *viewitLib*, a more general framework used for the quick development of highly specialised medical software. So far, viewitLib has been used in our department for development of medical image viewers, a craneotomy simulator, an application for analysis of Diffusion Tensor Imaging data and a surgical planner for the placement of hearing implants.

## 4.2 Workflow

This section describes the typical work flow followed in creation of a surgical plan using viewit-Spine, describing its use before and during intervention. Describing this procedure step-by-step is an adequate way to expose the software functionality, which is much more clear than listing all features without describing the context on which they are used.

### 4.2.1 Loading of pre-operative images

Creation of a new surgical plan begins with loading of the pre-operative 3D images of the patient. Although images of any modality can be loaded onto viewit-Spine (e.g. CAT, MR, PET, etc.) CAT images should be used in the majority of cases, as this modality offers high resolution and depicts bone with a high level of contrast.

The surgeon has two options to create a new surgical plan: from a file or from a DICOM series. Supported file formats are provided by ITK's classes and include ANALYZE (.hdr), GIPL (.gipl), NIfTI (.nii), Metaimage (.mha, .mhd), NRRD (.nrrd) and VTK (.vtk). However, these formats are more popular among researchers and developers rather than clinicians, who prefer the DICOM format as it is available on most modern hospitals. Viewit-Spine can create a new surgical plan from DICOM files using ITK's objects paired with the GDCM library, which provide functionality to handle all information found on the DICOM headers.

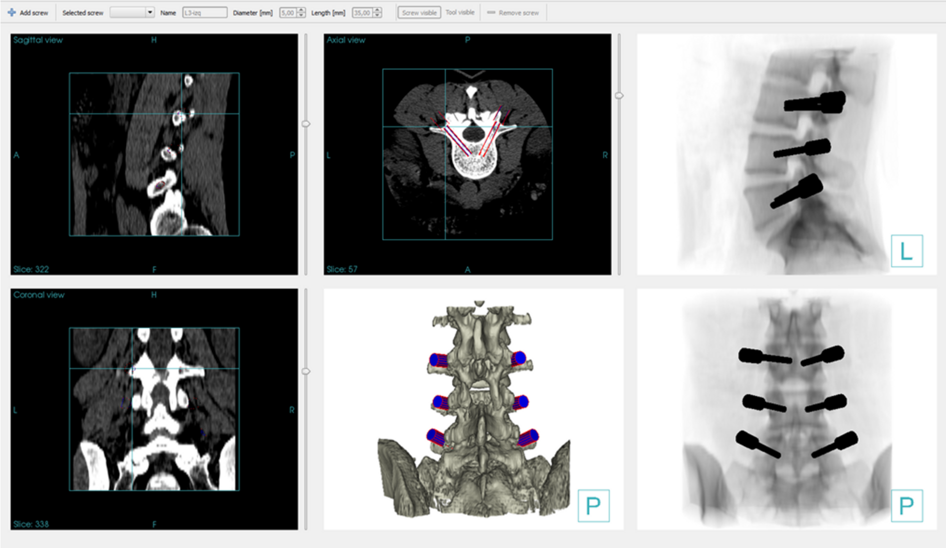
Name: L3-izq
Diameter [mm]: 5,00
Length [mm]: 35,00

Figure 4.1: viewit-Spine's main window, showing a complete surgical plan with 6 screws for a lumbar transpedicular fixation.

After choosing the image, viewit-Spine's main window will appear, showing the image on six different panels, as illustrated on Figure 4.1. These are three orthogonal views –sagittal, coronal and axial– and three 3D views, of which one is an opaque rendering of the spinal column and the other two are Digitally Reconstructed Radiographs (DRR).

Apart from the classical manipulation tools (i.e. window/level, zooming and panning) it is possible to measure distances in the orthogonal views by choosing the *Measure distance* tool, as shown on Figure 4.2. This tool is important for surgery planning, as it allows surgeons to measure how close a screw will pass from a pedicular wall and estimate the danger of breaching, and also to check whether a screw is placed too close to the spinal canal.

In the 3D views three different rendering algorithms can be used: Fixed point ray cast, standard ray cast and VTK GPU ray cast. Also, it is possible to switch between three transfer styles: XRay with geometric props, XRay with volumetric props and Bone as shown on Figure 4.3.

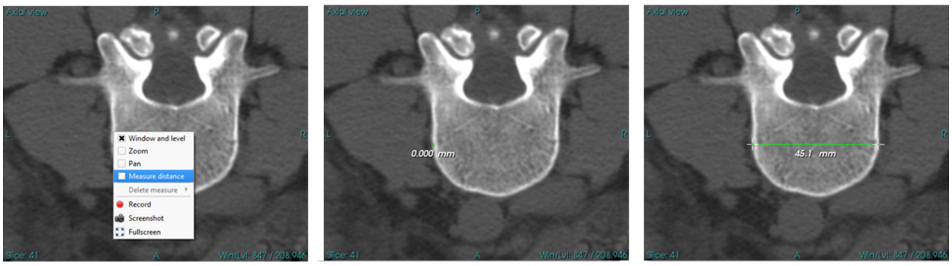

Figure 4.2: The Measure Distance tool in action: after its selection from the context menu, the user should click on two points to define a new measure.

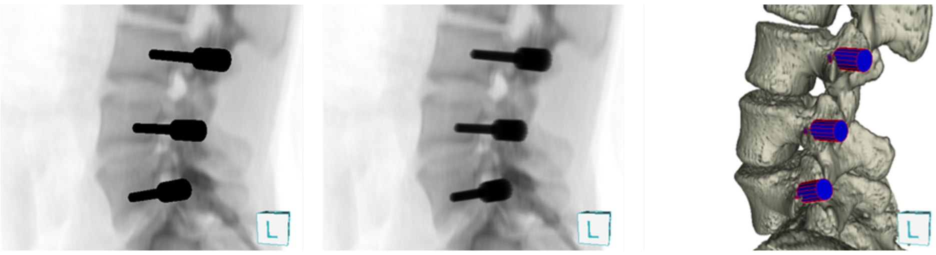

Figure 4.3: viewit-Spine's transfer styles for volume rendering: X-ray with geometric props (left), X-ray with volumetric props (centre) and Bone (right).

### 4.2.2 Screw placement and manipulation

Screws are inserted into the surgical plan in a very easy way clicking on its entry point and then on a second one, defining the screw's axial direction as shown on Figure 4.4. After doing this, a new screw is created and is shown on all orthogonal and 3D views. Afterwards, its position and orientation can be manipulated as well as its length and diameter, with values that reflect realistic measures of available surgical instrumental.

Every screw has an associated perforation tool, which has its tip located on the screw's insertion point as shown on Figure 4.5. This feature was of particular interest for surgeons, as they demanded a method to simulate radiographs which showed in advance how the insertion tool should be positioned to perforate the vertebrae. This can be achieved by using viewit-Spine's DRR panels, hiding the screw and showing its associated tool. In fact, during surgery it is not very useful to have a simulated

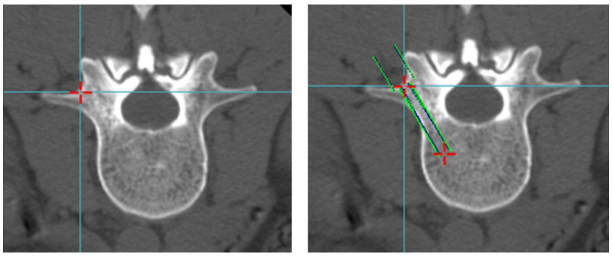

Figure 4.4: Two-click procedure to add a new screw to the surgical plan. Left: definition of the screw's insertion point. Right: definition of the second point that establishes the screw's orientation.

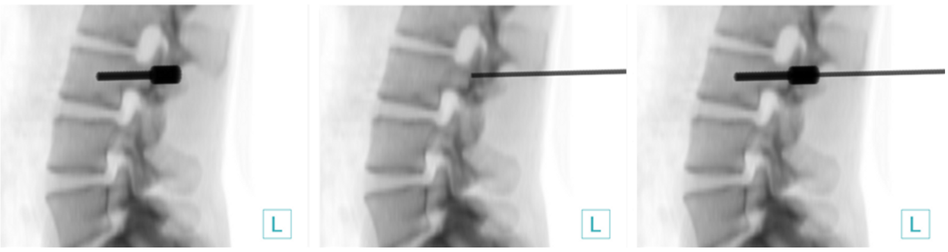

Figure 4.5: Simulated radiographs showing a screw (left), it corresponding insertion tool (centre) and both simultaneously (right)

radiograph of an inserted screw, as an image of that kind would show the result after a successful insertion, but would not serve as a reference image. For the latter purpose, it is better to use a DRR showing the insertion tool only.

### 4.2.3 DRR simulation and export

A feature which was requested by our team's surgeons was printing and export of simulated radiographs. The surgeons were keen on having a set of reference images which could be taken into the operating room and used to see the ideal position and orientation of the screw insertion.

These features were implemented on viewit-Spine. As written previously, the rightmost 3D views show DRRs which can be used for this purpose. These are updated whenever a change in the surgical plan happens, such as insertion of modification (i.e. displacement, rotation or change of dimensions) of a screw. However, rendering a screw on DRR is not very useful for a reference image, as it would show the ideal position of it after insertion. Then, it would be more useful to show the insertion tool rather than the screw and that is why tools can be displayed in their place.

### 4.2.4 Importing intra-operative images

All viewit-Spine's features described so far were designed for surgical planning or, in other words, the pre-operative stage of the intervention. However, the application also offers features for the intra-operative stage, in which the software is supposed to be running on a computer inside the operating room.

The first of these features is an x-ray image import command. When chosen, viewit-Spine tries to connect to an image server and asks for a radiograph. Image transmission is implemented by means of OpenIGTLink. When an image is requested, viewit-Spine sends a GET_IMAGE message to the server. The latter, after its reception, acquires the image and packs it into an IMAGE message, which is transmitted back to viewit-Spine.

The IMAGE message supports 2D or 3D images with metric information, including image matrix size, voxel dimensions, position and orientation. The body section of an IMAGE message consists of two parts: a header, used to transmit the metric information, and the body, which carries the binary data of the voxel values. Supported data types are 8, 16 and 32 bit integers or 32 or 64 bit floating points. In addition, data can be set to be scalar or vectors. Furthermore, OpenIGTLink supports partial image transfers, on which only a portion of the image is transmitted, which is a useful feature for real time applications.

### 4.2.5 Registration

According to the definitions of Section 3.2, x-ray images have their coordinates expressed in the $F$ coordinate system, centred on the marker attached to the patient. Thus, they carry information about the present location of the latter in the operating room. However, the pre-operative image is in a different coordinate system, $M$ corresponding to the CAT scanner frame of reference. Registration is thus needed to bring both

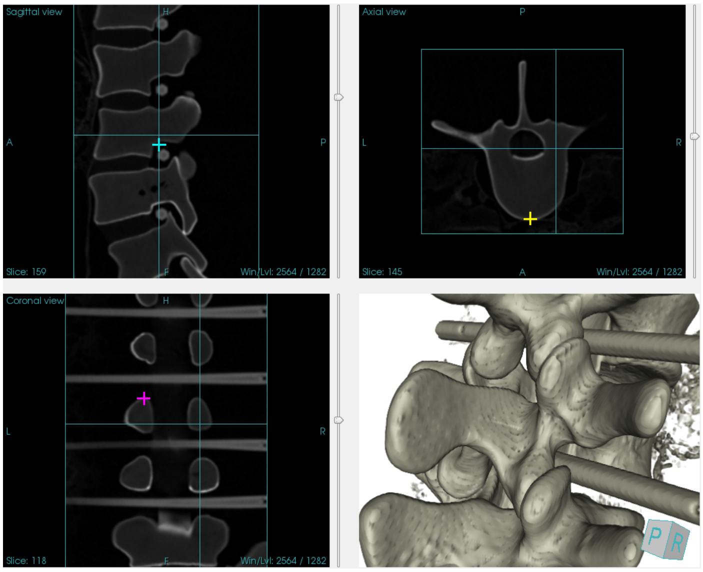

Figure 4.6: Placement of fiducials in a 3D CAT scan. Note the cyan, yellow and magenta points placed on the sagittal, axial and coronal views respecively.

coordinate systems into alignment.

viewit-Spine includes a software module which calls the registration application, which will be described in detail in Chapter 5. Currently, the software offers two default registration algorithms, based on features and intensity respectively. The feature-based algorithm aligns the 3D image to the 2D ones by finding the best match between a set of fiducial points defined on the 3D image and their corresponding projections on the 2D ones. These fiducial points need to be inserted by the user as illustrated on Figures 4.6 and 4.7, ideally on landmarks that can be easily identified on all images, such as pedicle edges or contours of the vertebral body. Successful registration needs a minimum of three fiducial points, defined on the 3D image and each of the 2D ones (e.g. if two x-rays are included, the user needs to define a total of nine points: three on the CAT scan, three on the first x-ray and another three in the second x-ray). Fiducial placement can be only done in the orthogonal views.

The feature-based registration is instantaneous, but its accuracy is low as it depends on the correct location of the fiducial points by the

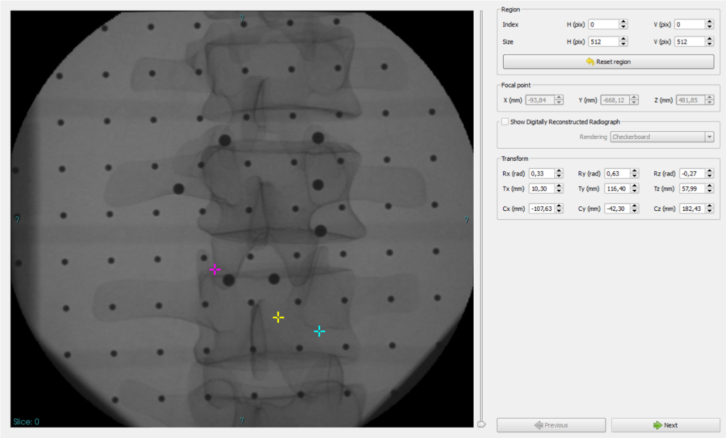

Region
Index H (pix) 0 V (pix) 0
Size H (pix) 512 V (pix) 512

Focal point
X (mm) -93,84 Y (mm) -668,12 Z (mm) 481,85

☐ Show Digitally Reconstructed Radiograph
Rendering Checkerboard

Transform
Rx (rad) 0,33 Ry (rad) 0,63 Rz (rad) -0,27
Tx (mm) 10,30 Ty (mm) 116,40 Tz (mm) 57,99
Cx (mm) -107,63 Cy (mm) -42,30 Cz (mm) 182,43

Figure 4.7: Placement of fiducials in a 2D x-ray image. Note how the fiducial colours match those of Figure 4.6.

user. On the other hand, the intensity-based registration method is much more accurate and does not require identification of landmarks, but suffers from low efficiency and a limited capture range, meaning that it is unable to correct large misalignment between images. However, the transform produced by the feature-based method can effectively be used as a good starting point for the intensity-based method. Despite that the registrations produced by the feature-based method alone are not accurate enough to be useful, they still bring the images close to alignment, to a point were the intensity-based method can finish the rest of the job. In this way, the strengths of both algorithms are combined obtaining a very useful registration method, at a cost of a minimal amount of user input.

### 4.2.6 Tracking

Once the pre and intra operative data have been registered it becomes possible to track the surgical tools using the optical system and render them in real time on the viewit-Spine's scene.

Transmission of tracking data was implemented by means of OpenIGTLink protocol version 2. This version of the protocol includes the TDATA message which is intended for transferring 3D positions of surgical tools and markers, measured by any type of position sensor, and continuously transferred as series of messages. OpenIGTLink's TDATA messages allow transmission of multiple tracked elements simultaneously. For our particular application, they contain two tracked elements, one for the x-ray calibration drum and another for the surgical tool.

### 4.2.7 Robot driving

viewit-Spine permits to control the surgical robot. Currently, the available functionality is limited as the whole system is still on its first stage of development.

Before transmission of commands to the robot, it is necessary to register the robot's base and the reference marker. To do this, the user should move the robot to different points in the workspace and capture them. For each acquired point, viewit-Spine sends two requests, one to the tracking data server of the point's current coordinates measured by the optical system, and another to the robot server, to get the current location's coordinates with respect to the robot base, measured by resolution of the robot's direct kinematics. A minimum of three points are needed to perform the calibration. According to the coordinates systems defined in Section 3.2 the calibration consists on finding transform $\mathbf{T}_B^F$.

Once the calibration has been performed, viewit-Spine becomes capable of transforming the screws' and tool's coordinates –originally in systems $M$ and $T$ respectively– to the robot's base frame of reference $B$. Therefore, the robot can be commanded to move to the desired positions for screw insertion.

## 4.3 Closing remarks

A fully featured surgical application, named viewit-Spine, has been presented in this chapter, designed the planning and execution of robotic-assisted spinal fusion surgeries. Despite its full set of features, its interface has been kept as simple as possible, greatly simplifying its use. In addition, its code has been ported to a customised software framework –named viewitLib– which is actively being used today for the development of several highly specialised medical applications.

# Chapter 5

# Registration of 2D and 3D images

Articles related to this chapter have been published in:

> *Bertelsen, A. and Borro, D. "2D-3D Registration with Multiple Fixed Images". The Source, Vol. 20, pp. 13–15. 2012.*
>
> *Bertelsen, A. and Borro, D. "An ITK-Based Framework for 2D-3D Registration with Multiple Fixed Images". Insight Journal, 2011.*

The robotic system proposed in this thesis requires the alignment of two different sets of images acquired from the patient. One is the pre-operative data –a 3D CT scan– while the other is a set of intra-operative 2D images taken with an x-ray machine, or c-arm. As both sets of data have inconsistent coordinates systems, they must be matched to successfully localise the patient within the operating room. This alignment process is known in the medical field as *registration* and is a keystone of the system proposed in this thesis: if registration is unsuccessful, it is not possible to locate the planned screw positions in the operating room, or drive the surgical robot. In fact, it is acknowledged that accurate registration of the patient's coordinate remains as the main challenge for orthopaedic robots, such as the one proposed in this work (Casals et al., 2009).

As will be seen, medical image registration is a well studied topic and a huge amount of research is already available. However, we noted a lack of an appropriate software library for our particular problem, which falls into the category of 2D-3D registration. Despite the large amount of research devoted to this subject, all developers willing to implement a registration application were forced to write their own software from scratch, wasting a considerable amount of time in writing and debugging.

Even the well-established ITK library –already introduced in this thesis– lacked from appropriate support for 2D-3D registration. For this reason, we considered that the best contribution to this field had to be of a technical nature and, thus, developed an extension for ITK to solve its most important limitations (Bertelsen and Borro, 2011; Bertelsen and Borro, 2012). We sincerely believe that a contribution of this kind was more valuable than adding another 2D-3D registration algorithm to the already long list of existing ones, claiming that the new one is better than others in determined circumstances.

This chapter gives a mathematical description of the 2D-3D registration problem and a general overview of the developed software library for its resolution. To illustrate the latter's capabilities, a sample application will be introduced and its performance will be evaluated using a standard protocol. We decided that giving a full description of the proposed ITK library was too technical for a doctoral thesis, as a considerable knowledge of the C++ programming language and the ITK library are needed to understand it. However, any software developer interested in the use of the proposed library can found its technical reference on Appendix D.

## 5.1 Problem description

### 5.1.1 2D-3D registration definition

As written previously, medical image registration aims to align two or more datasets in such a way that their anatomical structures are matched and their coordinate systems become consistent. In the last years, an enormous amount of research effort has been made in this subject and well-known references such as the works by Hajnal et al. (Hajnal et al., 2001), Maintz and Viergever (Maintz and Viergever, 1998) and Pluim et al. (Pluim et al., 2003) are available for the interested reader. According to Maintz and Viergever, the problem described in this thesis falls into the category of 2D-3D registration, due to the dimensionality of the pre-operative (3D) and intra-operative (2D) data. Registrations of this kind are not uncommon –in fact, they are found in a variety of image-guided therapy systems– and have been studied by a large number of researchers too, as a shown by a recent review by Markelj et al. (Markelj et al., 2012).

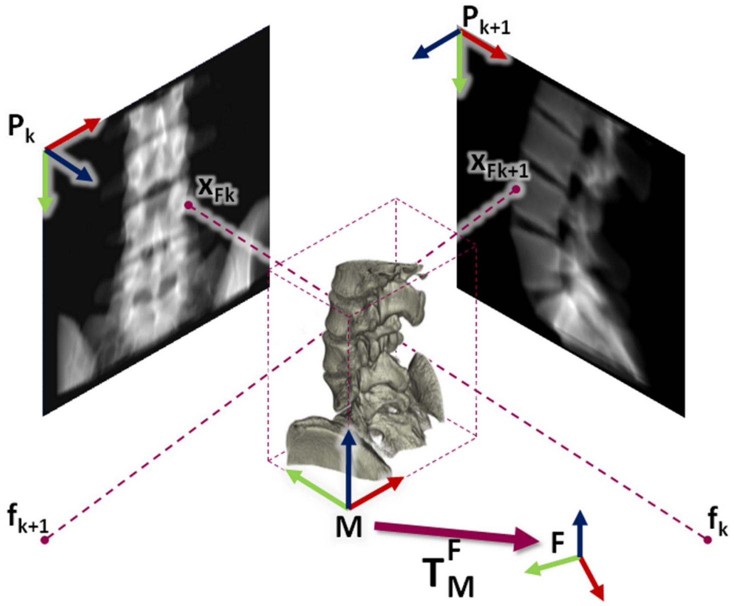

Figure 5.1: The 2D-3D registration problem, consisting in the finding of transform $\mathbf{T}_M^F$ which aligns the 3D image's frame $M$ to the fixed reference frame $F$. It is assumed that the 2D x-ray images' locations and orientations with respect to $F$ are known in advance, as well as the positions of their focal points $\mathbf{f}_k$.

The 2D-3D registration problem is illustrated on Figure 5.1. Following the conventions of Section 3.2, we define its objective as the finding of transform $\mathbf{T}_M^F$ which maps points from the 3D image's frame of reference $M$ to the fixed frame $F$, centred on the marker attached to the patient. A set of 2D x-ray images is defined in $F$, each one denoted with index $k$, as well as their corresponding focal points $\mathbf{f}_k$. If transform $\mathbf{T}_M^F$ is correctly set, the $k$-th 2D image should correspond to the projection of the 3D image on its plane. In other words, rays that go from a 2D image point $\mathbf{x}_{Fk}$ to the focal point $\mathbf{f}_k$ should pass exactly by the corresponding anatomical features depicted on the 2D image as well as in the 3D one. The reader must keep in mind that there is a unique frame $F$ for all 2D images and it is assumed that transforms that map points from the $k$-th image's pixel grid to $F$ are known in advance. Calculations of these transforms, denoted by $\mathbf{T}_{Pk}^F$, will be studied in Chapter 6.

As the fixed (2D x-rays) and moving (3D pre-operative) images have different dimensionality an intermediate step is required to bring them to dimensional correspondence. This can be achieved by bringing the 3D data into 2D by means of *projection* or by bringing the 2D data to 3D by means of *back-projection* or *reconstruction.* 2D-3D registration algorithms can be also grouped according to the type of data used to drive it, yielding *feature*, *intensity* and *gradient* based algorithms (Markelj et al., 2012). Feature-based strategies match the images by establishing correspondences between extracted features such as characteristic points, contours or surfaces. These methods are generally very efficient as they need to process a reduced amount of data. However, they also tend to be inaccurate, as feature extraction requires a previous segmentation step, which introduces an additional source of error. In fact, an inaccurate segmentation will produce a poor alignment, no matter how sophisticated the registration algorithm is.

On the other hand, intensity-based methods use all the voxels' intensities to drive the registration. In a similar way, gradient-based methods use the images' gradients, calculated on all pixels. These methods do not require segmentation and are more accurate than feature-based ones. However, they are less efficient as they require a much larger amount of data to work, rather than a reduced set of features. Besides, they are also not very robust, meaning that they are unable to correct large misalignments and, therefore, need a starting point close to the correct solution to work properly.

### 5.1.2 Measures of registration errors

As written in Chapter 3, rigid transforms are of our particular interest, as we will register images of vertebrae, which can be safely considered as rigid bodies as well as the skull, femur and other bones. To evaluate registrations' performance, three measures of errors have been studied, namely the Fiducial Localisation Error (FLE), Fiducial Registration Error (FRE) and Target Registration Error (TRE). We will see that these measures can be directly applied to point-based registration (i.e. feature-based using points) but, in the cases of intensity and gradient-based registrations, FLE and FRE make little sense, although TRE is accepted as a reliable measure of error.

Point-based registration has been normally used to find rigid transforms

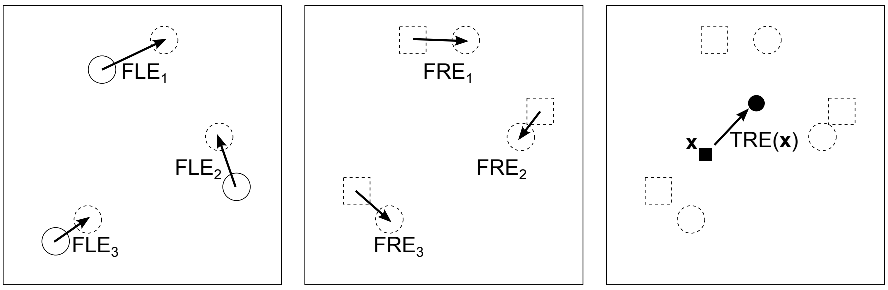

Figure 5.2: The different types of registration errors. The FLE measured at each fiducial is the distance between its real position (solid circle) and its measured position (dashed circle). The FRE at each fiducial measures the distance between its position in the first frame of reference and the one of its corresponding pair in the second (circles and squares respectively) after registration. The TRE, measured at a point $\mathbf{x}$, is the distance between the locations of a certain feature –not included in the registration– in both frames of reference (filled circle and square).

between two images, establishing a rotation and offset that take a set of points of the first image to the coordinates of the homologous points in the second one. Normally, these points –named *fiducial* points– are located on anatomical landmarks or by implantation of artificial markers. Advantages of the latter are their easier localisation on images and that their registration error depend only on the fiducial localisation, being thus independent of the imaged object. Therefore, it is possible to assess the clinical accuracy of marker-based systems on the basis of experiments made with phantoms or previous patients (Fitzpatrick and West, 2001).

If fiducial sets have the same number of points and each one in the first set has a corresponding one in the second, the rigid registration problem can be obtained by a closed-form solution, discovered independently by authors like Schönemann (Schönemann, 1966), Golub and van Loan (Golub and van Loan, 1983); Arun et al. (Arun et al., 1987), Horn (Horn, 1987) and Umeyama (Umeyama, 1991). Although the solution is unique, it can yield an imperfect registration due to the presence of errors in point localisation. As written previously, the three following error measures are commonly used:

- *Fiducial Localisation Error (FLE)*, which is the error in locating the fiducial points. Under normal circumstances, this error cannot be measured directly.

- *Fiducial Registration Error (FRE)*, which is the residual root-mean-square (RMS) distance between corresponding fiducial points after registration.
- *Target Registration Error (TRE)*, which is the distance between corresponding points other than the fiducials after registration.

Plenty of articles have been published about the properties of FRE and TRE. In 1998, Fitzpatrick et al. derived an equation for the estimation of the RMS value of FRE and TRE, consistent with previous literature (Fitzpatrick et al., 1998). In 1999, West and Fitzpatrick obtained expressions for the distribution of FRE and TRE (West et al., 1999) and, in 2001, they extended their solution considering the effects of anisotropy introduced by arbitrary rotations (Fitzpatrick and West, 2001). Fitzpatrick et al.'s findings can be summarised as follows:

- FRE and TRE are uncorrelated and registrations with low FRE values can yield high TRE.
- FRE does not depend on the fiducial configuration, whereas TRE has a strong dependency on it. Even more, poorly chosen fiducial configurations can yield low FRE and high TRE values.
- Counter-intuitively, TRE can be higher in the surroundings of the fiducial points chosen for registration.

All this makes FRE a poor index of registration accuracy and its use in medical equipment has been discouraged by the same authors. Nowadays, it is a standard practice not to use all available fiducials for registration computation, reserving a subset for the estimation of TRE and, thus, evaluate the registration's error more accurately.

It is clear that FLE and FRE can be applied directly on point-based registration. As intensity and gradient-based registration do not use segmented features at all, these error measures cannot be applied. The use of TRE, however, has been adopted in the development of standard datasets for registration evaluation, as it will be seen later. In this case, voxels positions between two images –for which their correct registration is known– can be used as target points for the calculation of TRE.

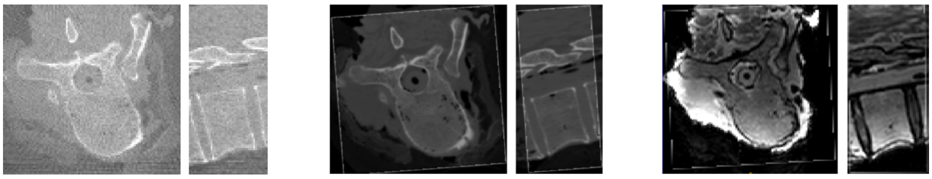

(a) 3DRX (b) CT (c) MR

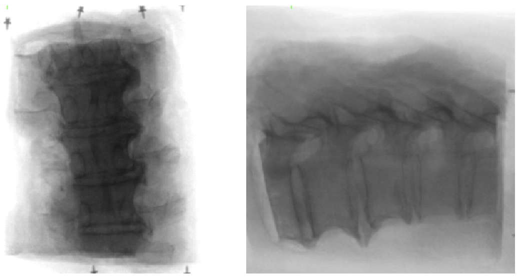

(d) AP x-ray (e) LAT x-ray

Figure 5.3: Axial and lateral cross-sections taken from the 3DRX, CT and MR images of the standard dataset by van de Kraats et al., along with its AP and LAT x-ray images.

### 5.1.3 Standard datasets and protocols

In 2005, van de Kraats et al. published a standardised method for the evaluation of 2D-3D registration algorithms, proposing measures for their accuracy and robustness. The authors presented a set of images –shown on Figure 5.3– consisting of CAT, MR, x-rays and three-dimensional radiographs (3DRX) of eight vertebrae, acquired on precise locations and with known transforms between their coordinate systems[1]. The deviations from these ground-truth transforms were measured with the mean Target Registration Error (mTRE), which gives a reliable measure of a transform's inaccuracy. Along with the images, the authors gave a set of 200 initial transforms, with initial mTRE values spread between 0 and 20 mm. Each evaluated method has to perform 1600 registrations (200 for each of the 8 vertebrae) and measure their final mTRE values. Registrations are considered successful if their final mTRE fall below 2 mm, and the *success ratio* is defined as the proportion of successful cases for a particular

---

[1] Dataset available from http://www.isi.uu.nl/Research/Databases

method. Also, the *capture range* is defined as the distance from the reference transform to the first 1 mm interval for which a registration was successful in less than 95% of cases (van de Kraats et al., 2005).

Since its introduction, multiple studies have followed van de Kraats et al.'s protocol for evaluation of registration methods. Tomaževič et al. first presented in 2003 a method which matched 3D normals to bony surfaces and 2D x-ray gradients back-projected to 3D (Tomaževič et al., 2003). Later, in 2006, they presented a different algorithm in which the a second 3D image was reconstructed from the 2D x-rays, effectively transforming the problem into a 3D-3D registration (Tomaževič et al., 2006). In 2008, Markelj et al. combined elements of the former two methods, reconstructing a 3D gradient image from the 2D x-ray gradients, and adding an additional search of the solution via the Random Sample Consensus algorithm (RANSAC). Markelj's et al. work gives a good overview of the current state of 2D-3D registration algorithms and, summarising their findings, we can observe that many existing methods achieve sub-pixel accuracy and that more recent ones give negligible improvements. As error levels are comparable the data's voxel sizes, we cannot expect further improvements in accuracy unless the resolution of image acquisition is improved. On the other hand, robustness remains and unsolved problem. According to Markelj et al., the most robust method –using 2 x-ray images– has a capture range of 11 mm and a success rate of 92%. Increasing the number of x-rays to 7 improves robustness by increasing the capture range to 14 mm and the success rate to 97%. Although these figures are remarkable, further improvements can be sought, in particular trying to keep the number of x-rays to a minimum, as increasing radiation doses is undesirable (Markelj et al., 2008a).

It must be noted that other standard datasets for 2D-3D registration evaluation exist, such as the one presented by Tomaževič et al. in 2004, which consisted of CAT, MR and x-ray images of a cadaveric spine (Tomaževič et al., 2004). In 2010, Markelj et al. presented a dataset of images of the spine and vertebrae consisting of CAT images taken from the Visible Human Project[2] and synthetic x-ray images generated using a ray-casting algorithm with an energy-conversion function (Markelj et al., 2010). In 2011, Pawiro et al. proposed an extensive dataset with CAT, MR and 3DRX images of a cadaver pig head with embedded fiducials. This dataset, according to the authors, was designed with radiosurgical

---

[2] http://www.nlm.nih.gov/research/visible/visible_human.html

applications in mind, which are more affected by soft tissue deformations and, therefore, could not be properly evaluated using other available datasets (Pawiro et al., 2011).

### 5.1.4 Available software

As said in the beginning of this chapter, researchers of 2D-3D registration methods suffered from the lack of appropriate software, forcing them to develop their own applications from scratch with a considerable waste of resources and time. Even the widely-used ITK did not offer suitable support for this problem. Despite that it offers classes for 2D-3D registration, it has considerable limitations which make its use impractical. Namely,

- A 3D image can be registered to a single 2D one. Registration of a 3D dataset to multiple 2D images is not supported.
- The orientation of 2D images is completely ignored during registration.
- Only one projection class is available, which is only compatible with rigid transforms. Affine and non-rigid transforms are unsupported.
- ITK's interpolation objects do not offer multi-threading, drastically reducing their performance.

Steininger et al. proposed an extension for ITK addressing the last two problems listed above, offering additional projection algorithms (such as wobbled splatting), adding support for affine transforms and implementing multi-threaded classes. However, they did not extend ITK's classes to handle multiple 2D images (Steininger et al., 2009).

We were aware of two other applications that were being written at the same time as this thesis, and which have only recently been released. One is the `elastix`[3] software – originally developed by Stefan Klein and Marius Staring(Klein et al., 2010)– which featured 2D-3D registration on version 4.5, released on September 12th, 2011. This version added support for 2D-3D registration by incorporating the work by van der Bom et al. and is able to handle multiple 2D images (van der Bom, 2010; van der Bom

---

[3] elastix can be downloaded from http://elastix.isi.uu.nl/index.php

et al., 2011). Another software developed simultaneously is `reg-2-3`, part of the `plastimatch` application suite[4]. This application, able to rigidly register a 3D image to multiple 2D projections, was released to the public on May 2011. The fact that these two programs were written at the same time as this work stresses the real need faced by researchers and clinicians, which could not be covered with previously available software.

## 5.2 Proposed solution

### 5.2.1 Proposed library and application

We propose an extension for ITK, addressing its most critical shortcomings for 2D-3D registration, that is, its inability to handle multiple 2D images and their respective orientations (Bertelsen and Borro, 2011; Bertelsen and Borro, 2012). The library is publicly available and can be downloaded at no cost for the user[5]. Alongside with the library, we developed a 2D-3D registration application named `multiImageRegistrator`, designed as a companion for viewit-Spine. This offers a great flexibility for the implementation of registration strategies and features

- Implementation of point and intensity-based algorithms.
- Support for multi-resolution strategies in intensity-based registration with tunable downsampling factors.
- Flexible chaining of registration stages: the user can define two or more registrations and order `multiImageRegistrator` to execute them sequentially, feeding the resulting transform of one stage as the starting point of the next.
- Two new similarity metrics for intensity-based registration, not included in ITK.

To the features above we should include the ones inherent to ITK, such as support for a large variety of medical imaging formats (e.g. ANALYZE, NIfTI, etc.) and multiple optimisation algorithms.

---

[4] plastimatch can be downloaded from http://plastimatch.org

[5] Library available at http://hdl.handle.net/10380/3264

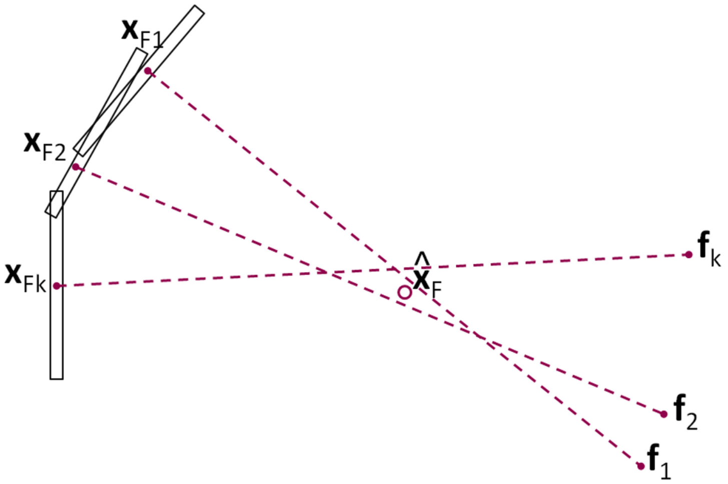

Figure 5.4: Reconstruction of a 3D point from its multiple projections $\mathbf{x}_{Fk}$. First, rays are back-projected from points $\mathbf{x}_{Fk}$ to their corresponding focal points $\mathbf{f}_k$ and, then, point $\hat{\mathbf{x}}_F$ is placed minimising the distance to all rays. In an ideal case, all rays should meet at a unique point.

### 5.2.2 Point-based registration

We decided to add a feature-based method in `multiImageRegistrator`, more as an initialiser than as an actual registration algorithm. As written previously, intensity-based methods are very accurate, thus we expected these algorithms to bring the images into their definitive alignment. However, they have the drawback of limited capture ranges and, thus, need to start close to the correct solution to converge. This starting point can be effectively set by a feature-based method, which does not necessarily need to be very accurate.

We designed the feature-based method to be as fast as possible, requiring a minimal amount of features, that is, three (or more if desired) non-collinear points in 3D along with their corresponding projections on each 2D image. We also decided that some user input could be tolerated if the number of features was kept as low as possible. In fact, surgeons can easily identify three points in the 3D image and their corresponding counterparts in the 2D data, a process which may seem trivial but is hard to implement properly in an automatic segmentation algorithm. The 2D points could be reconstructed in 3D and then registered almost instantaneously, producing a good starting point from which an intensity-based method can continue with the rest of the registration job (Hurvitz and Joskowicz, 2008).

Registration of two sets of 3D points, on which each point in the first group has a corresponding one in the second, is a well-known problem and has a closed-form solution proposed by Horn in 1987 (Horn, 1987). As written previously, the surgeon is expected to locate three 3D points in the CAT scan, but the rest are defined in the 2D images. Therefore, the latter must be taken first into the 3D space to use Horn's solution. Reconstruction of a 3D point from its 2D projections, shown on Figure 5.4, can be obtained as follows. Let $\mathbf{x}_M$ be a landmark point in the CAT scan and $\mathbf{x}_{Fk}$ be the corresponding projection of $\mathbf{x}_M$ onto the plane of the $k$-th x-ray image. Let $\mathbf{f}_k$ be the $k$-th x-ray image's focal point and $\mathbf{e}_k$ be the normalised vector that goes from $\mathbf{f}_k$ to projection $\mathbf{x}_{Fk}$

$$\mathbf{e_k} = \frac{\mathbf{x}_{Fk} - \mathbf{f}_k}{|\mathbf{x}_{Fk} - \mathbf{f}_k|} \tag{5.1}$$

The point $\hat{\mathbf{x}}_F$ minimises the distance to all back-projected rays which, in mathematical terms, equals to minimise the cross product between $(\hat{\mathbf{x}}_{Fk} - \mathbf{f}_k)$ and $\mathbf{e}_k$, which should be null if all rays intersected in a single point

$$(\hat{\mathbf{x}}_{Fk} - \mathbf{f}_k) \times \mathbf{e}_k = \mathbf{0} \tag{5.2}$$

Writing the previous equation in matrix form yields (omitting the $k$ index for clarity)

$$\begin{bmatrix} 0 & e_z & -e_y \\ -e_z & 0 & e_x \\ e_y & -e_x & 0 \end{bmatrix} \hat{\mathbf{x}}_F = \begin{bmatrix} f_y e_z - f_z e_y \\ f_z e_x - f_x e_z \\ f_x e_y - f_y e_x \end{bmatrix} \tag{5.3}$$

Stacking equations 5.3 for each x-ray image forms an over-determined system of 3 variables and $3N$ equations, where $N$ is the number of 2D images in the registration. Its resolution is obtained by using the Singular Value Decomposition of the left hand side matrix, yielding the optimal –in least-squares sense– approximation for point $\hat{\mathbf{x}}_F$ (Press et al., 2007). The reconstruction problem is repeated for each landmark point $\mathbf{x}_M$, obtaining a set of corresponding 3D landmarks $\hat{\mathbf{x}}_F$. Thus, the problem

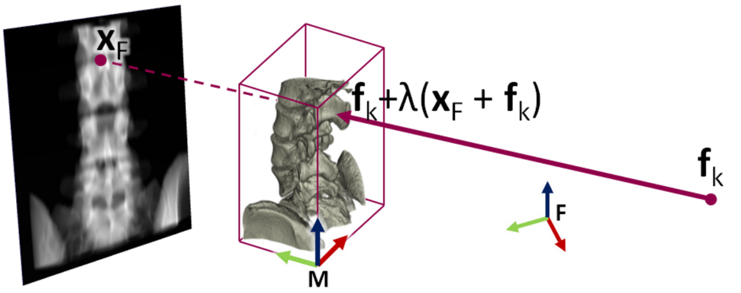

Figure 5.5: Illustration of the ray casting process. In the $k$-th image, pixel $\mathbf{x}_F$ has an intensity value equal to the integral of $\mathcal{M}$ sampled along the ray that goes from focal point $\mathbf{f}_k$ to $\mathbf{x}_F$, with $\mathcal{M}$ being the 3D pre-operative image. As points $\mathbf{f}_k$ and $\mathbf{x}_F$ are defined in frame $F$, transform $\mathbf{T}_F^M$ must be defined to sample the intensity values of $\mathcal{M}$ along the ray.

becomes a 3D-3D registration between two set of points with known correspondences, for which the Horn's algorithm is directly applied for its resolution. In our work, we used the ITK's implementation of it, included in the `LandmarkBasedTransformInitializer` class.

### 5.2.3 Intensity-based registration

As written previously, images in 2D-3D registration problems must be first taken to dimensional correspondence either by projection, back-projection or reconstruction: `multiImageRegistrator` does this by means of projection, producing 2D DRRs from the 3D CAT data. Let $\mathcal{P}_k$ be the projection of the 3D data into the plane of the $k$-th x-ray image, expressed as

$$\mathcal{P}_k(\mathbf{x}_F) = \int_0^1 M(\mathcal{T}_F^M(\mathbf{f}_k + \lambda(\mathbf{x}_F - \mathbf{f}_k)))d\lambda \tag{5.4}$$

Equation 5.4 corresponds to the ray-casting process, shown on Figure 5.5, in which the intensity of each projected pixel equals the integral along the ray that goes from it to the x-ray's focal point. Ray-casting is generally accepted as a good approximation of the x-ray formation process, although it ignores scattering.

Application of Equation 5.4 produces a projected image $\mathcal{P}_k$ which, if transform $\mathcal{T}_F^M$ is correct, should be very similar to the actual $k$-th x-ray image $F_k$. We define a similarity metric $S_k$, which is a function that measures the degree of similarity between both images, evaluated on a defined set of points. The problem of the projection based 2D-3D registration consists on finding the optimal transform $\dot{\mathcal{T}}_M^F$ which maximises the sum of all similarity metrics for the $N$ images.

$$\dot{\mathcal{T}}_F^M = \underset{\mathcal{T}_F^M}{\arg\max} \sum_{k=1}^{N} S_k(F_k, \mathcal{P}_k) \tag{5.5}$$

Therefore, a 2D-3D projection-based registration boils down to a single-valued optimisation problem. Thus, a great part of its resolution involves the proper choice of a similarity metric and optimisation algorithm.

The choice of the best similarity metric for 2D-3D registration has been the subject of a long debate with several published comparative studies which, unfortunately, have reported inconsistent (and sometimes contradictory) results. Citing a few, Penney et al. evaluated multiple metrics registering spinal datasets and concluded that Gradient Difference (GD) and Pattern Intensity (PI) were the most accurate and robust against outliers (Penney et al., 1998). Wu et al. tested different metrics on different imaging modalities and concluded that Normalised Cross Correlation (NCC) was the more accurate and robust for kV x-ray imaging; PI, GD and Gradient Correlation (GC) were the most accurate while NCC and Normalised Mutual Information (NMI) were the most robust for MV imaging; whereas NCC and NMI had the best robustness in a clinical study using MV x-ray imaging (Wu et al., 2009). Birkfellner et al. proposed the Stochastic Rank Correlation metric and presented results on which it achieved a superior performance against PI and NCC (Birkfellner et al., 2009). Gendrin et al. evaluated multiple metrics and concluded that gradient-based metrics were more accurate and robust, in particular when soft tissue and deformations were present on the images (Gendrin et al., 2011). Otake et al. evaluated a gradient-based metric against others based on information theory and obtained superior results with the former (Otake et al., 2012). However, as Otake et al. wrote, it is now acknowledged that there is no metric superior to all others and its choice has to consider the types of registered images and their quality. Furthermore, the combination of similarity metric and optimiser considerably affects the registration performance, as pointed out by van der Bom et al. (van der Bom et al., 2011).

In our proposed 2D-3D registration library, we decided to include three of the most used similarity metrics, namely Normalised Gradient Correlation, Gradient Difference and Pattern Intensity. According to the finding of other authors, these metrics perform well as long as the fixed and moving images do have similar distributions of intensity, which is the case for kV x-rays and DRRs generated from CAT data. In principle, the use of information-based metrics like Mutual Information (MI) and Normalised Mutual Information is unnecessary, as these were designed for multi-modal registration, that is, for images with marked differences in contrast (Pluim et al., 2003). This is an advantage, as information-based metrics require the calculation of the images' histograms on each iteration, considerably reducing their performance.

#### 5.2.3.1 Normalised Gradient Correlation

Normalised Gradient Correlation (NGC) averages the normalised cross-correlation of the fixed and projected images' gradients computed along $x$ and $y$ (Lemieux et al., 1994).

$$S_k = \frac{1}{2}\left( NCC\left(\frac{\partial F_k}{\partial x}, \frac{\mathcal{P}_k}{\partial x}\right) + NCC\left(\frac{\partial F_k}{\partial y}, \frac{\mathcal{P}_k}{\partial y}\right)\right) \tag{5.6}$$

$$NCC(F, M) = \frac{\sum_{\mathbf{x}} F(\mathbf{x})M(\mathbf{x})}{\sqrt{\sum_{\mathbf{x}} F(\mathbf{x})^2}\sqrt{\sum_{\mathbf{x}} M(\mathbf{x})^2}} \tag{5.7}$$

NGC evaluates the images' similarity based on their gradients and, therefore, is insensitive to low-frequency variations of intensity introduced by soft tissue. In other words, NGC evaluates how similar the images are by measuring the correlation of their borders, giving less weight to the the images' flat regions.

#### 5.2.3.2 Gradient Difference

The Gradient Difference (GD) metric, proposed by Penney et al., estimates the degree of similarity between two images based on their pixel-by-pixel subtraction of their gradients (Penney et al., 1998). Mathematically, it is defined as

$$S_k = \sum_{\mathbf{x}_F} \frac{\sigma_k^2}{\sigma_k^2 + \mathcal{D}_k^x(\mathbf{x}_F)} + \sum_{\mathbf{x}_F} \frac{\varsigma_k^2}{\varsigma_k^2 + \mathcal{D}_k^y(\mathbf{x}_F)} \tag{5.8}$$

where $\mathcal{D}_k^x$ and $\mathcal{D}_k^y$ are the differences between the gradients of fixed image $k$ and the ones of the moving image's projection $\mathcal{P}_k$ along $x$ and $y$

$$\mathcal{D}_k^x = \frac{\partial F_k}{\partial x} - \frac{\partial \mathcal{P}_k^{\mathcal{T}}}{\partial x} \tag{5.9}$$

$$\mathcal{D}_k^y = \frac{\partial F_k}{\partial y} - \frac{\partial \mathcal{P}_k^{\mathcal{T}}}{\partial y} \tag{5.10}$$

Terms $\sigma_k^2$ and $\varsigma_k^2$ are the variances from the gradient images of $F_k$

$$\sigma_k^2 = var(\frac{\partial F_k}{\partial x}) \tag{5.11}$$

$$\varsigma_k^2 = var(\frac{\partial F_k}{\partial y}) \tag{5.12}$$

GD uses the images' gradients rather than their intensities, just like NGC does, so it is also insensitive to low frequency variations. In addition, its reciprocal form (differences are placed in the denominator) makes it strong against thin artefacts with strong intensities, such as surgical wires present in the images.

#### 5.2.3.3 Pattern Intensity

Other metric is the Pattern Intensity (PI) proposed by Weese et al., which characterises the amount of 'structure' found in the pixel-by-pixel subtraction between the fixed and projected images (Weese et al., 1997). If the images are not properly registered, areas with large intensity variations –that is, 'structure'– will appear in the difference image. In turn, these structures should banish if registration was correct, leaving flat areas with low changes in intensity. The PI assigns values to the amount of structure found on a small moving kernel, according to the following formula

$$S_k = \sum_{\mathbf{x}_F} \sum_{\mathbf{u}_F} \frac{\sigma^2}{\sigma^2 + (\mathcal{I}_k(\mathbf{x}_F) - \mathcal{I}_k(\mathbf{u}_F))^2} \tag{5.13}$$

$$\mathcal{I}_k(\mathbf{x}) = F_k(\mathbf{x}) - \mathcal{P}_k(\mathbf{x}) \tag{5.14}$$

$$|\mathbf{x}_F - \mathbf{u}_F|^2 < r^2 \tag{5.15}$$

In Equation 5.13, term $\mathbf{x}_F$ represents the coordinates of each pixel taken into account for the metric calculation and $\mathbf{u}_F$, the coordinates of a moving kernel of radius $r$ centered on voxel $\mathbf{x}_F$. This kernel samples the image $\mathcal{I}_k$, obtained from the subtraction of the fixed and projected images. Terms $r$ and $\sigma^2$ are user-defined parameters. Parameter $r$ defines the radius of the moving kernel and $\sigma^2$ defines the sensitivity which determines if a intensity variation should be considered a structure or not.

The PI metric, differs from GD and NGC in that it does not compute the images' gradients. Instead, it uses direct subtraction between intensities of the fixed and projected images, but its moving kernel restricts the metric to the local features rather than the global ones, preventing soft tissue intensity variations from affecting the metric values. Like Gradient Difference, it also has a reciprocal form, which makes it strong against thin outliers like surgical instruments.

#### 5.2.3.4 Multi-resolution

Performing image registration using multi-resolution approaches is widely used to improve speed, accuracy and robustness. The basic idea is that registration is first performed at a coarse scale where image have fewer pixels. The transform determined at a coarse scale is used as a starting point for the next finer scale. The process is repeated until the finest possible scale is reached. This strategy greatly improves the registration robustness by eliminating local minima at coarser resolution stages (Ibáñez et al., 2005).

In our proposed library we strictly followed ITK's implementation of multi-resolution strategies, making sure that any software developer familiar with it could use our library with minimal effort. We kept ITK's

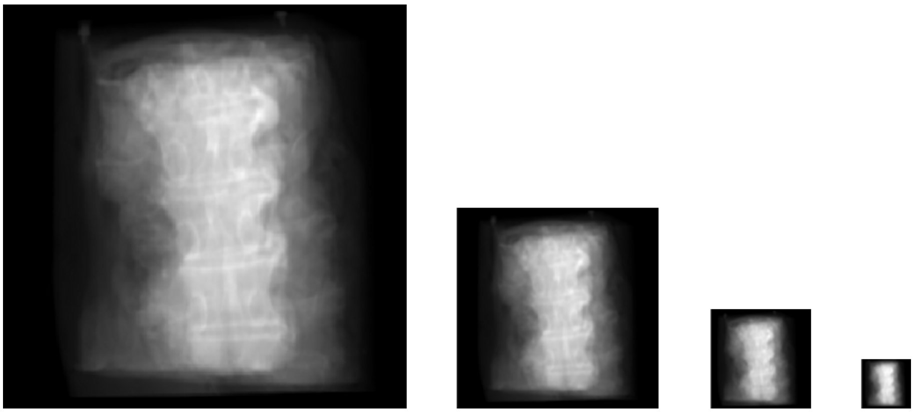

Figure 5.6: A sample x-ray image at multiple resolution levels. From left to right: original image (i.e. no downsampling), 2x, 4x and 8x downsampling levels.

pyramid classes, which produce images such as the ones shown on Figure 5.6, with tunable amounts of downsampling.

#### 5.2.3.5 Optimisers

According to Equation 5.5, our framework computes the similarity between all images as a single value, equal to the sum of metric between the 3D image and each of the 2D ones. This permits the use of virtually all ITK's optimisers for single-valued functions, which adds a great amount of flexibility to our library. As written previously, the registration performance is greatly affected by the combination of similarity metric and optimiser (van der Bom et al., 2011). Therefore, it is highly desirable to have a large number of options to handle as many types of registrations as possible.

In the current version of `multiImageRegistrator` it is possible to choose among ITK's Amoeba (i.e. Nelder-Meade downshill simplex), Powell (i.e. Powell-Brent using line search), FRPR (i.e. Fletch-Reeves-Polak-Ribiere conjugate gradient descent) and One-plus-One evolutionary (Styner et al., 2000) optimisers. In addition, it is possible to use the Exhaustive optimiser, which is actually a class that samples the similarity metric in a regular grid around a given position, to explore the function's shape and check for local minima or discontinuities. A large variety of problems can be handled with the present set of metrics,

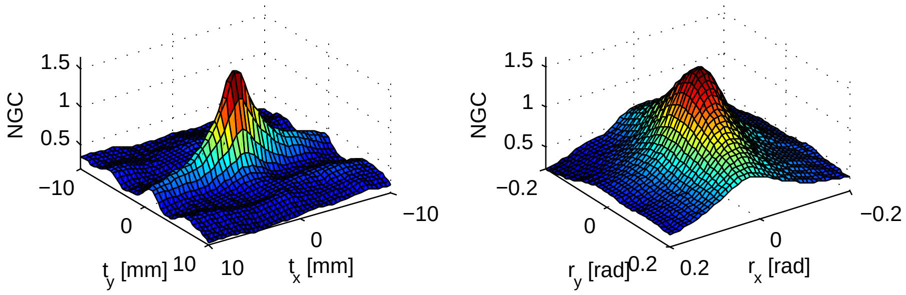

(a) Translations along $x$ and $y$ (b) Rotations around $x$ and $y$

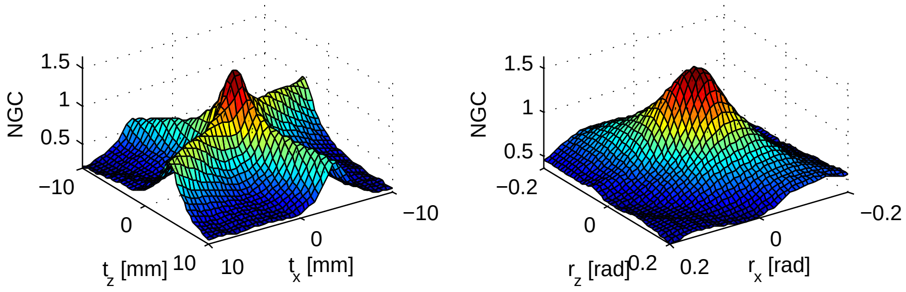

(c) Translations along $x$ and $z$ (d) Rotations around $x$ and $z$

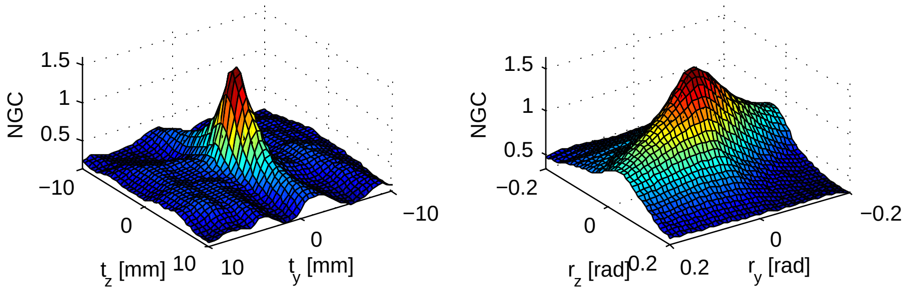

(e) Translations along $y$ and $z$ (f) Rotations around $y$ and $z$

Figure 5.7: Exhaustive search on the transform's parameter space using the Utrecht dataset, without downsampling. On all plots, the correct transform corresponds to the central position, which should have the maximum similarity.

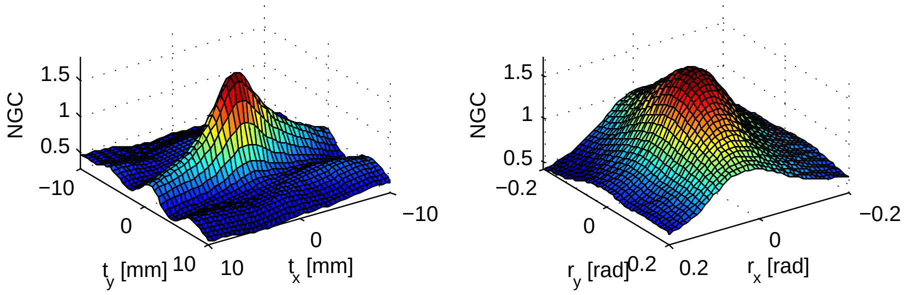

(a) Translations along $x$ and $y$ (b) Rotations around $x$ and $y$

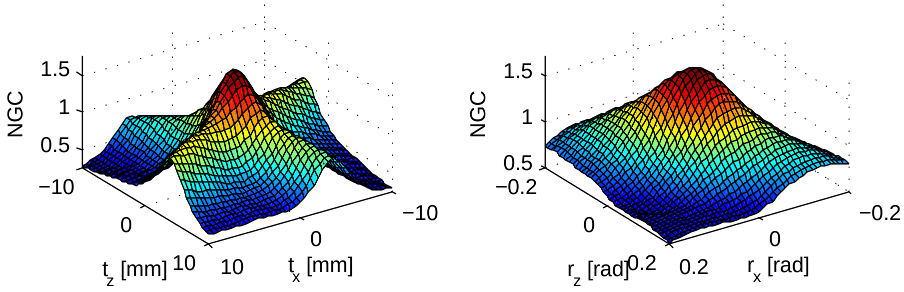

(c) Translations along $x$ and $z$ (d) Rotations around $x$ and $z$

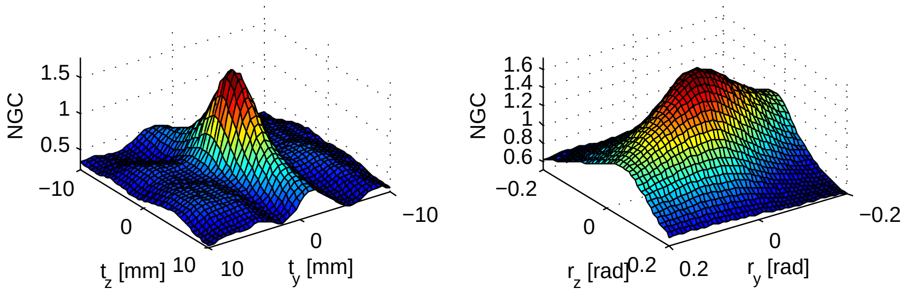

(e) Translations along $y$ and $z$ (f) Rotations around $y$ and $z$

Figure 5.8: Exhaustive search on the transform's parameter space using the Utrecht dataset, with a downsampling factor of 2x.

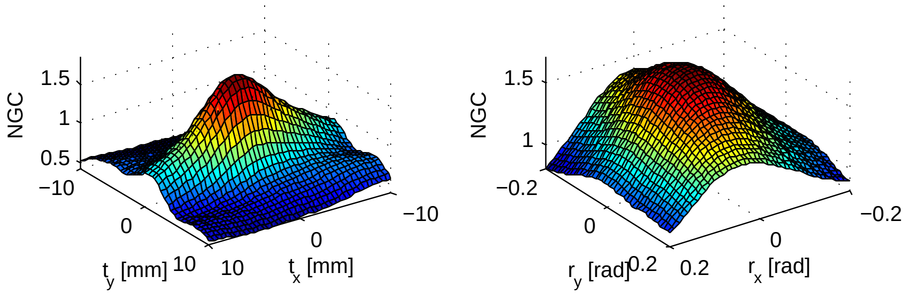

(a) Translations along $x$ and $y$ (b) Rotations around $x$ and $y$

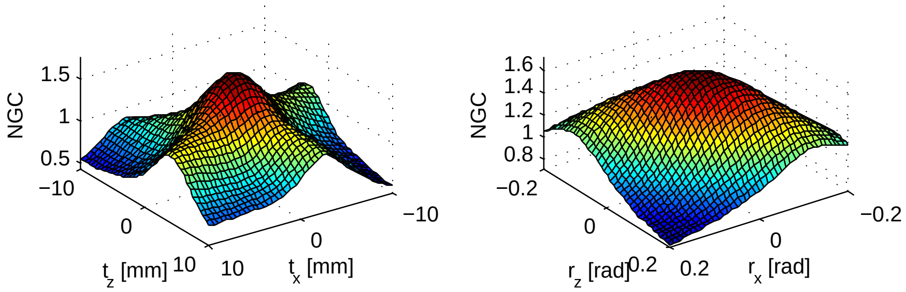

(c) Translations along $x$ and $z$ (d) Rotations around $x$ and $z$

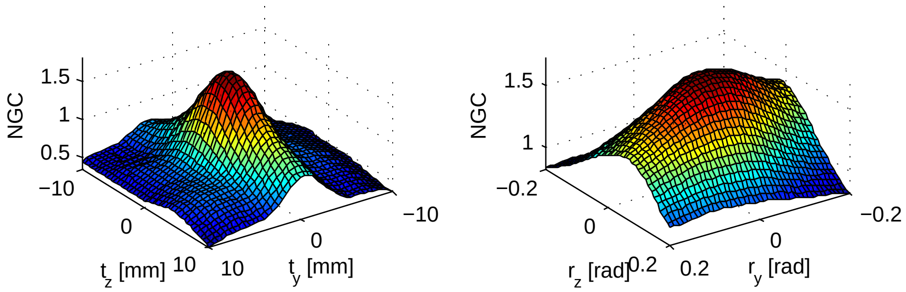

(e) Translations along $y$ and $z$ (f) Rotations around $y$ and $z$

Figure 5.9: Exhaustive search on the transform's parameter space using the Utrecht dataset, with a downsampling factor of 4x.

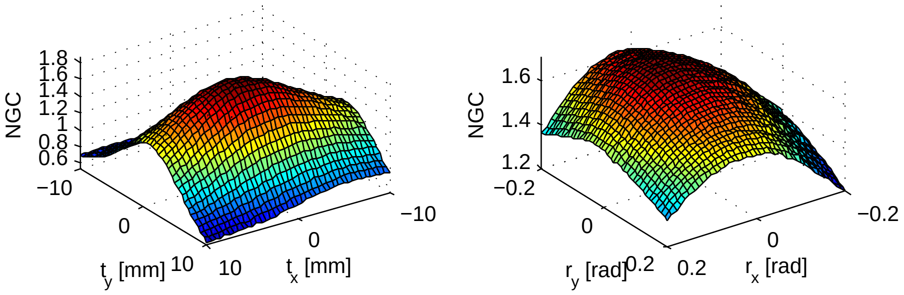

(a) Translations along $x$ and $y$ (b) Rotations around $x$ and $y$

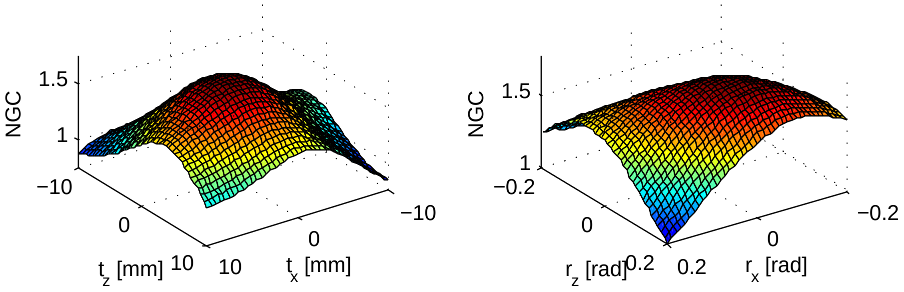

(c) Translations along $x$ and $z$ (d) Rotations around $x$ and $z$

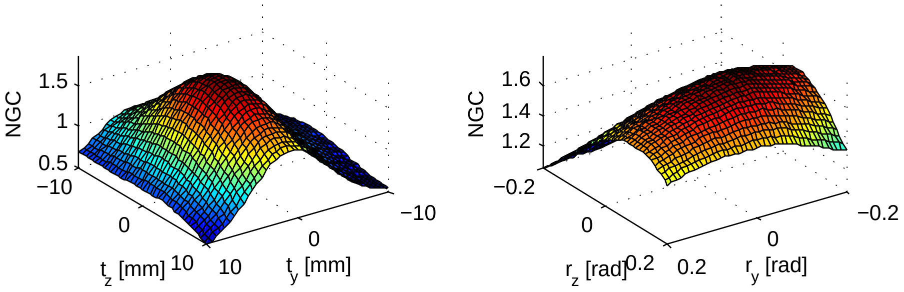

(e) Translations along $y$ and $z$ (f) Rotations around $y$ and $z$

Figure 5.10: Exhaustive search on the transform's parameter space using the Utrecht dataset, with a downsampling factor of 8x.

although it is quite easy to extend `multiImageRegistrator` to support other available optimisers, thanks to ITK's flexible architecture.

To make a good choice of optimiser for our particular problem –that is, registration of CT images to radiographs– we made an exploration of the transform parameters' space, plotting the NGC metric's shape around the optimum using ITK's Exhaustive optimiser. For this, we used van de Kraats et al.'s dataset, selecting the CAT image of its first vertebra and the included x-ray images, at four different resolution levels. The resulting functions, shown on Figures 5.7, 5.8, 5.9 and 5.10, reveal that NGC has a continuous shape and a well-defined maxima, two desirable features for optimisation. As the metric is not noisy and its local maxima are not pronounced, the use of global optimisation algorithms such as simulated annealing (Kirkpatrick et al., 1983; Černý, 1985), simultaneous perturbation and stochastic approximation (Spall, 1998) and evolutionary strategies are not mandatory. This is consistent with the study of van der Bom et al., who showed that the use of a conjugate gradient optimiser, paired with the NGC metric, produced results as good as stochastic and evolutionary algorithms (van der Bom et al., 2011). The Figures also reveal that the use of four resolution levels is adequate, as the similarity metric becomes smoother, no local maxima appear and the global maximum remains close to the real one in all levels. It must be noted that all metrics were calculated on small regions of the fixed images, which were of 146 by 75 pixels for the AP image and 166 by 69 pixels for the LAT one. The regions' size is decreased as the downsampling factor increases, and going beyond the 8x factor produces regions too small to be useful for the metric computation.

## 5.3 Evaluation

We evaluated a sample registration method (3D CAT image registered to 2 x-rays, NGC metric paired with the FRPR optimiser) using van de Kraats standardised protocol and its results in terms of its mTRE, capture range and success rate are presented on Table 5.1, for four different multi-resolution settings. Its data clearly shows how robustness increases by adding downsampling levels, as there is a clear improvement in terms of capture range and sucess rate, which reach values of 6 mm and 70.75% respectively. A graphical description of this improvement is given by

| Settings | mTRE [mm] | CR [mm] | SR [%] |
|---|---|---|---|
| No multiresolution | 0.39 | 3 | 35.06 |
| Multi-resolution, 2 levels | 0.37 | 4 | 45.56 |
| Multi-resolution, 3 levels | 0.37 | 4 | 55.75 |
| Multi-resolution, 4 levels | 0.37 | 6 | 70.75 |

Table 5.1: Mean Target Registration Errors (mTRE), Capture Ranges (CR) and Success Rates (SR) of a sample registration method implemented by `multiImageRegistrator` at four different multi-resolution settings.

the plots of Figure 5.11. On them, each point represents an individual registration, with its initial and final mTRE given by its horizontal and vertical coordinates respectively. Successful registration have final mTRE of less than 2 mm and, thus, lie below the horizontal line drawn on each plot. The diagonal line marks the line of no improvement, where registrations have equal initial and final mTRE. A good registration method should have most of its points below the 2mm line and no points above the line of no improvement. From Figure 5.11's plots it is clear how adding extra downsampling levels helps to register cases with higher initial mTRE, which cannot be handled when multi-resolution is not used.

On Table 5.2 we compared this sample method with other existing algorithms, such as the Intensity-based (IB) one proposed by Penney et al. (Penney et al., 1998), the Gradient-based and Reconstruction-based proposed by Tomaževič et al. (Tomaževič et al., 2003; Tomaževič et al., 2006). In addition, we also included the methods proposed by Markelj et al., named as Gradient-reconstruction-based (GRB), Robust GRB (RGRB) and RGRB extended (RGRBe) methods (Markelj et al., 2008b). From the table's data, we can conclude that the proposed algorithm has a very good accuracy and an acceptable robustness. In terms in capture range and success rate, the sample method outperformed the IB, GB, RB and GRB algorithms, but fell below the RGRB and RGRBe methods. This result is not surprising, as the latter two methods were designed specifically for robust registration, using the RANSAC algorithm to test multiple candidate registrations and choose the best one, avoiding local minima with high probability.

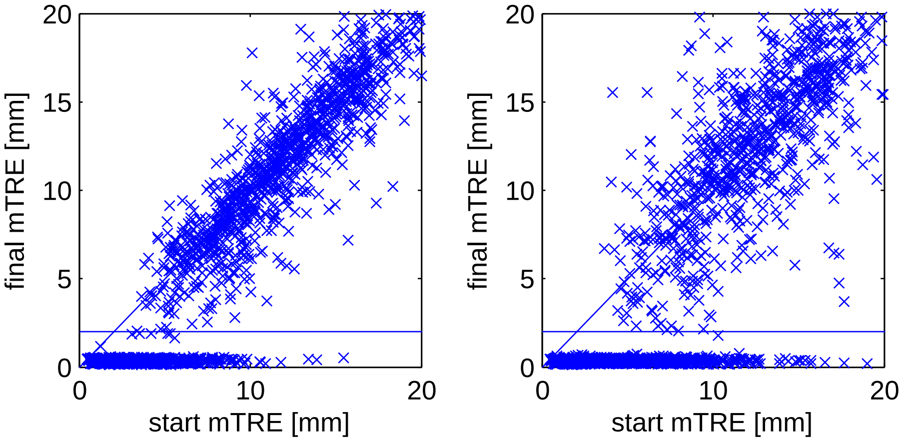

(a) No multi-resolution (b) 2 levels

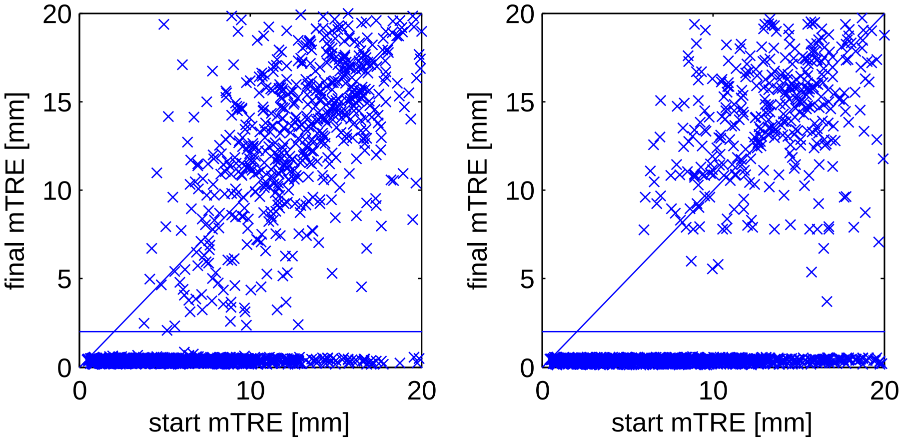

(c) 3 levels (d) 4 levels

Figure 5.11: The results for registration of CAT images to two x-rays for four multi-resolution levels, indicating the initial mTRE value before and after registration. It can be observed that adding downsampling levels effectively improves the registration robustness.

| Method | mTRE [mm] | CR [mm] | SR [%] |
|---|---|---|---|
| IB | 0.65 | 3 | - |
| GB | 0.38 | 6 | 56 |
| RB | 0.43 | 5 | 65 |
| GRB | 0.32 | 5 | 69 |
| **Sample method** | **0.37** | **6** | **71** |
| RGRB | 0.58 | 9 | 88 |
| RGRBe | 0.32 | 11 | 92 |

Table 5.2: Comparison of the sample registration method in terms of mTRE, CR and SR. All included algorithms were tested with 3D CAT images and 2 x-rays. Figures in non-bold font were taken from the work by Markelj et al. (Markelj et al., 2008b).

## 5.4 Discussion

The objective of this chapter, as written on its beginning, is giving a description of the proposed library and its capabilities, rather than proposing a novel 2D-3D registration algorithm. The sample algorithm, evaluated on the previous section, illustrates how our framework permits the implementation of a highly useful registration method with a minimal effort from the user. In fact, its execution only requires edition of a parameters file and no programming at all.

However, additional development is required on the library to reach clinically acceptable levels. Although sub-mm accuracy is already feasible, additional effort is required to increase robustness. Ideally, a success rate of 95% should be obtained as pointed out by Livyatan et al. (Livyatan et al., 2003). To obtain this, more sophisticated methods should be explored, such as global optimisation stages executed before the multi-resolution registration.

Another possibility to increase robustness –more specific to spinal applications– is to register multiple vertebrae simultaneously. In its present form, the library is only capable of registering a single vertebra, which can move with 6 degrees of freedom. Registering multiple vertebrae at the same time would be feasible without adding too many degrees of freedom, as the vertebrae's relative motion is restricted. In fact, although individual vertebrae move as a rigid body, their motion affect their neighbours in ways that have successfully been modelled (Kadoury et al., 2011). Therefore, it would be feasible to register the spine using algorithms designed for multiple rigid bodies with restricted relative motion, methods which have been used in other applications such as registration of foetal MR brain scans (Bertelsen et al., 2009).

The library's speed needs also to be increased to reach clinically acceptable levels. In particular, two elements should be addressed, the first being the ray-casting algorithm. Currently, the library is only capable of generating DRR using a ray-casting method that runs on the computer's processor, which is quite inefficient. Multiple research groups have studied this problem already and have proposed accelerated projection algorithms, such as the works by Russakoff et al (Russakoff et al., 2005) and Kubias et al. (Kubias et al., 2008). The second part that needs improvement is the similarity metric's gradient calculation, which needs to be updated on each iteration. Ideally, an analytical expression of this gradient should be formulated, although its determination would not be an easy task in particular if it was extended for metrics such as MI and NMI. This have lead other authors to choose optimisers that do not require gradients at all –such as Otake et al.– although we believe that their use can speed up the optimisation and make it more robust. In fact, van der Bom et al. concluded that the NGC metric paired with the FRPR conjugate-gradient optimiser yielded the best result when registering a kV x-ray image to a 3D CAT dataset (van der Bom et al., 2011). In addition, the metrics' shapes of Figures 5.7, 5.8, 5.9 and 5.10 are clearly good candidates for gradient-based optimisation, as they do not present too many local maxima or major discontinuities.

## 5.5 Closing remarks

We have presented a new software library for the implementation of 2D-3D registration applications, covering many of the shortcomings of other publicly available frameworks. We have demonstrated the main features and capabilities of the proposed library, describing a sample application bundled with the viewit-Spine surgical planner, previously described in this thesis. In its current form, the proposed framework is able to implement acceptable 2D-3D registration solutions with sub-millimetre accuracy, although additional work is required to reach clinically acceptable levels in terms of robustness and speed.

## Chapter 6

# Calibration and distortion correction of x-ray images

A synthesis of this chapter has been published in:

> *Bertelsen, A., Echeverría, M., Gómez, E., and Borro, D. "Distortion correction and calibration of intra-operative x-ray images using a constrained DLT algorithm". In Actas del XXX Congreso Anual de la Sociedad Española de Ingeniería Biomédica (CASEIB 2012). San Sebastián, Spain. 2012.*

Most modern hospitals have intra-operative fluoroscopic devices –known as 'c-arms'– which makes x-ray imaging a natural choice for the implementation of computer and robotic assisted surgeries. In this thesis, we have already said that these procedures need registration of the pre and intra operative images, which also requires an accurate knowledge of the x-ray image formation parameters. This makes c-arm's calibration and distortion correction necessary requisites for which reliable solutions must be developed.

## 6.1 Problem description

It is well accepted that c-arms can be modelled as pinhole cameras, borrowing terms from computer vision (Hartley and Zisserman, 2003). Calibration of this type of cameras consists in the estimation of its intrinsic (i.e. invariant to the c-arm's location) and extrinsic (i.e. variable with the c-arm's location) parameters. Intrinsic parameters are, mainly, the pixel's dimensions and the focal point location, whereas extrinsic parameters correspond to the c-arm's location with respect to a given frame of reference. Unfortunately, most c-arm's do not provide any of these: they normally lack from encoders to measure their angulation (extrinsic parameters) nor provide information about pixel size or focal point. To make matters worse, c-arm's intensifiers are affected by distortion, which is dependent on the curvature of its phosphorous panel and its surrounding electromagnetic field, influenced in turn by nearby metallic objects and the device's orientation (Rudin et al., 1991). This problem has been solved on more modern c-arms replacing image intensifiers by flat panel detectors with negligible distortion (Jaffray et al., 2002). However, this technology is quite recent and the majority of hospital do not have access to it yet.

Most c-arm calibration and distortion correction systems require use of a special device, known as 'drums', 'cages' or 'rings', which are attached to the intensifier before or during the intervention. Calibration drums normally consist of parallel plastic plates with embedded metallic fiducials, which are projected onto the x-ray images and segmented by specialised image processing algorithms. Their detected locations are then used to correct the effects of distortion and estimate the c-arm's parameters. Algorithms for these problems can be divided in two groups: off-line and on-line methods. Off-line approaches acquire a set of images with the attached calibration drum before intervention on some predefined positions. Calculation of intrinsic parameters and distortion corrections are performed for each position and saved. Then, the calibration device is removed and operation begins. Off-line approaches are simpler to implement, as no objects are present on the images used for calibration and, therefore, fiducial segmentation is greatly simplified. Their main drawback is that results are only valid for a reduced set of positions, and no others can be used during intervention. On the other hand, on-line approaches perform calibrations for each acquired x-ray image and, therefore, never remove the calibration drum during surgery. On-line approaches are inherently more reliable (they provide results adjusted to each image) and cope better with additional factors that may vary the intrinsic parameters, such as the c-arm's mechanical flexion which may displace the focal point between consecutive x-rays. The choice between off-line and on-line approaches also affects the calibration drum's design: off-line methods can use drums with denser fiducial grids, which produce more precise results (but only for a reduced set of positions), whereas on-line methods must use sparser grids, otherwise x-ray images would suffer from excessive occlusion. As we consider that limiting the calibration to a small set of positions is too restrictive, we opted for the flexibility of an on-line approach. This, however, has the trade-off of increased complexity of implementation, which we considered an acceptable price to pay to obtain higher precision and increased safety for the patient and clinical staff.

Calibration drums also have a second function, which is tracking of the c-arm's intensifier. The drums' frame serves as attachment for optical markers, thus enabling localisation of x-ray images in the moment of their acquisition. This, at the light of contents of Chapter 5, is critical for 2D-3D registration, as the latter requires knowledge of the x-rays' locations with respect to the operating room's coordinate system. In terms of the definitions of Section 3.2, this translates into the determination of transform $\mathbf{T}_{Pk}^{F}$, a problem which will also be covered in this chapter.

## 6.2 Previous work

Multiple on-line calibration algorithms have been proposed in the recent years, such as the ones proposed by Foley et al. (Foley et al., 2001), Tate et al. (Tate et al., 2001), Livyatan et al. (Livyatan et al., 2002), Merloz et al. (Merloz et al., 2007), Sadowsky (Sadowsky, 2008) and Zheng and Zhang (Zheng and Zhang, 2009). These studies have proposed multiple calibration drum designs, sometimes arranging the fiducial objects on a symmetrical arrangement (Foley et al., 2001; Merloz et al., 2007; Sadowsky, 2008). This approach, although valid, has an inconvenience: it impedes detection of image reflection. If the uncalibrated image is reflected –for any reason– an algorithm based on a symmetrical pattern would not detect it, giving a wrongly oriented image as result. In surgery, ensuring correct orientation of images is of critical importance, as a reflected image could lead surgeons to operate on the wrong side of the patient with terrible consequences. Therefore, asymmetrical designs of calibration drums are preferred, an approach followed by Tate et al. (Tate et al., 2001), Livyatan et al. (Livyatan et al., 2002) and Zheng and Zhang (Zheng and Zhang, 2009).

One of the most known on-line algorithms was published by Livyatan et

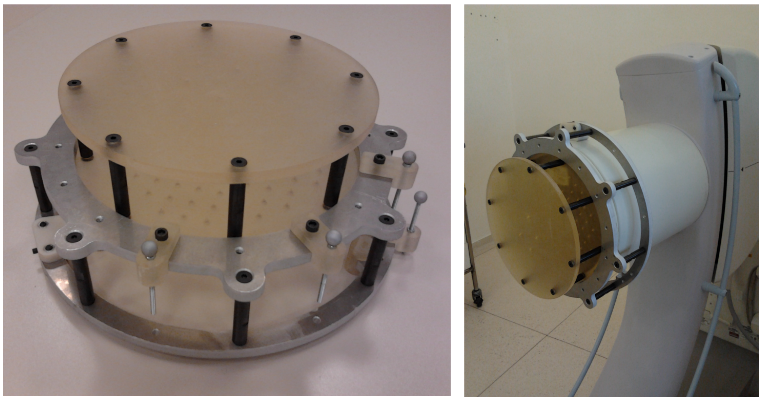

Figure 6.1: Left: photograph of the prototype calibration drum. Right: the drum mounted on the intensifier of a Siemens Powermobil c-arm.

al. in 2002, who proposed a method which performed distortion correction first followed by estimation of the c-arm parameters (Livyatan et al., 2002). The authors used the FluoroTrax calibration drum –previously used by Tate et al. (Tate et al., 2001)– consisting of two parallel plates with embedded fiducial beads arranged on an asymmetrical pattern. The beads' projections were segmented from the x-ray using standard image processing techniques and, then, the drum's centre and rotation were calculated and used to generate a ground-truth pattern of the proximal plate fiducials, which differed from the segmented ones due to distortion. The subtraction between both patterns generated a vector field, used to warp the x-ray image and correct the distortion effects (Wolberg, 1990). Finally, the corrected beads' locations were used as input for a calibration algorithm which estimated the c-arm's intrisic and extrinsic parameters (Gremban et al., 1988; Faugeras, 1993).

A different approach was presented by Zheng and Zhang in 2009, who also used a 2-plate drum, but with a less dense bead pattern (Zheng and Zhang, 2009). After segmentation of the fiducials –using a more sophisticated template matching algorithm– their method performed the correction and calibration steps in the opposite order: it first calibrated the c-arm using information taken from the central portion of the image and then generated a vector field used to undistort the x-ray. Zheng and Zhang used the Direct Linear Transform (DLT) algorithm for the c-arm calibration step, which is well known and widely used by computer vision researchers (Hartley and Zisserman, 2003).

## 6.3 Proposed solution

In this thesis we present a new method which combines the strengths of the previously described approaches: we propose the use of a less dense calibration drum, very similar to the one proposed by Zheng and Zhang, combined with some of the efficient segmentation steps used by Livyatan et al. Also, we propose the use of the *correction first - calibration second* approach, paired with a customised version of the DLT algorithm, with fewer degrees of freedom and higher stability. In this way, we have developed an algorithm which is fast, robust and accurate at the same time.

### 6.3.1 Prototype calibration drum

| Bead | $x$ [mm] | $y$ [mm] | $z$ [mm] |
|---|---|---|---|
| $D_1$ | 30 | -10 | 0 |
| $D_2$ | -10 | 30 | 0 |
| $D_3$ | -30 | -10 | 0 |
| $D_4$ | 9.25 | 27.75 | -75 |
| $D_5$ | -27.75 | 9.25 | -75 |
| $D_6$ | -27.75 | -27.75 | -75 |
| $D_7$ | 9.25 | -27.75 | -75 |

Table 6.1: Beads' coordinates in the proximal and distal plates of the calibration drum. All coordinates are measured in the drum's ($D$) coordinate system.

We built a custom calibration drum –shown on Figures 6.1 and 6.2– based on the design proposed by Zheng and Zhang (Zheng and Zhang, 2009), which has two parallel plastic plates with embedded fiducial beads of two different diameters, arranged on a not too dense pattern. The proximal plate has beads of 3 mm arranged on a cartesian grid with a separation of 20 mm, which are projected on each acquired x-ray image. In the latter, the small beads will not appear arranged exactly as in the cartesian grid,

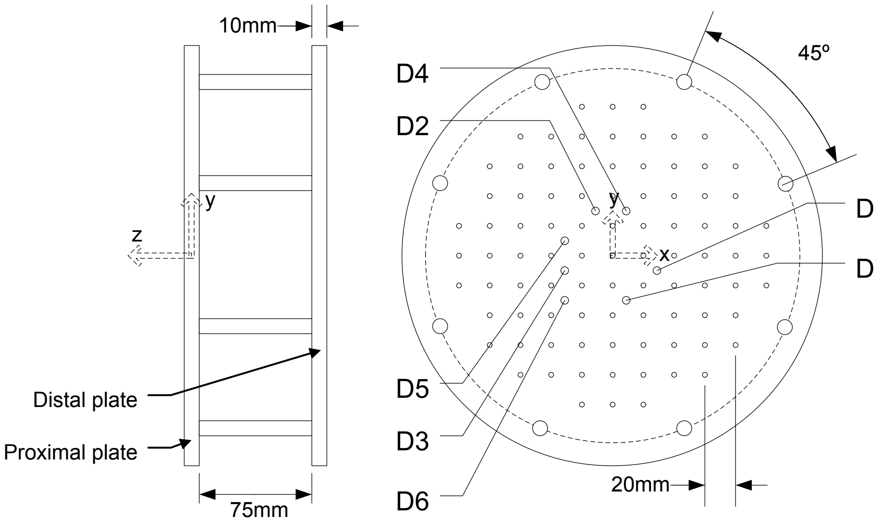

Figure 6.2: Schematic of the prototype calibration drum with lateral and bottom views. Large beads located on the proximal (D1 to D3) and distal plates (D4 to D7) are overlayed on the bottom view. The shown coordinate axes and origin correspond to the drum's ($D$) reference frame.

due to the distortion effects. However, as the grid's shape is known in advance, its undistorted positions can be inferred and used to warp the image undoing the effects of distortion. In addition to the small beads, the calibration drum has an asymmetrical pattern of three 5 mm beads, three of them placed on the proximal plate ($D_1$, $D_2$ and $D_3$) and four on the distal plate ($D_4$, $D_5$, $D_6$ and $D_7$) on the coordinates given on Table 6.1. This pattern is intentionally placed close to the image intensifier's centre, an area less affected by distortion compared with its edges. The pattern is used to estimate the relative displacement and rotation between the calibration drum and the image intensifier.

### 6.3.2 Segmentation

A specialised image processing algorithm, described on Figure 6.3, is executed to segment the projected beads on each acquired x-ray image. This algorithm first searches for the large beads by applying a median

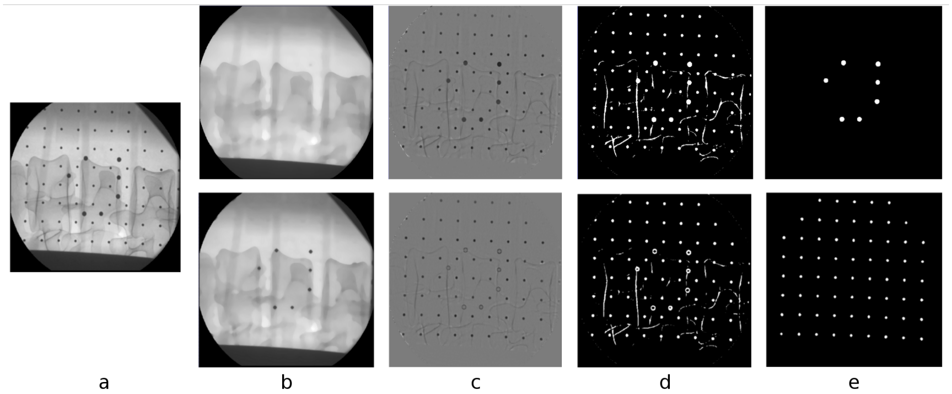

Figure 6.3: Segmentation process for the large (top row) and small beads (bottom row). Original images (a) are processed with a median filter (b) and the result is subtracted to the original obtaining a difference image (c). Images are binarised (d) and processed with a series of morphological operations to leave only the beads of interest (e).

filter to the image and subtracting the result to the original one. This gives a difference image which has pixel values close to zero everywhere except on the beads' locations, which have large negative values. The difference image is binarised using a threshold and a connected component analysis is performed to identify all objects in it. This binary image contains both beads and other spurious objects, so a morphological opening followed by three additional filtering operations are performed to discard objects which are too small, too large or not round enough to be considered beads. This gives as a binary image as result which only contains the large beads. Finally, each bead centroid is calculated with sub-pixel accuracy using the following formulae

$$\mathbf{x}_P = \frac{\sum_{\mathbf{x}\in\Omega} \mathbf{x}\mathcal{F}(\mathbf{x})}{\sum_{\mathbf{x}\in\Omega} \mathcal{F}(\mathbf{x})} \tag{6.1}$$

$$\mathcal{F}(\mathbf{x}) = \begin{cases} \mathcal{I}(\mathbf{x}) - \mathcal{T} & \text{if } \mathcal{I}(\mathbf{x}) \leq \mathcal{T} \\ 0 & \text{if } \mathcal{I}(\mathbf{x}) > \mathcal{T} \end{cases} \tag{6.2}$$

In Equation 6.1 $\Omega$ is a small neighbourhood around the detected bead, $\mathcal{I}(\mathbf{x})$ is the original image's value for pixel $\mathbf{x}$ and $\mathcal{T}$ is the Otsu's threshold

| Number | Rule |
|---|---|
| 1 | $0.9 \leq \frac{\lvert\overline{D_5D_4}\rvert}{\lvert\overline{D_1D_4}\rvert} \leq 1.1$ |
| 2 | $0.9 \leq \frac{\lvert\overline{D_6D_2}\rvert}{\lvert\overline{D_7D_2}\rvert} \leq 1.1$ |
| 3 | $85° \leq angle(\overline{D_2D_4}, \overline{D_3D_5}) \leq 95°$ |
| 4 | $0.9 \leq \frac{\lvert\overline{D_3D_5}\rvert}{\lvert\overline{D_6D_3}\rvert} \leq 1.1$ |
| 5 | $0.9 \leq \frac{\lvert\overline{D_6D_5}\rvert}{\lvert\overline{D_7D_6}\rvert} \leq 1.1$ |
| 6 | $85° \leq angle(\overline{D_6D_5}, \overline{D_7D_6}) \leq 95°$ |
| 7 | $85° \leq angle(\overline{D_3D_1}, \overline{D_6D_3}) \leq 95°$ |

Table 6.2: Geometrical rules for the identification of large beads.

calculated in the $\Omega$ neighbourhood of the original image (Otsu, 1979).

The procedure from median filtering to centroid calculation is repeated for the small beads using a different set of parameters (i.e. median filter size, threshold and size limits for the morphological operations). As the algorithm may not find all the small beads due to occlusion, a 4-th order polynomial interpolation is performed to obtain all the missing ones.

### 6.3.3 Bead identification

The seven large beads are identified using a set of geometrical rules similar to the ones proposed by Zheng and Zhang, determining which belong to the distal plate and which to the proximal one (Zheng and Zhang, 2009). These are listed on Table 6.2.

### 6.3.4 Distortion correction

As the distance between the proximal plate and the c-arm's intensifier is negligible in comparison with the focal distance, we can assume that the proximal plate's beads are directly overlayed on the image and, thus, no perspective effects are present. In fact, the separation between beads and the image intensifier is 5 mm and c-arms' focal distances are, normally, around 1000 mm. Assuming this, we can describe the transform to the proximal plate's beads from their projections as an affine transform

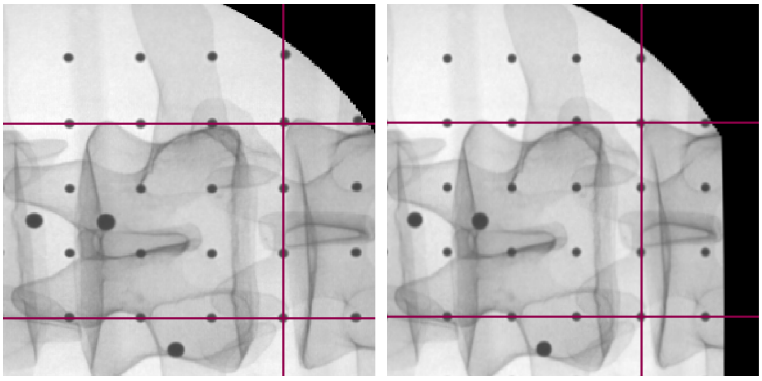

Figure 6.4: Correction of distortion effects. Note how the small beads in the top-right corner of the left image are not aligned with the grid. This effected is corrected when the effects of distortion are undone, as shown on the right image. Note also how the image aspect ratio changes, as the original (left) image does not have information of the pixels' dimensions, which are calculated by the proposed calibration algorithm.

composed of a scaling followed by a rotation and then an offsetting. Mathematically, this can be expressed as follows

$$\underbrace{\begin{bmatrix} c\varphi & -s\varphi \\ s\varphi & c\varphi \end{bmatrix}\begin{bmatrix} 1 & 0 \\ 0 & -1 \end{bmatrix}}_{\text{Rotation}}\underbrace{\begin{bmatrix} \Delta_x & 0 \\ 0 & \Delta_y \end{bmatrix}}_{\text{Scaling}}\begin{bmatrix} x_P^i \\ y_P^i \end{bmatrix}+\underbrace{\begin{bmatrix} x_D^0 \\ y_D^0 \end{bmatrix}}_{\text{Offset}}=\begin{bmatrix} x_D^i \\ y_D^i \end{bmatrix} \tag{6.3}$$

On Equation 6.3 terms $\Delta_x$ and $\Delta_y$ are the c-arm's detector pixel sizes in mm. Terms $c\varphi$ and $s\varphi$ are the cosine and sine of angle $\varphi$, which measures the relative rotation between the calibration drum and the image intensifier. Terms $x_D^0$ and $y_D^0$ are the coordinates –in mm– of the image corner with respect to the drum's $(D)$ coordinate system. Multiplication of the matrices of Equation 6.3 followed by a rearrangement of its terms, leaving $\Delta_x$, $\Delta_y$, $\varphi$, $x_D^0$ and $y_D^0$ as variables leads to the following linear system

$$\begin{bmatrix} x_P^i & 0 & 0 & y_P^i & 1 & 0 \\ 0 & x_P^i & -y_P^i & 0 & 0 & 1 \end{bmatrix} \begin{bmatrix} \Delta_x c\varphi \\ \Delta_x s\varphi \\ \Delta_y c\varphi \\ \Delta_y s\varphi \\ x_D^0 \\ y_D^0 \end{bmatrix} = \begin{bmatrix} x_D^i \\ y_D^i \end{bmatrix} \tag{6.4}$$

Stacking the equation system above for the three proximal beads yields the following system of 6 variables and 6 equations, which can be solved using any suitable algorithm.

$$\begin{bmatrix} x_P^1 & 0 & 0 & y_P^1 & 1 & 0 \\ 0 & x_P^1 & -y_P^1 & 0 & 0 & 1 \\ x_P^2 & 0 & 0 & y_P^2 & 1 & 0 \\ 0 & x_P^2 & -y_P^2 & 0 & 0 & 1 \\ x_P^3 & 0 & 0 & y_P^3 & 1 & 0 \\ 0 & x_P^3 & -y_P^3 & 0 & 0 & 1 \end{bmatrix} \begin{bmatrix} \Delta_x c\phi \\ \Delta_x s\phi \\ \Delta_y c\phi \\ \Delta_y s\phi \\ x_D^0 \\ y_D^0 \end{bmatrix} = \begin{bmatrix} 30 \\ 10 \\ -10 \\ 30 \\ -30 \\ -10 \end{bmatrix} \tag{6.5}$$

The solution of Equation 6.5 is used to generate the distortion-free pattern of the small beads, which is subtracted from the segmented beads locations generating a vector field. The latter is used in conjunction with a thin-plate spline interpolation algorithm to warp the image undoing the effects of distortion (Davis et al., 1997), as shown on Figure 6.4.

Note that we have used the subscript $P$ to denote the x-ray image's coordinate system. This is consistent with the definitions of Section 3.2, although we have dropped index $k$ as there is only one image involved in the present problem.

### 6.3.5 C-arm calibration

The vector field is also used to update the large beads' centroids, aiming to improve the following calibration calculations. For the latter, we adhere to the convention that c-arms can be modelled as linear projective cameras (Hartley and Zisserman, 2003). These are fully described by a projection matrix P of the form

$$\mathbf{P} = \mathbf{KR}\left[\mathbf{I}| - C\right] \tag{6.6}$$

On Equation 6.6 matrix **K** represents the intrinsic parameters whereas the extrinsic parameters are described by matrix **R** and point $C$. Following the convention of this thesis, extrinsic parameters correspond to the relative displacement and rotation between the calibration drum and the image plane or, in other words, between the coordinate systems $D$ and $P$.

Matrix **K**, containing the c-arm's intrinsic parameters, has the following form

$$\mathbf{K} = \begin{bmatrix} -f/\Delta_x & 0 & x_P^C \\ 0 & -f/\Delta_y & y_P^C \\ 0 & 0 & 1 \end{bmatrix} \tag{6.7}$$

Parameters $f/\Delta_x$ and $f/\Delta_y$ are the focal distances measured in pixels with $f$ being the focal distance in mm whereas $\Delta_x$ and $\Delta_y$ are the already calculated pixel sizes. Parameters $x_P^C$ and $y_P^C$ are the coordinates, in pixels, of the principal point, that is, the intersection of the normal ray that goes from the imaging plane to the focal point. It has been assumed that skewing is null (i.e. pixels are rectangular and **K**'s top element of its second column is zero). As pixel sizes are fixed, this model for **K** has only 3 degrees of freedom, which correspond to $x_P^C$, $y_P^C$ and $f$.

As said previously, matrix **R** represents the rotation between the drum and the c-arm's intensifier, which correspond to the already calculated $\varphi$ angle. Assuming that no rotation around $x$ and $y$ are present, **R** can be expressed as follows

$$\begin{aligned} R &= \begin{bmatrix} c\varphi & -s\varphi & 0 \\ s\varphi & c\varphi & 0 \\ 0 & 0 & 1 \end{bmatrix} \begin{bmatrix} 1 & 0 & 0 \\ 0 & -1 & 0 \\ 0 & 0 & -1 \end{bmatrix} \\ &= \begin{bmatrix} c\varphi & s\varphi & 0 \\ s\varphi & -c\varphi & 0 \\ 0 & 0 & -1 \end{bmatrix} \end{aligned} \tag{6.8}$$

Point $C$ corresponds to the focal point position with respect to the drum's ($D$) frame of reference. As the drum and the intensifier –and thus the image plane– form a rigid body, it is sufficient to know the principal point and focal distance to obtain $C$, using the solution of Equation 6.5.

$$\begin{bmatrix} C \\ 1 \end{bmatrix} = \underbrace{\begin{bmatrix} c\varphi & s\varphi & 0 & x_D^0 \\ s\varphi & -c\varphi & 0 & y_D^0 \\ 0 & 0 & -1 & 0 \\ 0 & 0 & 0 & 1 \end{bmatrix}}_{\mathbf{T}_P^D} \begin{bmatrix} \Delta_x x_P^C \\ \Delta_y y_P^C \\ f \\ 1 \end{bmatrix} \tag{6.9}$$

Please note that the 4-by-4 right-side matrix of Equation 6.9 corresponds to transform $\mathbf{T}_P^D$, which takes points from the image's frame to the drum's coordinates. This transform will be used again in Section 6.4.4.

To estimate $\mathbf{P}$ we used a customised version of the widely used DLT algorithm, which obtains the optimal projection matrix between a set of points and their corresponding projections (Hartley and Zisserman, 2003). However, the standard DLT algorithm has 11 degrees of freedom, so its use is not appropriate for the model described by Equations 6.6, 6.7, 6.8 and 6.9, which has only 3. Therefore, a constrained version of the DLT algorithm was used, which iteratively minimises the distance between the segmented points and the projected ones using an estimation of matrix $\mathbf{P}$ parametrised by $x_P^C$, $y_P^C$ and $f$.

$$\dot{\mathbf{P}} = \underset{(x_P^C, y_P^C, f)}{\arg\min} \sum_{i=1}^{7} |\mathbf{x}_P^i - \mathbf{P}(x_P^C, y_P^C, f)\mathbf{x}_D^i|^2 \tag{6.10}$$

Still, the standard algebraic DLT is used to obtain the starting values of $x_P^C$, $y_P^C$ and $f$ before minimisation of Equation 6.10. Resolution of the latter completes the calibration step.

## 6.4 Evaluation

We ran a series of experiments to evaluate the proposed algorithm, checking the accuracy of its segmentation and calibration stages, as well as its ability to reconstruct positions of 3D points from their projections. Results are presented in the following subsections.

### 6.4.1 Segmentation

Segmentation is a crucial step for the algorithm's correct execution, as the correction and calibration stages depend on the centroids found by the segmentation. Therefore, a poor segmentation will inevitably lead to a poor distortion correction and an inaccurate calibration.

To evaluate the segmentation's performance we imaged a radio-opaque human spine model (Sawbones, Vashon, USA) using a Siemens Powermobil c-arm on 12 different angles. For each x-ray image, we manually segmented the beads centroids and calculated the distance to the segmentations produced by the algorithm. Results, shown on Table 6.3 and Table 6.4, show that the algorithm has sub-pixel accuracy and average errors of 0.29 ± 0.14 pix (0.18 ± 0.08 mm) and 0.32 ± 0.19 pix (0.12 ± 0.07 mm) for the large and small beads respectively (note that, as pixels are not square, smaller pixel error does not necessarily lead to smaller errors in mm). These results are remarkable as they are lower than the average errors reported by Livyatan et al. (0.84 ± 0.48 pix / 0.36 ± 0.21 mm) and also by Zheng and Zhang (0.5 ± 0.3 pix / 0.18 ± 0.11 mm). The average maximum error for the large and small beads was found to be 0.5 pix (0.31 mm) and 1.0 pix (0.38 mm) respectively. Average execution time per image was 3 seconds on an Intel Core Quad Q9550 computer with 4 GB of RAM running Windows 7.

### 6.4.2 Calibration

We made an additional experiment to evaluate the impact of segmentation noise on the calibration stage. For this, we simulated an image with a pixel size of 0.4 by 0.3636 mm (11/10 aspect ratio) with the principal point on (255.5, 255.5) pix and the focal point on (0, 0, -950) mm. Then, we calculated the true projection matrix and obtained the true projections of the drum's large beads onto the image plane. Afterwards, we added noise to the projections and re-calculated the focal point to observe the deviation from the true one. We run the experiments adding uniform noise of [-0.5, 0.5] pix and [-1.0, 1.0] pix, which are reasonable assumptions considering the maximum values observed for the large beads segmentation results shown on Table 6.3. For each noise level, we used 1000 samples.

The distribution of noise for each coordinate of the focal point were

| Image | Mean [pix/mm] | Deviation [pix/mm] | Minimum [pix/mm] | Maximum [pix/mm] |
|---|---|---|---|---|
| 1 | 0.35/0.21 | 0.18/0.11 | 0.10/0.06 | 0.67/0.41 |
| 2 | 0.29/0.18 | 0.13/0.08 | 0.09/0.06 | 0.46/0.28 |
| 3 | 0.40/0.25 | 0.13/0.08 | 0.17/0.10 | 0.55/0.35 |
| 4 | 0.20/0.12 | 0.13/0.08 | 0.04/0.02 | 0.43/0.26 |
| 5 | 0.28/0.17 | 0.18/0.11 | 0.05/0.03 | 0.50/0.31 |
| 6 | 0.22/0.14 | 0.15/0.09 | 0.03/0.02 | 0.43/0.26 |
| 7 | 0.30/0.18 | 0.16/0.10 | 0.06/0.04 | 0.56/0.34 |
| 8 | 0.28/0.17 | 0.10/0.06 | 0.17/0.10 | 0.43/0.26 |
| 9 | 0.23/0.14 | 0.10/0.06 | 0.08/0.05 | 0.39/0.24 |
| 10 | 0.24/0.15 | 0.11/0.07 | 0.10/0.07 | 0.45/0.28 |
| 11 | 0.28/0.17 | 0.10/0.06 | 0.17/0.11 | 0.46/0.28 |
| 12 | 0.38/0.23 | 0.16/0.10 | 0.21/0.12 | 0.71/0.43 |

Table 6.3: Segmentation error for large beads.

| Image | Mean [pix/mm] | Deviation [pix/mm] | Minimum [pix/mm] | Maximum [pix/mm] |
|---|---|---|---|---|
| 1 | 0.29/0.11 | 0.19/0.07 | 0.03/0.01 | 1.37/0.50 |
| 2 | 0.43/0.17 | 0.47/0.18 | 0.03/0.01 | 2.46/0.94 |
| 3 | 0.35/0.13 | 0.20/0.07 | 0.03/0.01 | 1.03/0.41 |
| 4 | 0.27/0.10 | 0.16/0.06 | 0.00/0.00 | 1.12/0.41 |
| 5 | 0.30/0.11 | 0.13/0.05 | 0.02/0.01 | 0.53/0.21 |
| 6 | 0.26/0.10 | 0.13/0.05 | 0.03/0.01 | 0.56/0.22 |
| 7 | 0.29/0.11 | 0.12/0.05 | 0.07/0.03 | 0.61/0.22 |
| 8 | 0.29/0.11 | 0.15/0.06 | 0.01/0.00 | 0.62/0.23 |
| 9 | 0.33/0.13 | 0.17/0.06 | 0.05/0.02 | 0.78/0.29 |
| 10 | 0.34/0.13 | 0.16/0.06 | 0.06/0.03 | 0.70/0.25 |
| 11 | 0.34/0.13 | 0.19/0.07 | 0.03/0.01 | 1.12/0.45 |
| 12 | 0.35/0.13 | 0.20/0.08 | 0.02/0.01 | 1.05/0.39 |

Table 6.4: Segmentation error for small beads.

| Coord. | t-test p-value | Confidence interval for mean value [mm] | | Deviation |
|---|---|---|---|---|
| x | 0.8843 | -0.0427 | 0.0368 | 0.6404 |
| y | 0.2782 | -0.0663 | 0.0191 | 0.6879 |
| z | 0.795 | -951.3191 | -948.9895 | 18.7704 |

Table 6.5: Focal point errors for segmentation noise of 0.5 pix.

| Coord. | t-test p-value | Confidence interval for mean value [mm] | | Deviation |
|---|---|---|---|---|
| x | 0.6651 | -0.065 | 0.1019 | 1.3442 |
| y | 0.9941 | -0.0884 | 0.0089 | 1.4285 |

Table 6.6: Focal point errors for segmentation noise of 1.0 pix.

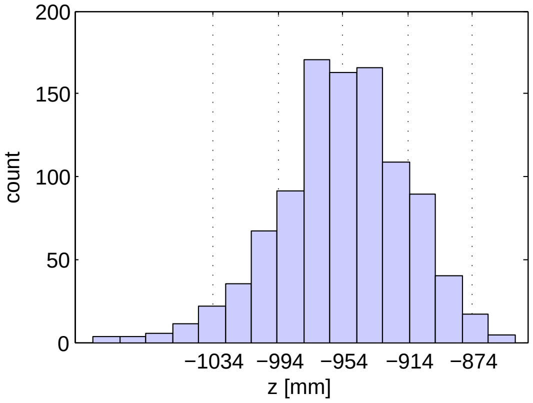

Figure 6.5: Focal distance distribution for 1.0 pix segmentation noise.

analysed using the Lilliefors test, checking whether it could be considered Gaussian, followed by a t-test. Results for the 0.5 pix noise are shown on Table 6.5, which shows that the focal point's $x$ and $y$ can be estimated with sub-millimetre precision and that the true mean for $z$ is contained within the confidence interval. The z-coordinate deviation was found to be 18.7704 mm, which is 2% of the true focal distance of 950 mm. All these results ensure that, at the current noise level, a very accurate estimation of the focal point can be obtained.

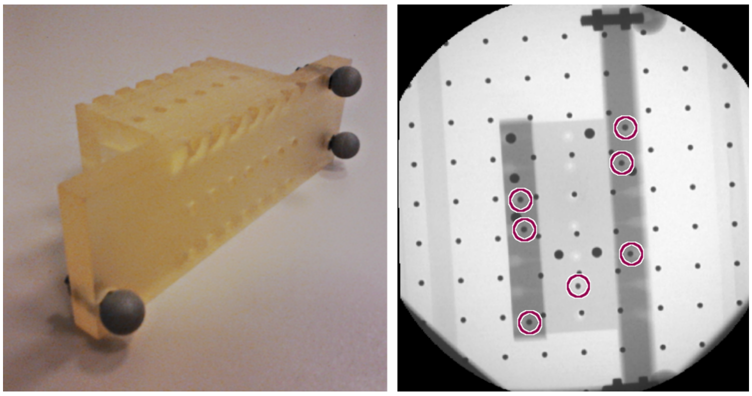

Figure 6.6: A photograph (left) and AP x-ray image (right) of the fabricated calibration phantom. The phantom beads' projections have been highlighted on the right image.

Results for the 1.0 pix noise are shown on Table 6.6. The $z$ coordinate is not shown as it null hypothesis of the Lilliefors test was rejected with p=0.00083 and, therefore, its distribution could not be considered Gaussian, as shown also on Figure 6.5. The observed distribution had a mean of -954.6648 mm and a deviation of 40.2108 mm, which is 4% of the true focal distance. The true values for $x$ and $y$ can be estimated at the current noise level although with slightly higher deviations –1.3442 and 1.4285 mm respectively– which still is a good result.

### 6.4.3 Registration using back-projection

To verify the validity of the proposed method we ran two final experiment to evaluate its capability to find locations of real-world points from their projections on the x-ray images. As seen on Chapter 5, this permits the spatial localisation of x-ray images and their focal points, forming the frame of reference required for 2D-3D registration.

For this purpose, we fabricated a calibration phantom object visible to the motion capture cameras and the c-arm. The phantom, shown on Figure 6.6, consists of a plastic structure built using rapid-prototyping techniques with seven embedded 1-mm steel spheres, distributed in an asymmetrical pattern. The latter was carefully chosen to permit the calculation of the relative pose between the c-arm and phantom by localisation of their

| Image | Pixel size [mm] | | Focal point $\mathbf{f}_D$ [mm] | | |
|---|---|---|---|---|---|
| | x | y | x | y | z |
| 0 (LAT) | 0.4006 | 0.3618 | -12.1085 | 1.8314 | -954.642 |
| 1 | 0.4008 | 0.3616 | -14.4358 | 2.9814 | -963.094 |
| 2 | 0.3991 | 0.3614 | -14.0972 | 2.3755 | -979.118 |
| 11 | 0.3998 | 0.3604 | -5.2517 | 1.967 | -974.021 |
| 12 | 0.4004 | 0.3614 | -2.6725 | 2.7349 | -974.725 |
| 13 | 0.4006 | 0.3616 | -2.4583 | 3.3062 | -945.354 |
| 14 | 0.4005 | 0.3614 | -1.9435 | 1.5287 | -953.367 |
| 15 | 0.3999 | 0.3623 | 0.0092 | 1.9005 | -968.392 |
| 16 | 0.3983 | 0.3640 | 1.6521 | 1.8459 | -975.438 |
| 17 | 0.4002 | 0.3619 | 2.9394 | 1.8398 | -975.602 |
| 18 (AP) | 0.4007 | 0.3614 | 3.7784 | 1.8734 | -1012.88 |

Table 6.7: Main calibration parameters of the x-ray images included in the first experiment.

projections. In addition, the phantom had three reflective markers to permit its tracking by the motion capture cameras. In the first experiment, described in this section, we obtained the real-world position of the phantom by back-projection of the beads segmented on the x-ray images. In the second experiment, we obtained the phantom's pose using the motion capture system.

A total of 19 x-ray images of the phantom were acquired using a Siemens Powermobil c-arm, with the calibration drum mounted on its intensifier. The phantom's centre was placed at an approximate distance of 350 mm, which a 36.08% of the c-arm's nominal focal distance of 970 mm. The c-arm was rotated around the phantom's long axis in steps of 5°, from 0° (LAT view, image number 0) to 90° (AP view, image number 18). Unfortunately, the operating room's table was not fully radiolucent and its metallic structure occluded large parts of images 3 to 10, making their calibration impossible. At the end, we were forced to discard these images from the experiment. Distortion was corrected from the remaining images using the proposed algorithm, calculating their corresponding projection matrices as well. The images' main calibration parameters –that is pixel size and focal point– are given on Table 6.7. Inspection of the table's data show that pixel sizes are estimated consistently and their theoretical aspect ratio of 11/10 –taken from the c-arm's manuals– is kept at all times. Focal points' coordinates are given in frame $D$, meaning that their magnitude in $z$ corresponds to the focal distance, which has an expected value of $970.6 \pm 17.85$ mm. This fits very well with the simulated bounds given on Section 6.4.2, but these results must be taken with some caution as the focal point is displaced due to the mechanical flexion of the c-arm. In fact, its $x$ coordinate –corresponding to the operating room's vertical axis– goes down as the c-arm approaches its lateral position. The mean value for the $y$ coordinate, less affected by flexion, is 2.199 mm and its observed deviation is 0.5695 mm, which is even lower than the simulated limits derived on Section 6.4.2. All this confirms the accuracy of the proposed method.

To calculate the relative pose between the phantom and drum –which means calculation of transform $\mathbf{T}_F^D$– we first segmented the phantom beads' projection on each image, denoted as $\mathbf{x}_P^i$, with $i = 1 \ldots 7$. Then, we defined a set of ground-truth points $\mathbf{x}_F^i$, which could be measured accurately from the fabrication blueprints. Transform $\mathbf{T}_F^D$ was parametrised with vector $\theta$, composed of its Euler angles and offset (please see Chapter 3 for details). Then, we iteratively minimised the sum of squared projection errors, defined as the distances between the segmented points $\mathbf{x}_P^i$ and the projections of $\mathbf{x}_F$. This translates into the following optimisation problem

$$\dot{\mathbf{T}}_F^D = \arg\min_{\theta} \sum_i |\mathbf{x}_P^i - \mathbf{P}\,\mathbf{T}_F^D(\theta)\,\mathbf{x}_F^i|^2 \qquad (6.11)$$

with $\mathbf{P}$ being the projection matrix estimated with the calibration algorithm proposed in this chapter, which remains fixed during the optimisation. Transform $\dot{\mathbf{T}}_F^D$ should be the one that registers the phantom's points to the projection geometry defined by matrix $\mathbf{P}$. Note that it is possible to find the transform using a subset of points $\mathbf{x}_P^i$ and $\mathbf{x}_F^i$, although the number of included point pairs must never fall below 3. In fact, it is advisable not to include all point pairs for registration, as doing so may over-fit available data and produce a transform unable to predict the location of points not included for its estimation. In our experiment, we used a subset of 4 point pairs for registration and the remaining 3 for the calculation of the Target Registration Error (TRE, please refer to Chapter 3 for details). The Fiducial Registration Error (FRE) was also calculated using the 4 point pairs used for estimation.

We registered the 11 x-ray images and measured their FRE and TRE,

| Image | RMS [pix/mm] | Mean [pix/mm] | Deviation [pix/mm] | Minimum [pix/mm] | Maximum [pix/mm] |
|---|---|---|---|---|---|
| 0 | 0.12/0.05 | 0.11/0.04 | 0.06/0.02 | 0.01/0.00 | 0.15/0.06 |
| 1 | 0.31/0.12 | 0.28/0.11 | 0.14/0.05 | 0.09/0.03 | 0.41/0.15 |
| 2 | 0.18/0.07 | 0.17/0.06 | 0.05/0.02 | 0.10/0.04 | 0.23/0.09 |
| 11 | 0.50/0.19 | 0.45/0.17 | 0.24/0.09 | 0.20/0.08 | 0.66/0.25 |
| 12 | 0.58/0.22 | 0.53/0.20 | 0.27/0.10 | 0.24/0.09 | 0.76/0.29 |
| 13 | 0.55/0.21 | 0.51/0.19 | 0.24/0.09 | 0.24/0.09 | 0.72/0.27 |
| 14 | 0.53/0.20 | 0.50/0.19 | 0.22/0.08 | 0.25/0.10 | 0.70/0.27 |
| 15 | 0.59/0.22 | 0.56/0.21 | 0.23/0.09 | 0.30/0.11 | 0.76/0.29 |
| 16 | 0.61/0.23 | 0.58/0.22 | 0.22/0.09 | 0.32/0.12 | 0.78/0.30 |
| 17 | 0.41/0.16 | 0.39/0.15 | 0.14/0.05 | 0.23/0.09 | 0.52/0.20 |
| 18 | 0.39/0.15 | 0.38/0.14 | 0.12/0.05 | 0.23/0.09 | 0.49/0.19 |
| Average | 0.43/0.16 | 0.40/0.15 | 0.18/0.07 | 0.20/0.08 | 0.56/0.21 |

Table 6.8: Projection FRE using a single x-ray image, first experiment.

| Image | RMS [pix/mm] | Mean [pix/mm] | Deviation [pix/mm] | Minimum [pix/mm] | Maximum [pix/mm] |
|---|---|---|---|---|---|
| 0 | 1.03/0.39 | 0.96/0.36 | 0.52/0.20 | 0.59/0.22 | 1.33/0.50 |
| 1 | 0.84/0.32 | 0.80/0.30 | 0.33/0.12 | 0.48/0.18 | 1.13/0.43 |
| 2 | 1.22/0.46 | 1.20/0.46 | 0.27/0.10 | 0.89/0.34 | 1.40/0.53 |
| 11 | 1.07/0.41 | 0.95/0.36 | 0.59/0.22 | 0.27/0.10 | 1.34/0.51 |
| 12 | 2.01/0.76 | 1.99/0.76 | 0.32/0.12 | 1.64/0.62 | 2.25/0.86 |
| 13 | 1.22/0.46 | 1.08/0.41 | 0.70/0.27 | 0.55/0.21 | 1.87/0.71 |
| 14 | 1.87/0.71 | 1.82/0.69 | 0.59/0.22 | 1.41/0.53 | 2.24/0.85 |
| 15 | 1.21/0.46 | 1.20/0.46 | 0.15/0.06 | 1.10/0.42 | 1.31/0.50 |
| 16 | 2.22/0.84 | 2.13/0.81 | 0.73/0.28 | 1.37/0.52 | 2.82/1.07 |
| 17 | 2.34/0.89 | 2.25/0.85 | 0.78/0.30 | 1.57/0.60 | 3.11/1.18 |
| 18 | 1.10/0.42 | 1.06/0.40 | 0.34/0.13 | 0.79/0.30 | 1.45/0.55 |
| Average | 1.46/0.56 | 1.40/0.53 | 0.48/0.18 | 0.97/0.37 | 1.84/0.70 |

Table 6.9: Projection TRE using a single x-ray image, first experiment.

shown on Tables 6.8 and 6.9. From the tables' data it can be seen that FRE has an expected value of 0.40 ± 0.18 pix (0.15 ± 0.07 mm) whereas TRE has an expected value of 1.40 ± 0.48 pix (0.53 ± 0.18 mm). Thus, sub-millimetre accuracy is obtained for FRE and TRE, ensuring that the method is capable to predict the location of real-world points which an accuracy level acceptable to surgical standards. These error levels are also good in comparison with other proposed methods. Livyatan et al. reported projection TRE with a mean of 0.92 mm and a deviation of 0.26 mm (Livyatan et al., 2002). Zheng and Zhang reported a projection TRE of 1.0 ± 0.4 pix which, using their reported pixel dimension of 0.355 mm, translates into a mean of 0.355 mm and a deviation of 0.142 mm (Zheng and Zhang, 2009). These authors, however, give very few details about their experimental methods, not even citing the used number of images used for their calculations, which casts some doubts about their remarkably low results.

Projection inherently loses information about a point's location along the x-ray's direction. Therefore, a minimum of 2 images acquired in different positions are needed to reconstruct a 3D point. To evaluate our method's capability for reconstruction, we defined all possible image pairs and reconstructed the positions of all phantom's beads using the point-based registration method introduced in Section 5.2.2. Then, we measured the errors between the reconstructed points' locations and the ground-truth ones taken from the phantom's design. Results for FRE and TRE on all image pairs are shown on Tables 6.10 and 6.11 respectively. Mean values for FRE and TRE were estimated to be 0.18 ± 0.12 mm and 0.77 ± 0.60 mm. These results demonstrate that the method is capable of accurate point reconstruction. In fact, 52 out of the total 55 image pairs have a TRE of less than 2 mm and 41 out of 55 pairs have sub-millimetre accuracy. Errors has a tendency to increase if the angular separation between images decreases. In fact, the worst error levels are found on image pairs with a separation of 5°. Removing these image pairs lowers the FRE to 0.15 ± 0.04 mm and the TRE to 0.59 ± 0.33 mm. Furthermore, removing all image pairs with separation of 10° or less reduced FRE to 0.14 ± 0.02 mm and TRE to 0.52 ± 0.26 mm. Our algorithm fares well compared with the one proposed by Livyatan et al. The authors evaluated their method using single images –therefore, without point reconstruction– although they reported a back-projection error of 0.59 ± 0.23 mm, defined as the minimum distance between the ground-truth point and the ray back-projected from the image

| Im | 1 | 2 | 11 | 12 | 13 | 14 | 15 | 16 | 17 | 18 |
|---|---|---|---|---|---|---|---|---|---|---|
| 0 | 0.33 | 0.21 | 0.14 | 0.14 | 0.13 | 0.13 | 0.14 | 0.14 | 0.09 | 0.09 |
| 1 | | 0.89 | 0.17 | 0.16 | 0.16 | 0.15 | 0.15 | 0.16 | 0.11 | 0.11 |
| 2 | | | 0.15 | 0.15 | 0.14 | 0.14 | 0.14 | 0.15 | 0.10 | 0.09 |
| 11 | | | | 0.23 | 0.16 | 0.14 | 0.16 | 0.16 | 0.13 | 0.12 |
| 12 | | | | | 0.18 | 0.16 | 0.17 | 0.17 | 0.14 | 0.14 |
| 13 | | | | | | 0.15 | 0.17 | 0.17 | 0.15 | 0.14 |
| 14 | | | | | | | 0.21 | 0.19 | 0.17 | 0.14 |
| 15 | | | | | | | | 0.19 | 0.28 | 0.20 |
| 16 | | | | | | | | | 0.56 | 0.29 |
| 17 | | | | | | | | | | 0.18 |

Table 6.10: Fiducial Registration Error (FRE) values observed in point reconstruction during the first experiment. Two x-ray images were used for all cases, with their numbers indicated by the top and leftmost values. All error measures are given in mm.

| Im | 1 | 2 | 11 | 12 | 13 | 14 | 15 | 16 | 17 | 18 |
|---|---|---|---|---|---|---|---|---|---|---|
| 0 | 1.22 | 1.31 | 0.44 | 0.52 | 0.44 | 0.23 | 0.30 | 0.56 | 0.60 | 0.33 |
| 1 | | 1.17 | 0.35 | 0.48 | 0.36 | 0.31 | 0.27 | 0.53 | 0.56 | 0.29 |
| 2 | | | 0.44 | 0.32 | 0.31 | 0.17 | 0.19 | 0.44 | 0.49 | 0.23 |
| 11 | | | | 2.18 | 0.64 | 0.83 | 0.79 | 0.96 | 0.91 | 0.38 |
| 12 | | | | | 1.67 | 0.60 | 0.61 | 0.73 | 0.76 | 0.39 |
| 13 | | | | | | 1.25 | 0.88 | 1.19 | 1.06 | 0.35 |
| 14 | | | | | | | 1.27 | 1.23 | 0.95 | 0.34 |
| 15 | | | | | | | | 2.29 | 1.24 | 0.52 |
| 16 | | | | | | | | | 0.89 | 1.33 |
| 17 | | | | | | | | | | 3.41 |

Table 6.11: Target Registration Error (TRE) values observed in point reconstruction during the first experiment. This table's structure is identical to the one of Table 6.10.

plane to the focal point (Livyatan et al., 2002). This error measure, although not equivalent to reconstruction error, should have similar values to the latter. Zheng and Zhang reported a back-projection error of 0.3 ± 0.1 mm only (Zheng and Zhang, 2009), although we have already written that we have doubts about their results due to the lack of experimental details given in their publication.

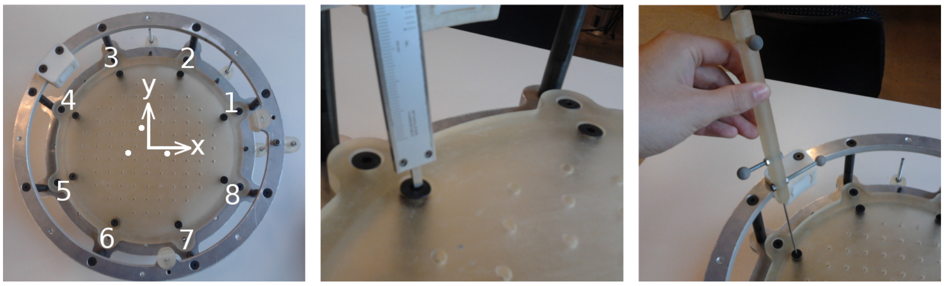

Figure 6.7: Determination of transform from frame $D$ to $X$. First, eight screws are identified following a counter-clockwise path from the proximal plate's $x$ axis (left). Then, their coordinates in $D$ are measured using the drum's blueprints and a calliper (centre). Finally, the same eight points are measured in $X$ using a calibrated probe (right) and the two point sets are registered, giving the transform as result.

### 6.4.4 Registration using motion capture

As written on Section 6.1, calibration drums are normally equipped with reflective markers to enable localisation of the c-arm in the operating room. Ultimately, this is used to detect the locations on which each x-ray image is acquired or, in terms of the definitions of Section 3.2, the finding of transforms $\mathbf{T}_{Pk}^{F}$ for each radiograph (for clarity, we will drop the $k$ index as we will normally work using a single image).

However, use of optical markers brings an additional problem: motion capture systems detect the centre of mass of the attached marker, not the drum's centre. In other words, this means that the optical tracker does not detect system $D$, instead it detects a new coordinate system denoted by letter $X$. Therefore, finding transform $\mathbf{T}_{P}^{F}$ requires passing first by frame $X$

$$\mathbf{T}_{P}^{F} = \mathbf{T}_{X}^{F}\mathbf{T}_{D}^{X}\mathbf{T}_{P}^{D} \tag{6.12}$$

In the equation above, $\mathbf{T}_{X}^{F}$ is given by the optical tracker and $\mathbf{T}_{P}^{D}$ was alculated on Equation 6.9. Only matrix $\mathbf{T}_{D}^{X}$ is needed to complete the calculation.

Transform $\mathbf{T}_{D}^{X}$ relates the coordinates of the drum's reflective spheres

| Image | Pixel size [mm] | | Focal point $\mathbf{f}_D$ [mm] | | |
|---|---|---|---|---|---|
| | x | y | x | y | z |
| 0 (LAT) | 0.4011 | 0.3624 | -8.9644 | 2.6626 | -971.845 |
| 1 | 0.4007 | 0.3620 | -8.0963 | 3.2980 | -960.197 |
| 2 | 0.4008 | 0.3615 | -8.7488 | 2.9986 | -967.047 |
| 8 | 0.4007 | 0.3616 | -3.5872 | 3.1344 | -969.772 |
| 9 | 0.4008 | 0.3615 | -2.5555 | 2.9555 | -963.967 |
| 10 | 0.4008 | 0.3616 | -1.2815 | 2.9316 | -970.017 |
| 11 | 0.4005 | 0.3615 | -0.0594 | 2.8217 | -962.515 |
| 12 | 0.4009 | 0.3614 | 1.4336 | 3.0685 | -964.857 |
| 13 | 0.4006 | 0.3616 | 3.6010 | 3.3533 | -955.192 |
| 14 | 0.4006 | 0.3617 | 3.9631 | 2.2782 | -979.76 |
| 15 | 0.4006 | 0.3617 | 4.8303 | 4.6861 | -1023.92 |
| 16 | 0.4005 | 0.3618 | 6.577 | 2.7826 | -979.176 |
| 17 | 0.4005 | 0.3618 | 7.5647 | 2.8575 | -979.221 |

Table 6.12: Main calibration parameters of the x-ray images included in the second experiment.

and its fiducial pattern, which remains invariant during the whole procedure. Therefore, calculation of this matrix is required only once and can be performed before the surgery. To do this, we followed the procedure shown on Figure 6.7. First, we identify eight screws on the drum's proximal plate, counted in counter-clockwise direction starting from the drum's $x$ axis. These are placed in accurate positions, with respect to frame $D$, due to the high precision of the machining process. Their $z$ coordinates of the screws' are measured using a calliper, taking into account that the $xy$ plane lies 5 mm below the plate's surface. Afterwards, we measure the screws' coordinates in frame $X$ with the help of a tracked pointer, also shown on Figure 6.7. The tool, previously calibrated using a procedure that will be described on Section 7.3, is detected by the motion capture system, which calculates its tip's positions with respect to frame $X$. After this, two sets of corresponding points are obtained, one measured in frame $D$ and the other in frame $X$. Finally, transform $\mathbf{T}_D^X$ is computed using Horn's algorithm for registration of point sets (Horn, 1987). The described procedure is able to compute the transform with a Fiducial Registration Error (FRE) between 0.6 and 1.0 mm.

| Image | RMS [pix/mm] | Mean [pix/mm] | Deviation [pix/mm] | Minimum [pix/mm] | Maximum [pix/mm] |
|---|---|---|---|---|---|
| 0 | 4.16/1.58 | 4.05/1.54 | 1.04/0.40 | 2.76/1.05 | 5.61/2.13 |
| 1 | 4.85/1.84 | 4.84/1.84 | 0.31/0.12 | 4.34/1.65 | 5.16/1.96 |
| 2 | 2.43/0.92 | 2.30/0.88 | 0.83/0.32 | 1.54/0.58 | 3.49/1.33 |
| 8 | 1.22/0.46 | 1.18/0.45 | 0.31/0.12 | 0.88/0.34 | 1.65/0.63 |
| 9 | 3.47/1.32 | 3.46/1.31 | 0.37/0.14 | 2.77/1.05 | 3.79/1.44 |
| 10 | 1.00/0.38 | 0.94/0.36 | 0.35/0.13 | 0.32/0.12 | 1.48/0.56 |
| 11 | 1.41/0.54 | 1.35/0.51 | 0.43/0.16 | 0.78/0.30 | 1.94/0.74 |
| 12 | 4.04/1.54 | 4.01/1.52 | 0.57/0.22 | 3.12/1.18 | 4.73/1.80 |
| 13 | 2.65/1.01 | 2.57/0.98 | 0.70/0.27 | 1.39/0.53 | 3.43/1.30 |
| 14 | 1.16/0.44 | 1.08/0.41 | 0.44/0.17 | 0.57/0.21 | 1.74/0.66 |
| 15 | 3.61/1.37 | 3.25/1.24 | 1.69/0.64 | 0.75/0.29 | 6.06/2.30 |
| 16 | 1.72/0.65 | 1.58/0.60 | 0.73/0.28 | 0.69/0.26 | 2.52/0.96 |
| 17 | 3.62/1.37 | 3.55/1.35 | 0.73/0.28 | 2.81/1.07 | 5.00/1.90 |
| Average | 2.72/1.03 | 2.63/1.00 | 0.65/0.25 | 1.75/0.66 | 3.58/1.36 |

Table 6.13: Projection TRE using a single radiograph, second experiment.

After completion of the calibration procedure described previously, we made a second imaging experiment following the protocol used on Section 6.4.3. Again, the calibration phantom was placed on the operating table and 19 images separated by 5° were acquired. For each image, its corresponding transform $\mathbf{T}_D^F$ was measured using the motion capture cameras to locate the x-ray imaging plane with respect to the operating room's coordinate $F$. Then, all images were calibrated and corrected using the algorithm described in the main sections of this chapter. Of the total 19 images, 6 had to be discarded due to obstruction of the operating room metallic structure or by failure to identify the drum's large beads. The images' pixel sizes and focal point are shown on Table 6.12. Again, it can be observed that pixel sizes are estimated with high consistency as well as the $y$ and $z$ coordinates of the focal point. The latter's displacement along $x$ due to the c-arm's flexion can be observed once again.

Table 6.13 shows the TRE for projections of real-world points $\mathbf{x}_F$ onto the planes of each x-ray image. Note that, as projections were not used for registration in this experiment (pose was determined with the motion capture cameras), it does not make sense to divide errors between FRE and TRE. As all phantom beads are considered target points, only TRE can be defined. Expected value for TRE was 2.63 ± 0.65 pix (1.00 ± 0.25 mm) and is, thus, higher than the ones shown on Tables 6.8 and 6.9 although still remains at acceptable levels. This increment is not surprising, as the use of motion capture adds additional sources of error such cameras' inaccuracies and the drum's calibration procedure described in the beginning of this section. In fact, the latter's error varies between 0.6 and 1.0 mm, which is much higher than the projection errors obtained in the first experiment.

| Im | 1 | 2 | 8 | 9 | 10 | 11 | 12 | 13 | 14 | 15 | 16 | 17 |
|---|---|---|---|---|---|---|---|---|---|---|---|---|
| 0 | 22,04 | 2,30 | 1,28 | 1,77 | 0,91 | 0,97 | 1,09 | 1,10 | 0,89 | 1,19 | 0,80 | 1,08 |
| 1 | | 17,71 | 1,82 | 1,24 | 1,72 | 1,43 | 2,11 | 1,20 | 1,19 | 1,15 | 1,13 | 1,24 |
| 2 | | | 0,91 | 1,65 | 0,49 | 0,62 | 0,98 | 0,82 | 0,52 | 0,92 | 0,48 | 0,77 |
| 8 | | | | 6,49 | 1,34 | 0,49 | 2,67 | 0,80 | 0,35 | 0,85 | 0,37 | 0,67 |
| 9 | | | | | 8,42 | 3,33 | 5,49 | 1,09 | 1,32 | 1,05 | 0,95 | 1,37 |
| 10 | | | | | | 2,30 | 3,93 | 1,87 | 0,68 | 1,39 | 0,62 | 0,60 |
| 11 | | | | | | | 9,68 | 1,54 | 0,69 | 1,54 | 0,51 | 0,87 |
| 12 | | | | | | | | 11,94 | 4,88 | 4,77 | 2,76 | 1,38 |
| 13 | | | | | | | | | 3,96 | 2,77 | 1,08 | 2,14 |
| 14 | | | | | | | | | | 3,88 | 0,63 | 1,78 |
| 15 | | | | | | | | | | | 4,21 | 4,58 |
| 16 | | | | | | | | | | | | 5,47 |

Table 6.14: Target Registration Error (TRE) values observed in point reconstruction during the second experiment. All values are in mm.

Following the first experiment's protocol, we also measured the TRE between the phantom beads' true locations and the the virtual points reconstructed from their projections on two x-ray images. Results for all possible image pairs are given on Table 6.14. The expected TRE was found to be 2.50 ± 3.56 mm, which is high and has an unacceptable deviation. However, as in the first experiment, it is evident that image pairs formed by radiographs with little angular separation have worse TRE. In fact all elements in the table's diagonal are greater than 2 mm (expect for the pair formed by images 2 and 8, which have an actual separation of 30°). Removing image pairs with 5° of separation lowers the expected value to 1.48 ± 1.12 mm, whereas removing the ones with 10° or less further reduces the expected TRE to 1.26 ± 0.91 mm. Once again, clinically acceptable error levels are attained if a sufficient angular separation is set between the image pair. These results, however, are higher than the ones obtained in the first experiment, in which motion capture was not used. Once again, it must be considered that the latter adds more sources of error, the most important being the calibration inaccuracies of the method for determination of Transform $\mathbf{T}_D^X$.

Comparison of results between the first and second experiment show clearly that registration of the c-arm to the reference coordinate frame is more accurate if direct back-projection is used, rather than relying on an motion capture system (although there is still room for improvement with the second). This, however, requires the use of special markers with a radio-opaque section, which should have a set of distinguishable features (such as beads of wires) so they could be easily segmented from the x-ray images. To be clinically acceptable, they should have a reduced size to fit into the c-arms field of view (typical values are in the order of 10 cms, which is not very large) and their mounting should have a minimal level of invasiveness, which is not easy in the human spine. Currently, researchers are working markers of this kind, such as the FTRAC originally developed by Jain et al. (Jain et al., 2005) and later used by Otake et al. for 2D-3D registration of phantom and femur images (Otake et al., 2012). Adaptation of these type of markers for spinal interventions raises new challenges which should be addressed in future research.

## 6.5 Closing remarks

We have presented a new automatic method for c-arm distortion correction and calibration, based on the use of an attachable drum consisting of parallel plastic plates with embedded radio-opaque beads. The proposed algorithm is fast, robust and accurate. Experimental results have shown that it has a segmentation error of 0.29 ± 0.14 pix (0.18 ± 0.08 mm) and 0.32 ± 0.19 pix (0.12 ± 0.07 mm) for the 5 mm and 3 mm drum's beads. These results are more accurate than other existing methods. In addition, the expected maximum segmentation error for large beads was found to be 0.5 pix, which permits accurate estimations of the c-arm's focal point with an expected deviation of 2% from the true focal distance.

The proposed method is also capable to accurately estimate the positions of points in space. We made a set of experiments using a phantom with embedded steel beads, of which a subset was used to register each radiograph position with respect to the phantom while the rest was used to asses the registration accuracy. In this scenario, a projection error of 0.53 ± 0.18 mm was obtained. Reconstruction of 3D points from their 2D projections was also possible with an observed error of 0.77 ± 0.60 mm, which can be effectively lowered to 0.52 ± 0.26 mm if a separation of 15° or more was kept between the images used for reconstruction. In all cases, sub-millimetre precision was attained. We also carried out a second experiment on which a motion capture system was used to determine the relative position between the image and phantom, rather than direct back-projection. In this case, we obtained projection errors of 1.00 ± 0.25 mm and reconstruction errors of 1.26 ± 0.91 mm. These results, although not completely contained in the sub-millimetric range, are acceptable for a surgical application. It is hypothesised that these values could be lowered if a more accurate calibration procedure between the drum and its attached optical markers was implemented. In all cases, present results demonstrate that the proposed method complies with surgical standards and could be effectively used as part of a CAS system.

## Chapter 7

# Prototype integration

In this chapter, we describe the integration of the different systems that compose the proposed robotic assistant. A completely functional pipeline was established, going from surgical planning to instrument placement by the robot, ensuring that the system is capable of accurately locate the patient in the operating room from the information contained in the surgical plan. Although it was not possible to include the 2D-3D registration in the prototype, this was replaced by a standard paired-point registration, based on probing a set of landmarks previously identified on the pre-operative scan. Despite that this has a lower accuracy than the 2D-3D registration method, overall accurate tool placement was attained.

This chapter begins giving brief descriptions of the used robot and motion capture systems. Then, a calibration procedure for the surgical tools will be presented, which is necessary to obtain Transforms $\mathbf{T}_T^H$ and $\mathbf{T}_T^E$ according to the definitions of Section 3.2. Afterwards, a procedure to find the transform going from the robot's base to the patient's optical marker –that is $\mathbf{T}_B^F$– will be described , completing the transform set required for the correct system operation (see Figure 3.1). Then, a correction procedure for transmission of coordinates from frame $M$ to $B$ will be presented, to solve ambiguities raised by the screws' axial symmetry. Afterwards, experimental methods and results will be presented, followed by the chapter's closing remarks.

## 7.1 Robot description

As written in this thesis' introduction, we used a PA-10 robot arm (Mitsubishi Heavy Industries Ltd., Kobe, Japan) for our system. This is a 7 DoF serial arm (a 6 DoF also exists) which offers high dexterity due to its redundant joint. It maximum load capacity is 98 N (i.e. 10 kg), can reach a distance of 1.03 m when fully extended and is able to move with a maximum speed of 1.55 m/s. Its 7 rotational joints are equipped with harmonic drives, which offer no backslash, good repeatability and are back-drivable. Joint positions are measured through resolvers at the joint output axes with a resolution of 0.000439° (Kennedy and Desai, 2005).

The PA-10 also offers an open architecture, permitting the development of custom control algorithms. In our case, we adapted it to work as a Collaborative Robot –or 'Cobot' for short– able to amplify the skills of the human operator, in our case, the surgeon. The cobot should be able to move synchronously with the surgeon when the latter dragged its end-effector. However, when approaching an area identified as critical, the cobot should oppose motion in that direction and move to a safer location. In a similar way, the cobot should be able to locate insertion points for instrumental –such as pedicle screws– and prevent the surgeon from moving away from their planned trajectories, providing stable and precise positioning. The surgeon, however, would always supervise the robot operation and take the necessary steps if an unexpected situation occurs. In this way, human and robot work cooperatively and obtain better results than the ones attainable by any of the two working on their own.

The previously described strategy requires the robot to know the patient's location accurately –which is, in summary, the main objective of this thesis– as well as a suitable control strategy to permit stable and synchronised motion with the one exerted by the surgeon. The second part –which falls outside the scope of this work– was implemented by means of an admittance control loop, which receives forces as inputs and outputs a response in form of acceleration, speed and position. Prevention of unwanted motions was obtained by means of virtual fixtures, which are protective margins placed around the screws' insertion points (Melo et al., 2012a; Melo et al., 2012b).

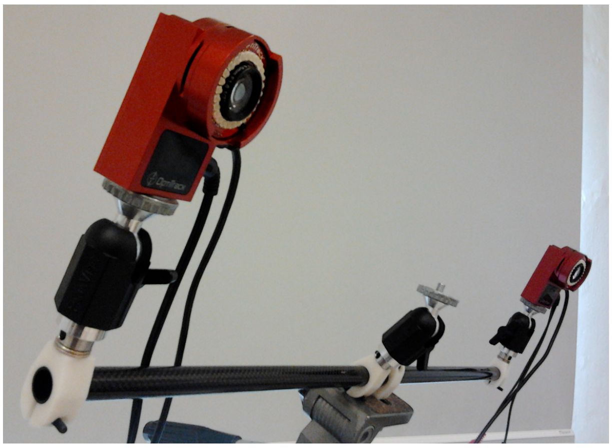

Figure 7.1: The OptiTrack motion capture system, configured with a stereo pair of V100:R2 cameras.

## 7.2 Motion capture system description

We chose the OptiTrack system (Natural Point Inc., Corvallis, Oregon, USA), which includes both hardware and software components for motion capture solutions used in a variety of markets ranging from film and gaming industries to biomechanical research. OptiTrack can be used with multiple cameras arranged in any pattern. In our research, we used a pair of V100:R2 cameras arranged in a stereo pair. These cameras offer high-speed sampling at 100 frames per second (FPS), which is considerable higher than the 60 FPS limit offered by other trackers such as the Polaris Spectra (Northern Digital Inc, Waterloo, Ontario, Canada) or the 48 FPS limit of the MicronTracker (Claron Technologies Inc., Toronto, Ontario, Canada). OptiTrack's cameras work by detection of infra-red light reflected on the surface of special spheres mounted on the tracked objects which, in our case, are the surgical tools, calibration drum (see Chapter 6) and one of the patient's vertebra. OptiTrack's accuracy depends on a variety of factors, namely the cameras' configuration, markers' arrangement on the trackable objects and their distance from the camera. Under normal circumstances –that is, the camera pair separated by 60 cms and placed 1 to 2 metres away from the trackable objects– we obtained back-projection errors in the order of 0.2 mm, identical to other commercially available trackers such as the Polaris (0.25 mm) or the MicronTracker (0.2 mm).

OptiTrack also includes the TrackingTools software for motion tracking of rigid objects, which comprises a standalone application as well as a programming library for C/C++. We used the latter to develop a custom application –named `trackingDataServer`– which served as an interface between OptiTrack and viewit-Spine, capturing motion tracking data and sending it to the rest of the system via the OpenIGTLink protocol (please refer to Appendix C for additional details).

## 7.3 Tool tip calibration

The motion capture system is unable to see the surgical tools' tips directly. In fact, it is only capable of seeing the reflective spheres mounted on a tool's handle and set its position on their centre of mass. Therefore, a calibration is required to locate a tool's tip with respect to the handle's coordinates which, in mathematical terms, translates into the finding of transform $\mathbf{T}_T^H$, where $T$ corresponds to the tip's coordinates and $H$ to the ones of the handle's markers.

We used a pivot calibration method proposed by Haidegger et al. to determine the relative position between the tool's tip and handle (Haidegger et al., 2008). Assuming that the tool is placed with its tip fitting inside a hole, let $\mathbf{x}_F$ be the unknown pivot point measured in coordinate system $F$ (i.e. patient's coordinate system). This point is actually the origin of coordinate system $T$, so it can be expressed as follows

$$\mathbf{x}_F = \mathcal{T}_H^F(\mathcal{T}_T^H(\vec{0})) \tag{7.1}$$

As shown on Figure 7.2, Transform $\mathcal{T}_T^H$ involves no rotation and only has an offset denoted by $\mathbf{p}$, corresponding to the distance between the tip and the handle markers' centre of mass. Taking this into account and replacing $\mathcal{T}_H^F$ by its rotation and offset, denoted by $\mathbf{R}$ and $\mathbf{s}$ respectively, gives the following expression

$$\mathbf{x}_F = \mathbf{R}\mathbf{p} + \mathbf{s} \tag{7.2}$$

Re-arranging the equation above yields

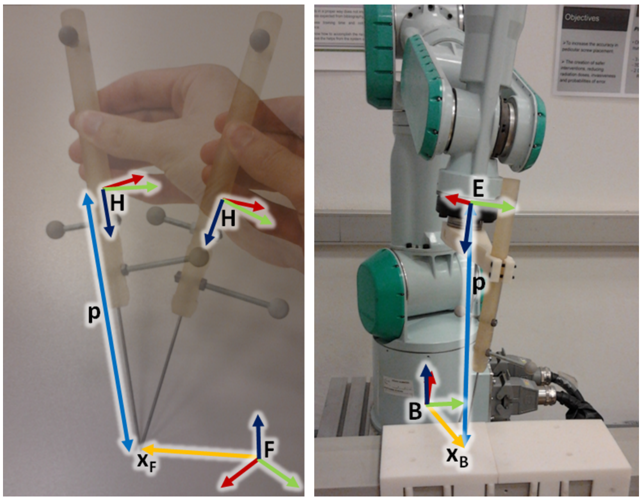

Figure 7.2: Left: pivot calibration procedure. Multiple measurements of the handle's markers are taken rotating the tool but keeping its tip in a fixed position. Transform equations are formed to obtain the values of $\mathbf{x}_F$ and $\mathbf{p}$ which remain constant. The tip's coordinate frame $T$ corresponds to a translation of frame $H$ along vector $p$ with no rotations. Right: analogous procedure to find the tip's position with respect to the robot's end-effector frame $E$.

$$\mathbf{R}\mathbf{p} - \mathbf{x}_F = -\mathbf{s} \tag{7.3}$$

The previous expression can be written as a linear system with 6 variables and 3 equations, like

$$\begin{bmatrix} \mathbf{R} & -\mathbf{I} \end{bmatrix} \begin{bmatrix} \mathbf{p} \\ \mathbf{x}_F \end{bmatrix} = -\begin{bmatrix} \mathbf{s} \end{bmatrix} \tag{7.4}$$

with $\mathbf{I}$ being the 3-by-3 identity matrix.

If additional measures are taken rotating the tool and keeping its tip in a fixed position, we obtain multiple measures of $\mathbf{R}$ and $\mathbf{s}$ but constant values of $\mathbf{x}_F$ and $\mathbf{p}$. This happens as the tool tip remains in place and its relative distance to the marker does not change. Stacking the equations above for all measurements yields the following linear system, over-determined if more than two measurements are taken

| | Mean | Deviation | Minimum | Maximum |
|---|---|---|---|---|
| FRE | 0.539 | 0.163 | 0.245 | 0.860 |
| TRE | 0.610 | 0.155 | 0.361 | 0.864 |

Table 7.1: Pivot calibration errors. All values are given in mm.

| | Mean | Deviation | Minimum | Maximum |
|---|---|---|---|---|
| FRE | 0.451 | 0.181 | 0.152 | 0.704 |
| TRE | 0.878 | 0.188 | 0.621 | 1.274 |

Table 7.2: Robot tool calibration errors. All values are given in mm.

$$\begin{bmatrix} \mathbf{R}^1 & -\mathbf{I} \\ \mathbf{R}_2 & -\mathbf{I} \\ \vdots & \vdots \\ \mathbf{R}_N & -\mathbf{I} \end{bmatrix} \begin{bmatrix} \mathbf{p} \\ \mathbf{x}_F \end{bmatrix} = - \begin{bmatrix} \mathbf{s}_1 \\ \mathbf{s}_2 \\ \vdots \\ \mathbf{s}_N \end{bmatrix} \tag{7.5}$$

The system in Equation 7.5 is solved using the Singular Value Decomposition algorithm, which obtains its least-squares optimal solution. Its goodness of fit is evaluated by the residual error, defined as

$$\epsilon = \sqrt{\frac{\sum_{k=1}^{N} |(\mathbf{R}_k\mathbf{p} + \mathbf{s}_k) - \mathbf{x}_F|^2}{N}} \tag{7.6}$$

which is analogous to the FRE, as it measures the goodness of fit with the same data used to estimate the transform. We implemented the algorithm above using Eigen 3.0.2 and integrated it to our software suite. To evaluate the algorithm's performance we executed 30 calibrations placing the tracked tool on 8 different poses. Of them, half were used for calibration and estimation of the FRE, while the remaining ones were used to estimate the TRE. Results are presented on Table 7.1, which show that expected value for the FRE is 0.539 ± 0.163 mm whereas TRE has an expected value of 0.610 ± 0.155 mm. No observed errors were above 1 mm, with the maximum being 0.86 and 0.864 for the FRE and TRE respectively.

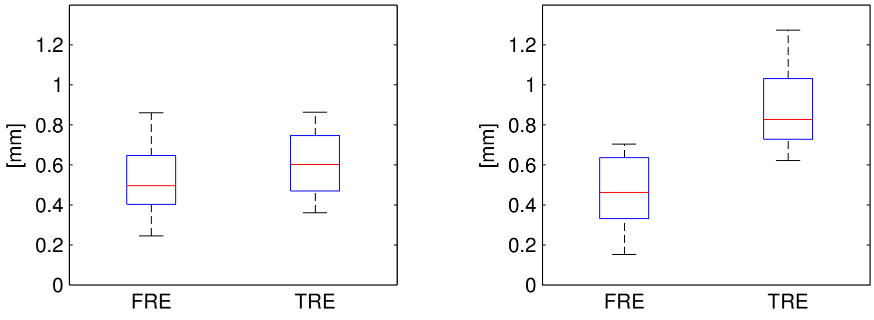

(a) Manual (b) Robot

Figure 7.3: FRE and TRE for the manual tool calibration (a) and the same procedure carried out with the tool mounted on the robot's end-effector (b). In these plots, and all subsequent ones used in this chapter, the boxes' middle red line marks the sample's median, whereas their lower and upper bounds correspond to the 25th and 75th percentiles respectively. Whiskers extend to the whole range of data not considered as outliers, while the latter are marked individually as crosses (no outliers are present in the plots above).

In Chapter 3 we mentioned that it is necessary to known the tip's position not only with respect to $H$, but also with respect to the robot end-effector's frame $E$, denoted by Transform $\mathbf{T}_T^E$. We implemented an analogous procedure to obtain this transform by taking measures of different robot poses, but keeping the tool's tip on a fixed position marked by a hole drilled on a plate. Observed calibration errors are summarised on Table 7.2 and also on Figure 7.3, which shows that FRE has an expected value of 0.451 ± 0.181 mm whereas TRE has an expected value of 0.878 ± 0.188 mm, the latter being slightly higher than the one observed for the manual calibration. This error increase may have been caused by the model used for resolution of the PA-10 kinematics, which uses fixed values for the robot's link lengths without taking into account possible deviations from the values published on its manual. Also, additional errors are caused by the difficulty of placing the robot on multiple positions around a single pivot, which had to be done manually. To solve this problem, a force-sensing strategy could be implemented, which could automatically place the robot tool in the bottom of conical drilled holes (Kazanzides et al., 1992). Thus,

| | Mean | Deviation | Minimum | Maximum |
|---|---|---|---|---|
| FRE | 0.704 | 0.109 | 0.524 | 0.896 |
| TRE | 0.781 | 0.120 | 0.594 | 1.001 |

Table 7.3: Robot base registration errors. All values are in mm.

the robot should only need to be taken to the cone's neighbourhood –on different orientations– and it would automatically descend to its bottom, which could be used as a pivot for the calibration procedure. To further increase accuracy, the robot's direct kinematics algorithm could be improved, taking into account factors such as joint offsets and non-ideal link lengths. These works, however, fall outside the scope of this thesis.

As a closing remark, it must be noted that these two calibrations can be made pre-operatively and remain constant during the whole surgery. Thus, it is not needed to update them during the intervention.

## 7.4 Robot base registration

Determination of screws' insertion points in robot coordinates requires finding of transform $\mathbf{T}_B^F$, which takes points from the robot base's frame $B$ to the patient's frame $F$. This, differing from the calibrations presented previously, must be obtained intra-operatively by a registration procedure.

Registration is carried out by moving the robot's tool around multiple points the workspace, measuring its tip's coordinates with respect to $F$ and $B$, simultaneously using the cameras and robot's direct kinematics. It must be noted that, to make points correspondent, the tool's tip calibration with respect to $H$ and $E$ must have been obtained in advance. At least three point-pairs are required, which are later registered using Horn's algorithm, already cited in this thesis (Horn, 1987).

The registration performance was evaluated acquiring multiple point pairs in a 125 by 90 by 50 mm space. Seven pairs were used to calculate the registration and evaluate its FRE, whereas eight were used to estimate its TRE. Results for a sample of 15 registrations are given on Table 7.3. From the table's data it can be seen that FRE and TRE have similar means and standard deviations. Both measures of error have slightly high values, with FRE and TRE estimated to be 0.704 ± 0.109 mm and 0.781 ± 0.120 mm respectively. As written in Section 7.3, we hypothesise these error indices could be lowered by improving the direct kinematics algorithm used by the current robot controller, taking into account joint offsets and non-ideal link lengths (Haidegger et al., 2008). In addition, the effects of different point pairs sampling patterns should be studied to improve the registration's accuracy. Empirically, we observed that point pairs should be acquired very close to the surgical area and spanning its three dimensions as much as possible. Failure to do so produced registrations with abnormal FRE values, in the order of 4 to 6 mm, which are unacceptable in a surgical application.

## 7.5 Correction of screws' normal vectors

A screw is symmetrical around its axis and can be completely defined by a point and a vector. However, vectors perpendicular to the axis are ambiguous, and this brings a problem when transferring a screw's pose into the robot base's frame of reference. If this not done carefully, the robot can be ordered to reach a position requiring unnecessary twisting of its joints, obstructing the surgeon access to the surgical area or, even worse, colliding with the patient. To solve this problem, we developed a method to correct the screws' normal vectors which is described below.

Let point $\mathbf{x}_M$ be a screw's position and normalised vector $\mathbf{a}_M$ its main axis, both measured with respect to the pre-operative image's frame of reference $M$. Also, let us assume that transform $\mathcal{T}_M^F$ is known, which takes coordinates from $M$ into the patient's frame $F$. Assuming too that $\mathcal{T}_F^B$ has been calculated using the method described in Section 7.4, it becomes possible to obtain transform $\mathcal{T}_M^B$, which takes coordinates from $M$ into the robot base's frame of reference $B$.

$$\mathcal{T}_M^B(\mathbf{x}_M) = \mathcal{T}_F^B(\mathcal{T}_M^F(\mathbf{x}_M)) \tag{7.7}$$

Let $\mathbf{x}_B$ and $\mathbf{a}_B$ be the screw's insertion point and axis measured with respect to frame $B$. Note that $\mathbf{a}_B$ is a vector, thus only rotations are applied during transformations.

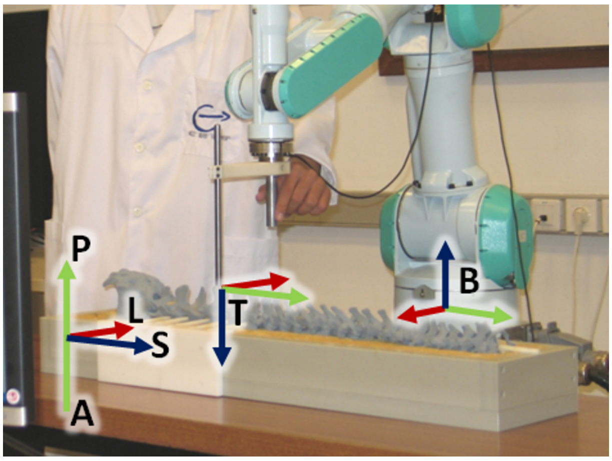

Figure 7.4: The robot's 'natural' pose for screw insertion, showing frames $T$ and $B$. Note how the $x$ (red), $y$ (green) and $z$ (blue) axes are located with respect to the patient's axes, set by the standard LPS (Left-Posterior-Superior) frame.

$$\mathbf{x}_B = \mathcal{T}_M^B(\mathbf{x}_M) \tag{7.8}$$

$$\mathbf{a}_B = \mathcal{T}_M^B(\mathbf{a}_M) \tag{7.9}$$

Let us assume that the patient lies in the prone position and the robot is mounted on the floor besides him or her. In this case, the robot's natural position for screw insertion would be the one shown on Figure 7.4, with frame $T$'s $x$, $y$ and $z$ axes pointing to the patient's Left, Superior and Anterior axes respectively. On the other hand, frame $T$'s axes expressed in terms of frame $B$ would correspond to the latter's $-x$, $y$ and $-z$.

A screw's axis matches $T$'s $z$ and, therefore, it is expected to be close to frame's $B$'s $-z$ axis. To prevent unnecessary rotation of the robot's joints, we expect the screw's $x$ and $y$ axes to be as similar as possible to frame $B$'s $-x$ and $y$ axes. Thus, the rotation matrix that goes from the screw's frame to $B$ should be similar to this

$$\mathbf{R} = \left[\begin{array}{cc|c} -1 & 0 & \\ 0 & 1 & \mathbf{a}_B \\ 0 & 0 & \end{array}\right] \tag{7.10}$$

However, the expression above is not a valid rotation matrix, as its columns do not form an orthonormal basis. However, we can use Gram-Schmidt normalisation process to obtain the closest rotation matrix, keeping its third column untouched (Strang, 2006). Let vectors $\mathbf{n}_B$ and $\mathbf{b}_B$ be the first and second columns of the matrix above. Also, let $\hat{\mathbf{n}}_B$ and $\hat{\mathbf{b}}_B$ a new pair of vectors which form an orthonormal basis with $\mathbf{a}_B$, obtained following the procedure below

$$\tilde{\mathbf{n}}_B = \mathbf{n}_B - (\mathbf{n}_B \cdot \mathbf{a}_B)\mathbf{a}_B \tag{7.11}$$

$$\hat{\mathbf{n}}_B = \frac{\tilde{\mathbf{n}}_B}{|\tilde{\mathbf{n}}_B|} \tag{7.12}$$

$$\tilde{\mathbf{b}}_B = \mathbf{b}_B - (\mathbf{b}_B \cdot \mathbf{a}_B)\mathbf{a}_B - (\mathbf{b}_B \cdot \hat{\mathbf{n}}_B)\hat{\mathbf{n}}_B \tag{7.13}$$

$$\hat{\mathbf{b}}_B = \frac{\tilde{\mathbf{b}}_B}{\left|\tilde{\mathbf{b}}_B\right|} \tag{7.14}$$

Note that $\mathbf{a}_B$ is assumed to be normalised, thus division by its norm is not needed. After the procedure written above, the new rotation matrix would be formed by concatenation of the new trio of orthonormal vectors

$$\mathbf{R} = \left[\ \hat{\mathbf{n}}_B \ \middle|\ \hat{\mathbf{b}}_B \ \middle|\ \mathbf{a}_B\ \right] \tag{7.15}$$

## 7.6 Overall positioning accuracy

To evaluate the overall system's accuracy we made an experiment ordering the robot to move to a set of points with positions known in advance and then measuring its positioning errors. For this purpose, we manufactured a phantom consisting of a plastic plate with 15 holes drilled on precise locations, using rapid-prototyping technology. Afterwards, we made a CT scan of the plate using a Siemens Somaton Definition scanner at the highest possible resolution, setting a pixel size of 0.488 by 0.488 by 0.3 mm. Afterwards, the holes' entry points were located on the CT image and their locations recorded. According to the definitions of Section 3.2, we will refer to these points as $\mathbf{x}_M$.

We then fabricated two surgical tools equipped with reflective markers, like the ones shown on Figure 7.2. Both tools were calibrated using the procedure presented on Section 7.3. One was reserved for manual uses and calibrated manually (FRE: 0.23 mm, TRE: 0.36) while the other was calibrated while mounted on the robot's end effector (FRE: 0.54 mm, TRE: 0.63 mm). Afterwards, we attached a reference marker to the phantom and performed the registration with the robot's base presented on Section 7.4 to determine Transform $\mathbf{T}_B^F$ (FRE: 0.55 mm, TRE: 0.71 mm). After registration, the plate was kept in a fixed position to keep its relative distance with the robot's base.

After completion of the registrations described above, only $\mathbf{T}_F^M$ remains unsolved for complete determination of all the system's transforms. Ideally, the 2D-3D registration algorithm presented on Chapter 5 should be used for this purpose but, as it was not possible, we opted for a standard paired-point registration. Using the calibrated manual tool, we probed the even points on the plate's surface, acquiring their coordinates on Frame $F$. These points were registered to frame $M$ using Horn's algorithm, which has been cited already in this work (Horn, 1987). The 7 points used for registration were also used for calculation of the registration's FRE, while the remaining 8 were reserved for calculation of its TRE.

After each registration, we loaded a surgical plan in viewit-Spine, containing the phantom's CT scan and multiple target points placed on its orifices. Then, we ordered the robot to move to the ones corresponding to the 8 points not used for calculation of Transform $\mathbf{T}_F^M$. Then, viewit-Spine executed the normal-correction strategy presented on Section 7.5 and transmitted its position and orientation to the robot via the OpenIGTLink interface. The robot, after reception of the target point, automatically moved to it and activated a virtual fixture along the the tool's axis, permitting us to manually move it but without deviating from its planned trajectory. To avoid accidental damage to the phantom, all transmitted points were placed 20 mm above the plate's surface.

For the 8 points, we measured its coordinates $\mathbf{x}_B$ and $\mathbf{x}_F$ measured with the robot's direct kinematics and the motion capture system respectively. Then, we transformed these points to frame $M$ as written below

| | Paired-point registration | | | |
|---|---|---|---|---|
| Experiment | FRE | TRE | TRE ($\mathbf{x}_B$) | TRE ($\mathbf{x}_F$) |
| 1 | 0.40 | 0.42 | 1.62 | 1.73 |
| 2 | 0.69 | 0.92 | 1.84 | 2.06 |
| 3 | 0.50 | 0.70 | 1.29 | 2.17 |
| 4 | 0.40 | 0.60 | 1.51 | 1.95 |
| 5 | 0.38 | 0.51 | 1.66 | 1.70 |
| 6 | 0.33 | 0.41 | 1.54 | 1.96 |
| 7 | 0.27 | 0.39 | 2.06 | 1.51 |
| 8 | 0.52 | 0.60 | 2.18 | 1.70 |
| 9 | 0.36 | 0.55 | 2.14 | 1.63 |
| 10 | 0.47 | 0.45 | 1.95 | 1.81 |
| 11 | 0.44 | 0.57 | 2.00 | 1.86 |
| 12 | 0.43 | 0.44 | 2.26 | 1.82 |
| Mean | 0.43 | 0.55 | 1.84 | 1.82 |
| Deviation | 0.11 | 0.15 | 0.31 | 0.19 |
| Minimum | 0.27 | 0.39 | 1.29 | 1.51 |
| Maximum | 0.69 | 0.92 | 2.26 | 2.17 |

Table 7.4: Overall positioning errors for all 12 experiments, with their observed mean, standard deviation, minima and maxima.

$$\mathbf{y}_M = \mathbf{T}_F^M \mathbf{T}_B^F \mathbf{x}_B \tag{7.16}$$

$$\mathbf{z}_M = \mathbf{T}_F^M \mathbf{x}_F \tag{7.17}$$

TRE were calculated for measurements in $B$ with the distances between $\mathbf{x}_B$ and $\mathbf{y}_B$. Analogously, the same error index was measured for $F$ with the distances between $\mathbf{x}_B$ and $\mathbf{z}_B$.

Twelve experiments were performed and their positioning results are summarised on Table 7.4 and also on Figure 7.5. Observation of the table's data shown that TRE measured from $B$ and $F$ have similar expected values: TRE measured from $B$ has an expected TRE of 1.84 ± 0.31 mm while the same error index measured from $F$ has an expected value of 1.82 ± 0.19 mm.

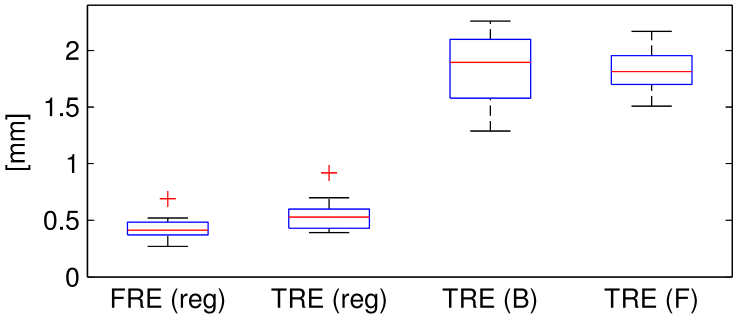

Figure 7.5: Overall positioning errors. This figure's data corresponds to the one presented on Table 7.4. For an explanation of the plot marks refer to Figure 7.3.

The first conclusion that can be drawn from the table above is that these error levels are within the range admitted for surgical applications, but only by a slight margin. As written on Chapter 2, most robotic systems for spinal surgery have reported error levels below 2 mm, an upper threshold adopted by various clinical researchers. Our results are, therefore, within the acceptable range but need to be taken to lower levels. A possible improvement would come from replacement of the registration algorithm used in the determination of $\mathbf{T}_F^M$. In the experiments, this had a mean TRE of 0.55 mm, whereas the sample 2D-3D registration algorithm presented in Chapter 5 had a mean TRE of 0.37 mm. As written in the same chapter, this error level is comparable to the pixel size of the used data and further improvements are unlikely. Therefore, we would expect to reduce registration errors from 0.55 to 0.37 at most. This, of course, is a slight improvement, so we do not expect this single change to reduce the observed positioning errors drastically. As written many times before in this chapter, we would expect accuracy to improve if more exact model of the PA-10 direct kinematics was used and the same can be repeated here, as it would impact directly positioning directly. Another factor that needs to be taken into account is Transform $\mathbf{T}_B^F$. Calculation of this matrix has a mean TRE of $0.878 \pm 0.188$ mm (and the one used in all experiments had a TRE of 0.71 mm), the higher of all used in the experiments. In addition, $\mathbf{T}_B^F$ remains being valid only if no relative motion occurs between the patient and robot. Great care was taken during the experiments to avoid this but, still, small motions could have occurred and remain undetected while still affecting the results. A naive solution would be to develop new fixation hardware to prevent relative motions between patient and robot, but this would not be a clinically acceptable solution. A different –and more realistic– solution would be visual servoing, that is, control of the PA-10 using visual feedback. In fact, current robot control is open-loop: when the robot moves to a target point it follows a model set by the registrations, which remain constant during the intervention. Thus, the accuracy of the robot positioning depends directly on the model's accuracy and the absence of perturbations. Using visual servoing would close the feedback channel and provide all the advantages offered by control theory. This, however, is a work that would require a considerable amount of time for its development and, unfortunately, could not be addressed in this thesis.

## 7.7 Closing remarks

In this chapter, we have presented the first working prototype of the robotic system proposed in this thesis. The integration of its individual components was presented, as well as the required procedures to complete all the registration required for its operation. In addition, the first experimental results on phantoms were presented, showing that the current prototype is able to position the surgical tools with errors of $1.84 \pm 0.31$ mm and $1.82 \pm 0.19$ mm if measured via the robot's kinematics or the used motion capture system. These error levels are sufficient for surgical practice, but further improvements would be desirable. A more exact model of the robot's direct kinematics, integration with the 2D-3D registration algorithm presented on Chapter 5 and implementation of visual servoing would be valuable additions that should be addressed in future works.

## Chapter 8

# Conclusions

## 8.1 Conclusions

This work has studied imaging processing techniques, aimed at the development of a robotic assistant for spinal fusion surgeries.

A fully featured surgical planning application –viewit-Spine– has been presented in this work, providing surgeons a powerful but yet easy-to-use piece of software. This serves also as core of the proposed system, as it also implements the functionality required for the execution stage of the intervention, namely registration of 2D-3D data, surgical tool tracking and transmission of commands to the surgical robot. In addition, viewit-Spine has given birth to a new software framework, named viewitLib, which has been already been deployed in multiple medical applications, such as a craneotomy simulators and a planner for implantation of hearing aids.

A new software library has been written for the registration of 2D-3D data, providing a much needed extension of the widespread ITK library. Originally, ITK was unable to handle registrations of a 3D dataset to multiple 2D images and also ignored the geometrical orientations of the latter. Both problems were effectively solved with the proposed software, which permits the implementation of efficient registration algorithms without having to write their code from scratch. Its was also demonstrated that the library, in its current form, is able to implement applications for registration of 3D CT data to 2D x-ray images with sub-millimetre accuracy (mean TRE of 0.37 mm), capable of matching datasets with misalignments of up to 6 mm and an overall success rate of 71%. These figures are in line with other modern registration methods, although there is still room for improvements in terms of robustness.

The problems of c-arm calibration and distortion correction were addressed in this work, proposing a new algorithm for their solution. The latter combined accurate segmentation and calculation of the c-arm's intrinsic and extrinsic parameters. In realistic conditions, it was observed that the proposed method achieved sub-millimetre accuracy in segmentation –overcoming other existing methods– and was able to estimate the c-arm's focal distance with an error of only 2% of its true value. Furthermore, the method was successfully tested in the reconstruction of 3D points from their 2D projections segmented from 2 x-ray images, attaining levels of error below a single millimetre. Accurate reconstructions were also possible using motion capture cameras to determine the c-arm's location, although errors increased to the range of 1 to 2 mm, which are still considered suitable for a medical application.

Finally, the first working prototype of the proposed robotic system was implemented, developing all necessary hardware and software to connect all its individual components. This prototype was tested on a positioning experiment, in which the robot was commanded to move automatically to a set of orifices of a plastic phantom. Overall positioning errors, measured via the robot's kinematics, was found to be 1.84 ± 0.31 mm, whereas the same errors measured via the motion capture cameras was 1.82 ± 0.19 mm. These values demonstrate that the prototype, in its current form, is able to work with the accuracy levels demanded by surgical practice, although additional improvements are required.

## 8.2 Future work

The following research lines are open for continuation of this work:

- The ray-casting algorithms used in the 2D-3D registration framework require a more efficient implementation, as they are currently too slow for clinical use. This problem has a large amount of redundant operations, thus good results may be obtained by parallelisation techniques such as multi-threading or the use of Graphical Processing Units (GPU).
- The capture range of the 2D-3D registration algorithms must be

improved. Nowadays, 2D-3D registration algorithms have reached levels of error similar to the voxel sizes of their data, thus further improvements may not be possible. However, improvement of their capture range remains an open issue. As 2D-3D registration problems have proven to be very specific, a tailor-made solution of registration in the spinal column should be sought rather than development of one capable of registering many different organs. A possible way to explore would be the registration of multiple vertebrae simultaneously, rather than the individual registration with 6 DoF developed for this thesis. It may be possible to define a registration on which all vertebrae could be transformed at the same time, taking care that they motion is restricted and they cannot move too far away from their neighbours.

- An analytical formula for the similarity metric's gradient should be implemented for 2D-3D registration. We observed that the latter's convergence is improved by adding gradient information but, unfortunately, it must be approximated by finite differences. This heavily affects the registration performance, so a more efficient solution should be sought by using an analytical function.

- The proposed library for 2D-3D registration could be extended to include back-projection and reconstruction, as currently only projection is supported.

- Direct projection of the moving image's gradient should be included in the 2D-3D registration library. Currently, the library only supports projection of DRRs, on which gradients are later computed by metrics such as Gradient Difference and Normalised Gradient Correlation. A more efficient approach would be an initial calculation of the 3D image gradients –which should be done only once– followed by their direct projection onto the x-ray planes. In this way, it would not be necessary to compute the DRRs' gradients on each iteration.

- Experiments carried out in this thesis show that accurate registration between a c-arm and the operating room's frame is possible by segmentation of radio-opaque features of specially-designed markers. Fabrication and testing of a marker of this kind –specifically designed for the requirements of spinal surgery– would be a research line deserving additional work.

- The overall positioning errors of the tested robotic prototype need improvement as they, although found to be sufficient, are just below the accepted threshold. It was observed that error measures involving the robot were higher than the ones measured with the motion capture system alone, which have lead us to conclude that the current direct kinematics model needs improvement. A possible strategy would be to extend it and consider additional factors such as joint offsets and non-ideal link lengths. In addition, visual servoing could be implemented to add an additional feedback channel and further reduce overall positioning errors.

- A more through testing of the integrated robotic system is required. This thesis' main objective was the implementation of the image processing techniques required for the whole system, while the robotic control strategies were developed in parallel. Thus, integration of both research lines was only reached at the end of this work's assigned period, permitting only the proof-of-concept of the whole system. It is necessary to fully integrate the robot and the 2D-3D registration and do a more thorough testing of the whole prototype, using animals or cadavers, to check if the sought objectives –that is, minimal invasiveness, reduced radiation, improved visualisation and higher accuracy– can be effectively attained.

## Appendix A

# Generated Publications

## Journals

Bertelsen, A., Melo, J., Sánchez, E., and Borro, D. “A review of surgical robot for spinal interventions”. *The international journal of medical robotics and computer assisted surgery*, (Accepted for publication).

Melo, J., Bertelsen, A., Borro, D., and Sánchez, E. “Nuevo asistente robótico para cirugía: arquitectura y algoritmos de control”. *Dyna Ingeniería e Industria*, Vol. 87, N. 3, pp. 647–654. 2012.

Bertelsen, A. and Borro, D. “2D-3D Registration with Multiple Fixed Images”. *The Source*, Vol. 20, pp. 13–15. 2012.

Bertelsen, A. and Borro, D. “An ITK-Based Framework for 2D-3D Registration with Multiple Fixed Images”. *Insight Journal*, 2011.

## Conferences

Bertelsen, A., Echeverría, M., Gómez, E., and Borro, D. “Distortion correction and calibration of intra-operative x-ray images using a constrained DLT algorithm”. In *Actas del XXX Congreso Anual de la Sociedad Española de Ingeniería Biomédica (CASEIB 2012)*. San Sebastián, Spain. 2012.

Buchart, C., Bertelsen, A., and Borro, D. “viewitLib - A framework for the development of software for medical images visualization”. In *Actas del XXX Congreso Anual de la Sociedad Española de Ingeniería Biomédica (CASEIB 2012).* San Sebastián, Spain. 2012.

Bertelsen, A., Melo, J., Sánchez, E., and Borro, D. “Implementation of a cooperative human-robot system for transpedicular fixation surgery”. In *Actas del XXIX Congreso Anual de la Sociedad Española de Ingeniería Biomédica (CASEIB 2011)*, pp. 303–306. 2011.

Bertelsen, A., Muñoz Barrutia, A., Tejada, S., Ortiz-de Solorzano, C., and Borro, D. “Segmentation of the skull from MR T1 images using label fusion”. In *Proceedings of the 32nd Annual International Conference of the IEEE EMBS*, pp. 3121 – 3124. Buenos Aires, Argentina. 2010.

## Appendix B

# Segmentation of the skull from MR $T_1$ images using label fusion

---

This chapter presents an algorithm for segmentation of the human skull from MR $T_1$ images using label fusion. The proposed method works by means of a non-rigid registration of a set of atlases to the input image, followed by a combination of their labels to produce the most probable segmentation. Prior information about the skull's shape is thus included implicitly and with high level of anatomical detail. Implementation aspects are presented in this chapter along with preliminary results of evaluations with synthetic and clinical images, which show good segmentation quality compared with other existing algorithms and ground-truth segmentations. The presented algorithms could be easily adapted for vertebrae segmentation, which would permit more accurate surgical planning based on MR images. This would reduce the amount of radiation absorbed by spinal surgery patients, which must undergo a CT scan before interventions and have radiographies acquired during its execution.

## B.1 Introduction

Bone is hardly visible in Magnetic Resonance (MR) images, which makes the segmentation of bony structures, such as the skull and vertebrae, difficult. On the contrary, bone has a very high level of contrast with soft tissue in Computerised Tomography (CT) which, added to its higher resolution, has made this imaging modality the method of choice for bone segmentation. However, clinicians try to avoid CT whenever possible as it exposes patients to ionising radiation. To cover the need of a technique able to make models of the skull which fits into standard clinical practice, in particular neurosurgery, a novel algorithm which segments the human skull from $T_1$ weighted images using a label fusion technique is proposed in this chapter.

Little attention has been paid to the segmentation of the skull on MR images, due to the difficulties it presents and the advantages that CT offers for it. A good review of previous research can be found in the article by Dogdas et al.(Dogdas et al., 2005). Early methods were limited to bidimensional images or required manual labelling. One of the first works that proposed a fully automatic and tridimensional method was written by Rifai et al.(Rifai et al., 2000), who presented an iterative method based on level sets and estimation of partial volumes. Later, Dogdas et al.(Dogdas et al., 2005) proposed an algorithm based on thresholding and mathematical morphology, designed for the production of models usable in electroencephalography (EEG) and magnetoencephalography (MEG). In 2006, Péchaud et al.(Péchaud et al., 2006) proposed a segmentation method which labelled the skull setting thresholds on lines perpendicular to the brain, defining the boundaries of a surface which was later deformed to match the patient's anatomy. Although Péchaud's original method used complementary information from $T_1$ and $T_2$ weighted images to discriminate between bone and cerebro-spinal fluid (CSF) it could also work using only $T_1$ images. In 2008, Ghadimi et al.(Ghadimi et al., 2008) presented a segmentation algorithm for neonatal scans based on the use of an atlas, in which –differing from label fusion– the latter was used to weight the probability that a voxel belonged to the skull boundaries.

As said previously, the algorithm proposed in this chapter is based on label fusion. This technique consists in the combination of multiple atlases, i.e. standard images which have been previously segmented using a reliable method. The shape of these atlases is matched to the input image's using registration and then their labels are propagated. The resulting label combination is fused to produce the most probable segmentation, using rules like majority voting. Label fusion techniques are currently being developed for segmentation of bodies (for example, deep brain structures) which cannot be identified solely on their image features –such as intensity–

and require previous knowledge about their shape and topology. Label fusion offers interesting advantages for skull segmentation as it enables the inclusion of prior information about shape in an implicit way. This is desirable as bone is difficult to detect in MR and its low intensity level can lead algorithms to incorrectly segment structures actually filled with air or CSF. Additionally, label fusion stores shape information implicitly, avoiding the need for complex models, and also offers high levels of anatomical detail. Despite these advantages, label fusion has never been used before for skull segmentation. The closest techniques -which still have marked differences- are active modelling (Shan et al., 2007) and statistical shape modelling (Lüthi et al., 2008; Wang et al., 2009).

This chapter is organised as follows. In Section B.2 the proposed algorithm is described. Section B.3 provides a description of the evaluation experiments and their results. The latter are discussed in Section B.4 and conclusions are provided in Section D.5.

## B.2 Methodology

The proposed method is adapted from the algorithms originally designed for deep brain segmentation (Aljabar et al., 2007; Babalola et al., 2009) and consists of the following steps:

1. Registration of the input MR image to the Montreal Neurological Institue (MNI) standard space using an affine transformation.

2. Evaluation of the similarity between the affine-transformed input and all atlases.

3. Ranking of the atlas images based on their similarity scores.

4. Selection of a subset with the highest ranking atlases.

5. Non-rigid registration of the selected atlases to the affine-transformed input image, using free form deformations (FFD).

6. Application of the FFD followed by the inverted affine transformation on the atlases' label images, taking them to the input image's original coordinate space.

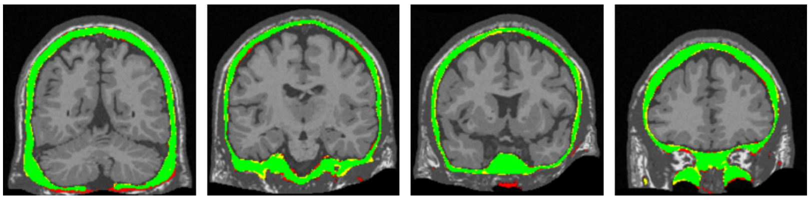

Figure B.1: Coronal slices from a sample segmentation of a synthetic image using the proposed method. Correct voxels, false positives and false negatives are colored in green, yellow and red respectively.

7. Fusion of the transformed label images to form the final segmentation.

The Normalised Mutual Information (NMI) metric was used to rank similarity between images and to drive all registrations (Studholme et al., 1999). For the non-rigid ones we used the Image Registration Toolkit's (IRTK)[1] implementation of the FFD models described by Schnabel et al.(Schnabel et al., 2001) using three consecutive coefficient grids with spacings of 32, 16 and 8 mm. Fusion of the transformed label images was carried out by majority voting (Rohlfing et al., 2004) followed by extraction of its largest connected component.

## B.3 Experiments and results

We tested the algorithm's ability to segment synthetic and clinical data. In the first experiment, used as a proof of concept and for parameter tuning, we segmented a group of synthetic images, setting one as input and using the rest as atlases. The second experiment, in which clinical data was used, compared the resulting segmentations with ground truth label maps obtained from corresponding CT images. We also compared our method against other existing algorithms using multiple quality metrics.

The atlases required by our method were built from the BrainWeb database[2] which has a group of synthetic $T_1$ volumes with corresponding fuzzy label maps of 12 kinds of tissues (Aubert-Broche et al., 2006). We registered the synthetic $T_1$ images to the MNI standard space using FFD

---

[1] Available from http://www.doc.ic.ac.uk/~dr/software/

[2] Available from http://mouldy.bic.mni.mcgill.ca/brainweb

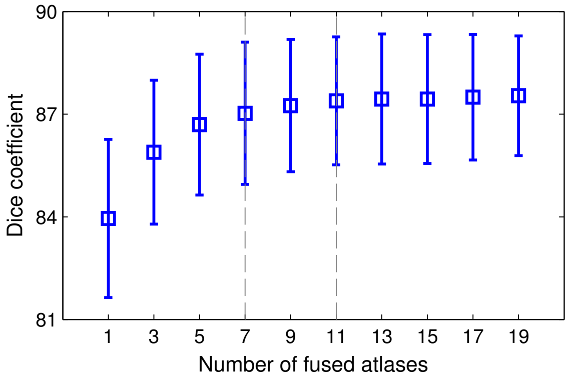

Figure B.2: DC for segmentation of synthetic images varying the number of fused atlases, which produces best results between 7 and 11 (squares mark the mean and error bars' length equal two times the standard deviation).

and then generated a binary label map of the skull by combination of the bone and marrow maps. Afterwards, we validated our method running a series of segmentations excluding one from the set and setting it as input, assessing the result's quality by comparison with the excluded atlas' label map. We repeated each segmentation varying the number of fused atlases from 1 to 19 to determine the value that produced optimal results. The segmentations' quality was evaluated using the Dice Coefficient (DC), defined as

$$DC(S,R) = \frac{2|S \bigcap R|}{|S| + |R|} \times 100 \tag{B.1}$$

where $R$ corresponds to the reference –i.e. the atlas' label map– and $S$ to the segmentation produced by the algorithm.

Fig. B.1 shows a sample MR image and its obtained segmentation, which shows a good match with the ground truth. The DC's mean and deviation for all segmentations appear on Fig. B.2, which shows how adding an additional atlas produces a sharp increase in DC when their number is low, but the improvement becomes less significant as more are included. As processing time increases linearly with the number of atlases, we ran a 2-way ANOVA analysis to determine the optimal value, found between 7 and 11. For the following experiments, we set this to 9.

After validation with synthetic data we proceeded to a more rigorous

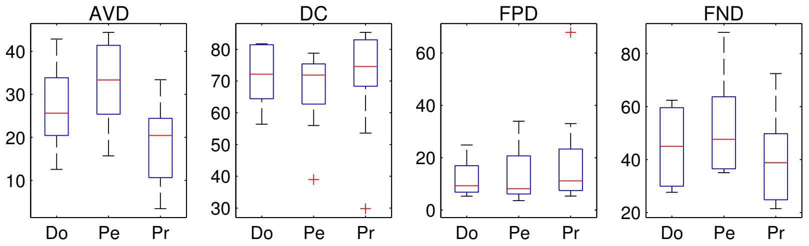

Figure B.3: Box-and-whisker plots for the performance metrics of the Dogdas05 (Do), Péchaud06 (Pe) and the proposed (Pr) algorithms (boxes' middle line mark the median, upper and bottom lines mark the first and third quartiles, whiskers extend to the valid range of data and outliers are marked individually). The proposed method shows better (i.e. lower) AVD, although it has little difference with the rest in terms of DC, FPD and FND.

evaluation using clinical images but with the same 20 images from BrainWeb as atlases. For this purpose, we compared segmentations from pairs of CT and $T_1$ images taken from the Retrospective Image Registration Evaluation (RIRE) Project database[3], a set designed for evaluation of registration algorithms which has images of numerous imaging modalities –such as MR, CT and PET– from multiple patients (Fitzpatrick et al., 1998). We chose 9 out of the 18 available patients, keeping only the high resolution ones (256×256×128 voxels, voxel size of 0.98×0.98×1.4 mm). Field inhomogeneities were corrected in all MR images using the Non-parametric Non-uniformity Normalisation (N3) algorithm (Sled et al., 1998; Tustison and Gee, 2010) and ground truth segmentations were obtained from the CT images using the method proposed by Westin et al.(Westin et al., 1997), which uses an adaptive threshold able to recover thin planar structures, usually lost using conventional algorithms. The ground-truth segmentations were later checked by an expert clinician.

We compared the performance of our method against two additional ones based on works written by Dogdas et al.(Dogdas et al., 2005) and Péchaud et al.(Péchaud et al., 2006), already presented in Section B.1. The studied algorithms were named after their main author's name and publication year and their public implementations were used: *Dogdas05* method was taken from BrainSuite 9.01[4] and *Péchaud06* was taken from

---

[3] Available from http://www.insight-journal.org/rire/

[4] Available from http://www.loni.ucla.edu/Software/BrainSuite

FSL 4.1[5]. It must be noted that the Péchaud06 method uses only $T_1$ images, as we considered that including a method that used both $T_1$ and $T_2$ images was inappropriate for this study. We also intended to include statistical segmentation algorithms –like the ones proposed in (Lüthi et al., 2008) and (Wang et al., 2009)– but the number of images in the BrainWeb and RIRE datasets was insufficient for these to work properly.

We used two similarity metrics to evaluate the algorithms' performance: the DC, defined in Eq. (B.1), and the Average Volume Difference (AVD) defined as

$$AVD(S,R) = \frac{|V_S - V_R|}{V_R} \times 100 \tag{B.2}$$

where $V_R$ and $V_S$ are the estimated volumes of the reference and segmented images respectively. Two variants of the DC were included as additional quality metrics: the False Positive Dice (FPD) and False Negative Dice (FND), which quantifies over and under segmentation respectively.

$$FPD(S,R) = \frac{2|S \bigcap \bar{R}|}{|S| + |R|} \times 100 \tag{B.3}$$

$$FND(S,R) = \frac{2|\bar{S} \bigcap R|}{|S| + |R|} \times 100 \tag{B.4}$$

All the included methods work better on the cranium as they were designed for procedures such as EEG and MEG, which do not require reconstruction of the facial bones. For this reason, the latter were not included for all metrics' evaluations.

The results' distribution appear on Fig. B.3, which suggests that the proposed method has an overall good quality, reflected on its high DC values, low AVD and no significant differences with the others in FPD and FND. A sample result is shown on Fig. B.4, which illustrates how accurately the proposed method labels the cranium.

## B.4 Discussion

Two-way ANOVA analyses were made on the quality metrics, evaluating if the proposed method produced a significant difference. These were carried

---

[5] Available from http://www.fmrib.ox.ac.uk/fsl

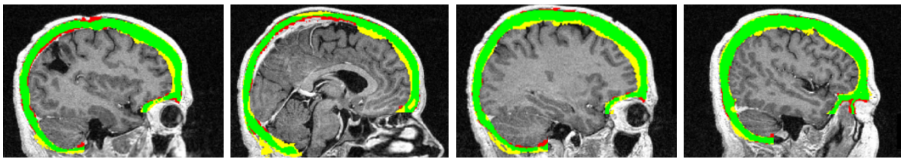

Figure B.4: Sample clinical result with color coding as in Fig. B.1 (no segmentation is shown on facial bones as they were excluded from the metrics' calculation).

| Metric | Methods | Lower bound | Mean | Upper bound |
|---|---|---|---|---|
| AVD | Do vs Pr | 0.4693 | 9.0264 | 17.5836 |
| AVD | Pe vs Pr | 5.7362 | 14.293 | 22.8505 |
| DC | Do vs Pr | -6.6928 | -1.8425 | 3.0079 |
| DC | Pe vs Pr | -9.7532 | -4.9028 | -0.0525 |

Table B.1: Confidence intervals for comparisons of AVD and DC metrics (methods are considered statistically different at a 98.75% level if the interval does not contain the origin).

out at a 95% confidence level and used Bonferroni's correction. Table B.1 shows the results for the similarity metrics which supported the hypothesis that the proposed method has a better AVD. In terms of DC, no significant difference was found between Dogdas05 and the proposed method, but the latter was found to be superior than Péchaud06 by a slight margin. However, it must be highlighted that AVD is less reliable than DC, as the former only measures the volume ratio between the evaluated segmentations and does not take their shapes into account. DC does not have this problem, as it evaluates the segmentations' coherence voxel by voxel. Therefore, it is not possible to state that the proposed method is superior only by its AVD, as the DC values does not support this claim. However, these results are preliminary and must be confirmed by an experiment with a larger sample of data.

Table B.2 shows the results of the ANOVA analysis on the FPD and FND metrics which confirm that the proposed method has a performance similar to the other ones. No significant differences can be observed apart from the lower FND compared with Péchaud06.

Finally, it must be noted that the proposed algorithm is slower than the others due to the large number of non-rigid registrations required,

| Metric | Methods | Lower bound | Mean | Upper bound |
|---|---|---|---|---|
| FPD | Do vs Pr | -6.3144 | -2.6438 | 1.0268 |
| FPD | Pe vs Pr | -6.282 | -2.6144 | 1.0592 |
| FND | Do vs Pr | -2.2194 | 6.3288 | 14.877 |
| FND | Pe vs Pr | 3.8688 | 12.417 | 20.9652 |

Table B.2: Confidence intervals for comparisons of FPD and FND.

which were performed serially. A considerable speed-up would be obtained with a parallel implementation and by a careful tuning of the registrations' parameters.

## B.5 Conclusions

We have presented a new segmentation method able to extract the skull from $T_1$ images using label fusion. Preliminary experiments show that the method has a high level of accuracy and that it obtains segmentations of good quality, in line with other available techniques and ground truth label maps. Statistical analysis shows that it has better AVD values than other methods but similar levels of DC. In all cases, none of the studied algorithms surpassed the proposed one.

The proposed version of the algorithm used binary label maps. Uncertainty could be included by the use of fuzzy ones, which may produce more accurate maps of bone. This would require a study of new label fusion methods –majority voting would no longer be applicable– which is considered for future work, along with experiments with a larger sample of images and parallelisation of the algorithm to increase its speed.

Although the algorithm was designed for skull segmentation, it could be extended to segment other bony structures –provided that a suitable set of atlases is available– such as vertebrae. The latter would be of particular interest for surgical applications, as it would permit more accurate planning based on MR scans. Although pre-operative use of the latter is not uncommon in modern hospitals, they are not well suited for using Computer Assisted Surgery (CAS) systems. The latter are effective in reducing the amount of surgical errors, but normally require the acquisition of pre-operative CT scans, which are easier to register with the intra-operative x-ray images. This, in fact, even increases the amount of radiation absorbed by spinal surgery patients, which is an undesirable side effect (Tjardes et al., 2010). Design of a CAS system for spinal surgery based on pre-operative MR scans would require special methods for segmentation of bony structures from the MR scan and their later registration to intra-operative radiographies, for which the presented method could play an important role.

## Appendix C

# Used software libraries

The viewit-Spine application was developed with a set of state-of-the-art software libraries, many of them with their source code available. Description of them will be given in the following sections.

## C.1 ITK

The Insight Tookit (ITK) is an open-source software toolkit for medical image processing, which offers a large selection of algorithms for filtering, segmentation and registration. Segmentation is the process of identifying and classifying data found in a digitally sampled image, such as CT, MRI or ultrasound images. Registration, a term which has already appeared in this thesis, is the task of aligning two or more images, defining a geometrical transform that maps homologous points between them. ITK is managed by Kitware Inc. (www.kitware.com) and is implemented in C++, with interfaces for interpreted programming languages such as Python.

ITK is copyrighted by the Insight Software Consortium, a non-profit alliance of organisations and individuals interested on its support. ITK is open-source, meaning that its source code is freely available, and it can be used with almost no restrictions, even in commercial products.

For development of viewit-Spine we took advantage of the large amount of file formats supported by ITK, which greatly simplified image reading and writing. In addition, ITK offers built-in support for the DICOM format using the Grassroots DCM (GDCM) library, which is also open-source and distributed under a unrestrictive license similar to BSD.

For the development of viewit-Spine we used ITK version 3.20.0. Although it is possible to use ITK with its built-in GDCM version, we preferred to use a different version due to incompatibilities with the data received from our collaborators. Thus, we developed our software using GDCM version 2.0.12.

## C.2 VTK

The Visualization Toolkit (VTK) is an open-source, freely available software system for 3D computer graphics, image processing and visualization. VTK consists of a C++ class library and several interfaces for languages such as Java, Tcl/Tk and Python. VTK supports a large variety of visualisation algorithms for scalar, vector, tensor and volumetric data; and advanced modelling techniques like implicit modelling, polygon reduction and Delaunay triangulation. Besides, VTK offers a set of classes for user interaction, supports parallel processing and runs on Linux, Windows and Mac platforms (Kitware, 2010).

Like ITK, VTK is managed by Kitware Inc. and serves as and ideal companion for the first library. Despite that ITK was designed for medical image processing, it lacks from any classes for visualisation, as these task is expected to be done through VTK. Also, VTK is distributed under the BSD license, so its use has little restrictions and can be incorporated in commercial products.

For the development of viewit-Spine, VTK was used for all visualisation tasks, like display of the pre-operative data in different forms, modelling of screws and user interaction for manipulation of elements that formed the surgical plan. During development, we used VTK version 5.6.0.

## C.3 OpenIGTLink

OpenIGTLink is a networking library which provides a standardised protocol for communications among computer and devices in operating rooms for a wide variety of image guided interventions, defining its own message formats and rules for data exchange over local area networks. OpenIGTLink is open-source and available free of charge for any purpose, including development of commercial applications (Tokuda et al., 2009).

The increasing number of available image guided therapy system raises the problem of standardisation of communication between them. For this purpose, Ethernet and TCP/IP (Transmission Control Protocol / Internet Protocol) networks are natural choices: Ethernet offers flexibility, high bandwidth and is available on most modern personal computers, which run operating systems that support the TCP/IP model. In fact, the DICOM standard defines how medical images are transmitted over TCP/IP networks. Despite that most hospitals host DICOM compatible networks, this standard has not been practical for image guided therapy applications, due to the large amount of redundant information found in DICOM images which prevents data transfer at the required real-time frame rates. Furthermore, DICOM does not define a standard protocol for transmission of synchronised images and tracking data. To overcome this problem, developers of medical equipment have developed propietary interfaces for their own products, such as BrainLAB's VectorVision Link and the ones available on Medtronic's StealthStation system and Intuitive Surgical's da Vinci robot. Proprietary interfaces bring the unavoidable problem of forcing academic researchers to negotiate access privileges and adapt their software to specific devices, reducing modularity and flexibility, often at a cost of massive software re-development. In addition, interaction of commercial and research software may produce licence incompatibilities between them, which may not have a reasonable solution (Tokuda et al., 2009).

OpenIGTLink proposes a simple and extensible protocol for exchange of tracking data, images and control signals among tracking devices, imaging scanners and systems software. Its minimum data unit is called message, which is formed by a 58-byte header followed by a body section. The header structure is common for all message types, even for user-defined ones, which allows receivers to easily handle every type of message, including those of unknown type. This allows developers to define custom messages while maintaining the compatibility with other software which cannot interpret their user-defined messages.

The header includes information about the protocol version number, message type, device name, an 8-byte time stamp, an 8-byte unsigned integer with the body size and an 8-byte redundancy check. Currently, the OpenIGTLink protocol has two versions with their defined message types. Protocol version 1 has the IMAGE, POSITION, TRANSFORM,

| Message type | Description |
|---:|---|
| TRANSFORM | Homogeneous 4 by 4 linear affine transform. |
| POSITION | Alias of QTRANS. |
| IMAGE | 2D or 3D image with metric information. |
| STATUS | Current status of the message sender. |
| CAPABILITY | List of message types supported by the sender. |
| QTRANS | Rigid transform transmitted as an offset vector and a quaternion. |
| IMGMETA | Extra image information such as patient name, record number or image modality. |
| LBMETA | List of labels found on a segmented image. |
| COLORT | Color table associated to transmitted images. |
| POINT | Information of fiducial points, commonly used in surgical planning. |
| TRAJ | Information about 3D trajectories used for surgical planning and guidance. |
| TDATA | Information stream about 3D positions and orientations of surgical tools and markers. |
| QTDTA | Same as TDATA, but representing rotation information as quaternions. |
| SENSOR | Sensor readings with specified unit types. |
| STRING | Character strings of variable length. |
| NDARRAY | N-dimensional numerical arrays. |
| BIND | Container for transmission of multiple OpenIGTLink messages packed into a single one. |
| POLYDATA | Polygonal 3D data. |

Table C.1: Message types supported by OpenIGTLink protocol versions 1 and 2

STATUS and CAPABILITY messages, whereas protocol version 2 added the QTRANS, IMGMETA, LBMETA, COLORT, POINT, TRAJ, TDATA, QTDATA, SENSOR, STRING, NDARRAY, BIND and POLYDATA messages. All OpenIGTLInk messages are described briefly on Table C.1

For the development of viewit-Spine, we used OpenIGTLink version 1.9.0 with protocol version number 2.

## C.4 Eigen

Eigen (http://eigen.tuxfamily.org) is a C++ library for linear algebra, which supports matrix and vector manipulation, numerical solvers and decomposition algorithms. Eigen is open-source and distributed under the LGPL3+ library, which permits its use on closed-source projects without having to disclose the source code.

Although we used ITK for most numerical operations –most of them related to registration– we still had to use a linear algebra library for resolution of linear systems, such as the one found in the surgical tool's tip calibration routine described in Section 7.3. We chose Eigen 3.0.2 due to its easy-to-use interface and simple inclusion in larger software projects.

## C.5 Qt

Qt is an extensive C++ software library for application development, which offers a framework for design of Graphical User Interfaces and a large collection of standard classes, such as strings, lists and hash tables. Qt also permits development of cross-platform projects, that is, applications which can be compiled on different operating systems such as Windows, Linux or MacOS without changes in the source code. Furthermore, Qt includes additional modules which provide higher-level functionality, such as networking, use of web-based content, support for the Extensible Markup Language (XML) and use of OpenGL. Qt is open-source and is distributed under a dual-licensing system, which offers a commercial license for its use on propietary software and a LGPL license for non-commercial uses.

Qt's simple and powerful interface for development of graphical interfaces came as a natural choice for development of viewit-Spine, added to its easy support for VTK objects needed for rendering and visualisation of medical datasets. For the development of our project, we used Qt version 4.7.1 used under the LGPL license version 2.1.

## C.6 CMake

CMake is not a software library but an build system, which offers a set of tools for software compilation, testing and packaging. CMake is used to control software compilation using a simple platform and compiler independent configuration files. Use of CMake permits development of platform-independent projects, on which the same source code can be compiled on different operating systems using multiple compiling environments, such as Microsoft Visual Studio or standard Unix Makefiles.

Although Qt also permits cross-platform compilation, we preferred to use CMake as it integrates better with ITK, VTK and OpenIGTLink. During development of viewit-Spine, we managed the multiple software projects using CMake version 2.8.6.

## Appendix D

# An ITK-Based Framework for 2D-3D Registration with Multiple Fixed Images

This appendix describes an extension of the Insight Toolkit (ITK, www.itk.org) for 2D-3D registration with multiple fixed images, that is, registration of a three-dimensional dataset to a group of fixed planar projections. 2D-3D registration is possible with ITK's standard classes but with several limitations: the number of fixed images is restricted to one and the moving image's orientation axes are ignored, which greatly complicates the registration definition. Both problems are solved by the proposed framework, which permits multi-resolution intensity-based registration with an arbitrary number of fixed images, with all images defined in any orientation. In addition, the framework provides implementations of the Normalized Gradient Correlation and Pattern Intensity metrics, which are commonly used in 2D-3D registration but were not present in ITK. This appendix gives a detailed description of the proposed framework, along with examples that show its capabilities in registrations of real and simulated images of the spine.

## D.1 Introduction

Registration techniques of pre-operative and intra-operative images are prerequisites for a large variety of image guided interventions, such as radiotherapy planning, minimally invasive surgery and endoscopic procedures. Among these techniques, 2D-3D registration consists of the matching of a moving 3D dataset to one or more fixed 2D projections. Most of the time, the 3D data comes in the form of a CT or MR scan, while 2D images are x-rays acquired with a C-arm. A recent study by Markelj et al. gives a comprehensive review of the large amount of strategies developed by different research groups to solve this problem(Markelj et al., 2012). Roughly, 2D-3D registration algorithms can be grouped according to the type of data used –features, intensity or gradients– and the dimensional correspondence used to evaluate the images' similarity –projection, back-projection and reconstruction– where projective intensity-based registration is the most common strategy. Algorithms of this type generate Digitally Reconstructed Radiographs (DRR) projecting the 3D image onto the x-rays' planes. Similarities between the DRRs and x-rays are then evaluated using a metric which compares their intensities voxel-by-voxel. The 3D image is transformed and the DRRs are regenerated until the similarity metric reaches its maximum. As some spatial information is inherently lost on the DRR generation, multiple projections acquired in different orientations are used to ensure that all directions can be observed. Traditionally, two projections are used, which are acquired in the Antero-Posterior (AP) and Lateral (LAT) orientations.

The Insight Toolkit (ITK, www.itk.org), a widely used open-source software library for medical image processing, gives limited support for 2D-3D registration. Using the standard ITK classes, it is possible to implement projective intensity-based registrations, but with considerable limitations:

- Only one fixed image can be included in the registration.
- The orientation axes of the moving image are ignored, which complicates the geometric definition of the registration.
- Only one ray-casting algorithm is available for DRR generation, which only supports rigid transformations.
- No support for multi-threading is available.

This work proposes a set of classes based on ITK 3.14.0 which solves the first two problems listed above. The proposed framework allows implementation of registrations which accept one, two or more fixed images and register the moving dataset to all of the fixed images simultaneously, considering the orientation information present in the moving image.

Although the proposed framework does not address the latter two problems –non-rigid transformations and multi-threading support– the interested reader should consult the work by Steininger et al. (Steininger et al., 2009), who proposed an ITK extension which solved the aforementioned issues.

## D.2 Definition of the 2D-3D registration problem

The 2D-3D intensity-based registration problem is defined as follows. Let $M$ be the moving 3D image and $F_k$ with $k = 0..N-1$ the set of $N$ fixed 2D images. All fixed images $F_k$ have physical coordinates measured in the same coordinate system, denoted with the letter $F$. Following ITK's convention, let $\mathcal{T}_F^M$ be a geometrical transform which takes a point $\mathbf{x}_F$ from the fixed images' physical coordinate space $F$ to the moving image's physical coordinate space $M$.

Also, let us assume that for each fixed image $F_k$ a corresponding 2D image $\mathcal{P}_k^{\mathcal{T}}$ exists, which is the projection of the moving image onto the plane of $F_k$ after application of transform $\mathcal{T}_F^M$. In other words, $\mathcal{P}_k^{\mathcal{T}}$ is the $k$-th DRR, mathematically defined as

$$\mathcal{P}_k^{\mathcal{T}}(\mathbf{x}_F) = \int_0^1 M(\mathcal{T}_F^M(\mathbf{e}_k + \lambda(\mathbf{x}_F - \mathbf{e}_k)))\mathrm{d}\lambda \tag{D.1}$$

that is, the intensity value at point $\mathbf{x}$ of $\mathcal{P}_k^{\mathcal{T}}$ equals the integral of the moving image $M$ intensities sampled along the ray that goes from $\mathbf{x}_F$ to the projection's focal point $e_k$, after application of transform $\mathcal{T}_F^M$. The ray equation is parametrised using the variable $\lambda$: if $\lambda$ is 0 the ray is in $\mathbf{x}_F$, if $\lambda$ is 1 the ray is the focal point $e_k$. It is assumed that a direct integration of the voxel values of $M$ gives a DRR useful for registration purposes, so no intensity corrections are needed. This, projection algorithm is known as ray-casting and provides a useful, although simplified, model of the x-ray images' formation process.

Let $S_k$ be a metric which computes the similarity between $F_k$ and

$\mathcal{P}_k^{\mathcal{T}}$ on a defined set of points $\mathbf{x}_F^k$. The problem of intensity-based 2D-3D registration consists of finding the optimal transform $\dot{\mathcal{T}}_F^M$ which maximises the sum of all similarity metrics $S_k$

$$\begin{aligned}\dot{\mathcal{T}}_F^M &= \arg\max_{\mathcal{T}_F^M} \sum_{k=1}^{K} S_k \\ &= \arg\max_{\mathcal{T}_F^M} \sum_{k=1}^{K} S_k(F_k, \mathcal{P}_k^{\mathcal{T}}, \mathbf{x}_F^k) \qquad \text{(D.2)}\end{aligned}$$

## D.3 Framework for intensity-based registration

In terms of programming, ITK provides classes for all objects involved in the registration: transform, metric, optimizer and interpolator, used to sample the moving image's values on non-grid positions. All of these objects are plugged into a registration method class, which makes all the necessary internal connections and coordinates the optimization to find the optimal transform parameters. Usually, the registration method object is an instance of `ImageRegistrationMethod`, which expects a generic transform, interpolator and a metric object subclassed from `SingleValuedCostFunction`, as it must return a single real value as a quality measure of the match between the fixed and moving images. For the same reason, the used optimizer must be designed to find the optimum of single-valued cost function and must be subclassed from `SingleValueNonLinearOptimizer`. Multi-resolution registration is possible by using the `MultiResolutionImageRegistrationMethod`, which requires filters of class `MultiResolutionPyramidImageFilter` to generate the downsampled versions of the moving and fixed images. For 2D-3D registration, ITK provides the `RayCastInterpolateImageFunction` for generation of DRR using the standard ray-casting algorithm.

Any developer familiar with ITK's paradigm should be able to adjust to the proposed one with minimal effort, as the former has been largely respected. Registration objects work in almost identical way, although they are instances of the new `MultiImageToImageRegistrationMethod` and `MultiResolutionMultiImageToImageRegistrationMethod`

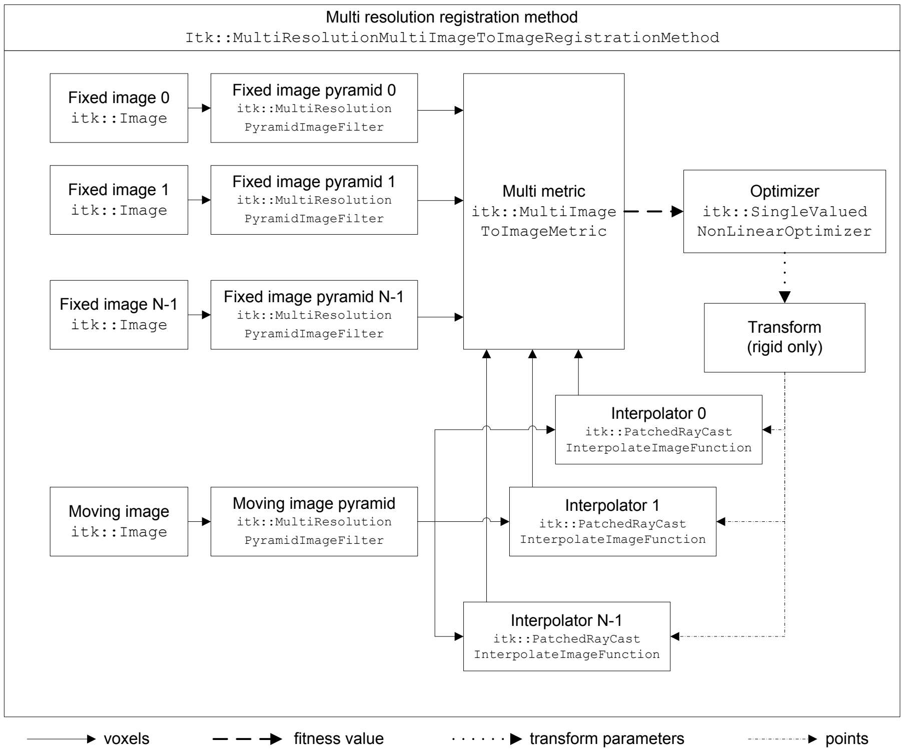

Figure D.1: Connection diagram of the proposed framework's classes. The main differences between this framework and the ITK's current one are the use of the `MultiImageToImageMetric` class instead of the standard metric object and the use of multiple interpolators. Also note that registration is encapsulated in a new class.

classes. Its main difference with the standard classes is the use of multiple fixed images, pyramid filters and interpolators instead of the single ones needed in ITK. Optimizers remain as subclasses of `SingleValuedNonLinearOptimizer`, but metric objects have been replaced by the new `MultiImageToImageMetric` class which, like in standard ITK, return a single real value, but accept multiple fixed images as input instead of the single one permitted by ITK's metrics. Concrete implementations of the Gradient Difference, Normalized Gradient Correlation and Pattern Intensity metrics for multiple fixed images are provided, which are widely-used in 2D-3D registration. In addition, a new ray-casting interpolator class named `PatchedRayCastInterpolateImageFunction` is provided, which fixes some of the bugs present in the original implementation. A schematic of the framework's classes is shown in Figure D.1, which shows how objects are connected for a typical registration problem.

Detailed descriptions of all classes present in the proposed framework are given in the sections below.

### D.3.1 Registration methods

The main class of the framework is the `MultiImageToImageRegistrationMethod`, which coordinates all objects required in the registration process, which are the images, transform, metric, optimizer and interpolators. As `MultiImageToImageRegistrationMethod` was subclassed from `ProcessObject`, a call to the `Update` method is all that is needed to execute the registration once its components have been plugged in. Multi-resolution registration can be done by using the `MultiResolutionMultiImageToImageRegistrationMethod`, a subclass of `MultiImageToImageRegistrationMethod`.

The moving image, transform and optimizer can be set on a `MultiImageToImageRegistrationMethod` object using the standard `SetMovingImage`, `SetTransform` and `SetOptimizer` methods, also present in ITK's original registration classes. Addition of the metric requires creation of an `MultiImageToImageMetric` instance, which should be later plugged into the registration object using the `SetMultiMetric` method. Adding the fixed images, regions, masks and interpolators is different, as multiple objects need to be plugged in rather than just one. The proposed framework offers two different ways to do this. The first and recommended way is to create each object individually and plug them into the registration using the corresponding `Add` method. The `MultiImageToImageRegistrationMethod` has implementations of the `AddFixedImage`, `AddFixedImageRegion`, `AddFixedImageMask` and `AddInterpolator` methods for insertion of fixed images, regions, masks and interpolators respectively. For example, the code to add two fixed images should be as follows

```
typedef itk::Image<short,3>  FixedImageType;
typedef itk::Image<short,3>  MovingImageType;

typedef itk::MultiImageToImageRegistrationMethod
         <FixedImageType,MovingImageType> RegistrationType;

const unsigned int FImgTotal = 2;

RegistrationType::Pointer registration =
                                   RegistrationType::New();

for( unsigned int f=0; f<FImgTotal; f++ )
  {
  FixedImageType::Pointer fixedImage;

// do something here to read or create a fixed image

  registration->AddFixedImage( fixedImage );
  }
```

The second way to define fixed images, regions and interpolators is to store them in `std::vector` objects and plug them into the registration using `SetFixedMultiImage`, `SetFixedMultiImageRegion`, `SetFixedMultiImageMask` or `SetMultiInterpolator` methods respectively. The code to add a set of fixed images should look like the written below:

```
RegistrationType::FixedMultiImageType fixedMultiImage;

for( unsigned int f=0; f<FImgTotal; f++ )
  {
  FixedImageType::ConstPointer fixedImage;

// do something here to read or create a fixed image

  fixedMultiImage.push_back( fixedImage );
  }

registration->SetFixedMultiImage( fixedMultiImage );
```

Usually, the elements of these types of arrays are `const` so care must be taken to store them correctly. The `MultiInterpolatorType` has an additional problem: its elements are of type `InterpolateImageFunction::Pointer` so, if this type of array was created, the user should define the interpolator, cast it to `InterpolateImageFunction::Pointer`, store it and finally plug it into the registration method. All these steps can be avoided if the `AddInterpolator` method is used instead, which can receive a `Pointer` of any subclass of `InterpolateImageFunction` and, normally, leads to simpler code. As an example, compare the code snippet given below, which uses the `AddInterpolator` method,

```
typedef itk::PatchedRayCastInterpolateImageFunction
                <MovingImageType,double> InterpolatorType;

for( unsigned int i=0; i<FImgTotal; f++ )
  {
  InterpolatorType::Pointer interpolator =
                                   InterpolatorType::New();

// Here, code to define the interpolator's focal point,
// transform, etc.

  registration->AddInterpolator( interpolator );
  }
```

with the following one, which uses the `SetMultiInterpolator` method.

```
typedef itk::PatchedRayCastInterpolateImageFunction
                <MovingImageType,double> InterpolatorType;

typedef RegistrationType::BaseInterpolatorPointer
                                   BaseInterpolatorPointer;
typedef RegistrationType::MultiInterpolatorType
                                     MultiInterpolatorType;

MultiInterpolatorType multiInterpolator;

for( unsigned int i=0; i<FImgTotal; f++ )
  {
  InterpolatorType::Pointer interpolator =
```

```
                                     InterpolatorType::New();

// Here, code to define the interpolator's focal point,
// transform, etc.

  multiInterpolator.push_back(
    static_cast<BaseInterpolatorPointer>( interpolator ) );
  }
registration->SetMultiInterpolator( multiInterpolator );
```

Although both snippets implement the same function –addition of multiple interpolators to the registration method– the first one is much simpler.

The `MultiImageToImageRegistrationMethod` class and its subclasses expect that the number of defined regions, masks and interpolators is exactly equal to the number of fixed images. However, if no regions have been set for the fixed images, `MultiImageToImageRegistrationMethod` will use their buffered regions by default. Also, if no masks are defined, they will be ignored during registration. It is also possible to define masks for only some of the fixed images, by calling the `AddFixedImageMask` method with a `NULL` argument for the ones that should not be masked.

`MultiResolutionMultiImageToImageRegistrationMethod` implements multi-resolution registration with multiple fixed images. The class interface was kept as similar as possible to the available `itk::MultiResolutionImageRegistrationMethod`, so the user must provide the filters that generate the images for each resolution level. The filter for the moving image is set with the `SetMovingImagePyramid` method and the ones used for the fixed images are set with the `AddFixedImagePyramid` or `SetFixedMultiImagePyramid` methods. The number of resolution levels can be set using the `SetNumberOfLevels` method, which will define a default schedule for the different resolution levels. Finer control over the amount of blurring and downsampling is achieved with the `SetSchedules` method, which receives two matrices –one for the moving image and one for the fixed ones– whose elements define the downsampling factor applied in each dimension (column) for each resolution level (row). In 2D-3D registration, using `SetSchedules` is always recommended, as the fixed images' downsampling factor along the slice direction must be equal to 1 at all resolution levels (in other words, all elements on the third column of the fixed images' schedule matrix must be equal to 1).

Finally, note in the code snippets given above that both the fixed and moving images have been defined with the same number of dimensions, three. Despite that the fixed images are usually 2D, they must be defined as 3D images with a single slice, to ensure that ITK handles their orientation and origin information correctly.

### D.3.2 Transform

When the `PatchedRayCastInterpolateImageFunction` class is used for 2D-3D registration, the framework can only use rigid transforms such as `TranslationTransform` and `Euler3DTransform`. Despite this limitation, the proposed classes can still be used on plenty of applications, as 2D-3D registration is commonly used on rigid body structures such as the vertebrae, skull, pelvis and femur (Markelj et al., 2012).

### D.3.3 Metric

Equation D.2 states that the degree of similarity in registrations with multiple fixed images can be calculated as the sum of individual similarity metrics between the moving image and each of the fixed ones. To implement this functionality, a new class named `MultiImageToImageMetric` was written, which internally stores an array of individual metrics and returns their sum when its value is requested by the `GetValue` method.

Like the existing `ImageToImageMetric` class, `MultiImageToImageMetric` was derived from `SingleValuedCostFunction`, so it could be easily incorporated into the standard ITK's registration framework. Hence, the standard `GetValue`, `GetDerivatives` and `GetValueAndDerivatives` methods are present. Calls to `GetValue` return the sum of the internal array of metrics while `GetDerivatives` return an estimation of the functions' derivatives using the central differences method, with a variable step size set with the `SetDerivativeDelta` method. `GetDerivatives` is defined as `virtual`, so developers can replace it with a more efficient method, as the central differences method requires multiple calls to

`GetValue`, which can be slow and inaccurate for some applications.

The `MultiImageToImageMetric` and its internal metric type `ImageToImageMetric` are defined as purely virtual and cannot be instantiated. Concrete implementations of similarity metrics are implemented by the `MultiImageToImageMetric` subclasses, which are responsible for redefinition of the internal metric type. Currently, the proposed framework has multi-image implementations of the Mean Squares, Gradient Difference, Normalized Gradient Correlation and Pattern Intensity metrics.

#### D.3.3.1 Mean Squares

The `MeanSquaresMultiImageToImageMetric` offers an implementation of the well-known average of squared differences metric, based on the sum of multiple instances of `MeanSquaresImageToImageMetric`. This metric requires both images to have similar intensity scales to work properly, which is very difficult to achieve in 2D-3D registration using DRRs. Thus, this function serves more as an example of how `MultiImageToImageMetric` must be subclassed rather than for actual use.

Although `MeanSquaresMultiImageToImageMetric` has an analytical formula for its gradient, it is not used when `GetDerivative` is called. The `MeanSquaresMultiImageToImageMetric` gradient calculation assumes that valid points are only found in the overlapping regions between the fixed and moving images which, in the case of 2D-3D registration, are non-existent. Thus, the available analytical formula could not be used and was replaced by the finite differences method, which, despite being less efficient, makes no assumptions about overlap and calculates a correct estimate of the function's gradient.

#### D.3.3.2 Gradient Difference

The `GradientDifferenceMultiImageToImageMetric` implements the Gradient Difference metric proposed by Penney et al. (Penney et al., 1998) for multiple fixed images. The proposed framework also includes a version for single fixed image registration named `GradientDifferenceSingleImageToImageMetric`. Gradient

Difference estimates the degree of similarity based on the image obtained by subtraction between the gradients of the fixed and projected images. Mathematically, it is defined as

$$S_k = \sum_{\mathbf{x}_{Fk}} \frac{\sigma_k^2}{\sigma_k^2 + GD_k^i(\mathbf{x}_{Fk})} + \sum_{\mathbf{x}_{Fk}} \frac{\varsigma_k^2}{\varsigma_k^2 + GD_k^j(\mathbf{x}_{Fk})} \tag{D.3}$$

where $GD_k^i$ and $GD_k^j$ are the differences between the gradients of fixed image $k$ and the ones of the moving image's projection $\mathcal{P}_k^{\mathcal{T}}$ along $i$ and $j$, defined as the first and second directions in the fixed image's coordinate system.

$$GD_k^i = \frac{\delta F_k}{\delta i} - \frac{\delta \mathcal{P}_k^{\mathcal{T}}}{\delta i} \tag{D.4}$$

$$GD_k^j = \frac{\delta F_k}{\delta j} - \frac{\delta \mathcal{P}_k^{\mathcal{T}}}{\delta j} \tag{D.5}$$

Terms $\sigma_k^2$ and $\varsigma_k^2$ are the variances from the gradient images of $F_k$

$$\sigma_k^2 = var(\frac{\delta F_k}{\delta i}) \tag{D.6}$$

$$\varsigma_k^2 = var(\frac{\delta F_k}{\delta j}) \tag{D.7}$$

Gradient Difference reduces the effects of low frequency intensity changes, such as the ones introduced by soft tissue, by using the images' gradients rather than their intensities. In addition, its reciprocal form (differences are placed in the function's denominator) makes it strong against thin artefacts with strong intensities, such as surgical instruments present in the images (Penney et al., 1998).

Note that the framework includes an implementation of the Gradient Difference metric despite that ITK already has one. The main reason is that the original implementation, called `GradientDifferenceImageToImageMetric` always pre-computes the moving image gradient. If it was used in a metric for multiple fixed images, ITK's implementation would compute multiple identical versions of this gradient and waste considerable amounts of memory by storing them.

#### D.3.3.3 Normalized Gradient Correlation

`NormalizedGradientCorrelationMultiImageToImageMetric` implements the Normalized Gradient Correlation metric for multiple fixed images, based on the `NormalizedGradientCorrelationImageToImageMetric` class also included in the proposed framework. This metric computes the average of the normalized cross-correlation between the gradients of the fixed and projected images computed along directions $i$ and $j$ (Lemieux et al., 1994).

Normalized Gradient Correlation is defined as

$$S_k = NCC\left(\frac{\partial F_k}{\partial i}, \frac{\mathcal{P}_k^{\mathcal{T}}}{\partial i}, \mathbf{x}_F^k\right) + NCC\left(\frac{\partial F_k}{\partial j}, \frac{\mathcal{P}_k^{\mathcal{T}}}{\partial j}, \mathbf{x}_F^k\right) \tag{D.8}$$

with $NCC(F, M, \mathbf{x})$ the Normalized Cross Correlation between images $F$ and $M$ evaluated on points $\mathbf{x}$

$$NCC(F, M, \mathbf{x}) = \frac{\sum_{\mathbf{x}} F(\mathbf{x}) M(\mathbf{x})}{\sqrt{\sum_{\mathbf{x}} F(\mathbf{x})^2} \sqrt{\sum_{\mathbf{x}} M(\mathbf{x})^2}} \tag{D.9}$$

Normalized Gradient Correlation, like Gradient Difference, is insensitive to low-frequency variations introduced by soft tissue, as images' gradients are used to compute the metric rather than their intensities.

#### D.3.3.4 Pattern Intensity

The `PatternIntensityMultiImageToImageMetric` implements the Pattern Intensity metric proposed by Weese et al. (Weese et al., 1997) for multiple fixed images. Like the two metrics introduced in the previous sections, its version for registrations with a single fixed image is also included in the proposed framework under the name `PatternIntensityImageToImageMetric`. Pattern intensity characterises the structures found on the difference image $ID_k$, obtained after subtraction of the fixed image $F_k$ and the projection $\mathcal{P}_k^{\mathcal{T}}$. If the moving image is not registered properly, areas with large intensity variations, that is 'structures', will appear in the difference image $ID_k$. In turn, structures will vanish if registration is correct, leaving areas with low changes in intensity. The pattern intensity metric assigns values to the amount of structures found on a small moving kernel, according to the following formula

$$S_k = \sum_{\mathbf{x}_F^k} \sum_{\mathbf{u}_F^k} \frac{\sigma^2}{\sigma^2 + (ID_k(\mathbf{x}_F^k) - ID_k(\mathbf{u}_F^k))^2} \tag{D.10}$$

$$|\mathbf{x}_F^k - \mathbf{u}_F^k|^2 < r^2 \tag{D.11}$$

In Equation D.10, term $\mathbf{x}_F^k$ represents the coordinates of each voxel taken into account for the metric calculation and $\mathbf{u}_F^k$, the coordinates of a moving kernel of radius $r$ centered on voxel $\mathbf{x}_F^k$. This kernel samples the image $ID_k$, obtained from the subtraction of the fixed and projected images

$$ID_k = F_k - \mathcal{P}_k^{\mathcal{T}} \tag{D.12}$$

Also, terms $r$ and $\sigma^2$ are user-defined parameters. Parameter $r$ defines the radius of the moving kernel. Parameter $\sigma^2$ defines the sensitivity which determines if a intensity variation should be considered a structure or not. These parameters can be set using the `SetRadius` and `SetSigma` methods. The default value is 3 voxels for $r$ and 10 for $\sigma$.

The Pattern Intensity metric, differs from Gradient Difference and Normalized Gradient Correlation in that it does not compute the images' gradients. Instead, it uses direct subtraction between intensities of the fixed and projected images, but its moving kernel restricts the metric to the local features rather than the global ones, preventing soft tissue intensity variations from affecting the metric values. Like Gradient Difference, it also has a reciprocal form, which makes it strong against thin outliers like surgical instruments.

### D.3.4 Optimizer

The proposed framework works with any optimizer derived from the `SingleValuedNonLinearOptimizer` class. Van der Bom et al.

experimented with different combinations of metrics and optimizers for registration of a CT scan to a single x-ray of a human skull, demonstrating that proper combinations can considerably affect the registration performance (van der Bom et al., 2011). The best performing combination was the Normalized Gradient Correlation metric paired with a conjugate gradient descent optimization algorithm, such as the one implemented by the `FRPROptimizer` class. However, it should be noted that registration problems are highly specific and the best combination of metric and optimizer for one may not be the best for another.

### D.3.5 Interpolator

The proposed framework includes a new interpolator class, named `PatchedRayCastInterpolateImageFunction`, which projects a 3D image onto a plane using the ray casting algorithm, integrating the intensity values along rays that go from all voxels on the imaging plane to a defined focal point, as defined in Equation D.1. Ray casting offers a simplified model of the x-ray formation process, ignoring effects such as scattering, and has become a widely used algorithm for DRR generation.

The `PatchedRayCastInterpolateImageFunction` is based on the existing `itk::RayCastInterpolateImageFunction`, which has many limitations that have prevented its widespread use. Most importantly, the moving image's orientation was completely ignored, so its axes were always assumed to be parallel to $x$, $y$ and $z$. `PatchedRayCastInterpolateImageFunction` solves the aforementioned problem by offering calculations of the rays' direction with all the images' orientation taken into account. The class interface was kept identical to `RayCastInterpolateImageFunction`, thus the input image and focal point are set using the `SetInputImage` and `SetFocalPoint` methods.

However, not all limitations of the ITK's ray caster were addressed. Among the ones left unsolved were the lack of support for multi-threading and the bilinear scheme used for interpolation, which could be extended to tri-linear. These improvements were left for future work.

## D.4 Example applications

Source code is included with this appendix[1] and can be compiled on multiple platforms using CMake 2.6.2 or newer (http://www.cmake.org). Unit tests are provided for all the framework's classes, which can be executed using CMake's testing program, CTest. Unit testing requires a set of sample images, provided in the `Data` directory found within the source code's root directory.

In addition to the unit tests, two sample applications are provided: `MultiImageSearch` and `MultiImageRegistration`, which give an example of the framework's capabilities. Descriptions of these applications are given in the following sections, along with results with simulated data, that is, using DRRs as reference images instead of actual radiographs. The `MultiImageRegistration` is also tested with real images obtained from a public database.

### D.4.1 Exhaustive search for intensity-based registration

The `MultiImageSearch` example is an example application that evaluates a chosen registration metric for various translation values using the `ExhaustiveOptimizer`. The search is repeated on three resolution levels with downsampling factors of 4, 2 and 1 (1 meaning no downsampling). The results of this application should be plotted to examine the metric's shape around the optimum and design a suitable optimization strategy.

The `MultiImageSearch` command line looks as follows

```
MultiImageSearch [m] [N] [f1] [f1Px] [f1Py] [f1Pz] ... [fN]
  [fNPx] [fNPy] [fNPz] [mc] <sigma> [sx] [sy] [sz] [ds]
```

where $m$ is the moving image's file name, $N$ the number of fixed images, $fk$ with $k = 1..N$ the $k$'th fixed image's file name and $fkPx$, $fkPy$ and $fkPz$ the real-world coordinates of the $k$'th image's focal point. Argument $mc$ is the metric class, which can take values of $gd$, $gc$ or $pi$ for Gradient Difference, Normalized Gradient Correlation or Pattern Intensity respectively. Parameter $sigma$ must only be given when the

---

[1] Source code can be downloaded from http://hdl.handle.net/10380/3264

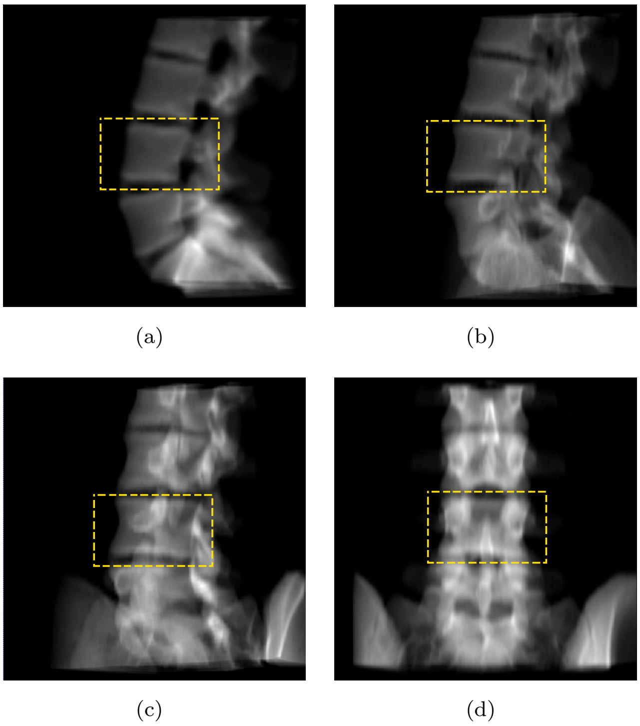
(a) (b) (c) (d)

Figure D.2: DRRs used as fixed images with their regions of interest (a) 0° LAT view (b) 30° (c) 60° (d) 90° AP view

Pattern Intensity metric is chosen, and sets the $\sigma$ value for Equation D.10. Parameters $sx$, $sy$ and $sz$ define the search grid for each dimension, with the total number of steps being $2 \times s + 1$ centred around 0.0. Parameter $ds$ controls the step size in millimetres.

Calling `MultiImageSearch` on the `Data` directory with the following parameters

```
MultiImageSearch moving.thr.mha  2 fixedAP.roi.mha 0 1000 0
  fixedLAT.roi.mha -1000 0 0 gd 25 25 0 0.4
```

evaluates the Gradient Difference metric around the optimum transform, which is the identity, on a 51 by 51 grid with different translation values on the $x$ and $y$ axes. The moving image `moving.thr.mha` is a CT scan of the spine lumbar section, thresholded for a more realistic generation

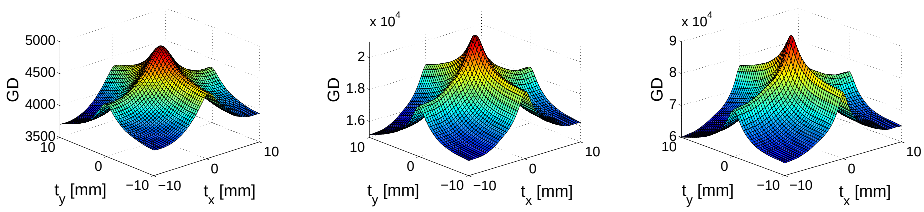

(a) GD, 4x downsampling (b) GD, 2x downsampling (c) GD, no downsampling

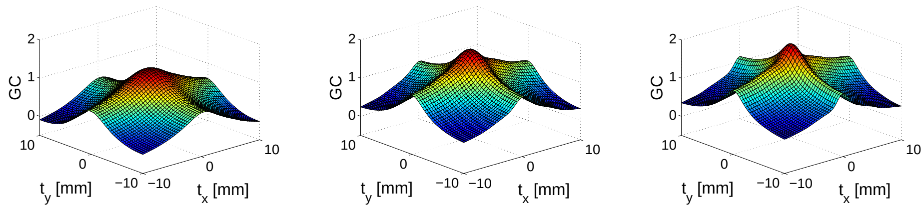

(d) GC, 4x downsampling (e) GC, 2x downsampling (f) GC, no downsampling

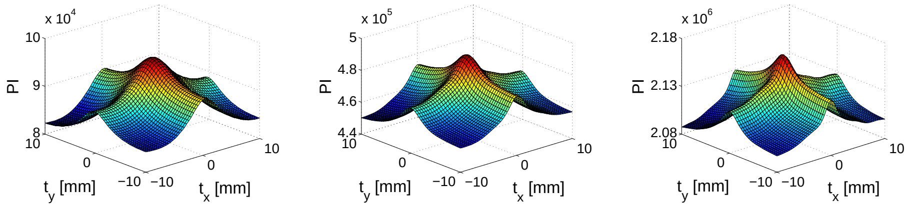

(g) PI, 4x downsampling (h) PI, 2x downsampling (i) PI, no downsampling

Figure D.3: Metrics' plots around the optimum transform for different translation values. Tested metrics are Gradient Difference (top row), Normalized Gradient Correlation (middle row) and Pattern Intensity (bottom row). Resolution level changes across columns with downsampling factors of 4 (left column), 2 (middle column) and 1 (right column).

of DRRs and located with the real-world origin inside the L4 vertebra. Images `fixedLAT.roi.mha` and `fixedAP.roi.mha`, shown in Figure D.2(a) and D.2(d), are lateral (LAT) and antero-posterior (AP) simulated projections of the CT dataset, cropped to show only vertebra L4. Focal point for the LAT projection is $(-1000, 0, 0)$ and, for the AP projection, $(0, 1000, 0)$. Changing argument *gd* to *gc* or *pi* (setting $\sigma$ to 2000 when Pattern Intensity is chosen) makes the same experiment changing only the

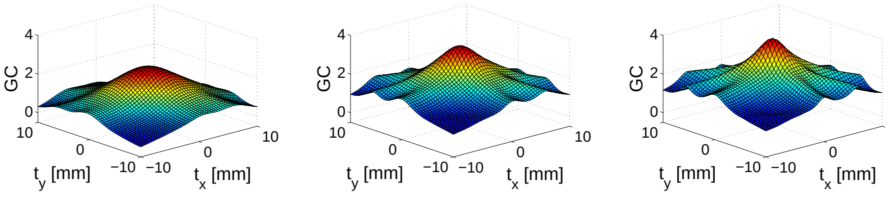

(a) (b) (c)

Figure D.4: Normalized Gradient Correlation plots around the optimum transform using 4 fixed images. Comparison with the metric using 2 fixed images (middle row of Figure D.3) show that additional ridges appear on the normal directions of the added images, which are effectively filtered at low resolution levels.

similarity metric. The resulting plots for all metrics on all resolution levels are shown in Figure D.3. Note that the optimum is well-defined on all resolution levels and that narrow ridges are present along the $x$ and $y$ axes, which can slow down an optimizer's convergence. These ridges are effectively reduced at lower resolution levels.

Extra images can be added into the registration by modifying the command line. For example, calling `MultiImageSearch` with the following arguments

```
MultiImageSearch moving.thr.mha 4 fixedLAT.roi.mha -1000 0
  0  fixed30.roi.mha -866.0254 500 0   fixed60.roi.mha
  -500 866.0254 0 fixedAP.roi.mha 0 1000 0 gc 25 25 0 0.4
```

performs an exhaustive search of the Normalized Gradient Correlation metric, but using four fixed images instead of two. Apart from the LAT and AP views, corresponding to 0° and 90°, two extra views with angles of 30° and 60°, shown in Figure D.2(b) and D.2(c), were added into the metric calculation. Results shown on Figure D.4 depict the metric around the optimum for the three tested resolution levels. Note that additional ridges appear, which correspond to the normal directions of the added images.

### D.4.2 Multi-resolution intensity-based registration

The `MultiImageRegistration` example performs a rigid registration of the moving image to the set of fixed images given as input. The Normalized Gradient Correlation metric is used to evaluate the images' similarity, which is optimised using the Fletcher-Reeves Polak-Ribiere (FRPR) Conjugate Gradient algorithm(Press et al., 2007). Three resolution levels are used, with downsampling factors of 4 and 2 for the first and second. The images' original resolutions are used in the last level.

The `MultiImageRegistration` is called with a command line similar to the previous example

```
MultiImageRegistration [m] [N] [f1] [f1Px] [f1Py] [f1Pz]...
  [fN] [fNPx] [fNPy] [fNPz]  [oDir] <inT>
```

with the main difference being the last two arguments. The *oDir* argument is the name of the directory where the registration results should be stored and *inT* the input transform in the ITK's format. In the output directory, `MultiImageRegistration` will save the `outTransform.txt` file with the output transform, the `outMatrix.txt` text file with the same transform but written as a 4 by 4 matrix, the `inMatrix.txt` file with the input transform matrix and the moving image's projections named `projectionk.mha` with $k$ from 0 to $N-1$. Lastly, subtraction between the projections and the fixed images are stored as `subtractionk.mha`.

Running `MultiImageRegistration` with the following parameters

```
MultiImageRegistration moving.thr.mha  2 fixedAP.roi.mha 0
  1000 0 fixedLAT.roi.mha -1000 0 0 outDir inTransform.txt
```

registers the CT scan of the previous examples to its DRRs taken at the LAT and AP orientations. Results are saved in the `outDir` directory and `inTransform.txt` is an example transform which serves as a starting point for the registration, with angles of -0.1, -0.2 and 0.2 radians for the $x$, $y$ and $z$ axes (-5.73°, -11.4592° and 11.4592° respectively) and displacements of -4.9, -4.7 and 0.7 millimetres along $x$, $y$ and $z$. After registration, transform parameters are set to -0.0003, 0.0002 and 0.0003 radians (-0.0172°, 0.0115° and 0.0172° respectively) and -0.0029, 0.0168

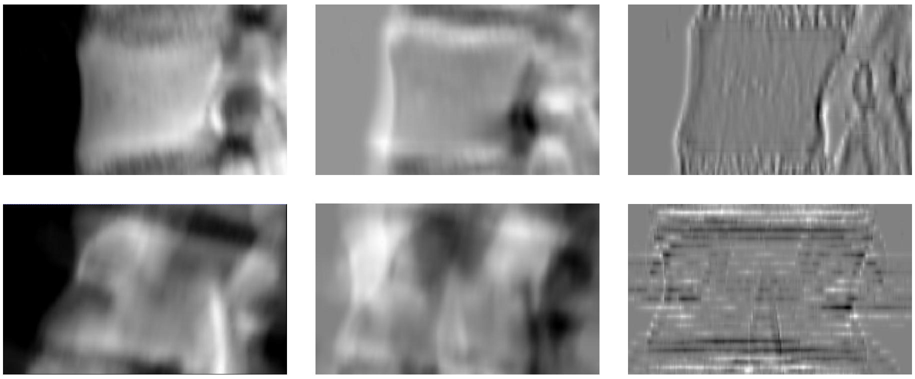

Figure D.5: Results of the `MultiImageRegistration` program using a LAT (top row) and AP (bottom row) fixed images. Figures show the projections before registration (left column), the subtraction between each projection and its corresponding fixed image before registration (middle column) and the subtraction after registration (right column).

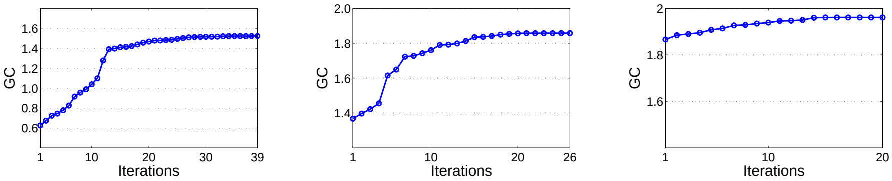

(a) (b) (c)

Figure D.6: Normalized Gradient Correlation plots of the `MultiImageRegistration` example for all three resolution levels (a) 4x downsampling (b) 2x downsampling (c) no downsampling

and -0.0147 mm, which is quite close to the correct transform which has all its parameters equal to zero. Figure D.5 shows the projections' aspect before registration and the subtractions between the projections before and after registration, which clearly show how matching between the images is improved. Figure D.6 shows the Normalized Gradient Correlation metric evolution for the three resolution levels of the registration.

Testing of the `MultiImageRegistration` application with a more

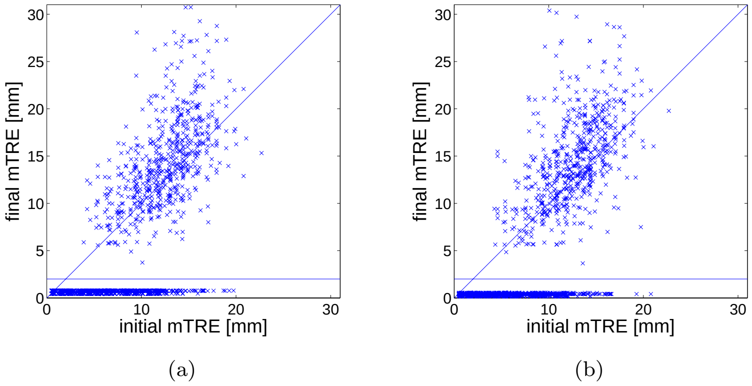

(a) (b)

Figure D.7: Standard evaluation of the `MultiImageRegistration` application using 2 x-ray images for registration of a 3DRX (a) and a CT (b) datasets. Each point represent a registration result on eight different vertebrae (200 registration per vertebra, 1600 in total). Registration are considered successful when their final mTRE is less than 2mm, indicated by the plots' horizontal line.

realistic input was done using the dataset provided by the Image Sciences Institute of the University of Utrecht (http://www.isi.uu.nl/Research/Databases/GS/), comprised of CT, MR, three-dimensional radiography (3DRX) and fluoroscopy images of eight different vertebrae and complemented with a standardised protocol for evaluation of registration algorithms (van de Kraats et al., 2005). The aforementioned protocol defines the ground-truth transform for each image and 200 initial transforms with mean Target Registration Errors (mTRE) uniformly distributed between 0 and 20 mm. Combination of the vertebrae and starting transforms give a total of 1600 registrations for evaluation of each algorithm, which are considered successful if their final mTRE is below 2 mm. The protocol also establishes calculation of the methods' capture range as the value of the initial mTRE with a percentage of successful registrations of 95%.

The `MultiImageRegistration` was evaluated with the 3DRX and CT images. The MR images were not used as their intensities have no direct relation with the x-rays', which prevents the use of intensity-based methods. Figure D.7 shows the initial and final mTRE for each of the 1600 registrations performed for each imaging modality. For the 3DRX, mean mTRE of the successful registrations was 0.5827 mm, success rate was 62.06% and capture range was 6.6864 mm. For the CT images mean mTRE was 0.3511 mm, success rate was 61.31% and capture range was 7.5229 mm. Comparison of these values with evaluations of other algorithms under the same protocol (Markelj et al., 2008a) show that `MultiImageRegistration` fares well in comparison with intensity-based (Penney et al., 1998), gradient-based (Tomaževič et al., 2003) and reconstruction-based methods (Tomaževič et al., 2006), but requires additional robustness to reach the level of more sophisticated methods, such as the Robust Gradient Reconstruction-Based Extended method (RGRBe) proposed by Markelj et al (Markelj et al., 2008a).

Due to licensing reasons, it is not possible to include the used datasets with this article. However, they are available for public use on the Image Sciences Institute website (http://www.isi.uu.nl/Research/Databases/GS/) and interested readers are encouraged to download them for their own research.

## D.5 Conclusions and future work

A framework for 2D-3D registration has been proposed which effectively increases the ITK capabilities for this type of application. The framework allows registration of a single moving 3D image to multiple fixed 2D projections, which solves the ITK's limit of a single fixed image per registration. In addition, both moving and fixed images can be defined in any position and orientation in space, which solves the problem of the moving image's orientation which, in the original ITK implementation, was completely ignored and assumed to be parallel to the world's axes. Two additional similarity metrics were added –Normalized Gradient Correlation and Pattern Intensity– and a new implementation of the Gradient Difference metric was proposed. The framework's interface has been kept similar to the one used by ITK, so any developer familiar with the toolkit should become accustomed to the proposed framework with minimal effort. Source code, unit tests and example applications are provided, along with results that demonstrate the framework's capabilities with real and simulated data.

Future work should address limitations such as the lack of support for multi-threading and the restriction for transforms, which are currently limited to rigid ones due to the ray-casting algorithm's implementation. In addition, only intensity based registration was addressed, which prevents the application of the framework in cases where a direct correlation between the intensities of the moving and fixed images does not exist, such as the case of registration of 3D MR images to multiple x-ray projections. For this, gradient-based methods could be used (Markelj et al., 2012), which would require additional extensions to ITK.

# References

Aljabar, P., Heckemann, R., Hammers, A., Hajnal, J., and Rueckert, D. “Classifier Selection Strategies for Label Fusion Using Large Atlas Databases”. In Ayache, N., Ourselin, S., and Maeder, A., editors, *Medical Image Computing and Computer-Assisted Intervention ( MICCAI 2007)*, volume 4791 of *Lecture Notes in Computer Science*, pp. 523–531. Berlin, Heidelberg. 2007.

Arun, K. S., Huang, T. S., and Blostein, S. D. “Least-Squares Fitting of Two 3-D Point Sets”. *IEEE Transactions on Pattern Analysis and Machine Intelligence*, Vol. PAMI-9, N. 5, pp. 698–700. September, 1987.

Ascari, L., Stefanini, C., Bertocchi, U., and Dario, P. “Robot-assisted endoscopic exploration of the spinal cord”. *Proceedings of the Institution of Mechanical Engineers, Part C: Journal of Mechanical Engineering Science*, Vol. 224, N. 7, pp. 1515–1529. January, 2010.

Aubert-Broche, B., Griffin, M., Pike, G. B., Evans, A. C., and Collins, D. L. “Twenty new digital brain phantoms for creation of validation image data bases.” *IEEE transactions on medical imaging*, Vol. 25, N. 11, pp. 1410–6. November, 2006.

Babalola, K. O., Patenaude, B., Aljabar, P., Schnabel, J., Kennedy, D., Crum, W., Smith, S., Cootes, T., Jenkinson, M., and Rueckert, D. “An evaluation of four automatic methods of segmenting the subcortical structures in the brain”. *NeuroImage*, Vol. 47, N. 4, pp. 1435–1447. October, 2009.

Badaan, S., Petrisor, D., Kim, C., Mozer, P., Mazilu, D., Gruionu, L., Patriciu, A., Cleary, K., and Stoianovici, D. “Does needle rotation improve lesion targeting?” *The international journal of medical robotics + computer assisted surgery : MRCAS*, Vol. 7, N. 2, pp. 138–47. June, 2011.

Bertelsen, A., Aljabar, P., Xue, H., Srinivasan, L., Hayat, T., Allsop, J., Rueckert, D., Rutherford, M., and Hajnal, J. V. “Improved slice to volume reconstruction of the fetal brain for automatic cortex segmentation”. In *Proceedings of the 17th Annual Meeting of the ISMRM*, p. 6281. Honolulu, Hawai’i, USA. 2009.

Bertelsen, A. and Borro, D. “An ITK-Based Framework for 2D-3D Registration with Multiple Fixed Images”. *Insight Journal*, 2011.

Bertelsen, A. and Borro, D. “2D-3D Registration with Multiple Fixed Images”. *The Source*, Vol. 20, pp. 13–15. 2012.

Bertelsen, A., Echeverría, M., Gómez, E., and Borro, D. “Distortion correction and calibration of intra-operative x-ray images using a constrained DLT algorithm”. In *Actas del XXX Congreso Anual de la Sociedad Española de Ingeniería Biomédica (CASEIB 2012)*. San Sebastián, Spain. 2012.

Bertelsen, A., Melo, J., Sánchez, E., and Borro, D. “Implementation of a cooperative human-robot system for transpedicular fixation surgery”. In *Actas del XXIX Congreso Anual de la Sociedad Española de Ingeniería Biomédica (CASEIB 2011)*, pp. 303–306. 2011.

Bertelsen, A., Melo, J., Sánchez, E., and Borro, D. “A review of surgical robot for spinal interventions”. *The international journal of medical robotics and computer assisted surgery*, (Accepted for publication).

Bertelsen, A., Muñoz Barrutia, A., Tejada, S., Ortiz-de Solorzano, C., and Borro, D. “Segmentation of the skull from MR T1 images using label fusion”. In *Proceedings of the 32nd Annual International Conference of the IEEE EMBS*, pp. 3121 – 3124. Buenos Aires, Argentina. 2010.

Birkfellner, W., Stock, M., Figl, M., Gendrin, C., Hummel, J., Dong, S., Kettenbach, J., Georg, D., and Bergmann, H. “Stochastic rank correlation: a robust merit function for 2D/3D registration of image data obtained at different energies.” *Medical physics*, Vol. 36, N. 8, pp. 3420–8. August, 2009.

Boschetti, G., Rosati, G., and Rossi, A. "A haptic system for robotic assisted spine surgery". *Proceedings of 2005 IEEE Conference on Control Applications, 2005. CCA 2005.*, pp. 19–24. 2005.

Buchart, C., Bertelsen, A., and Borro, D. "viewitLib - A framework for the development of software for medical images visualization". In *Actas del XXX Congreso Anual de la Sociedad Española de Ingeniería Biomédica (CASEIB 2012)*. San Sebastián, Spain. 2012.

Casals, A., Frigola, M., and Amat, J. "La Robótica, una valiosa herramienta en Cirugía". *Revista Iberoamericana de Automática e Informática Industrial*, Vol. 6, N. 1, pp. 5–19. January, 2009.

Chung, G. B., Kim, S., Lee, S. G., Yi, B.-J., Kim, W., Oh, S. M., Kim, Y. S., So, B. R., Park, J. I., and Oh, S. H. "An image-guided robotic surgery system for spinal fusion". *International journal of control, automation, and systems*, Vol. 4, N. 1, pp. 30 – 41. 2006.

Cleary, K., Clifford, M., Stoianovici, D., Freedman, M., Mun, S. K., and Watson, V. "Technology improvements for image-guided and minimally invasive spine procedures." *IEEE transactions on information technology in biomedicine : a publication of the IEEE Engineering in Medicine and Biology Society*, Vol. 6, N. 4, pp. 249–61. December, 2002.

Cleary, K., Watson, V., Lindisch, D., Taylor, R. H., Fichtinger, G., Xu, S., White, C. S., Donlon, J., Taylor, M., Patriciu, A., Mazilu, D., and Stoianovici, D. "Precision placement of instruments for minimally invasive procedures using a "needle driver" robot." *The international journal of medical robotics + computer assisted surgery : MRCAS*, Vol. 1, N. 2, pp. 40–7. January, 2005.

Davis, M. H., Khotanzad, A., Flamig, D. P., and Harms, S. E. "A physics-based coordinate transformation for 3-D image matching." *IEEE transactions on medical imaging*, Vol. 16, N. 3, pp. 317–28. June, 1997.

Devito, D. P., Kaplan, L., Dietl, R., Pfeiffer, M., Horne, D., Silberstein, B., Hardenbrook, M., Kiriyanthan, G., Barzilay, Y., Bruskin, A., Sackerer, D., Alexandrovsky, V., Stüer, C., Burger, R., Maeurer, J., Gordon, D. G., Schoenmayr, R., Friedlander, A., Knoller, N., Schmieder, K., Pechlivanis, I., Kim, I.-S., Meyer, B., and Shoham, M. "Clinical Acceptance and Accuracy Assessment of Spinal Implants Guided With SpineAssist Surgical Robot: Retrospective Study." *Spine*, Vol. 35, N. 24, pp. 2109–2115. November, 2010.

Dogdas, B., Shattuck, D. W., and Leahy, R. M. "Segmentation of skull and scalp in 3-D human MRI using mathematical morphology." *Human brain mapping*, Vol. 26, N. 4, pp. 273–85. December, 2005.

Dozio, L. and Mantegazza, P. "Real time distributed control systems using RTAI". In *Sixth IEEE International Symposium on Object-Oriented Real-Time Distributed Computing, 2003.*, pp. 11–18. Hakodate, Hokkaido, Japan. 2003.

Faugeras, O. *3D computer vision: a geometric viewpoint.* MIT Press. 1993.

Fitzpatrick, J. M. and West, J. B. "The distribution of target registration error in rigid-body point-based registration." *IEEE transactions on medical imaging*, Vol. 20, N. 9, pp. 917–27. September, 2001.

Fitzpatrick, J. M., West, J. B., and Maurer, C. R. "Predicting error in rigid-body point-based registration." *IEEE transactions on medical imaging*, Vol. 17, N. 5, pp. 694–702. October, 1998.

Foley, K. T., Simon, D. A., and Rampersaud, Y. R. "Virtual fluoroscopy: computer-assisted fluoroscopic navigation." *Spine*, Vol. 26, N. 4, pp. 347–51. February, 2001.

Gendrin, C., Markelj, P., Pawiro, S. A., Spoerk, J., Bloch, C., Weber, C., Figl, M., Bergmann, H., Birkfellner, W., Likar, B., and Pernus, F. "Validation for 2D/3D registration. II: The comparison of intensity- and gradient-based merit functions using a new gold standard data set." *Medical physics*, Vol. 38, N. 3, pp. 1491–502. March, 2011.

Gerszten, P. C., Burton, S. A., Ozhasoglu, C., and Welch, W. C. "Radiosurgery for spinal metastases: clinical experience in 500 cases from a single institution." *Spine*, Vol. 32, N. 2, pp. 193–9. January, 2007.

Ghadimi, S., Abrishami-Moghaddam, H., Kazemi, K., Grebe, R., Goundry-Jouet, C., and Wallois, F. "Segmentation of scalp and skull in neonatal MR images using probabilistic atlas and level set method."

*Conference proceedings : ... Annual International Conference of the IEEE Engineering in Medicine and Biology Society. IEEE Engineering in Medicine and Biology Society. Conference*, Vol. 2008, pp. 3060–3. January, 2008.

Golub, G. H. and van Loan, C. F. *Matrix Computations*. Johns Hopkins University Press, Baltimore, MD. 1983.

Gomes, P. "Surgical robotics: Reviewing the past, analysing the present, imagining the future". *Robotics and Computer-Integrated Manufacturing*, Vol. 27, N. 2, pp. 261–266. April, 2011.

Gray, H. *Anatomy of the human body* (ISBN: 1-58734-102-6). Philadelphia Lea & Febiger, 20th edition. 1918.

Gremban, K., Thorpe, C., and Kanade, T. "Geometric camera calibration using systems of linear equations". In *Proceedings of IEEE International Conference on Robotics and Automation*, pp. 562–567. 1988.

Hadomi, O. "Robotic Spine Surgery by Mazor Robotics". 2012.

Haidegger, T., Xia, T., and Kazanzides, P. "Accuracy improvement of a neurosurgical robot system". In *2008 2nd IEEE RAS & EMBS International Conference on Biomedical Robotics and Biomechatronics*, pp. 836–841. October, 2008.

Hajnal, J. V., Hawkes, D. J., and Hill, D. L. *Medical image registration* (ISBN: 978-0-8493-0064-6). CRC Press. 2001.

Hamilton, A. J., Lulu, B. A., Fosmire, H., Stea, B., and Cassady, J. R. "Preliminary clinical experience with linear accelerator-based spinal stereotactic radiosurgery." *Neurosurgery*, Vol. 36, N. 2, pp. 311–9. February, 1995.

Hartley, R. and Zisserman, A. *Multiple view geometry in computer vision* (ISBN: 0521 54051 8). Cambridge University Press, 2nd edition. 2003.

Hempel, E., Fischer, H., Gumb, L., Höhn, T., Krause, H., Voges, U., Breitwieser, H., Gutmann, B., Durke, J., Bock, M., and Melzer, A. "An MRI-Compatible Surgical Robot for Precise Radiological Interventions". *Computer Aided Surgery*, Vol. 8, N. 4, pp. 180–191. January, 2003.

Ho, A. K., Fu, D., Cotrutz, C., Hancock, S. L., Chang, S. D., Gibbs, I. C., Maurer, C. R., and Adler, J. R. “A study of the accuracy of cyberknife spinal radiosurgery using skeletal structure tracking.” *Neurosurgery*, Vol. 60, N. 2 Suppl 1, pp. ONS147–S156; discussion ONS156. 2007.

Holly, L. T. “Image-guided spinal surgery.” *The international journal of medical robotics + computer assisted surgery : MRCAS*, Vol. 2, N. 1, pp. 7–15. March, 2006.

Horn, B. “Closed-form solution of absolute orientation using unit quaternions”. *Journal of the Optical Society of America*, Vol. 4, N. 4, pp. 629–642. 1987.

Hurvitz, A. and Joskowicz, L. “Registration of a CT-like atlas to fluoroscopic X-ray images using intensity correspondences”. *International Journal of Computer Assisted Radiology and Surgery*, Vol. 3, N. 6, pp. 493–504. October, 2008.

Ibáñez, L., Schroeder, W., Ng, L., and Cates, J. *The ITK Software Guide* (ISBN: 1-930934-15-7). Kitware Inc., 1st edition. 2005.

Jaffray, D. A., Siewerdsen, J. H., Wong, J. W., and Martinez, A. A. “Flat-panel cone-beam computed tomography for image-guided radiation therapy.” *International journal of radiation oncology, biology, physics*, Vol. 53, N. 5, pp. 1337–49. August, 2002.

Jain, A., Kon, R., Zhou, Y., and Fichtinger, G. “C-Arm calibration - is it really necessary?” In Duncan, J. S. and Gerig, G., editors, *Medical Image Computing and Computer-Assisted Intervention ( MICCAI 2005)*, volume 3749 of *Lecture Notes in Computer Science*, pp. 639–646. Berlin, Heidelberg. 2005.

Jin, H., Hu, Y., Li, F., and Zhang, J. “Safety Design and Control Algorithm for Robotic Spinal Surgical System”. In *2011 First International Conference on Robot, Vision and Signal Processing*, pp. 190–194. November, 2011.

Jin, H., Wang, L., Hu, Y., Zhang, J., and Zheng, Z. “Design and control strategy of robotic spinal surgical system”. In *The 2011 IEEE/ICME International Conference on Complex Medical Engineering*, pp. 627–632. May, 2011.

Ju, H., Zhang, J., An, G., Pei, X., and Xing, G. "A Robot-Assisted System for Minimally Invasive Spine Surgery of Percutaneous Vertebroplasty Based on CT Images". In *2008 IEEE Conference on Robotics, Automation and Mechatronics*, pp. 290–295. September, 2008.

Kadoury, S., Labelle, H., and Paragios, N. "Automatic inference of articulated spine models in CT images using high-order Markov Random Fields." *Medical image analysis*, Vol. 15, N. 4, pp. 426–37. August, 2011.

Kantelhardt, S. R., Martinez, R., Baerwinkel, S., Burger, R., Giese, A., and Rohde, V. "Perioperative course and accuracy of screw positioning in conventional, open robotic-guided and percutaneous robotic-guided, pedicle screw placement." *European spine journal : official publication of the European Spine Society, the European Spinal Deformity Society, and the European Section of the Cervical Spine Research Society*, Vol. 20, N. 6, pp. 860–8. June, 2011.

Karas, C. S. and Chiocca, E. A. "Neurosurgical robotics: a review of brain and spine applications". *Journal of Robotic Surgery*, Vol. 1, N. 1, pp. 39–43. February, 2007.

Kazanzides, P., Zuhars, J., Mittelstadt, B., and Taylor, R. "Force sensing and control for a surgical robot". In *Proceedings 1992 IEEE International Conference on Robotics and Automation*, pp. 612–617. Nice. 1992.

Kennedy, C. and Desai, J. "Modelling and control of the Mitsubishi PA-10 robot arm harmonic drive system". *IEEE/ASME Transactions on Mechatronics*, Vol. 10, N. 3, pp. 263–274. June, 2005.

Kim, M. J., Ha, Y., Yang, M. S., Yoon, D. H., Kim, K. N., Kim, H., Yang, J. W., Lee, J. Y. K., Yi, S., Jung, W. J., and Rha, K. H. "Robot-assisted anterior lumbar interbody fusion (ALIF) using retroperitoneal approach." *Acta neurochirurgica*, Vol. 152, N. 4, pp. 675–9. April, 2010.

Kim, S., Chung, J., Yi, B.-J., and Kim, Y. S. "An assistive image-guided surgical robot system using O-arm fluoroscopy for pedicle screw insertion: preliminary and cadaveric study." *Neurosurgery*, Vol. 67, N. 6, pp. 1757–67; discussion 1767. December, 2010.

Kirkpatrick, S., Gelatt, C. D., and Vecchi, M. P. "Optimization by simulated annealing." *Science (New York, N.Y.)*, Vol. 220, N. 4598, pp. 671–80. May, 1983.

Kitware. *VTK User's Guide* (ISBN: 978-1-930934-23-8). Kitware Inc., 11th edition. 2010.

Klein, S., Staring, M., Murphy, K., Viergever, M. a., and Pluim, J. P. W. "Elastix: a Toolbox for Intensity-Based Medical Image Registration." *IEEE transactions on medical imaging*, Vol. 29, N. 1, pp. 196–205. January, 2010.

Kostrzewski, S., Duff, J. M., Baur, C., and Olszewski, M. "Robotic system for cervical spine surgery." *The international journal of medical robotics + computer assisted surgery : MRCAS*, Vol. 8, N. 2, pp. 184–190. June, 2012.

Kubias, A., Deinzer, F., Feldmann, T., Paulus, D., Schreiber, B., and Brunner, T. "2D/3D image registration on the GPU". *Pattern Recognition and Image Analysis*, Vol. 18, N. 3, pp. 381–389. September, 2008.

Lee, J., Hwang, I., Kim, K., Choi, S., Chung, W. K., and Kim, Y. S. "Cooperative robotic assistant with drill-by-wire end-effector for spinal fusion surgery". *Industrial Robot: An International Journal*, Vol. 36, N. 1, pp. 60–72. 2009.

Lee, J., Kim, S., Kim, Y. S., Chung, W. K., and Kim, M. "Automated surgical planning and evaluation algorithm for spinal fusion surgery with three-dimensional pedicle model". In *2011 IEEE/RSJ International Conference on Intelligent Robots and Systems*, pp. 2524–2531. September, 2011.

Lee, J. Y. K., O'Malley, B. W., Newman, J. G., Weinstein, G. S., Lega, B., Diaz, J., and Grady, M. S. "Transoral robotic surgery of craniocervical junction and atlantoaxial spine: a cadaveric study." *Journal of neurosurgery. Spine*, Vol. 12, N. 1, pp. 13–8. January, 2010.

Lemieux, L., Jagoe, R., Fish, D. R., Kitchen, N. D., and Thomas, D. G. "A patient-to-computed-tomography image registration method based on digitally reconstructed radiographs." *Medical physics*, Vol. 21, N. 11, pp. 1749–60. November, 1994.

Lieberman, I. H., Togawa, D., Kayanja, M. M., Reinhardt, M. K., Friedlander, A., Knoller, N., and Benzel, E. C. "Bone-mounted miniature robotic guidance for pedicle screw and translaminar facet screw placement: Part I–Technical development and a test case result." *Neurosurgery*, Vol. 59, N. 3, pp. 641–50; discussion 641–50. September, 2006.

Livyatan, H., Yaniv, Z., and Joskowicz, L. "Robust Automatic C-Arm Calibration for Fluoroscopy-Based Navigation: A Practical Approach". In Dohi, T. and Kikinis, R., editors, *Medical Image Computing and Computer-Assisted Intervention ( MICCAI 2002)*, volume 2489 of *Lecture Notes in Computer Science*, pp. 60–68. Berlin, Heidelberg. October, 2002.

Livyatan, H., Yaniv, Z., and Joskowicz, L. "Gradient-based 2-D/3-D rigid registration of fluoroscopic X-ray to CT." *IEEE transactions on medical imaging*, Vol. 22, N. 11, pp. 1395–406. November, 2003.

Lüthi, M., Lerch, A., Albrecht, T., Krol, Z., and Vetter, T. "A hierarchical, multi-resolution approach for model-based skull-segmentation in MRI volumes". In *Conference Proceedings 3D-Physiological Human*. Zermat, Switzerland. 2008.

Maintz, J. and Viergever, M. A. "A survey of medical image registration". *Medical Image Analysis*, Vol. 2, N. 1, pp. 1–36. March, 1998.

Markelj, P., Likar, B., and Pernus, F. "Standardized evaluation methodology for 3D/2D registration based on the Visible Human data set." *Medical physics*, Vol. 37, N. 9, pp. 4643–7. October, 2010.

Markelj, P., Tomaževič, D., Likar, B., and Pernuš, F. "A review of 3D/2D registration methods for image-guided interventions." *Medical image analysis*, Vol. 16, N. 3, pp. 642–61. April, 2012.

Markelj, P., Tomaževič, D., Pernuš, F., and Likar, B. "Robust 3-D/2-D registration of CT and MR to X-ray images based on gradient reconstruction". *International Journal of Computer Assisted Radiology and Surgery*, Vol. 3, N. 6, pp. 477–483. July, 2008.

Markelj, P., Tomazevic, D., Pernus, F., and Likar, B. T. "Robust gradient-based 3-D/2-D registration of CT and MR to X-ray images."

*IEEE transactions on medical imaging*, Vol. 27, N. 12, pp. 1704–14. December, 2008.

Mastrangelo, G., Fedeli, U., Fadda, E., Giovanazzi, A., Scoizzato, L., and Saia, B. "Increased cancer risk among surgeons in an orthopaedic hospital." *Occupational medicine (Oxford, England)*, Vol. 55, N. 6, pp. 498–500. September, 2005.

Melo, J., Bertelsen, A., Borro, D., and Sánchez, E. "Nuevo asistente robótico para cirugía: arquitectura y algoritmos de control". *Dyna Ingeniería e Industria*, Vol. 87, N. 3, pp. 647–654. 2012.

Melo, J., Sanchez, E., and Diaz, I. "Adaptive admittance control to generate real-time assistive fixtures for a COBOT in transpedicular fixation surgery". In *2012 4th IEEE RAS & EMBS International Conference on Biomedical Robotics and Biomechatronics (BioRob)*, pp. 1170–1175. June, 2012.

Melzer, A., Gutmann, B., Remmele, T., Wolf, R., Lukoscheck, A., Bock, M., Bardenheuer, H., and Fischer, H. "INNOMOTION for percutaneous image-guided interventions: principles and evaluation of this MR- and CT-compatible robotic system." *IEEE engineering in medicine and biology magazine : the quarterly magazine of the Engineering in Medicine & Biology Society*, Vol. 27, N. 3, pp. 66–73. 2008.

Merloz, P., Troccaz, J., Vouaillat, H., Vasile, C., Tonetti, J., Eid, A., and Plaweski, S. "Fluoroscopy-based navigation system in spine surgery". *Proceedings of the Institution of Mechanical Engineers, Part H: Journal of Engineering in Medicine*, Vol. 221, N. 7, pp. 813–820. January, 2007.

Moche, M., Zajonz, D., Kahn, T., and Busse, H. "MRI-guided procedures in various regions of the body using a robotic assistance system in a closed-bore scanner: preliminary clinical experience and limitations." *Journal of magnetic resonance imaging : JMRI*, Vol. 31, N. 4, pp. 964–74. April, 2010.

Muacevic, A., Staehler, M., Drexler, C., Wowra, B., Reiser, M., and Tonn, J.-C. "Technical description, phantom accuracy, and clinical feasibility for fiducial-free frameless real-time image-guided spinal radiosurgery." *Journal of neurosurgery. Spine*, Vol. 5, N. 4, pp. 303–12. October, 2006.

Niesing, B. “Robots for spine surgery”. *Fraunhofer magazine*, pp. 46–47. 2001.

Onogi, S., Gotoh, M., Nakajima, Y., Koyama, T., Tamura, Y., Kobayashi, E., Sugano, N., Sakuma, I., and Yonenobu, K. “Vertebral robotic puncture for minimally invasive spinal surgery: puncture accuracy evaluation for vertebral model”. *International journal of computer assisted radiology and surgery*, Vol. 4, N. supplement 1, pp. 121–122. 2009.

Onogi, S., Morimoto, K., Sakuma, I., Nakajima, Y., Koyama, T., Sugano, N., Tamura, Y., Yonenobu, S., Momoi, Y., Duncan, J., and Gerig, G. “Development of the Needle Insertion Robot for Percutaneous Vertebroplasy”. In Duncan, J. S. and Gerig, G., editors, *Medical Image Computing and Computer-Assisted Intervention (MICCAI 2005)*, volume 3750 of *Lecture Notes in Computer Science*, pp. 105–113. Berlin, Heidelberg. 2005.

Ortmaier, T., Weiss, H., Döbele, S., and Schreiber, U. “Experiments on robot-assisted navigated drilling and milling of bones for pedicle screw placement.” *The international journal of medical robotics + computer assisted surgery : MRCAS*, Vol. 2, N. 4, pp. 350–63. December, 2006.

Ortmaier, T., Weiss, H., Hagn, U., Grebenstein, M., Nickl, M., Albu-Schaffer, A., Ott, C., Jorg, S., Konietschke, R., Le-Tien, L., and Hirzinger, G. “A hands-on-robot for accurate placement of pedicle screws”. In *Proceedings 2006 IEEE International Conference on Robotics and Automation, 2006. ICRA 2006.*, number May, pp. 4179–4186. 2006.

Otake, Y., Armand, M., Armiger, R. S., Kutzer, M. D., Basafa, E., Kazanzides, P., and Taylor, R. H. “Intraoperative Image-based Multiview 2D/3D Registration for Image-Guided Orthopaedic Surgery: Incorporation of Fiducial-Based C-Arm Tracking and GPU-Acceleration.” *IEEE transactions on medical imaging*, Vol. 31, N. 4, pp. 948–62. April, 2012.

Otsu, N. “A Threshold Selection Method from Gray-Level Histograms”. *IEEE Transactions on Systems, Man, and Cybernetics*, Vol. 9, N. 1, pp. 62–66. 1979.

Pawiro, S. A., Markelj, P., Pernus, F., Gendrin, C., Figl, M., Weber, C., Kainberger, F., Nöbauer-Huhmann, I., Bergmeister, H., Stock, M., Georg, D., Bergmann, H., and Birkfellner, W. “Validation for 2D/3D registration. I: A new gold standard data set.” *Medical physics*, Vol. 38, N. 3, pp. 1481–90. March, 2011.

Péchaud, M., Jenkinson, M., and Smith, S. “MRI-based estimation of brain, skull and scalp surfaces”. Technical report, Oxford University, Oxford, United Kingdom. 2006.

Penney, G. P., Weese, J., Little, J. A., Desmedt, P., Hill, D. L., and Hawkes, D. J. “A comparison of similarity measures for use in 2-D-3-D medical image registration.” *IEEE transactions on medical imaging*, Vol. 17, N. 4, pp. 586–95. August, 1998.

Pieper, S., Lorensen, B., Schroeder, W., and Kikinis, R. “The NA-MIC Kit: ITK, VTK, Pipelines, Grids and 3D Slicer as An Open Platform for the Medical Image Computing Community”. In *3rd IEEE International Symposium on Biomedical Imaging: Macro to Nano, 2006.*, pp. 698–701. 2006.

Pluim, J. P. W., Maintz, J. B. A., and Viergever, M. A. “Mutual-information-based registration of medical images: a survey.” *IEEE transactions on medical imaging*, Vol. 22, N. 8, pp. 986–1004. August, 2003.

Ponnusamy, K., Chewning, S., and Mohr, C. “Robotic approaches to the posterior spine.” *Spine*, Vol. 34, N. 19, pp. 2104–9. September, 2009.

Press, W. H., Teukolsky, S. A., Vetterling, W. T., and Flannery, B. P. *Numerical recipes* (ISBN: 978-0-521-88068-8). Cambridge University Press, third edition. 2007.

Rampersaud, Y. R., Simon, D. A., and Foley, K. T. “Accuracy requirements for image-guided spinal pedicle screw placement.” *Spine*, Vol. 26, N. 4, pp. 352–9. February, 2001.

Rifai, H., Bloch, I., Hutchinson, S., Wiart, J., and Garnero, L. “Segmentation of the skull in MRI volumes using deformable model and taking the partial volume effect into account”. *Medical Image Analysis*, Vol. 4, N. 3, pp. 219–233. September, 2000.

Rohlfing, T., Brandt, R., Menzel, R., and Maurer, C. R. “Evaluation of atlas selection strategies for atlas-based image segmentation with application to confocal microscopy images of bee brains.” *NeuroImage*, Vol. 21, N. 4, pp. 1428–42. April, 2004.

Romanelli, P. and Adler, J. R. “Technology Insight: image-guided robotic radiosurgery–a new approach for noninvasive ablation of spinal lesions.” *Nature clinical practice. Oncology*, Vol. 5, N. 7, pp. 405–14. July, 2008.

Rosati, G., Rossi, A., Boschetti, G., and Trevisani, A. “First experimental results of an integrated robotic system for haptic teleoperation”. In *2007 IEEE International Symposium on Industrial Electronics*, pp. 3138–3143. June, 2007.

Rudin, S., Bednarek, D. R., and Wong, R. “Accurate characterization of image intensifier distortion.” *Medical physics*, Vol. 18, N. 6, pp. 1145–51. 1991.

Russakoff, D. B., Rohlfing, T., Mori, K., Rueckert, D., Ho, A., Adler, J. R., and Maurer, C. R. “Fast generation of digitally reconstructed radiographs using attenuation fields with application to 2D-3D image registration.” *IEEE transactions on medical imaging*, Vol. 24, N. 11, pp. 1441–54. November, 2005.

Sadowsky, O. *Image registration and hybrid volume reconstruction of bone anatomy using a statistical shape atlas*. PhD thesis, The Johns Hopkins University. 2008.

Santos-Munné, J. J., Peshkin, M. A., Stulberg, S. D., Mirkovic, S., and Kienzle, T. C. “A Stereotactic / Robotic System for Pedicle Screw Placement”. In Morgan, K., Satava, R., Sieburg, H., Mattheus, R., and Christensen, J., editors, *Proceedings of the Medicine Meets Virtual Reality III Conference*, pp. 326–333. San Diego. 1995.

Sautot, P., Cinquin, P., Lavallee, S., and Troccaz, J. “Computer assisted spine surgery: A first step toward clinical, application in orthopaedics”. In *Proceedings of the Annual International Conference of the IEEE Engineering in Medicine and Biology Society*, pp. 1071–1072. October, 1992.

Schnabel, J. A., Rueckert, D., Quist, M., Blackall, J., Castellano-Smith, A., Hartkens, T., Penney, G., Hall, W., Liu, H., Truwit, C., Gerritsen, F., Hill, D., and Hawkes, D. "A Generic Framework for Non-rigid Deformation Based on Non-uniform Multi-level Free-form Deformations". In Niessen, W. J. and Viergever, M. A., editors, *Medical Image Computing and Computer-Assisted Intervention ( MICCAI 2001)*, volume 2208 of *Lecture Notes in Computer Science*, pp. 573–581. Berlin, Heidelberg. October, 2001.

Schönemann, P. "A generalized solution of the orthogonal Procrustes problem". *Psychometrika*, Vol. 31, pp. 1–10. 1966.

Shan, Z. Y., Hua, C.-H., Ji, Q., Parra, C., Ying, X., Krasin, M. J., Merchant, T. E., Kun, L. E., and Reddick, W. E. "A knowledge-guided active model method of skull segmentation on T1-weighted MR images". In *Proceedings of SPIE*, volume 6512, pp. 65122R–65122R–6. 2007.

Shoham, M. "Robotic Surgery: Enabling Technology?" In Rosen, J., Hannaford, B., and Satava, R. M., editors, *Surgical Robotics*, chapter 11, pp. 247–255. Springer US, Boston, MA. 2011.

Shoham, M., Burman, M., Zehavi, E., Joskowicz, L., Batkilin, E., and Kunicher, Y. "Bone-mounted miniature robot for surgical procedures: concept and clinical applications". *IEEE Transactions on Robotics and Automation*, Vol. 19, N. 5, pp. 893–901. October, 2003.

Singer, G. "Occupational radiation exposure to the surgeon." *The Journal of the American Academy of Orthopaedic Surgeons*, Vol. 13, N. 1, pp. 69–76. January, 2005.

Sled, J. G., Zijdenbos, A. P., and Evans, A. C. "A nonparametric method for automatic correction of intensity nonuniformity in MRI data." *IEEE transactions on medical imaging*, Vol. 17, N. 1, pp. 87–97. February, 1998.

Song, Y., An, G., and Zhang, J. "Positioning Accuracy of a Medical Robotic System for Spine Surgery". In *2009 2nd International Conference on Biomedical Engineering and Informatics*, pp. 1–5. 2009.

Spall, J. "Overview of the Simultaneous Perturbation Method for Efficient Optimization". *Johns Hopkins APL Technical Digest*, Vol. 19, N. 4, pp. 482 – 492. 1998.

Steininger, P., Neuner, M., and Schubert, R. "An extended ITK-based Framework for Intensity-based 2D/3D-Registration". 2009.

Stoianovici, D., Cleary, K., Patriciu, A., Mazilu, D., Stanimir, A., Craciunoiu, N., Watson, V., and Kavoussi, L. "Acubot: a robot for radiological interventions". *IEEE Transactions on Robotics and Automation*, Vol. 19, N. 5, pp. 927–930. October, 2003.

Strang, G. *Linear algebra and its applications* (ISBN: 978-0-534-42200-4). Thomson Brooks/Cole, 4th edition. 2006.

Studholme, C., Hill, D., and Hawkes, D. "An overlap invariant entropy measure of 3D medical image alignment". *Pattern Recognition*, Vol. 32, N. 1, pp. 71–86. January, 1999.

Styner, M., Brechbühler, C., Székely, G., and Gerig, G. "Parametric estimate of intensity inhomogeneities applied to MRI." *IEEE transactions on medical imaging*, Vol. 19, N. 3, pp. 153–65. March, 2000.

Sukovich, W., Brink-Danan, S., and Hardenbrook, M. "Miniature robotic guidance for pedicle screw placement in posterior spinal fusion: early clinical experience with the SpineAssist." *The international journal of medical robotics + computer assisted surgery : MRCAS*, Vol. 2, N. 2, pp. 114–22. June, 2006.

Tate, P. M., Lachine, V., Fu, L., Croitoru, H., and Sati, M. "Performance and Robustness of Automatic Fluoroscopic Image Calibration in a New Computer Assisted Surgery System". In *Medical Image Computing and Computer-Assisted Intervention ( MICCAI 2001)*, pp. 1130–1136. 2001.

Tjardes, T., Shafizadeh, S., Rixen, D., Paffrath, T., Bouillon, B., Steinhausen, E. S., and Baethis, H. "Image-guided spine surgery: state of the art and future directions." *European spine journal : official publication of the European Spine Society, the European Spinal Deformity Society, and the European Section of the Cervical Spine Research Society*, Vol. 19, N. 1, pp. 25–45. January, 2010.

Togawa, D., Kayanja, M. M., Reinhardt, M. K., Shoham, M., Balter, A., Friedlander, A., Knoller, N., Benzel, E. C., and Lieberman, I. H. "Bone-mounted miniature robotic guidance for pedicle screw and translaminar facet screw placement: part 2–Evaluation of system accuracy.” *Neurosurgery*, Vol. 60, N. 2 Suppl 1, pp. ONS129–39; discussion ONS139. February, 2007.

Tokuda, J., Fischer, G. S., Papademetris, X., Yaniv, Z., Ibanez, L., Cheng, P., Liu, H., Blevins, J., Arata, J., Golby, A. J., Kapur, T., Pieper, S., Burdette, E. C., Fichtinger, G., Tempany, C. M., and Hata, N. “OpenIGTLink: an open network protocol for image-guided therapy environment.” *The international journal of medical robotics + computer assisted surgery : MRCAS*, Vol. 5, N. 4, pp. 423–34. December, 2009.

Tomaževič, D., Likar, B., and Pernuš, F. “”Gold standard” data for evaluation and comparison of 3D/2D registration methods.” *Computer aided surgery : official journal of the International Society for Computer Aided Surgery*, Vol. 9, N. 4, pp. 137–44. January, 2004.

Tomaževič, D., Likar, B., and Pernuš, F. “3-D/2-D registration by integrating 2-D information in 3-D.” *IEEE transactions on medical imaging*, Vol. 25, N. 1, pp. 17–27. January, 2006.

Tomaževič, D., Likar, B., Slivnik, T., and Pernuš, F. “3-D/2-D registration of CT and MR to X-ray images.” *IEEE transactions on medical imaging*, Vol. 22, N. 11, pp. 1407–16. November, 2003.

Tovar-Arriaga, S., Tita, R., Pedraza-Ortega, J. C., Gorrostieta, E., and Kalender, W. A. “Development of a robotic FD-CT-guided navigation system for needle placement-preliminary accuracy tests.” *The international journal of medical robotics + computer assisted surgery : MRCAS*, Vol. 7, N. 2, pp. 225–36. June, 2011.

Tustison, N. and Gee, J. “N4ITK: Nick’s N3 ITK Implementation for MRI Bias Field Correction”. *Insight Journal*, 2010.

Umeyama, S. “Least-squares estimation of transformation parameters between two point patterns”. *IEEE Transactions on Pattern Analysis and Machine Intelligence*, Vol. 13, N. 4, pp. 376–380. April, 1991.

van de Kraats, E. B., Penney, G. P., Tomaževič, D., van Walsum, T., and Niessen, W. J. “Standardized evaluation methodology for 2-D-3-D registration.” *IEEE transactions on medical imaging*, Vol. 24, N. 9, pp. 1177–89. September, 2005.

van der Bom, I. M. J. *2D-3D image registration in diagnostic and interventional x-ray imaging* (ISBN: 9789039354513). PhD thesis, Utrecht Univeristy. 2010.

van der Bom, I. M. J., Klein, S., Staring, M., Homan, R., Bartels, L. W., and Pluim, J. P. W. *Evaluation of optimization methods for intensity-based 2D-3D registration in x-ray guided interventions*, volume 7962. Society of Photo-Optical Instrumentation Engineers (SPIE). 2011.

Černý, V. "Thermodynamical approach to the traveling salesman problem: An efficient simulation algorithm". *Journal of Optimization Theory and Applications*, Vol. 45, N. 1, pp. 41–51. January, 1985.

Wang, D., Shi, L., Chu, W. C. W., Cheng, J. C. Y., and Heng, P. A. "Segmentation of human skull in MRI using statistical shape information from CT data." *Journal of magnetic resonance imaging : JMRI*, Vol. 30, N. 3, pp. 490–8. September, 2009.

Wang, T., Luan, S., Hu, L., Liu, Z., Li, W., and Jiang, L. "Force-based control of a compact spinal milling robot." *The international journal of medical robotics + computer assisted surgery : MRCAS*, Vol. 6, N. 2, pp. 178–85. June, 2010.

Weese, J., Buzug, T. M., Lorenz, C., and Fassnacht, C. "An Approach to 2D / 3D Registration of a Vertebra in 2D X-ray Fluoroscopies with 3D CT Images". *Lecture Notes in Computer Science*, Vol. 1205, pp. 119–128. 1997.

West, J., Fitzpatrick, J. M., Wang, M. Y., Dawant, B. M., Maurer, C. R., Kessler, R. M., and Maciunas, R. J. "Retrospective intermodality registration techniques for images of the head: surface-based versus volume-based." *IEEE transactions on medical imaging*, Vol. 18, N. 2, pp. 144–50. February, 1999.

Westin, C.-F., Bhalerao, A., Knutsson, H., and Kikinis, R. "Using local 3D structure for segmentation of bone from computer tomography images". In *Proceedings of IEEE Computer Society Conference on Computer Vision and Pattern Recognition*, pp. 794–800. 1997.

Wolberg, G. *Digital image warping* (ISBN: 0818689447). 1st edition. 1990.

Wu, J., Kim, M., Peters, J., Chung, H., and Samant, S. S. “Evaluation of similarity measures for use in the intensity-based rigid 2D-3D registration for patient positioning in radiotherapy.” *Medical physics*, Vol. 36, N. 12, pp. 5391–403. December, 2009.

Yang, M. S., Jung, J. H., Kim, J. M., Kim, C. H., Yi, S., Ha, Y., Kim, K. N., and Yoon, D. H. “Current and Future of Spinal Robot Surgery”. *Korean Journal of Spine*, Vol. 7, N. 2, pp. 61–65. June, 2010.

Yu, C., Main, W., Taylor, D., Kuduvalli, G., Apuzzo, M. L. J., and Adler, J. R. “An anthropomorphic phantom study of the accuracy of Cyberknife spinal radiosurgery.” *Neurosurgery*, Vol. 55, N. 5, pp. 1138–49. November, 2004.

Zheng, G. and Zhang, X. “Robust automatic detection and removal of fiducial projections in fluoroscopy images: an integrated solution.” *Medical engineering & physics*, Vol. 31, N. 5, pp. 571–80. June, 2009.